FUEL COMPOSITION TRANSIENTS IN SOLID OXIDE FUEL CELL GAS TURBINE HYBRID SYSTEMS FOR POLYGENERATION APPLICATIONS

FUEL COMPOSITION TRANSIENTS IN SOLID OXIDE FUEL CELL GAS TURBINE HYBRID SYSTEMS FOR POLYGENERATION APPLICATIONS

By NOR FARIDA BINTI HARUN, B. Eng, M. Eng

A Thesis
Submitted to the School of Graduate Studies
in Partial Fulfilment of the Requirements
for the Degree of
Doctor of Philosophy

McMaster University

DOCTOR OF PHILOSOPHY (2015) McMaster University
(Chemical Engineering) Hamilton, Ontario

TITLE : Fuel Composition Transients in Solid Oxide Fuel Cell Gas Turbine Hybrid Systems for Polygeneration Applications
AUTHOR : Nor Farida Harun, B.Eng. (Universiti Teknologi Malaysia), M.Eng. (Universiti Teknologi Malaysia)
SUPERVISOR : Assistant Professor Thomas A. Adams II
NUMBER OF PAGES : xvii, 137

ABSTRACT

The potential of Solid Oxide Fuel Cell Gas Turbine (SOFC/GT) hybrid systems for fuel flexibility makes this technology greatly attractive for system hybridization with various fuel processing units in advanced power generation systems and/or polygeneration plants. Such hybrid technologies open up the possibility and opportunities for improvement of system reliabilities and operabilities. However, SOFC/GT hybrid systems have not yet reached their full potential in term of capitalizing on the synergistic benefits of fuel cell and gas turbine cycles.

Integrating fuel cells with gas turbine and other components for transient operations increases the risk for exposure to rapid and significant changes in process dynamics and performance, which are primarily associated with fuel cell thermal management and compressor surge. This can lead to severe fuel cell failure, shaft overspeed, and gas turbine damage. Sufficient dynamic control architectures should be made to mitigate undesirable dynamic behaviours and/or system constraint violations before this technology can be commercialized. But, adequate understanding about dynamic coupling interactions between system components in the hybrid configuration is essential.

Considering this critical need for system identification of SOFC/GT hybrid in fuel flexible systems, this thesis investigates the dynamic performance of SOFC/GT hybrid technology in response to fuel composition changes. Hardware-based simulations, which combined actual equipment of direct-fired recuperated gas turbine system and simulated fuel cell subsystem, are used to experimentally investigate the impacts of fuel composition changes on the SOFC/GT hybrid system, reducing potentially large inaccuracies in the dynamic study.

The impacts of fuel composition in a closed loop operation using turbine speed control were first studied for the purpose of simplicity. Quantification of safe operating conditions for dynamic operations associated with carbon deposition and compressor stall and surge was done prior to the execution of experimentation. With closed loop tests, the dynamic performance of SOFC/GT hybrid technology due to a transition in gas composition could be uniquely characterized, eliminating the interactive effects of other process variables and disturbances. However, for an extensive system analysis, open loop tests (without turbine speed control) were also conducted such that potential coupling impacts exhibited by the SOFC/GT hybrid during fuel transients could be explored. Detailed characterization of SOFC/GT dynamic performance was performed to identify the interrelationship of each fuel cell variable in response to fuel composition dynamics and their contributions to operability of the system.

As a result of lowering LHV content in the fuel feed, which involved a transition from coal-derived syngas to humidified methane composition in the SOFC anode, the system demonstrated a dramatic transient increase in fuel cell thermal effluent with a time scale of seconds, resulting from the conversion of fuel cell thermal energy storage into chemical energy. This transient was highly associated with the dynamics of solid and gas temperatures, heat flux, heat generation in the fuel cell due to perturbations in methane reforming, water-gas shifting, and electrochemical hydrogen oxidation.

In turn, the dramatic changes in fuel cell thermal effluent resulting from the anode composition changes drove the turbine transients that caused significant cathode airflow

fluctuations. This study revealed that the cathode air mass flow change was a major linking event during fuel composition changes in the SOFC/GT hybrid system. Both transients in cathode air mass flow and anode composition significantly affected the hybrid system performance. Due to significant coupling between fuel composition transitions and cathode air mass flow changes, thermal management of SOFC/GT hybrid systems might be challenging. Yet, it was suggested that modulating cathode air flow offered promise for effective dynamic control of SOFC/GT hybrid systems with fuel flexibility.

ACKNOWLEDGEMENTS

In The Name of Allah, The Most Beneficent, The Most Merciful.. Subhanallah..

First and foremost, I would like to thank my supervisor, Dr. Thomas A. Adams II, and my technical advisor from NETL, Dr. David Tucker for their guidance throughout my PhD project. I greatly appreciate their patience in teaching and supporting me. Indeed, both of you are really special and respectful persons in my life. Thanks very much for the encouragement and all opportunities given to me. I always remember my first trip going to the U.S to visit NETL in 2011, the trip that drove me to experience and explore a new life that I have never imagined. I also want to express my gratitude to my PhD committee members, Dr. Chris Swartz and Dr. Tony Petric as well as Prof. Alberto Traverso from University of Genoa, Italy for giving valuable inputs to the project.

Thanks to my family, ibu and abah, my sisters and my brothers including the two little angles in my family for their endless love and encouragement. I am so blessed to have such a wonderful and awesome family who are always there for me whenever ups and downs, keeping me motivated and happy during my study. Thanks for believing in me without a slightest doubt.

Special thanks to Zamry and Erlita for being my best companions when I faced a lot of hard times along my PhD journey and my stay abroad. Thanks a lot for your understanding, friendship, and financial supports :p . I also want to thank Nana Zhou from Chongqing University, China for being my best friend during my stay in Morgantown. Thanks Zamry, Erlita and Nana, thanks for everything! There is no word that can describe how special you guys in my life!

To Paolo, I am very lucky to know you. I really appreciate your guidance and your help in HyPer research, especially when nothing was working previously. Working with you was always fun and motivated! Big thanks to Valentina and Alessio for helping me in many ways. Definitely you guys added my list of Italian friends.

I want to express my thanks to the NETL family too, Dave Ruehl and other technicians for providing technical supports to keep the facility running for my tests. To my bestfriends, Zai, Ana, and Ala, and to the MyMac members, the 8th St girls, the Gilmore girls and all, whoever I might forget to mention here, many thanks for your time, helps, and motivation.

You are all the greatest blessings in my life. With your never ending loves, prayers and encouragement, nothing is impossible for me. I am truly thankful, JZK.

TABLE OF CONTENTS

Abstract iii
Acknowledgements v
Table of Contents vi
List of Figures ix
List of Tables xiv
List of Abbreviations and Symbols xv
Declaration of Academic Achievement xvii

1 Introduction 1
1.1 Emerging Solid Oxide Fuel Cell Technologies Toward Energy Sustainability 1
1.2 Role of Solid Oxide Fuel Cell Gas Turbine Hybrid in Meeting Future Energy Needs 4
1.3 Research Motivation: Potential and Challenges in Solid Oxide Fuel Cell Gas Turbine (SOFC/GT) Hybrid Systems for Fuel Flexible Operations 6
1.4 Problem Statement 8
1.5 Research Objective 8
1.6 Thesis Outline 9
1.7 References 11

2 Fuel Composition Transients in Fuel Cell Turbine Hybrid for Polygeneration Applications 14
2.1 Publication Highlights 14
2.2 Abstract 15
2.3 Introduction 15
2.4 Methodology 17
2.4.1 1D-Real Time Fuel Cell Dynamic Model 17
2.4.2 SOFC Fuel Composition Scoping Study 19
2.4.3 Hardware-based Hybrid Test Facility 21
2.4.4 Hardware-based Simulation Procedures 21
2.5 Results and Discussion 22
2.5.1 The Dynamic Response of Thermal Effluent 22
2.5.2 The Impact of Thermal Effluent on Turbine Load 24
2.5.3 The Response of Turbine Inlet Temperature and SOFC Cathode Inlet Temperature 26
2.5.4 The Dynamic Behaviour of the System Air Mass Flow 29
2.5.5 The Transient Impact on the Fuel Cell Performance 31
2.6 Conclusion 32
2.7 Acknowledgement 33
2.8 References 33

3 Open Loop and Closed Loop Performance of Solid Oxide Fuel Cell Turbine Hybrid Systems during Fuel Composition Changes 35
3.1 Publication Highlights 35
3.2 Abstract 36
3.3 Introduction 36
3.4 SOFC/GT Hybrid Test Facility 38
3.5 Hardware-based Simulation of SOFC/GT Hybrid 39
3.6 Test Procedure 41
3.7 Result and Analysis 43
3.7.1 Fuel Cell Thermal Effluent, Q, and Turbine Temperatures 43
3.7.2 Cathode Inlet Mass Flow 46
3.7.3 Cathode Inlet Pressure 47
3.7.4 Cathode Inlet Temperature 47
3.7.5 Analysis of Mitigating versus Propagating Effects 49
3.7.5.1 Open Loop Transients 49
3.7.5.2 Closed Loop Transients 50
3.8 Conclusions and Future Work 50
3.9 Acknowledgement 51
3.10 References 52

4 Impact of Fuel Composition Transients on SOFC Performance in Gas Turbine Hybrid Systems 53
4.1 Publication Highlights 53
4.2 Abstract 54
4.3 Introduction 54
4.4 Methodology 56
4.4..1 Hardware System 56
4.4.2 Model Description 57
4.4.3 Hardware-based Simulation of SOFC Fuel Composition Transient 59
4.5 Results and Discussions 60
4.5.1 Distributed Analysis for the Initial Steady State with Coal-Derived Syngas Feed 60
4.5.2 Transient Analysis of Fuel Composition Change Impacts 62
4.5.2.1 Compositional Gradient and Localized Fuel Utilization 62
4.5.2.2 Current Density, Nernst Potential, and Electrochemical Losses 67
4.5.2.3 Fuel Cell Thermal Performance 71
4.5.2.4 Dynamic Response of Fuel Cell Thermal Effluent 77
4.6 Conclusions 78
4.7 Acknowledgement 78
4.8 References 79

5 Coupling Effects of Fuel Composition Transition and Cathode Air Mass Flow on Dynamic Performance of SOFC/GT Hybrid Systems 82
5.1 Publication Highlights 82

5.2 Abstract 83
5.3 Introduction 83
5.4 Background 85
5.5 Methodology 86
5.5.1 Description of Hardware-based Simulation System 86
5.5.2 Open Loop and Closed Loop Test Procedures 88
5.6 Results and Discussion 90
5.6.1 Turbine Speed and Cathode Air Mass Flow Transient Responses 90
5.6.2 Transient Characterization of Fuel Cell Thermal Performance 91
Fuel Cell Cathode Solid Temperature 91
Spatial Gradient of Fuel Cell Solid Temperature 93
Fuel Cell Cathode Gas Temperature 94
Cathode Solid and Gas Temperature Difference and Heat Flux 96
Fuel Cell Heat Generation 99
5.6.3 Transient Analysis of Fuel Compositions 100
Methane, CH_4 100
Other Fuel Composition Gradients and Fuel Utilization 101
5.6.4 Current density 106
5.6.5 Transient Analysis of Fuel Cell Thermal Energy Storage and Fuel Cell Thermal Effluent 107
5.7 Conclusions 108
5.8 References 109

6 Degradation Analysis of SOFC for Various Syngas Compositions in IGFC Systems 111
6.1 Publication Highlights 111
6.2 Abstract 112
6.3 Introduction 112
6.4 SOFC Model 113
6.5 Test Procedure 115
6.6 Results and Discussion 117
6.6.1 Composition Gradients 117
6.6.2 Fuel Utilization 120
6.6.3 Fuel Cell Solid Temperature 121
6.6.4 Nernst 123
6.6.5 Current Density 123
6.6.6 Degradation Rate 124
6.7 Conclusions 126
6.8 References 127

7 Conclusions 130
7.1 Summary 130
7.2 Concluding Remarks and Contribution 131
7.3 Recommendation for Future Works 135

LIST OF FIGURES

Chapter 1:

Figure 1.1: Basic configuration of an SOFC unit……2
Figure 1.2: Innovation of Brayton cycle to SOFC/GT hybrid systems……..4
Figure 1.3: Bypass configuration in the SOFC/GT hybrid system……..5
Figure 1.4: Hybrid test facility at NETL……..9

Chapter 2:

Figure 2.1: Flow diagram of the hardware-based hybrid test facility at NETL……..18
Figure 2.2: Results of scoping studies (a) real response during the entire course of offline simulation (b) normalized plot for the first 10 second transient period……20
Figure 2.3: Transition in fuel heating values (LHV) between syngas to humidified methane of three different compositions……20
Figure 2.4: Block diagram of the load-based speed controller……22
Figure 2.5: Real-time dynamic response and estimated steady state profile……..23
Figure 2.6: Dynamic profiles of thermal effluent, turbine speed and turbine load (a) The real response over 7,000 seconds, (b) normalized plot of (a), and (c) the real response over 1,050 seconds……..25
Figure 2.7: Normalized profiles of thermal effluent, turbine speed, and turbine load over 10 seconds after the step time……25
Figure 2.8: The effect of thermal effluent on turbine temperatures and SOFC cathode inlet temperature (a) the real response over 7,000 seconds, (b) the normalized plot of (a), and (c) normalized plot for the response over 1,050 seconds……..27
Figure 2.9: Normalized plots of thermal effluent, turbine temperatures and SOFC cathode inlet temperature over the first 50 seconds……..28
Figure 2.10: Turbine cycle efficiency……29
Figure 2.11: The SOFC cathode inlet flow and the compressor intake air flow transients (a) the real response over 7,000 seconds (b) normalized plot of (a)……..30
Figure 2.12: SOFC performance during fuel composition dynamics (a) the real response over 7,000 seconds (b) normalized plot of (a) ……31

Chapter 3:

Figure 3.1: The recuperated SOFC/GT hybrid test facility at NETL [1]……..37
Figure 3.2: Hardware-based simulations of SOFC/GT hybrid system……..40
Figure 3.3: Load based speed control scheme [1]……42
Figure 3.4: Turbine speed and turbine load responses for open and closed loop configurations……..43
Figure 3.5: A comparison profiles of fuel cell thermal effluent for open loop and closed loop tests……..44

Figure 3.6: A comparison of turbine inlet and exhaust temperatures for open loop configuration versus closed loop configuration, (a) the real profiles, and (b) the normalized profiles……45
Figure 3.7: A comparison of cathode inlet mass flow for open loop configuration versus closed loop configuration……46
Figure 3.8: Normalized profiles of, (a) system mass flow, compressor discharge pressure and turbine speed for open loop configuration, and (b) system mass flow, compressor discharge pressure and turbine load for closed loop configuration……47
Figure 3.9: A comparison of cathode inlet pressure for open loop configuration versus closed loop configuration……48
Figure 3.10: Normalized profiles of, (a) system pressures and turbine speed for open loop configuration, and (b) system pressures and turbine load for closed loop configuration……48
Figure 3.11: A comparison of cathode inlet temperature for open loop configuration versus closed loop configuration……49

Chapter 4:
Figure 4.1: The physical system of SOFC/GT hybrid test facility at NETL [25]……56
Figure 4.2: 1D-Real time fuel cell dynamic model……58
Figure 4.3: Distributed profiles of composition gradient in the anode at the initial steady state using syngas feed, (a) real values on mole-basis, and (b) normalized values……61
Figure 4.4: Nernst potential, current density, and electrochemical losses at the initial steady state using syngas feed, (a) real values, and (b) normalized values……62
Figure 4.5: Variations in methane partial pressure, (a) a 3D mesh plot, as function of local position along the cell node and time, and (b) distributed profiles at time 1 s, 250 s, 1,500 s, and 7,000 s after the step change……63
Figure 4.6: Transient response of carbon monoxide composition, (a) a 3D mesh plot, as function of local position along the cell node and time, and (b) Distributed profiles at time 1 s, 250 s, 1,500 s, and 7,000 s after the step change……63
Figure 4.7: Transient response of carbon dioxide composition, (a) a 3D mesh plot, as function of local position along the cell node and time, and (b) distributed profiles at time 1 s, 250 s, 1,500 s, and 7,000 s after the step change……64
Figure 4.8: Hydrogen mole fraction gradient, (a) a 3D mesh plot, as function of local position along the cell node and time, and (b) distributed profiles at time 1 s, 250 s, 1,500 s, and 7,000 s after the step change……65
Figure 4.9: Water mole fraction gradient, (a) a 3D mesh plot, as function of local position along the cell node and time, and (b) distributed profiles at time 1 s, 250 s, 1,500 s, and 7,000 s after the step change……66

Figure 4.10: Localized fuel utilization, (a) a 3D mesh plot, as function of local position along the cell node and time, and (b) distributed profiles at time 1 s, 250 s, 1,500 s, and 7,000 s after the step change……..67
Figure 4.11: Local current density, (a) a 3D mesh plot, as function of local position along the cell node and time, and (b) distributed profiles at time 1 s, 250 s, 1,500 s, and 7,000 s after the step change……68
Figure 4.12: Nernst potential distribution, (a) a 3D mesh plot, as function of local position along the cell node and time, and (b) distributed profiles at time 1 s, 250 s, 1,500 s, and 7,000 s after the step change……..68
Figure 4.13: Activation loss distribution, (a) a 3D mesh plot, as function of local position along the cell node and time, and (b) distributed profiles at time 1 s, 250 s, 1,500 s, and 7,000 s after the step change……..69
Figure 4.14: Ohmic loss profile, (a) a 3D mesh plot, as function of local position along the cell node and time, and (b) distributed profiles at time 1 s, 250 s, 1,500 s, and 7,000 s after the step change……70
Figure 4.15: Transient profile of diffusion loss, (a) a 3D mesh plot, as function of local position along the cell node and time, and (b) distributed profiles at time 1 s, 250 s, 1,500 s, and 7,000 s after the step change……70
Figure 4.16: The dynamic profiles of fuel cell temperature, (a) a 3D mesh plot, as function of local position along the cell node and time, and (b) distributed profiles at time 1 s, 250 s, 1,500 s, and 7,000 s after the step change……71
Figure 4.17: Fuel cell cathode inlet conditions……72
Figure 4.18: Spatio-fuel cell temperature gradient, dT/dx……..73
Figure 4.19: Average solid temperature profile, (a) average solid temperature profile as a function of time, and (b) temporal changes of average solid temperature, $dTave/dt$……73
Figure 4.20: Cathode gas temperature profiles, (a) a 3D mesh plot, as function of local position along the cell node and time, and (b) distributed profiles at time 1 s, 250 s, 1,500 s, and 7,000 s after the step change……74
Figure 4.21: Fuel cell heat generation, (a) a 3D mesh plot, as function of local position along the cell node and time, and (b) distributed profiles at time 1s, 250 s, 1,500 s, and 7,000 s after the step change……75
Figure 4.22: The profile of solid-gas temperature difference ($Tsolid - Tgas$), (a) distributed temperature profile across the cell at different time, and (b) average temperature difference as function of time……76
Figure 4.23: (a) Fuel cell model thermal effluent transient, (b) Dissipation of fuel cell thermal energy storage……77

Chapter 5:
Figure 5.1: Basic flow diagram of a SOFC/GT hybrid system……84

Figure 5.2: Comparison of fuel cell solid temperature performance, (a) between the open loop and closed loop with 13.6% CH_4 content, and (b) between the open loop (13.6% CH_4) and the closed loop (14% CH_4)……..86
Figure 5.3: The layout of SOFC/GT testing facility at NETL……..87
Figure 5.4: Comparison of variations in turbine speed and cathode air mass flow for open loop and closed loop……..90
Figure 5.5: Fuel cell solid temperature as a function of time, (a) open loop (b) closed loop……..91
Figure 5.6: Comparison of fuel cell solid temperature performance, between the open loop and the closed loop tests (a) distributed data as a function of time, and (b) the response of solid temperature difference at selected fuel cell nodes……..92
Figure 5.7: Cathode inlet temperature profiles for the open loop and closed loop systems using 13.6% CH_4 content and for the closed loop operation using 14% CH_4 content……..93
Figure 5.8: Spatial temperature gradient as a function of time, (a) open loop transient response (b) comparison of open loop and closed loop solid temperature gradients at critical nodes……..94
Figure 5.9: The difference in solid temperature gradient at critical nodes……..94
Figure 5.10: Fuel cell gas temperature as a function of time, (a) open loop transient response content (b) comparison of open loop and closed loop transients…95
Figure 5.11: Crossover points in fuel cell gas temperature difference between the open loop and the closed loop for selected local fuel cell positions……96
Figure 5.12: Fuel cell solid-gas temperature difference as a function of time, (a) open loop transient response, (b) comparison of open loop and closed loop transients……97
Figure 5.13: Heat flux of a fuel cell stack as a function of time, (a) open loop transient response, (b) comparison of open loop and closed loop transients……..97
Figure 5.14: Normalized profiles of total heat flux in a fuel cell stack for open loop and closed loop, (a) over 5,500 s of test period, (b) over the first 200 s after fuel composition transition……98
Figure 5.15: Fuel cell heat generation as a function of time, (a) open loop transient response (b) comparison of open loop and closed loop transients……..99
Figure 5.16: Methane mole fraction as a function of time, (a) open loop transient response (b) comparison of open loop and closed loop transients……..100
Figure 5.17: Carbon monoxide mole fraction as a function of time, (a) open loop transient response (b) comparison of open loop and closed loop transients……102
Figure 5.18: Carbon dioxide mole fraction as a function of time, (a) open loop transient response (b) comparison of open loop and closed loop transients……103
Figure 5.19: Hydrogen mole fraction as a function of time, (a) open loop transient response (b) comparison of open loop and closed loop transients……..104

Figure 5.20: Water mole fraction as a function of time, (a) open loop transient response (b) comparison of open loop and closed loop transients……105
Figure 5.21: Fuel utilization in open loop and closed loop cases……105
Figure 5.22: Fuel cell current density as a function of time (a) open loop transient response (b) comparison of open loop and closed loop transients……106
Figure 5.23: Dissipation of fuel cell thermal energy storage and fuel cell thermal effluent and for the open loop and the closed loop tests……107

Chapter 6:

Figure 6.1: Distributed profiles of CH_4 mole fraction for the five fuel compositions studied ……117
Figure 6.2: Distributed profiles of CO mole fraction for the five fuel compositions studied ……118
Figure 6.3: Distributed profiles of H_2 mole fraction for the five fuel compositions studied ……118
Figure 6.4: Distributed profiles of CO_2 mole fraction for the five fuel compositions studied ……119
Figure 6.5: Distributed profiles of H_2O mole fraction for the five fuel compositions studied ……120
Figure 6.6: Distributed data of fuel utilization for the five fuel compositions studied ……120
Figure 6.7: Distributed data of fuel cell solid temperature for the five fuel compositions studied……121
Figure 6.8: Distributed data of fuel cell solid temperature gradient, dT/dx for the five fuel compositions studied……122
Figure 6.9: Distributed data of Nernst potential for the five fuel compositions studied ……123
Figure 6.10: Distributed data of current density for the five fuel compositions studied ……124
Figure 6.11: Distributed data of degradation rate impacts for the five fuel compositions studied……125

LIST OF TABLES

Chapter 2:

Table 2.1: SOFC operating conditions and parameters……..19
Table 2.2: Coal-derived syngas and humidified methane compositions on mole basis……..22

Chapter 3:

Table 3.1: SOFC parameters and initial operating conditions……40
Table 3.2: Coal-derived syngas and humidified methane compositions……42
Table 3.3: Summary of open loop and closed loop transient response……51

Chapter 4:

Table 4.1: Inlet conditions for fuel cell cathode and anode streams……58
Table 4.2: Specification of SOFC system parameters……58

Chapter 5:

Table 5.1: SOFC parameters and initial operating conditions ……89

Chapter 6:

Table 6.1: Fuel compositions studied for SOFC systems (mole %)……116
Table 6.2: Fuel cell stack inputs for different fuel compositions……116
Table 6.3: Average fuel cell solid temperature……122
Table 6.4: The maximum and overall degradation rate……126

LIST OF ABBREVIATIONS AND SYMBOLS

Abrreviations:

1D	One dimensional
act	Activation
APU	Auxiliary power unit
BGL	British Gas Lurgi
dif	Diffusion
DC	Direct current
DOE	Department of Energy
GT	Gas turbine
HiLS	Hardwar e-in the loop-simulations
IEA	International Energy Agency
IGFC	Integrated gasification fuel cell
LHV	Low heating value
NETL	National Energy Technology Laboratory
ohm	Ohmic
PEMFCs	Proton exchange membrane fuel cells
PID	Proportional-Integral-Derivative (controller)
TET	Turbine exhaust temperature
TIT	Turbine inlet temperature
TPB	Triple phase boundary
SECA	The Solid State Energy Conversion Alliance
shift	Water-gas shift
SMR	Steam methane reforming
SOFC	Solid oxide fuel cell
SOFC/GT	Solid oxide fuel cell gas turbine hybrid technologies
WGS	Water-gas shift

Symbols:

A_{react}	Area of reaction, m^2
F	Faraday's constant, C/mol
FU	Fuel utilization
i	Current density, A/cm^2
i_0	Exchange current density, A/cm^2
j	Node number
n	Number of electrons transfer per reaction
K_p	Equilibrium constant
T	Temperature, K
p	Partial pressure, atm
Q	Model predicted fuel cell thermal effluent, kW
R	Area specific resistance, Ω-m^2
r_d	Degradation rate, %/1000hr
r_{sr}	Reformed methane rate [mol/s]

R_u	Ideal gas constant, J/mol-K
α	Charge transfer coefficient
η	Turbine cycle efficiency, ratio (Chapter 2)
dT/dx	Temperature gradient between fuel cell nodes, K/cm
$\boldsymbol{dT_{ave}/dt}$	Temporal changes of average solid temperature, K/s
$T_{solid} - T_{gas}$	Solid-gas temperature difference, °C
V	Voltage, V
V_{Nernst}	Nernst potential, V
Δ	Variation
$\Delta G^{\circ}_{H_2O}$	Standard Gibbs free energy, kJ
ΔH°	Heat of reaction at a reference condition, kJ/mol
ΔH_1 or ΔH_2	Sensible heat, kW
x	Mole fraction
η	Electrochemical loss, V (Chapter 6)

DECLARATION OF ACADEMIC ACHIEVEMENT

The majority of the work described in this thesis, including experimental design and execution, data collection and analysis, as well as thesis writing, were completed by the author of this thesis, with the following exceptions.

- In general, I had help from the U.S. Department of Energy, National Energy Technology Laboratory (NETL) - a research scientist, Dr. David Tucker, a post graduate researcher/control engineer, Dr. Paolo Pezzini, a visiting scholar, Dr. Nana Zhou (University of Chongqing), and a PhD candidate, Valentina Zaccaria (University of Genoa), a project technician, Dave Ruehl, to execute all the tests. Each test required at least three authorized operators (including myself), due to the complexity of the system and experimental works presented herein. The control strategies used during the test were primarily developed by Dr. Paolo Pezzini and Dr. David Tucker. The integration of the fuel cell dynamic model (software) with hardware part of the system through an interface platform was also accomplished by the author, with some help from Dr. Paolo Pezzini.

- **Chapter 2:** Dr. David Tucker was responsible to guide the experimental design and data analysis since he was the principle investigator of the hybrid test facility at NETL. Dr. Thomas A. Adams II helped to determine the direction of the case study, assisted in the preparation of manuscript, editing and organizing the final version.

- **Chapter 3:** Both Dr. Thomas A. Adams II and Dr. David Tucker helped to finalize the content of the manuscript.

- **Chapter 4:** Dr. David Tucker assisted with data analysis and interpretation, as well as editing and preparation/submission of the manuscript. Meanwhile, Dr. Thomas A. Adams II provided helps in the preparation/revision process of the first draft to strengthen the content of the manuscript.

- **Chapter 5:** Dr. David Tucker provided support for the analysis of system identification. Both Dr Thomas A. Adams II and Dr. David Tucker assisted in the editing and preparation of the manuscript.

- **Chapter 6:** Dr. David Tucker helped with identifying the experimental design, and editing of manuscript. Valentina Zaccaria assisted with data analysis and interpretation, as well as the preparation of the manuscript. The empirical expression of fuel cell degradation rate presented in this section was developed in Valentina's study. Both Dr. Thomas A. Adams II and Dr. Alberto Traverso contributed their constructive comments in preparing and finalizing the manuscript.

1 INTRODUCTION

1.1 Emerging Solid Oxide Fuel Cell Technologies Toward Energy Sustainability

The most critical issues associated with power generation today are related to improvement of system efficiency and environmental impacts. Since electricity generation are primarily based on fossil fuel combustion, mostly coal and natural gas electricity generation was claimed as the largest contributor of sulfur compounds and noxious emissions, leading to global warming and pollutions [1, 2]. Yet, with the existing energy infrastructures, fossil based energy systems are unquestionably important and more reliable for heat production for almost all applications including commercial, residential, industries, and transportation [2, 3].

Today, the reliability on clean, efficient, and environmental-friendly energy technologies grows significantly with increasing energy demand and the need for a transition to low-emission and low-carbon world. To address the issues of global climate change and gas emission management, there are a lot of ongoing efforts, involving innovation of the current energy infrastructures or development of new advanced energy systems that are more sustainable [4]. The 'future' energy systems should be able to provide long-terms benefits to society in terms of addressing energy needs, including heat, electricity, and cooling for economic growth, as well as addressing vital requirements for safety, health, and environment.

One such alternative to traditional power generation systems that has the potential to fulfil environmental and economic critical needs is solid oxide fuel cell (SOFC) technology [5, 6]. Solid oxide fuel cells create DC power and heat from direct conversion of chemical energy of a fuel gas via electrochemical reactions (i.e. fuel oxidation) with low noise and vibration. As compared to other fuel cell technologies, such as the proton exchange membrane fuel cells (PEMFCs) that require relatively pure hydrogen and operate at a temperature of below 90 °C, SOFCs operate at higher operating temperature, approximately between 600 °C to 1000 °C. The high operating temperature of SOFCs is mutually beneficial for other power generation technologies, such that SOFCs can be integrated into the current

energy infrastructure such as gas turbines, gasifiers, etc. [7]. In addition, SOFCs are also resistant to CO poisoning. Thus, SOFCs can use various type of fuels including carbon monoxide and hydrocarbon, which can be coal-derived syngas, biomass, natural gas, methanol, and diesel to produce electricity [7, 8]. This increases the flexibility in the choice of fuels. Since no mechanical motion is involved, and potential for greater system flexibilities exist, SOFCs have received considerable attention in wide applications, ranging from stationary power generation (centralized power generation and distributed power generation) to transportation (auxiliary power unit for vehicles) at flexible module sizes [5, 6, 9].

The working principles of SOFCs are similar to batteries but SOFCs can continuously generate electricity if fuel and oxidant (i.e. air or oxygen) are constantly supplied to the system. The basic configuration of planar SOFCs is shown in Figure 1.1. An SOFC unit is generally fabricated with three main layers of solid structures called the anode, ion conducting electrolyte, and cathode. On top of that, there are channels constructed in an SOFC subsystem to deliver fuels and oxidant along the fuel cell length. The anode channels are used for fuel transportation, whereas cathode channels are for oxidant flow [10].

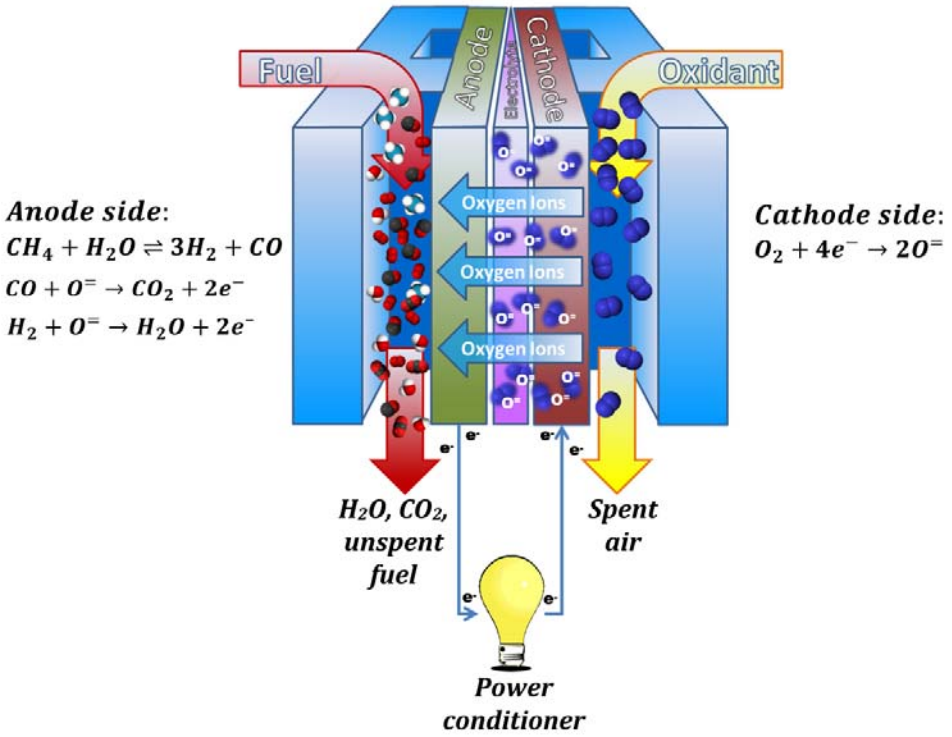

Figure 1.1: Basic configuration of an SOFC unit

During SOFC operations, oxygen anions, $O^{=}$ generated from the reaction between oxygen and electrons (Eq. 1), travel from the cathode interface through the electrolyte to the anode interface, at which oxygen ions will be consumed to oxidize fuels. Hydrogen oxidation (Eq. 2) takes place in SOFCs, producing heat, electricity, and waste gases H_2O and CO_2, depending on the fuel types [10]. For example, steam methane reforming described in Eq. 3

may occur in the high operating temperature SOFCs if methane or methane-content gas is used. With the presence of CO and H_2O in the system, the formation of H_2 can also be promoted through water-gas shift equilibrium shown in Eq. 4, resulting in the production of waste gas CO_2 from the anode channel.

Oxygen reduction (cathode side):
$$1/2\, O_2 + 2e^- \rightarrow O^= \quad (1)$$

Hydrogen oxidation (anode side):
$$H_2 + O^= \rightarrow H_2O + e^- \quad (\Delta H^\circ = -286\ kJ/mol) \quad (2)$$

Steam methane reforming:
$$CH_4 + H_2O \rightleftharpoons 3H_2 + CO \quad (\Delta H^\circ = 206\ kJ/mol) \quad (3)$$

Water-gas shifting:
$$CO + H_2O \rightleftharpoons H_2 + CO_2 \quad (\Delta H^\circ = -41\ kJ/mol) \quad (4)$$

The Nernst potential for SOFCs is based on an expression shown in Eq. 5, assuming direct electrochemical oxidation of carbon species is negligible compared to hydrogen oxidation and the reforming and shifting of hydrocarbon fuels at the anode. This function reveals that the maximum voltage of fuel cells is correlated to temperature, as well as the partial pressure of H_2 and H_2O in the anode and O_2 in the cathode. However, the actual cell voltage is calculated by subtracting cell polarization losses from the Nernst. In Eq. 5, the net value of the first term, which consists of the Gibbs free energy of water at the standard condition, is a positive value. Meanwhile, the net value of the second term, as a function of temperature and component partial pressure is usually a negative value, especially if operating the system in excess water condition. In this case, there is an inverse effect of fuel cell temperature on the Nernst potential.

Nernst potential:
$$V_{Nernst} = -\frac{\Delta G^\circ_{H_2O}}{2F} + \frac{R_u T}{2F} ln\left[\frac{p_{H_2}.p_{O_2}^{0.5}}{p_{H_2O}}\right] \quad (5)$$

Although Eq. 5 indicates that Nernst potential may reduce with the increase in fuel cell temperature for certain conditions, operating SOFCs at high temperature provides some advantages over the polarization losses, particularly ohmic losses, which reduces with increasing temperature. Operating SOFCs at high temperature also generate high quality of waste heat from its exhaust stream that contains significant amount of energy from some unutilized combustible fuel. However, optimal temperature and fuel utilization must be chosen according the fuel cell fabrication and materials of construction. Technically, it is difficult to operate high temperature SOFCs at high fuel utilization (above 90%) since this can lead to accelerated degradation rate of the fuel cell systems [11]. Unexpected metal oxidation may occur in fuel starvation states, which consequently cause material failure. Delaminating and cracking due to nickel oxidation at the anode side, as well as chromium

deposition and microstructural changes are the potential issues that can inhibit efficient SOFC operations [6, 10, 12].

Considering the material problems with the existing SOFC technologies, the Solid State Energy Conversion Alliance (SECA) program in the United States takes a lead in the development of commercially relevant and robust SOFC systems, with a goal of reducing stack costs, increasing cell efficiency, and increase cell longevity. The undergoing research broadly focuses on degradation process of anode/electrolyte/cathode components, cathode materials and microstructural engineering, catalytic fuel reforming, and many others [8].

1.2 Role of Solid Oxide Fuel Cell Gas Turbine Hybrid in Meeting Future Energy Needs

Solid oxide fuel cell gas turbine (SOFC/GT) hybrid systems have been discovered as a promising alternative energy technology to standalone SOFC systems as well as conventional power generation technologies. SOFC/GT hybrid systems offer remarkable potentials that are cost competitive with existing combined cycle energy systems and enhanced efficiency up to 75% LHV on natural gas, or 60% HHV of coal, with minimal emissions [6, 9, 13-15]. Integration of a high temperature SOFC with a gas turbine engine in a recuperated cycle shown in Figure 1.2 is one of the most common hybrid approaches [16, 17]. As configured in Figure 1.2, this hybrid technology is based on a direct thermal coupling scheme, utilizing the net thermal effluent from an SOFC subsystem for additional power generation from a gas turbine to supplement SOFC power. Thus, the system allows for an increase in total system efficiency [9, 13, 14]. The net thermal effluent of an SOFC includes thermal energy of by-product heat generation of an operating SOFC, plus the heat released from the oxidation of SOFC anode off-gas. With this feature, SOFC/GT hybrid systems do not require any combustion in the gas turbine itself.

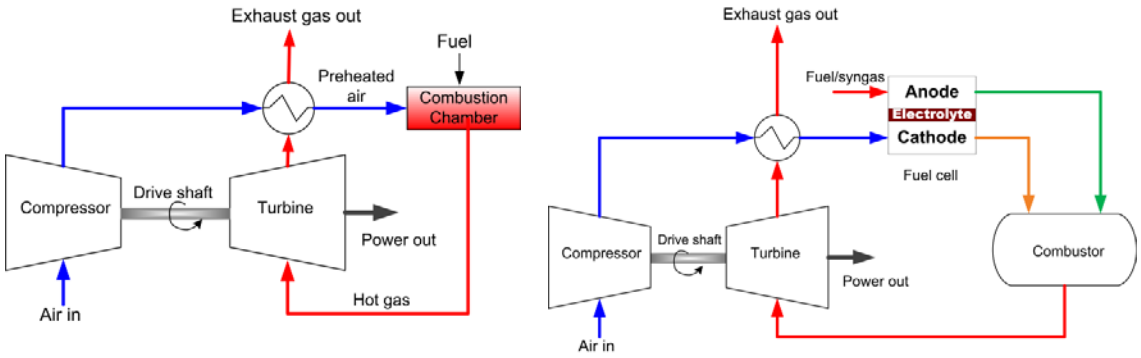

(a) (b)

Figure 1.2: Innovation of recuperated cycle to SOFC/GT hybrid systems

An important aspect of SOFC/GT is the synergistic integration benefits of fuel cells and gas turbines that inherently enhance system reliability and operability. From the design standpoint, this system permits pressurized fuel cell operations in which the compressed air from compressor discharge is channelled to the cathode side of an SOFC fuel subsystem

through recuperation of gas turbine exhaust. Operating SOFC systems under pressure offers an improvement in fuel cell efficiency with regard to enhancement of Nernst potential [10, 18]. The preheating of fuel cell cathode air flow will further improve the efficiency of the entire cycle [13, 14].

In the hybrid configuration, high cathode cooling air flow is granted by gas turbine operation without reduction in efficiency, providing means for better fuel cell thermal management [19]. It has been shown that modulation of cathode air flow into SOFC subsystems is critical for fuel cell temperature controls [20, 21]. Small transient changes in cathode air flow can significantly affect the performance of SOFC/GT hybrid systems [22]. Cathode air flow management in SOFC/GT hybrid system can be practically realized using bypass valves. With certain control strategies via bypass modulation, it is also possible for the hybrid system to have turndown rate up to 93%, allowing for load following operations [19, 23]. An example of the SOFC/GT hybrid system with bypass valves is shown in Figure 1.3.

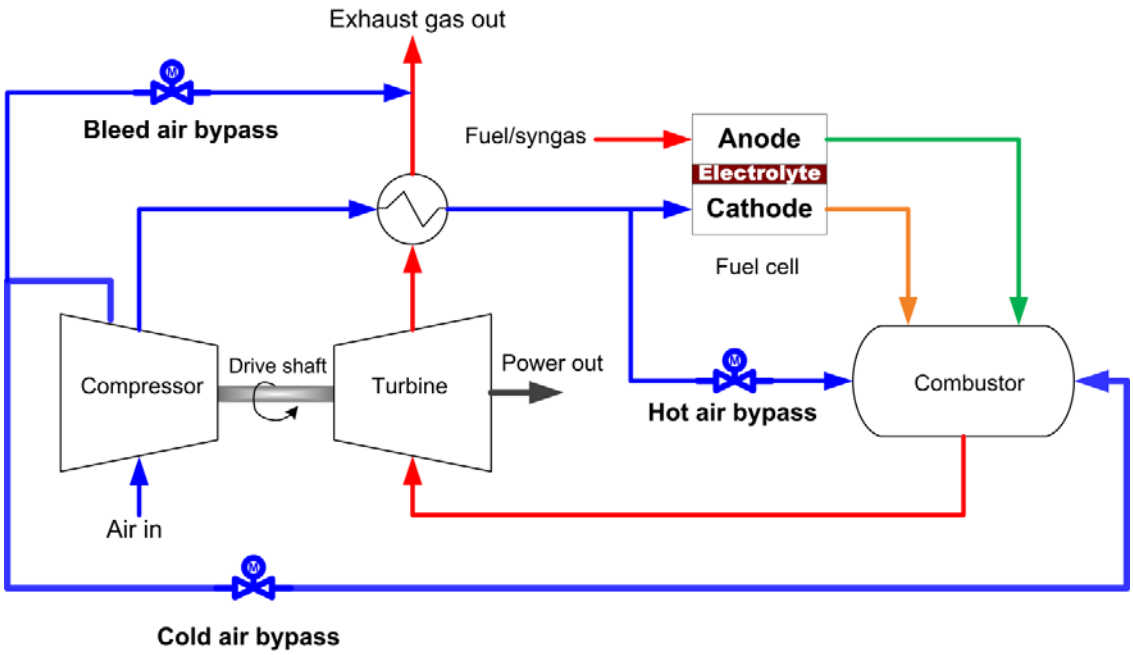

Figure 1.3: Bypass configuration in the SOFC/GT hybrid system

Considering the limitation of high fuel utilization in SOFC systems, hybridizing an SOFC and a gas turbine as a bottoming cycle provides solutions to work around this problem. Prior work has shown that the total efficiency of SOFC/GT hybrid was insensitive to fuel utilization (FU) in a range between a 57% to an 85% FU [24]. Interestingly, this implied that it is feasible for the hybrid systems to run at a lower fuel utilization (i.e. by increasing fuel flow) than in the standalone configuration without efficiency penalties in system performance. Since the resulting unspent fuel from an operating SOFC subsystem in SOFC/GT hybrid is eventually used by the gas turbine to power compressor for cathode air supply and cathode air preheating, the final total system efficiency can be maintained at

higher level. Undoubtedly, operating at a lower fuel utilization reduces taxing operating conditions in the SOFC subsystem, which potentially extend the fuel cell lifetime [25]. Furthermore, anode recycle, which is usually employed in SOFC systems to boost the efficiency at low fuel utilization operations, is not necessarily required in SOFC/GT hybrid systems. This leads to less problematic issues in controlling the effects of composition gradients on SOFC performance.

1.3 Research Motivation: Potential and Challenges in Solid Oxide Fuel Cell Gas Turbine (SOFC/GT) Hybrid Systems for Fuel Flexible Operations

Mostly, hydrogen can be fed directly to fuel cell systems in which the highest ideal fuel cell potential can be achieved with dry/pure hydrogen. In fact, hydrogen is not readily available to be an ideal fuel for future power conversion systems due to generation and handling issues associated with storage and distribution [26]. However, high temperature fuel cells, including SOFCs relax the dependency on hydrogen as the main fuel, expanding the number of potential fuels that can be used [10, 27]. The elevated temperature allows the system to perform direct internal conversion of hydrocarbon to hydrogen via reactions of CO and CH_4 with H_2O, respectively in water-gas shift and steam reforming [10].

With the aforementioned features, the potential of SOFC/GT can be further improved through advanced integration cycles with different fuel processing infrastructures. Depending on applications, SOFC/GT hybrid cycles can be integrated to coal gasifiers, biomass gasifiers, and fuel reformers, etc. for fuel supply in larger system operations [16, 28, 29]. But direct utilization of natural gas in SOFC/GT is also possible [30]. However, almost all of fuel coupling schemes are technically susceptible to significant composition fluctuations as a consequence of changes in feedstock quality, operating conditions, or even the fuel processing technologies [31]. This consequently imposes significant perturbations on SOFC systems. As such, the ability of SOFCs to run in fuel flexible environments is beneficial to handle variability in fuel compositions, minimizing the detrimental transient impacts on the system performance and life.

Furthermore, the advantage of SOFC fuel flexibilities can also be capitalized on a power generation plant to take advantage of current economic conditions as well as to meet new environmental restrictions placed. Carbon tax, price of fuels and electricity may require a significant shift in the fuel compositions and/or fuel types used, such that, it could improve the economic viability of the plant [29]. For example, a shift from an initial operation utilizing coal-derived syngas to natural gas is more profitable if the prices of natural gas drops and/or new carbon tax increases.

Another example of potential SOFC/GT applications as the power conversion system is in flexible polygeneration systems, which co-produce electricity with fuels or chemicals [28, 31]. In this polygeneration system, an SOFC/GT hybrid system is coupled with chemicals or fuel production sections, with a goal of maximizing efficiency and plant profit, corresponding to monthly or daily fluctuations in energy prices. More electricity and less fuel are produced during the day when the prices of power prices are high, and the reversed mixture of polygeneration products is produced at night when the power prices are low. To fulfil the production target, significant changes in fuel feed conditions with regard to flow rate, composition, and heating value must be performed to modify the product envelope. In

the worst case, supplementing natural gas as an auxiliary fuel feed to electricity generation subsection might be beneficial in the polygeneration plant when there is maximum utilization of syngas in chemicals or fuel production subsection. These cases demonstrate a critical need for sufficient transient capabilities in SOFC/GT hybrid sections.

Due to high coupling between the fuel cell and other system components, such as a gas turbine and fuel processor, transitioning fuel compositions or fuel types in SOFC subsystem might be very challenging. Since each of the system components has different nonlinear behaviours, effective control architectures must be developed and proven to address potential technical challenges in dynamic operation modes of SOFC/GT hybrid systems. Prior works have shown that there are three major dynamic issues and operational sensitivities associated to the hybrid system.

- **Fuel cell thermal management:** Small transient changes in cathode air mass flow can cause dramatic effects on the hybrid system performance, leading to problematic fuel cell thermal gradients across the fuel cell length [22]. In turn, changes in cathode mass flow in the hybrid configuration are strongly coupled the speed of turbine shaft and compressor dynamics [21, 32]. The impacts of flow perturbations resulting from turbomachinery dynamics is more significant than the impacts of temperature fluctuations [14]. It is believed that managing cathode air flow during transient events is critical to avoid over-cooling or over-heating the fuel cell stacks.

- **Compressor stall and surge**: Sudden reduction in fuel/thermal input going into gas turbine and introduction of pressure losses between compressor and gas turbine in the hybrid configuration can lead to decrease in compressor surge margin. This subsequently results in compressor stall and surge. Such transient events put the hybrid system at the highest risk of turbine damage because of instability in the dynamics of turbomachinery [33]. The transients of compressor stall and surge can occur very quickly, just within a few seconds. Ultimately, this event can result in catastrophic failure of the fuel cell due to intolerable pressure difference between anode and cathode streams. Turbine damages due to compressor stall and surge during fuel cell hybrid operations have been discovered through the experience of NETL researchers.

- **Fuel cell degradation:** Degradation mechanisms, such as oxidation of anode material and microstructural changes in fuel cell systems can be accelerated by carbon deposition, high fuel utilization and current density, high anode-cathode pressure difference, etc. This eventually inhibits efficient working performance of the fuel cells as well as reduces the fuel cell lifetime. However, to make the system economically viable, certain control strategies must be developed to mitigate the degradation impacts.

1.4 Problem Statement

The tightly interactive effects between each component in SOFC/GT hybrid configuration during transient events always leads to complicated dynamic operability that requires problematic control development. But, it is important to have good control schemes for improvement of transient capabilities and operating flexibilities, rejecting any system disturbance associated with rapid cycling changes that ultimately modify system pressure, mass flow, and pressure in the system. However, if dynamic controls are to be developed to take advantage of the extensive operating envelope offered by SOFC/GT hybrids, detailed system identification is required to adequately develop understanding about dynamic coupling interactions between system components in hybrid configuration, especially the fuel cell, gas turbine, compressor and heat exchangers.

Motivated by the previously mentioned advantages and challenges in SOFC/GT systems, this project investigates transient behaviours of SOFC/GT hybrid cycle with regard to its potential for fuel flexibilities. This study focuses on detailed analyses of SOFC/GT system performance during fuel composition transients. In general, there are a few research questions that are addressed in this study regarding:

- impacts of fuel composition dynamics on the fuel cell and the balance of the plant
- flexibility of the SOFC/GT hybrids to deal with fuel composition variations
- associated operability limitations and technical issues during operations
- potential control strategies that could be implemented to mitigate any negative impacts on the system before catastrophic failure takes place (i.e. due to the compressor and turbine stall and surge as well as fuel cell damage due to material starvation and thermal stress).

SOFC/GT hybrids are complex systems. Real responses due to process perturbations cannot be accurately estimated, and in fact, the ability to prevent failures under real conditions cannot be predicted by simulation only. To the best of our knowledge, almost all existing studies to date focused on steady state operations, with very limited experimental data and/or validated simulation works. Therefore, in this project, the response of SOFC/GT hybrid systems to fuel composition transients was experimentally investigated using hardware-based simulations in real-time. A hybrid test facility of a recuperated fuel cell gas turbine system developed by the U.S department of Energy, National Energy Technology Laboratory (NETL) shown in Figure 1.4 was used. This system incorporated actual equipment of direct-fired recuperated gas turbine and simulated fuel cell subsystem, reducing the drawbacks of potentially large inaccuracies in fully simulation approaches of highly integrated energy system.

1.5 Research Objective

With the aim of characterizing the SOFC/GT system performance under fuel composition changes, a step change from coal-derived syngas composition to methane-rich gas composition was implemented, representing the worst and most extreme case study of

fuel composition transitions. Details of the research objectives for this study are listed as following:

a. To determine the operational boundaries of fuel composition changes that could be used without violating the allowable thermal gradient and/or causing carbon deposition in the fuel cell, and causing stalls/surge in the turbomachinery
b. To investigate the correlation among the key process variables in the fuel cell subsystem and turbomachinery section during fuel composition transition
c. To evaluate the coupling impacts of fuel cell dynamic performance on the balance of the plant (the recuperated gas turbine cycle)
d. To clarify the linking events existing in the SOFC/GT hybrid systems that might mitigate or propagate the effects of fuel composition changes on the hybrid system
e. To identify potential opportunities for dynamic controls of SOFC/GT hybrid systems during fuel composition changes.

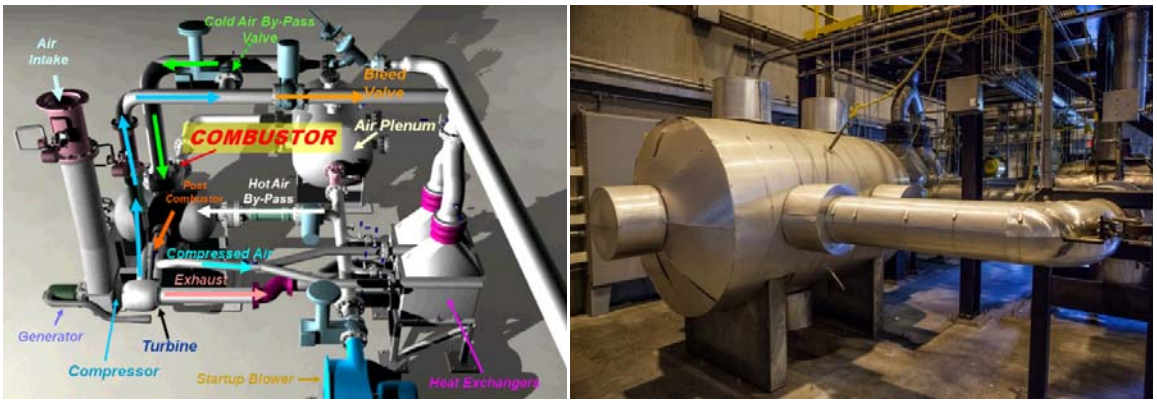

Figure 1.4: Hybrid test facility at NETL

1.6 Thesis Outline

This thesis is structured based on 7 chapters, led by the *Introduction* in **Chapter 1**, and ending with *Conclusions* in **Chapter 7**. Main contents of the thesis are organized as the following:

- **Chapter 2**. *Fuel Composition Transients in Fuel Cell Turbine Hybrid for Polygeneration Applications*:

  This chapter presents exploration of dynamic issues associated with fuel composition changes in the case of a transition from coal-derived syngas to humidified methane. Prior to the real experimental works, preliminary tests were required to identify the operational boundaries of fuel compositional changes that could be used without violating the allowable thermal gradient and/or causing carbon deposition in the fuel cell, and causing stalls/surge in the turbomachinery. The step-by-step approach taken to identify the operational restrictions was

explained herein. In favour of simplicity, the hardware-based simulations carried out at this stage were in closed loop mode. As such, the closed loop performance provided valuable insights of relationships among the key process variables in a base condition with very minimal disturbances and risks of system failure. The subsequent impacts of the fuel cell dynamic performance (driven by fuel composition changes) on gas turbine cycle was evaluated thoroughly.

- **Chapter 3**. *Open Loop and Closed Loop Performance of Solid Oxide Fuel Cell Turbine Hybrid Systems during Fuel Composition Changes*:

  This stage attempted to study a different step change in fuel composition, as well as to quantify the difference between open loop and closed loop system performance using the existing control approach. However, the focus up to this point was the investigation of the coupling effects between the fuel cell behaviours and the gas turbine cycle as a result of the step change in fuel composition. The limits for open loop tests were identified, such that the demonstration test could be done safely. A comparison between open loop and closed loop system performance was investigated and the interactions among fuel cell process variables were characterized carefully. The results were discussed in terms of mitigating/propagating influences and the control effects of the case of closed loop test. Therefore, it offered some insight into the real dynamic trajectory of the process variables, and its significance to the system as the result of fuel composition perturbations. This finding is generally not known because dynamic studies of SOFC operations are rare. Hence, this discovery was quite useful for identifying the operational boundaries, which can then lead to better control systems.

- **Chapter 4**. *Fuel Composition Transition Impacts on Dynamic Performance of Fuel Cells in SOFC/GT Hybrid Systems*:

  As an extension from the investigation presented in Chapter 2, this section primarily focuses on dynamic characterization of fuel cell parameters. The fuel cell parameters discussed in this chapter were related to dynamic thermal performance including solid and gas temperature on the cathode side, axial heat generation within the cell, partial pressures of major components in the anode side, Nernst potential, polarization losses, and local current density. The detailed dynamic trajectories of each key fuel cell variables were evaluated thoroughly to quantify their contributions to operability and controllability of the hybrid system. The analyses were based on distributed profiles across the fuel cell length resulted from the closed loop operation.

- **Chapter 5**. *Coupling Effects of Fuel Composition Transition and Cathode Air Mass Flow on Dynamic Performance of SOFC/GT Hybrid Systems*:

  Chapter 5 is dedicated to a more serious discussion on the dynamic performance of SOFC/GT hybrid systems, leading to system identification of this technology during fuel composition transients. Similarly, the finding obtained in Chapter 3 was

expanded and presented herein. This chapter particularly emphasizes the characterization of linking dynamic events associated with fuel composition changes (i.e. cathode air mass flow variations). Comparison of the open loop dynamic performance and closed loop performance for the important fuel cell parameters was carried out to determine the integration issues that could affect the dynamic performance of SOFC/GT hybrid system as well as to identify potential opportunities for dynamic controls of SOFC/GT hybrid systems during fuel composition changes.

- **Chapter 6**. *Degradation Analysis of SOFC for Various Syngas Compositions in IGFC Systems*:

  This section presents the impacts of fuel composition on fuel cell degradation rate, which was based on various coal-derived syngas resulting from different gasifier technologies. All of the syngas compositions used in this study contained a different level of methane content. The degradation rate was evaluated using the empirical expression, indicating a correlation to three key fuel cell operating parameters; current density, fuel utilization and cell temperature. The performance of fuel cell for each fuel composition was explained and compared to the case of humidified hydrogen to determine their influence on the degradation rate.

1.7 References

[1] Exxonmobil, 2012, "2012 The Outlook for Energy: A View to 2040," Exxonmobil, Irving, Texas.
[2] The U.S. Deparment of State, 2014, "U.S Climate Action Report (2014 CAR)".
[3] Hackett, J. T., 2011, "Prudent Development: Realizing the Potential of North America's Abundant Natural Gas and Oil Resources," the U.S Department of Energy, the National Petroleum Council.
[4] International Energy Agency, 2012, "Energy Technology Perspectives 2012: Pathways to a Clean energy System."
[5] Andújar, J. M., and Segura, F., 2009, "Fuel Cells: History and Updating. A Walk Along Two Centuries," Renewable and Sustainable Energy Reviews, 13(9), pp. 2309-2322.
[6] Adams, T. A. II, Nease, J., Tucker, D., and Barton, P. I., 2013, "Energy Conversion with Solid Oxide Fuel Cell Systems: A Review of Concepts and Outlooks for the Short- and Long-Term," Ind. Eng. Chem. Res., 52(9), pp. 3089–3111.
[7] Stambouli, A. B., and Traversa, E., 2002, "Solid Oxide Fuel Cells (SOFCs): A Review of an Environmentally Clean and Efficient Source of Energy," Renewable and Sustainable Energy Reviews, 6(5), pp. 433-455.
[8] Williams, M. C., Strakey, J. P., Surdoval, W. A., and Wilson, L. C., 2006, "Solid Oxide Fuel Cell Technology Development in the U.S," J. Solid State Ionics, 177(19–25), pp. 2039-2044.
[9] Fontell, E., Phan, T., Kivisaari, T., and Keränen, K., 2006, "Solid Oxide Fuel Cell System and the Economical Feasibility," ASME J. Fuel Cell Sci. Technol 3(3), pp. 242-253.

[10] EG&G Technical Services, I., 2004, Fuel Cell Handbook, U.S. Department of Energy, Office of Fossil Energy, National Energy Technology Laboratory, Morgantown, West Virginia.
[11] Müller, A., Weber, A., Beie, H. J., Krügel, A., Gerthsen, D., and Ivers-Tiffée, E., 1998, "Influence of Current Density and Fuel Utilization on the Degradation of the Anode," the 3rd European Solid Oxide Fuel Cell Forum Nantes France.
[12] Liu, P., Pistikopoulos, E. N., and Li, Z., 2009, "A Mixed-integer Optimization Approach for Polygeneration Energy Systems Design," Comput. Chem. Eng., 33(3), pp. 759-768.
[13] Winkler, W., Nehter, P., Williams, M. C., Tucker, D., and Gemmen, R., 2006, "General Fuel Cell Hybrid Synergies and Hybrid System Testing Status," J. Power Sources, 159(1), pp. 656-666.
[14] Tucker, D., Shelton, M., and Manivannan, A., 2009, "The Role of Solid Oxide Fuel Cells in Advanced Hybrid Power Systems of the Future," The Electrochemical Society Interface, The Electrochemical Society.
[15] McLarty, D., Kuniba, Y., Brouwer, J., and Samuelsen, S., 2012, "Experimental and Theoretical Evidence for Control Requirements in Solid Oxide Fuel Cell Gas Turbine Hybrid Systems," J. Power Sources, 209(2012), pp. 195-203.
[16] Zhang, X., Chan, S. H., Li, G., Ho, H. K., Li, J., and Feng, Z., 2010, "A Review of Integration Strategies for Solid Oxide Fuel Cells," J. Power Sources, 195(3), pp. 685-702.
[17] Harun, N.F., Tucker, D., and Adams, T.A. II, 2014, "Fuel Composition Transients in Fuel Cell Turbine Hybrid for Polygeneration Applications," ASME J. Fuel Cell Sci. Technol., 11(6), pp. 061001-061001-8.
[18] Zhou, L., Cheng, M., Yi, B., Dong, Y., Cong, Y., and Yang, W., 2008, "Performance of an Anode-supported Tubular Solid Oxide Fuel Cell (SOFC) under Pressurized Conditions," Electrochimica Acta, 53(16), pp. 5195-5198.
[19] Tucker, D., Liese, E., and Gemmen, R., 2009, "Determination of the Operating Envelope for a Direct Fired Fuel Cell Turbine Hybrid using Hardware Based Simulation," Proceedings of the International Colloquium on Environmentally Preferred Advanced Power Generation (ICEPAG 2009), Newport Beach, CA, Feb. 10–12, Paper No. ICEPAG2009-1021.
[20] Banta, L. E., Restrepo, B., Tsai, A. J., and Tucker, D., 2010, "Cathode Temperature Management During Hybrid System Startup," ASME Paper No. FuelCell2010-33121.
[21] Tucker, D., Lawson, L., and Gemmen, R., 2005, "Characterization of Air Flow Management and Control in a Fuel Cell Turbine Hybrid Power System using Hardware Simulation," ASME Paper No. PWR2005-50127.
[22] Zhou, N., Yang, C., and Tucker, D., 2015, "Evaluation of Cathode Air Flow Transients in a SOFC/GT Hybrid System using Hardware in the Loop Simulation," ASME J. Fuel Cell Sci. Technol., 12(1), pp. 011003-011003-7.
[23] Restrepo, B., Banta, L. E., and Tucker, D., 2011, "Characterization of a Solid Oxide Fuel Cell Gas Turbine Hybrid System Based on a Factorial Design of Experiments using Hardware Simulation," ASME Paper No. FuelCell2011-54146.
[24] Haynes, C., and Wepfer, W. J., 2000, "Design for Power of a Commercial Grade Tubular Solid Oxide Fuel Cell," Energy Convers. Manage., 41(11), pp. 1123–1139.
[25] Tucker, D., Abreu-Sepulveda, M., and Harun, N. F., 2014, "SOFC Lifetime Assessment in Gas Turbine Hybrid Power Systems," ASME J. Fuel Cell Sci. Technol., 11(5), pp. 051008-051008-7.

[26] Chen, Y.-H., Chen, C.-Y., and Lee, S.-C., 2011, "Technology forecasting and patent strategy of hydrogen energy and fuel cell technologies," Int. J. Hydrogen Energy, 36(12), pp. 6957-6969.
[27] Eguchi, K., Kojo, H., Takeguchi, T., Kikuchi, R., and Sasaki, K., 2002, "Fuel Flexibility in Power Generation by Solid Oxide Fuel Cells," J. Solid State Ionics, 152–153(2002), pp. 411-416.
[28] Adams, T. A. II, and Barton, P. I., 2011, "Combining Coal Gasification, Natural Gas Reforming, and Solid Oxide Fuel Cells for Efficient Polygeneration With CO_2 Capture and Sequestration," Fuel Process. Technol., 92(10), pp. 2105-2115.
[29] Adams, T. A. II, 2014, "Future Opportunities and Challenges in the Design of New Energy Conversion Systems," Comp. Chem. Eng., Volume 34, pp. 5-14.
[30] Brouwer, J., 2006, "Hybrid Gas Turbine Fuel Cell Systems," The Gas Turbine Handbook, U.S. Department of Energy, National Energy Technology Laboratory, Morgantown, pp. 127-163.
[31] Chen, Y., Adams, T. A. II, and Barton, P. I., 2011, "Optimal Design and Operation of Flexible Energy Polygeneration Systems," Ind. Eng. Chem. Res., 50(8), pp. 4553-4566.
[32] Tucker, D., Tsai, A., Jablonski, P., Hughes, D. O., Haynes, C. L., and Sellers, J., 2010, "Initial Transient Response during Fuel Cell Turbine Hybrid System Startup," Proceedings of the International Colloquium on Environmentally Preferred Advanced Power Generation (ICEPAG 2010), Costa Mesa, CA, Feb. 9-11, Paper No. ICEPAG2010-3414.
[33] Pezzini, P., Tucker, D., and Traverso, A., 2013, "Avoiding Compressor Surge during Emergency Shut-Down Hybrid Turbine Systems," ASME J. Gas Turbines Power, 135(10), pp. 102602-102602-10.

2 FUEL COMPOSITION TRANSIENTS IN FUEL CELL TURBINE HYBRID FOR POLYGENERATION APPLICATIONS

"Reproduced from "Harun, N.F., Tucker, D., and Adams, T. A. II, 2014, "Fuel Composition Transients in Fuel Cell Turbine Hybrid for Polygeneration Applications," *ASME. J. Fuel Cell Sci. Technol.,* 11(6), pp. 061001-061001-8. doi:10.1115/1.4028159", with permission from ASME"

2.1 Publication Highlights

This section provides some background on exploration study of fuel composition changes in solid oxide fuel cell gas turbine hybrid systems. The discussion is primarily based on prior methodology taken in scoping studies that leads to real-time tests and the impacts of fuel composition changes on turbomachinery subsystem.

The scoping studies and the tests using hardware-based simulation facility in this publication were conducted by me. However, I also got some help from several operators at the U.S. Department of Energy, National Energy Technology Laboratory (NETL) - a research scientist, Dr. David Tucker, a post graduate researcher/control engineer, Dr. Paolo Pezzini, a visiting scholar, Dr. Nana Zhou (University of Chongqing), and a PhD student, Valentina Zaccaria (University of Genoa). Both Dr. Thomas A. Adams II and Dr. David Tucker helped me in analyzing the data and finalizing the content of the manuscript.

Fuel Composition Transients in Fuel Cell Turbine Hybrid for Polygeneration Applications

Authors: Nor Farida Harun[a], David Tucker[b], and Thomas A. Adams II[a]
[a]Department of Chemical Engineering, McMaster University, 1280 Main Street West, Hamilton, Ontario L8S 4L7, Canada
[b]U.S. Department of Energy, National Energy Technology Laboratory, 3610 Collins Ferry Road, Morgantown, West Virginia 26507-0880, United States

2.2 Abstract

Transient impacts on the performance of solid oxide fuel cell/gas turbine (SOFC/GT) hybrid systems were investigated using hardware-in-the-loop simulations (HiLS) at a test facility located at the U.S. Department of Energy, National Energy Technology Laboratory. The work focused on applications relevant to polygeneration systems which require significant fuel flexibility. Specifically, the dynamic response of implementing a sudden change in fuel composition from syngas to methane was examined. The maximum range of possible fuel composition allowable within the constraints of carbon deposition in the SOFC and stalling/surging of the turbine compressor system was determined.

It was demonstrated that the transient response was significantly impact the fuel cell dynamic performance, which mainly drives the entire transient in SOFC/GT hybrid systems. This resulted in severe limitations on the allowable methane concentrations that could be used in the final fuel composition when switching from syngas to methane. Several system performance parameters were analyzed to characterize the transient impact over the course of two hours from the composition change.

2.3 Introduction

Polygeneration systems have been recognized as promising near-future energy technologies. The distinctive feature of polygeneration system development is the integration of multiple processes to optimally co-produce multiple products such as powers and chemicals (i.e. liquid fuels). Through heat and mass integration between processes, system flexibility, and optimal energy resources utilization, it is possible to achieve higher energy conversions, higher system efficiencies, and/or lower to zero CO_2 emissions compared to standalone plants [1-4].

Plant revenue generation can also be maximized by constructing a process which can operate flexibly in terms of the types and amounts of the products produced. In flexible polygeneration systems, product portfolios can be adjusted dynamically depending on the market requirements – product demands, market prices, and also the carbon tax on CO_2 emissions. If the prices and/or the demand are high, the system is allowed to transition between various steady states by redistributing certain internal streams toward either power, fuel, or chemicals production trains to maximize the product generation. This can make it more profitable over "static" polygeneration systems which are unable to change their outputs flexibly. For example, previous studies have shown that adding daily flexibility

to a polygeneration system can result in up to a 13% larger net present value if the turndown ratio of the individual process sections is 50%, and up to 62% higher net present value if the turndown ratio is 100% [5].

The polygeneration system discussed in this work consists of a hybrid system in the power generation section, which combines a state-of-the-art natural gas combustion turbine with solid oxide fuel cells (SOFCs). This configuration is able to provide solutions for existing technology gaps in systems which include SOFCs. For instance, it is technically difficult to achieve high fuel utilization in SOFCs (>90%), making it expensive to maximize power generation, and leading to consequences such as shorter cell lifetimes. However, by hybridizing a fuel cell with a gas turbine as a bottoming cycle, it is possible to work around this problem. The fuel cell can operate at a lower fuel utilization (50-70%) than in the stand-alone SOFC systems [6]. The anode exhaust from the SOFC will still contain a significant amount of energy, which used to fuel the gas combustion turbine for additional power [7]. The end result is that the total system efficiency of the hybrid SOFC/GT system can be maintained at a high level while extending the lifetime of fuel cell by operating the fuel cell in less taxing conditions [8].

The polygeneration system studied in this work contains separate trains for the production of electricity, Fischer-Tropsch liquid fuels (such as diesel and gasoline), and methanol [9]. The off-gases from the fuel and methanol production trains contain a significant amount of energy in the form of H_2, CO, and/or CH_4, and so are fed to the SOFC/GT hybrid system in addition to the primary feed. The process is flexible such that the proportion of fuels, methanol, and power can be changed during the process. As a result, both the flow rate and composition of the feed to the SOFC/GT system changes whenever the product portfolio is changed.

However, there are limits to how much the SOFC fuel composition and rate can be changed during operation. In the SOFC/GT system, the tight integration between the SOFC stacks and the gas turbine results in many operational challenges which could possibly cause major failure incidents during system operations. For example, the temperature gradient across each fuel cell cannot exceed 12 K/cm, so rapid cooling or heating of the fuel cell stack must be avoided. In addition, the high-temperature, high-energy anode exhaust generated by the cell which then fuels the turbine-generator must also satisfy the design requirements of the turbomachinery.

Therefore, investigations of the dynamic response of the SOFC/GT hybrid system are crucial to quantify the system operability limits, prevent any damage regarding the thermal and material stress in the fuel cell, and prevent stall and/or surge in the turbomachinery. The goal of this paper is to characterize the transient impacts on the performance of the SOFC/GT hybrid system under SOFC fuel composition changes. Since the turndown of gasifier systems is quite limited, natural gas was considered as a supplementary fuel for power generation during peak chemical production or syngas utilization.

The dynamic response data generated from this study is a requirement for the development of control strategies to mitigate system potential failures. To the best of our knowledge, no such transient studies in the fuel composition of SOFC/GT systems have been attempted previously.

2.4 Methodology

SOFC/GT hybrid systems are complex systems. Real responses due to process perturbations cannot be accurately estimated, and in fact, the ability to prevent failures under real conditions cannot be predicted by simulation only. Therefore, to study the transient impacts on the SOFC/GT system, hardware-in-the loop simulations were performed with the following conditions:

a. The composition of the fuel feed to the SOFC was step-changed from coal-derived syngas to a methane-rich gas.
b. The mass flow rate of the fuel feed was kept constant.
c. The SOFC current was kept constant.
d. The turbine speed was maintained constant by using load-based speed control.
e. Certain safety and heat management control settings for the balance of plant were fixed for this study. Specifically, the bleed air, cold air and hot air bypass valves were positioned at the minimal requirements and not changed during the course of experiment [10-12].

Using the aforementioned approaches, the impact of SOFC fuel composition changes can be studied by removing the interaction effects of SOFC fuel flow rate and current transients.

2.4.1 1D-Real Time Fuel Cell Dynamic Model

A one-dimensional (1D) thermal and electrochemical model of a planar SOFC was developed previously in MATLAB Simulink® using a combination of finite difference and finite volume discretization techniques [13]. As configured in Figure 2.1, the fuel cell system model comprises of a fuel cell with cathode air and fuel as the model inputs, and a post combustor after the fuel cell to oxidize the unutilized fuel. The model uses a user-specified fuel input rate for the anode and real-time sensor data for the real cathode feed stream. The model simulates the pre-heating of the cathode feed and the dynamics of the cells. The model adds the thermal energy content of the post combustor exhaust and then subtracts out the energy consumption of the preheater to arrive at the net thermal effluent.

The 1D, distributed, real-time fuel cell model allows the user to evaluate the SOFC dynamic performance across the cell with spatial and temporal resolution, not only limited to the thermal profiles (solid and oxidant stream temperatures), but also including electrochemical characterization such as Nernst potential, electrochemical losses, current density, and fuel composition gradients. SOFC dimensions and operating conditions such as number of cells in a stack, SOFC current, SOFC fuel flow and fuel composition, can be defined and modified by the user depending on the study orientation. In this study, the SOFC stack size was fixed with a total of 2500 cells. Since the fuel cell model has been computationally designed for a single cell unit, the total inlet and outlet mass flow of the SOFC system are equivalent to the accumulated mass flow of the total number of cells. The detailed description of the model regarding the computational model and approaches including the

model validation has been published previously [13]. The operating conditions of the fuel cell model used for the test are specified in Table 2.1.

For real-time hardware-in-the-loop simulations, this model is coupled to the hardware-based hybrid facility by interfacing the MATLAB Simulink® fuel cell model to dSPACE real-time hardware. The SOFC cathode inlet air conditions of the model (i.e., mass flow rate, temperature and pressure) are given by the actual sensor measurements (FT-380, TE-326 and PT-305) from the operating hybrid test facility which are updated in the model every 80ms. Nevertheless, the normal sampling rates of the hardware system is as fast as 5ms.

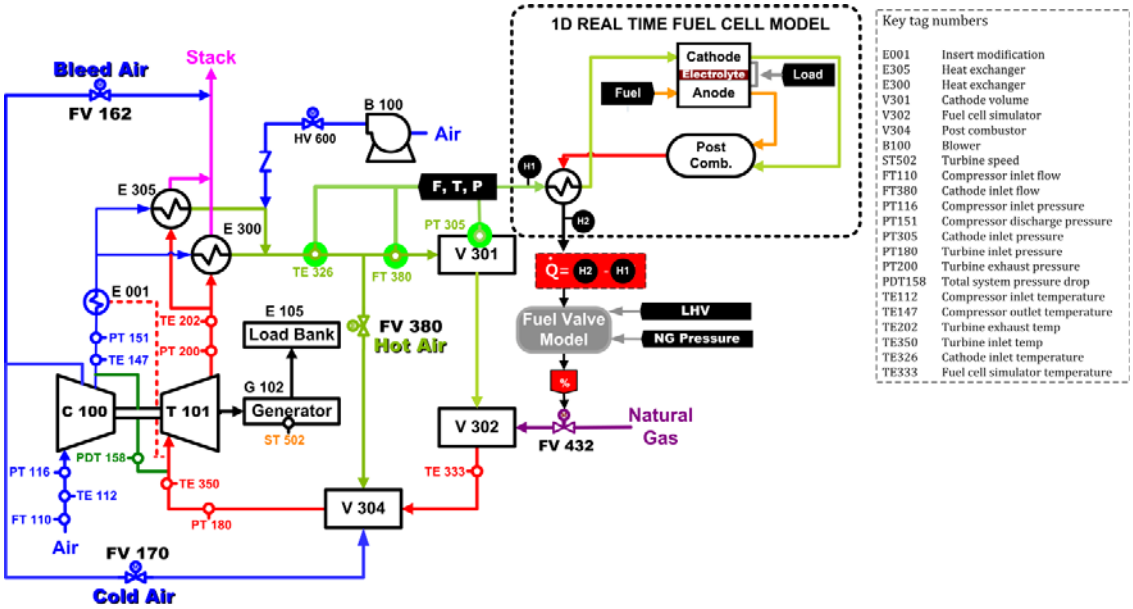

Figure 2.1: Flow diagram of the hardware-based hybrid test facility at NETL

This fuel cell model can also be utilized for offline simulations. Offline application is usually required for scoping studies to predict the SOFC dynamic response prior to real experiments. In offline simulations, the inlet conditions of SOFC cathode air can be constant or dynamic inputs, extracted from the historical experimental data.

To be specific, the model output thermal effluent, Q, can be defined as the additional sensible heat that needs to be added to the system, such that, the net thermal effluent exiting the simulated fuel cell system is the same as the sensible heat exiting the fuel cell simulator, V-302, in the hardware system. In other words, Q represents the difference in the sensible heat between the final stream leaving the simulated fuel cell system and the air stream entering the fuel cell (Figure 2.1). In theory, this value accounts for the total thermal energy of by-product heat generation of an operating fuel cell, plus the heat released from the oxidation of anode-off gas in the post combustor.

Table 2.1: SOFC operating conditions and parameters

System parameter	
Fuel cell load	220 A
Number of cell	2500
Anode recycle	0%
Initial fuel cell temperature	1073.15 K
Total stack mass	3500 kg
Heat capacity of stack	2625 kJ/K
Fuel cell cathode inlet condition	
Air mass flow rate	1.03 kg/s
Air temperature	978.15 K
Air pressure	346 kPa
Air composition	21% O_2, 79% N_2
Fuel cell anode inlet condition	
Fuel mass flow rate	0.145 kg/s
Fuel temperature	1073.15 K
Fuel pressure	346 kPa
Fuel cell nominal condition	
Cell voltage	0.83 V
Fuel utilization	67%

2.4.2 SOFC Fuel Composition Scoping Study

A scoping study to determine appropriate compositions of methane to use for tests was conducted. There are two main concerns when considering the fuel composition:

a. *No carbon deposition in the SOFC*. If pure methane is used, it is likely to cause carbon deposition in the SOFCs, especially at low temperatures, which can result in serious damage to SOFC materials. Based on known effects of the relative atomic C-H-O composition of the feed on deposition rates, the maximum allowable humidified methane composition to prevent carbon deposition at the specified operating conditions is about 43% methane/57% steam [14, 15].

b. *Tolerable heat change available in the bottom cycle of the SOFC/GT hybrid configuration*. It is crucial to ensure that the amount of heat going to the turbine as a result of the change in SOFC fuel composition must be within certain tolerable limits. This is to prevent permanent destruction of equipment during system operations. The limits are imposed by the existing emergency and control strategy employed to safely operate the facility, acceptable turbine load frequencies, and turbine torques as well as compressor stall and surge limits.

For safety reasons, the scoping study was conducted in offline simulations using the fuel cell dynamic model. A set of constant fuel cell cathode inlet conditions such as mass

flow, temperature, and pressure were used without coupling the fuel cell model with the hardware system facility.

The first case study was a step change from coal-derived syngas to humidified methane at 43% methane (57% steam). As presented in Figure 2.2, this transient resulted in a rapid and significant change in the thermal effluent, Q. The increase in Q from about 500 kW to 2500 kW (i.e. 500%) just in 6 seconds after switching the composition, as illustrated in Figure 2.2b, was predicted to produce substantial process perturbations in the turbine system. Hence, this would effectively destroy the turbine since only approximately a limit of 20% increase in Q could be tolerated, which was determined from the previous experience.

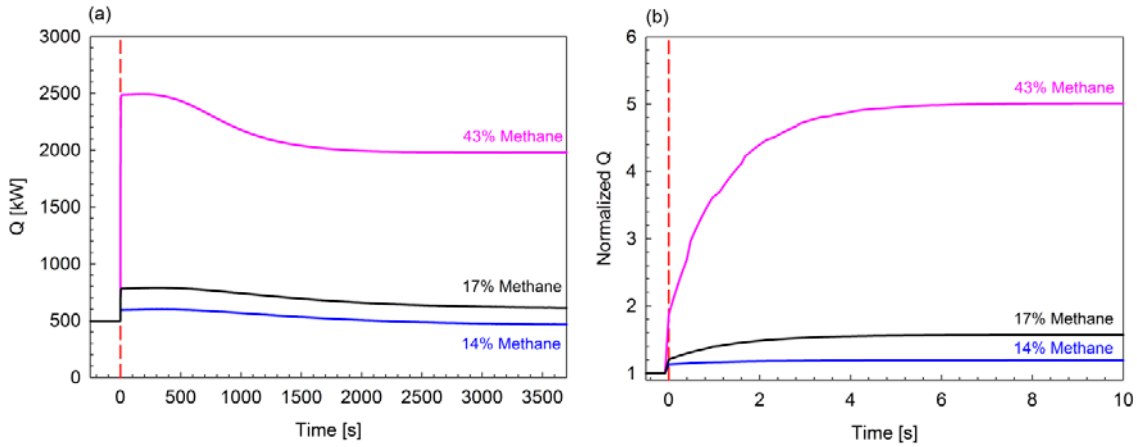

Figure 2.2: Results of scoping studies (a) real response during the entire course of offline simulation (b) normalized plot for the first 10 second transient period

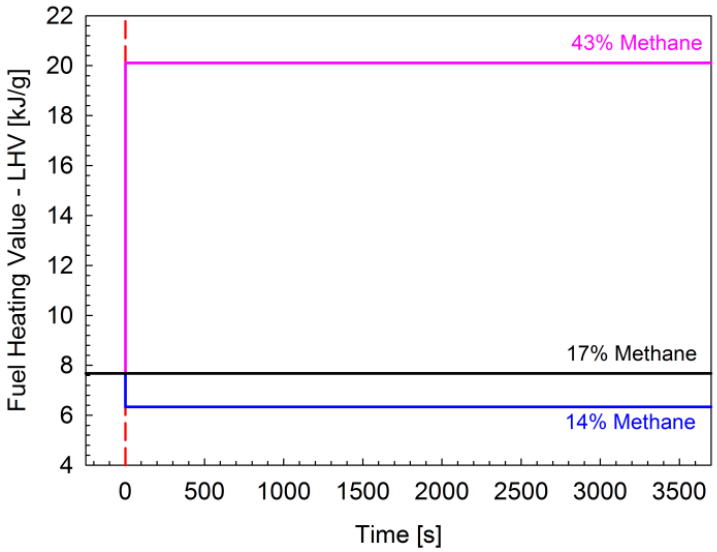

Figure 2.3: Transition in fuel heating values (LHV) between syngas to humidified methane of three different compositions

As illustrated in Figure 2.3, a fuel containing 17% methane has the same lower heating value (LHV) as the coal-derived syngas. Despite this, a switch from coal-derived syngas to 17% methane caused an approximately 60% increase in Q over the first few seconds (Figure 2.2b), which is still dangerous to the facility.

Ultimately, humidified methane with 14% methane, which represents 17.43% LHV change, was selected as the best test case to use in the full hardware-in-the-loop experiments. As shown in Figure 2.2a, the final steady state Q for 14% methane was similar to the coal-derived syngas, and the peak Q increase during the transient is approximately 17%, within the 20% safety limit (Figure 2.2b).

2.4.3 Hardware-based Hybrid Test Facility

A pilot scale, hardware-based facility of the SOFC/GT hybrid system located at U.S. Department of Energy, National Energy Technology Laboratory in Morgantown, West Virginia was used in this study. As shown as in Figure 2.1, the fuel cell system model is integrated to the hardware systems for hardware-in-the-loop simulations.

The major equipment involved in the hardware section includes a single shaft turbine (T-101) with a synchronous generator (G-102), an air compressor (C-100), exhaust heat recuperators (E-300 and E-305), pressure vessels (V-301 and V-304) and a large piping volume. A 200 L air plenum (V-301) and a 600L pressure vessel (V-304) has been constructed to represent cathode air volume and post combustion, physically simulating the real fluid dynamic behaviour of the SOFC/GT hybrid system. For safe operations and air thermal management, this facility has been equipped with several bypass valves which consist of cold air (FV-170), hot air (FV-380) and bleed air (FV-162) valves [16].

In the development of turbine speed control strategies, an external load bank (E-105), which provides resistive load on the turbine shaft, is manipulated to maintain turbine speed constant. The turbine speed is an average measurement from rotational speed optical sensors, ST-502, in the generator shaft. During hardware-in-the-loop simulations, a natural gas burner, V-302 is used to supply the simulated net thermal effluent to the turbomachinery system. A physical fuel valve, FV-432, is driven by the feedforward Q calculated in the model. A controller reads Q in real time and then, considering the current heating value, temperature and pressure of the natural gas available to the pilot facility, adjusts the gas control value (FV-432) such that the real gas delivered to the combustor hardware has a total thermal energetic content equal to the net thermal effluent [11].

2.4.4 Hardware-based Simulation Procedures

After achieving the nominal turbine speed, the system with 40kW turbine load was brought to a new steady state of the entire hybrid test facility including the heat recuperation system (E-300 and E-305) and the post combustor (V-304). For this stage, since the post combustor has the largest heat capacity in the system configuration, the steady state condition was indicated by a temperature change of the post combustor volume by less than 0.25 K/min [11, 17].

Likewise, at the specified fuel cell operating conditions, the fuel cell system model was then independently driven to a steady, preheated condition with 220 A fuel cell electric load. Syngas was used as the initial SOFC fuel composition in the experiment described in Table 2.2.

The corresponding fuel utilization at a constant SOFC fuel mass flow rate of 145 g/s used in this study was approximately 67%. The SOFC fuel flow was determined by matching the model predicted thermal effluent, $\dot{Q}$ with the turbine energy requirement at a 40 kW turbine load. The system was then taken off the fuel valve speed control algorithms and put into an open loop operation, before switching the entire hybrid test facility to the fuel cell model control.

Table 2.2: Coal-derived syngas and humidified methane compositions on mole basis

Composition	Syngas	Methane
X_{CH4}	0.000	0.140
X_{CO2}	0.120	0.000
X_{CO}	0.286	0.000
X_{H2}	0.291	0.000
X_{H2O}	0.271	0.860
X_{N2}	0.032	0.000
X_{O2}	0.000	0.000

The fuel cell model control was engaged after a steady state in the SOFC and turbine systems were verified. When the system was in the state of this controller, the resulting perturbations in Q directly affected the fuel valve opening to supply an equivalent amount of heat to the turbine, which consequently caused turbine speed variations. Thus, turbine load was adjusted by the load-based speed control system to maintain a constant turbine speed. The schematic of the load-based speed controller is shown in Figure 2.4.

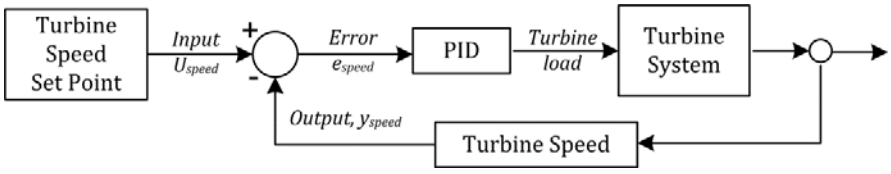

Figure 2.4: Block diagram of the load-based speed controller

2.5 Results and Discussion

2.5.1 The Dynamic Response of Thermal Effluent

The transient impact on the thermal effluent, Q, is presented in Figure 2.5. The actual dynamic response data was collected from the hardware-in-the-loop simulation. Two hours was sufficient to see the most rapidly changing portions of the transients. However, after two hours, the system did not reach steady state, but was slowly decreasing. As such, the

steady state could not be determined experimentally within a reasonable amount of time. Instead, a good estimate for the steady state condition was determined by simulating the 1D SOFC model offline (in an open-loop configuration) using inputs to the SOFC equal to the near-steady state values of the hardware-in-the-loop system after two hours. This steady state estimate is shown as an asymptotic lower bound in Figure 2.5, and is only slightly lower than the real system after two hours.

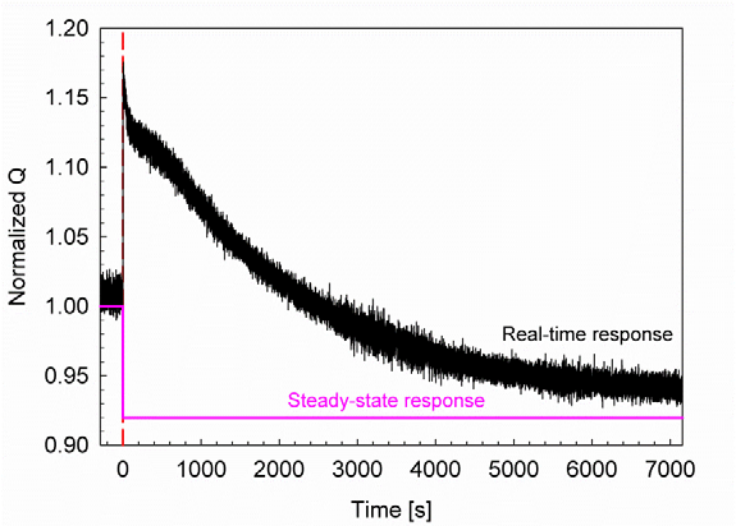

Figure 2.5: Real-time dynamic response and estimated steady state profile

Overall, an approximately 8% decrease in the steady state thermal effluent was observed, in response to a 17.43% reduction in the fuel heating value. However, although the chemical energy content decreased as a result of the step change (Figure 2.2), the system exhibited a rapid and significant inverse response immediately following the step change, such that Q increased by about 17% (Figure 2.5), from about 750 kW to 880 kW, before decaying toward its steady state value.

The collected experimental data from this study shows that the inverse response in Q is highly correlated to the fuel cell thermal performance. The temporal and spatial solid temperature analysis demonstrated a sudden temperature drop in the fuel cell, which was induced by the endothermic steam methane reforming kinetics. Since the fuel cell contained a huge amount of thermal energy storage at the respective operating temperature and total stack heat capacity (Table 2.1), a small variation in the temperature could result in substantial impact on the thermal energy storage.

Thus, it was expected that the drastic transient in Q over the first few seconds was strongly associated to the significant change in the SOFC stored thermal energy. Meanwhile, the subsequent Q decay was a result of complex interaction factors between chemical and electrochemical activities in the fuel cell. The detailed transient analysis of the fuel cell response is extensive and will be presented in future work.

2.5.2 The Impact of Thermal Effluent on Turbine Load

In general, the amount of heat supplied to the turbine is directly proportional to the model predicted thermal effluent, Q. Intuitively, an increase in Q causes a rise in turbine inlet temperature, therefore the turbine speed. However, in this study, as depicted in Figure 2.6, turbine speed was held constant at 40,500 rpm, by varying turbine load. For this reason, the resulting heat variation going to the turbomachinery was demonstrated by the change in turbine load.

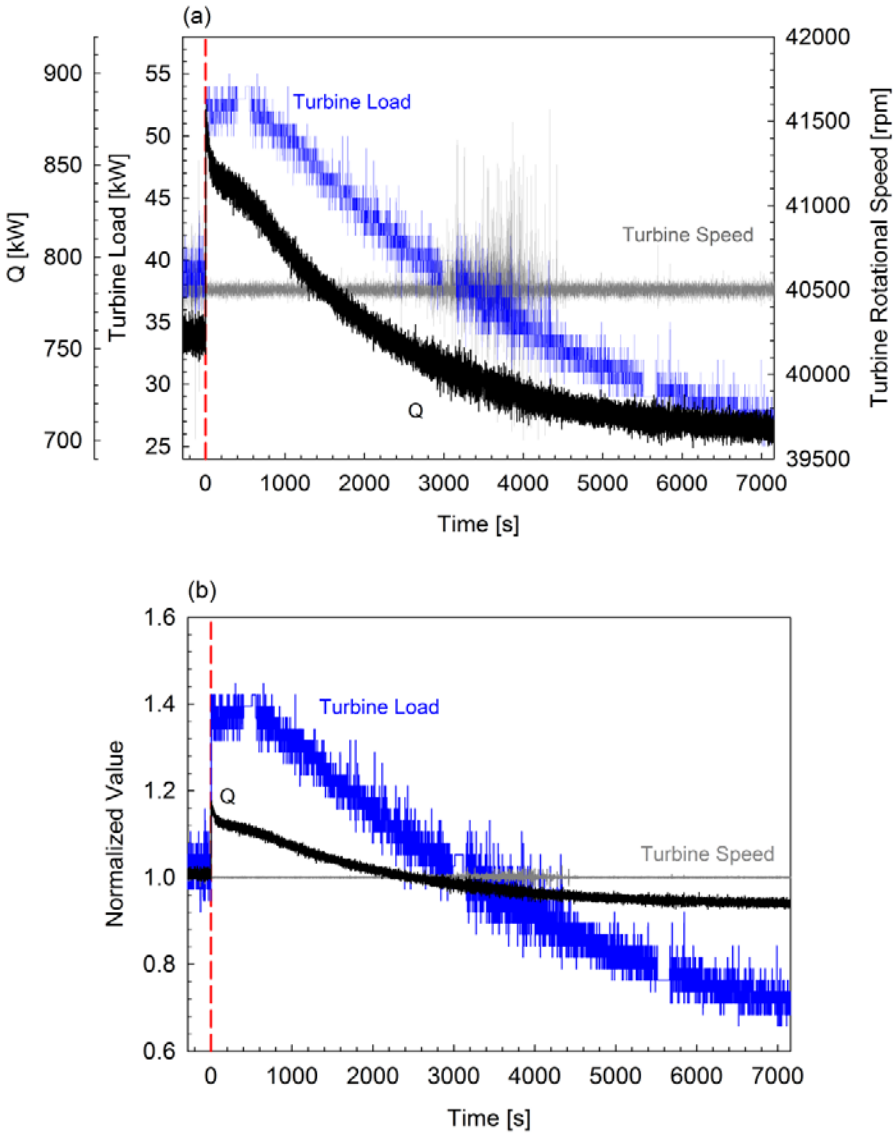

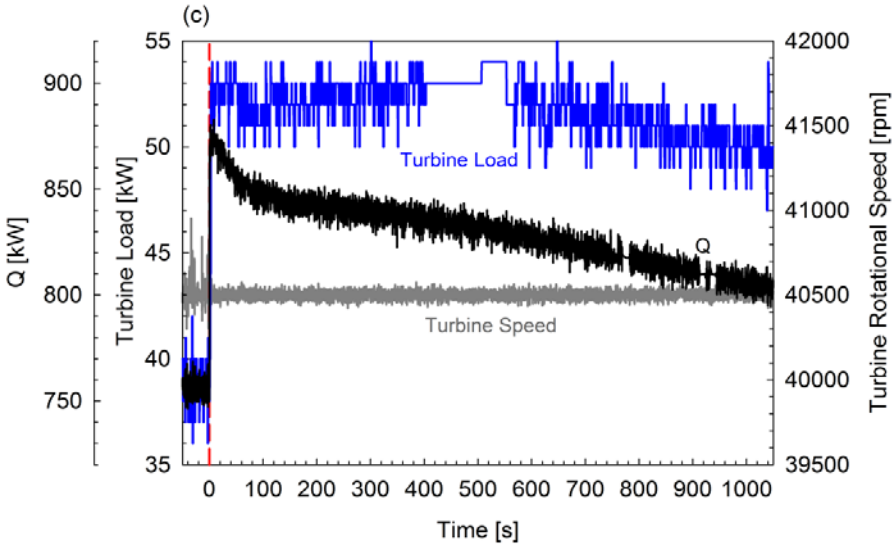

Figure 2.6: Dynamic profiles of thermal effluent, turbine speed and turbine load (a) The real response over 7,000 seconds, (b) normalized plot of (a), and (c) the real response over 1,050 seconds

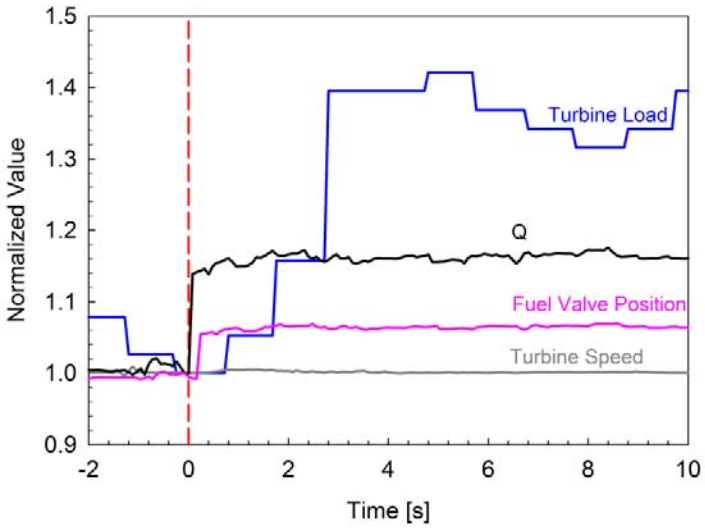

Figure 2.7: Normalized profiles of thermal effluent, turbine speed, and turbine load over 10 seconds after the step time

As expected, the overall corresponding turbine load profile followed the trend of the Q transient closely, featuring the same inverse response and slow decay characteristics (Figure 2.6a). The step time for the transient initiation is represented by the red dashed line. The turbine load was sensitive to changes in Q, resulting in an initial 40% increase from 38 kW to 53 kW, for only a 17% increase in Q (Figure 2.6). As shown in Figure 2.7, the substantial increase in turbine load of 40% was identified at 3 seconds after the step change.

Therefore, a significant rise in turbine speed in a short period after the transient would be expected if the load-based speed control were not used. This case would cause an instability in the turbine-compressor system which would likely result in serious equipment damage.

However, during the course of the first 10 minute transient period, as shown in Figure 2.6c, the turbine load response did not follow the gradual decrease in Q, but instead remained approximately constant. This is due to the strong influence of turbine inlet temperature, which is discussed in the following section. From this study, it was also demonstrated that, the PID control scheme used to control the turbine speed was very effective at maintaining a near constant speed despite the disturbance.

2.5.3 The Response of Turbine Inlet Temperature and SOFC Cathode Inlet Temperature

The influence of turbine inlet temperature and turbine exhaust temperature as presented in Figure 2.8 was studied to evaluate the resulting turbine load and cathode inlet temperature profiles. A strong correlation between turbine inlet temperature and turbine load can be seen clearly in Figure 2.8b and Figure 2.8c. Over the course of the experiment, the turbine load exhibited transient behaviour closely to the change in the turbine inlet temperature, to maintain a constant turbine speed. As soon as the composition change was initiated at 0 second, a 17% increase in Q resulted in an average of 5% rise in turbine inlet temperature and 40% increase in turbine load.

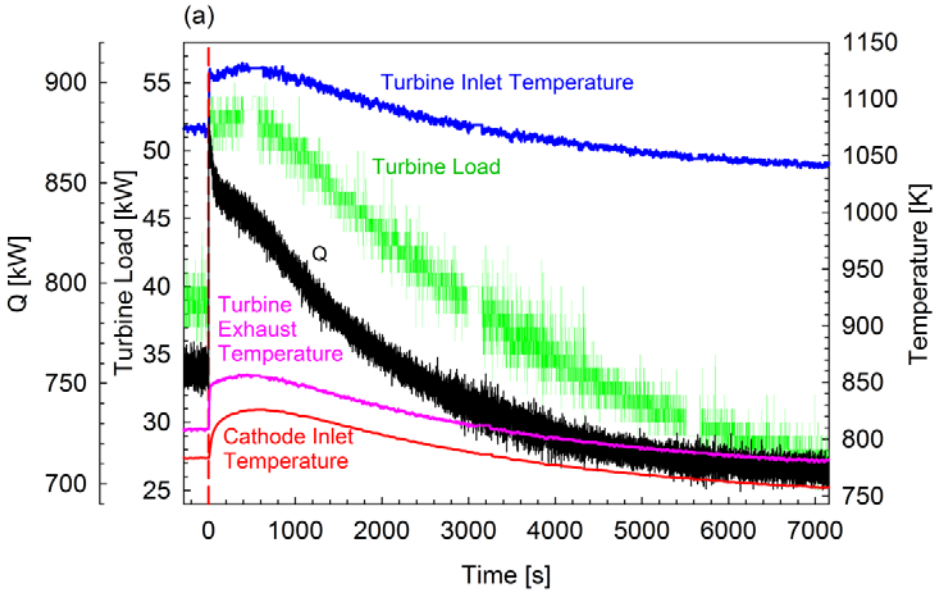

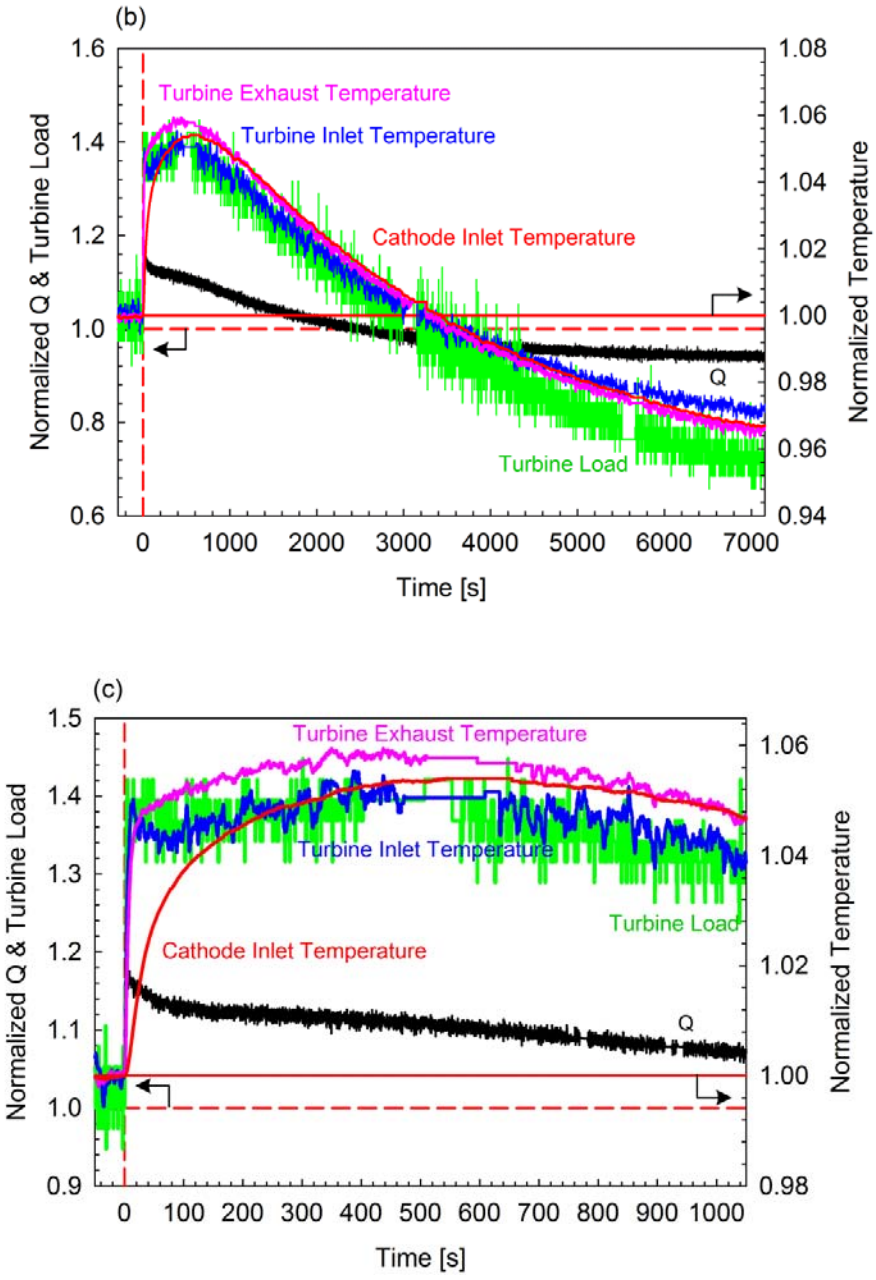

Figure 2.8: The effect of thermal effluent on turbine temperatures and SOFC cathode inlet temperature (a) the real response over 7,000 seconds, (b) the normalized plot of (a), and (c) normalized plot for the response over 1,050 seconds

As shown in Figure 2.8, the cathode inlet temperature was demonstrated to be proportionally related to turbine inlet temperature, which strongly influenced the turbine exhaust temperature and so, the recuperation heat. It was also expected that the change in cathode inlet temperature would be affected by the compressor inlet flow that supplies air

to cool the SOFC stack. However, the variation of the compressor inlet flow was not significant enough to affect the cathode inlet temperature, as presented in Figure 2.11. Therefore, only turbine exhaust temperature and corresponding recuperation heat in the heat exchangers (E-300 and E-305) have great determining impacts on the dynamic behaviour of cathode inlet temperature.

As demonstrated in Figure 2.9, significant delays among turbine inlet temperature, turbine exhaust temperature and cathode inlet temperature are noticeable. Obviously, the cathode inlet temperature has the longest time delay of several minutes as compared to the turbine temperatures. This is due to the heat recuperation system at the facility (Figure 2.8c).

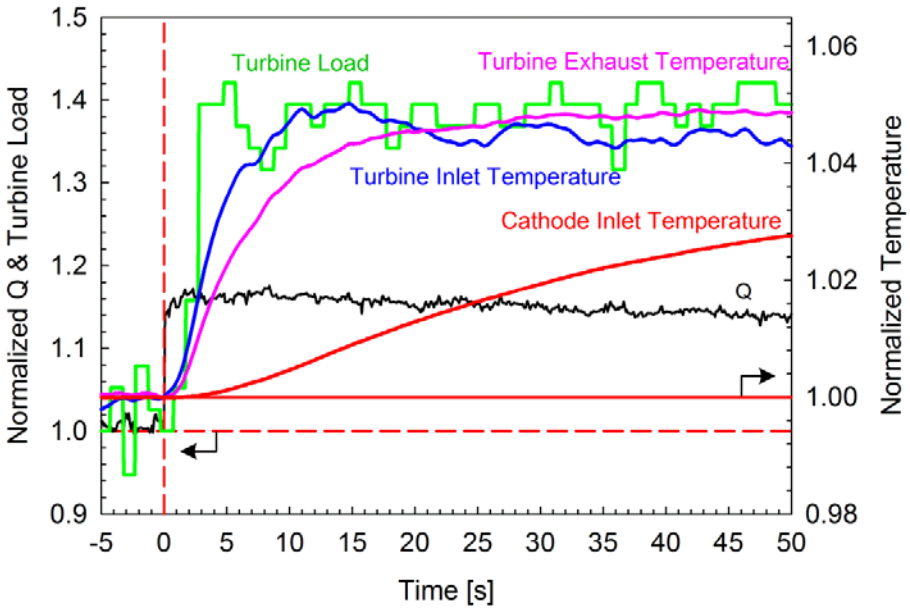

Figure 2.9: Normalized plots of thermal effluent, turbine temperatures and SOFC cathode inlet temperature over the first 50 seconds

As the result of the step change in the fuel composition, the other interesting turbine system behaviour was observed. Figure 2.8b reveals that over the course of the first 3,000 seconds of the experiment, the magnitude of change in the turbine exhaust temperature is higher than the magnitude of change in the turbine inlet temperature. As expected, this was due to the reduction in the turbine cycle efficiency by 4% after the transient, as provided in Figure 2.10, but slowly increased to a higher efficiency at the near-steady state condition. The turbine cycle efficiency was able to recover at around 3,157 seconds after the step time.

The turbine cycle efficiency, η, was calculated based on the net work generated by the turbine, divided by the amount of the heat supplied to the turbine system [18]. The conditions of the inlet and outlet stream for turbine/compressor are required. The heat capacities of combustion gas and air are assumed to be 1.148 kJ/kg.K and 1.005 kJ/kg.K respectively at the process conditions.

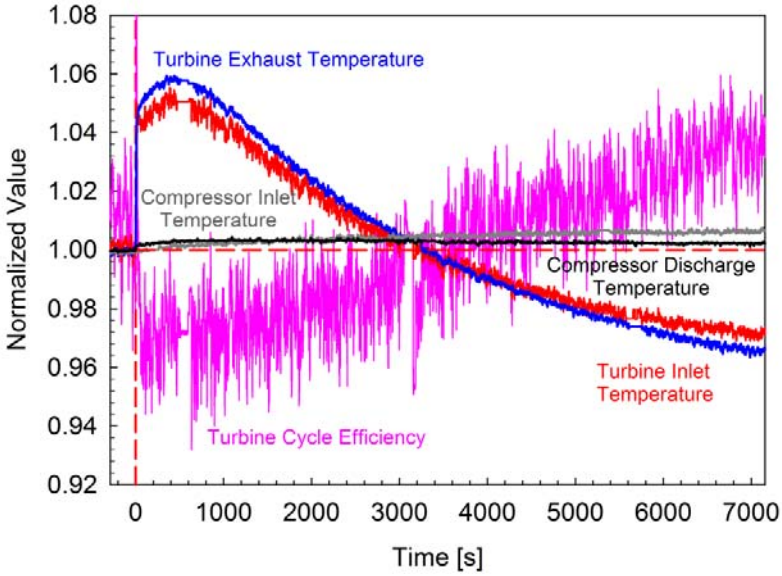

Figure 2.10: Turbine cycle efficiency

2.5.4 The Dynamic Behaviour of the System Air Mass Flow

The dynamic response of turbine load with corresponding compressor inlet flow and compressor discharge pressure transients is shown in Figure 2.11. As the consequent impact of 40% initial increase in turbine load, the compressor inlet air mass flow reduced by approximately 4%, which was imposed by a slight increase (1%) in compressor discharge pressure. Decreasing the compressor inlet mass flow by 4%, from 1.94 kg/s to 1.86 kg/s ultimately reduced the cathode feed mass flow by 2% to 1.01 kg/s, as shown in Figure 2.11b.

In this study, all other valve positions were held constant over the entire course of experiment. Therefore, the reduction in the compressor inlet mass flow rate has a direct relationship to the reduction in the cathode inlet mass flow rate.

The increase of compressor discharge pressure was due to the increase in torque placed on the turbine shaft as a result of the control action to maintain the turbine speed. Thus, the change in compressor discharge pressure modified the compressor pressure ratio, since there was no significant change in the compressor inlet pressure. The ambient pressure during the period of time studied was fairly constant with about 0.03% variation.

Based on a standard compressor performance map, which is the pressure ratio as function of the compressor inlet air mass flow, a shift along the synchronous constant speed line with the decreased compressor air mass flow causes the increased compressor pressure ratio, or vice-versa. This would be expected to eventually bring the system close to the compressor stall line.

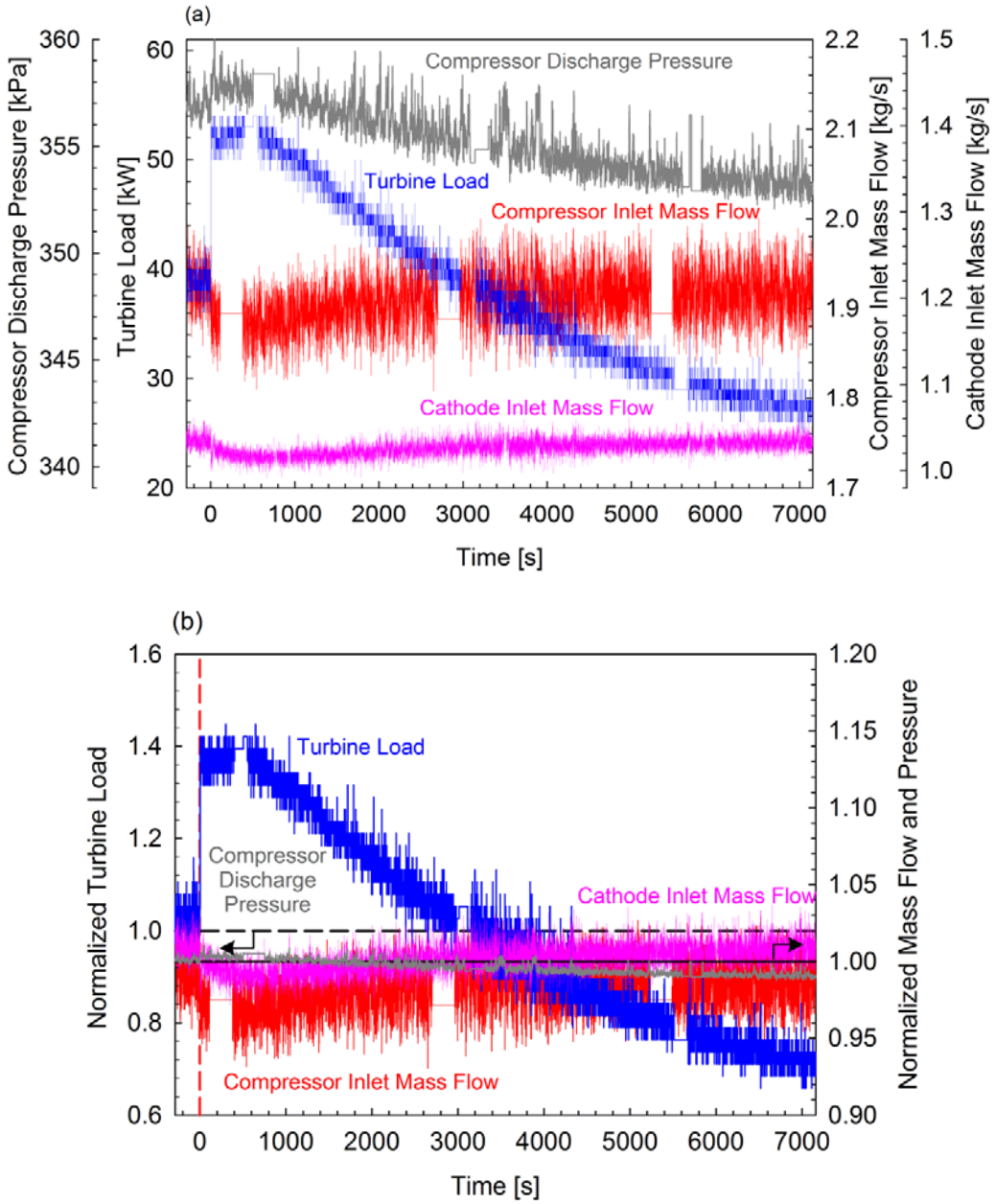

Figure 2.11: The SOFC cathode inlet flow and the compressor intake air flow transients (a) the real response over 7,000 seconds (b) normalized plot of (a)

2.5.5 The Transient Impact on the Fuel Cell Performance

The corresponding dynamic SOFC performance such as fuel utilization, operating cell voltage and SOFC stack power is plotted in Figure 2.12. An increase in the fuel utilization from 0.67 to 0.71 was demonstrated when transitioning syngas feed to humidified methane feed at a reduced lower heating value and a constant SOFC current. But, the fuel utilization was remained constant over the remaining course of the test.

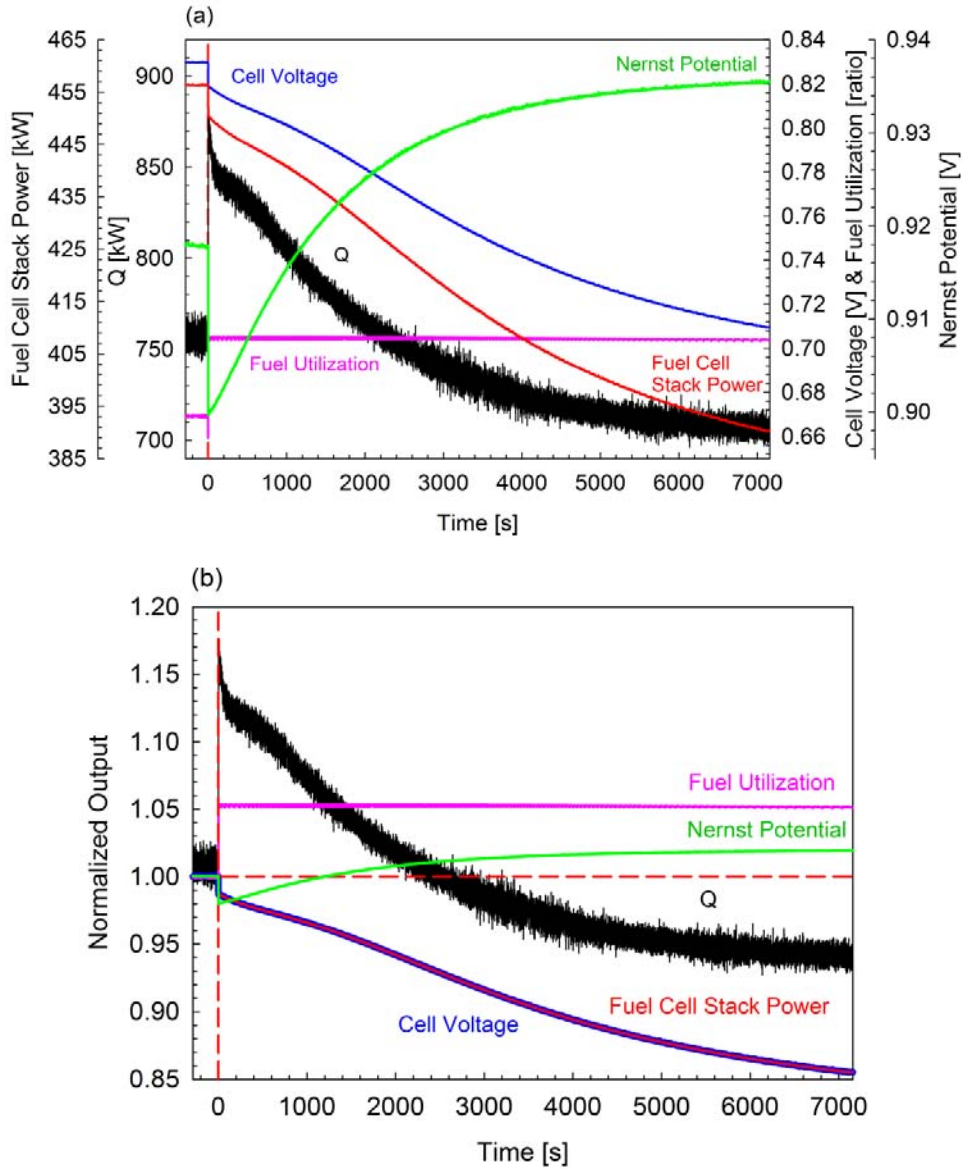

Figure 2.12: SOFC performance during fuel composition dynamics (a) the real response over 7,000 seconds (b) normalized plot of (a)

The change in fuel utilization was primarily driven by the variation in the hydrogen partial pressure as well as the other compositional gradient. The immediate shift in the anode feed composition played a great role in determining the fuel cell chemical and electrochemical potentials.

The simulated Nernst potential dynamic (i.e. the maximum ideal operating voltage) was also presented in Figure 2.12. Interestingly, as demonstrated in Figure 2.12a, the response of Nernst potential was inversely correlated to the dynamic transient of Q. An immediate reduction in the Nernst potential by 2% was evident just after the fuel change, following by an increase to the maximum potential of 0.936 V at 7,000 seconds. Analysis identified that the Nernst potential was highly dependent on the fuel cell temperature and the compositional gradient.

The variation in the Nernst potential, however, was not linearly associated to the transient in the operating cell voltage. The operating cell voltage was evaluated based on the Nernst potential, subtracting it from the electrochemical losses in the simulated fuel cell. Similar to the initial drastic reduction of Nernst potential, the operating cell voltage decreased significantly by 2% after changing to humidified methane. For the remaining time studied, the operating cell voltage kept decreasing from 0.82 V to the final voltage of 0.71 V. It was hypothesized that during this period, the reduction in the cell voltage was dominated by the significant increase in electrochemical losses.

Figure 2.12b shows the resulting impact on the stack power, in which there was a positive relationship between the cell voltage and the stack power. Both voltage and stack power were proportionately reduced by about 15% over the course of 7,000 seconds.

2.6 Conclusion

The scoping studies showed that the SOFC fuel composition step-change with the same fuel heating value was not possible to perform due to the transient increase in the thermal effluent. The change in the thermal effluent exceeded the tolerable limit of turbine system.

Changing the SOFC fuel composition to humidified methane at 14% methane was a reasonable test case for the exploration of the dynamic behaviour using hardware-in-the-simulations. From the steady state analysis, it was expected that the thermal effluent would be reduced to the final steady state value by about 8%, as reflected by a 17.43% reduction in the fuel low heating value. However, the inverse response with substantial increase in the thermal effluent was verified in real-time coupled simulation. This transient continued for about 40 minutes before decreasing towards the same direction of the final steady state value.

The data presented in this study clearly indicated that operating SOFC/GT hybrid systems with sudden changes in fuel composition for operation flexibility requires advanced control strategies. The composition transient has a significant impact on the fuel cell performance which eventually needs careful thermal management to mitigate unfavourable impacts on the fuel cell.

Plans for the future work to thoroughly analyze and describe the total SOFC system performance including the distributed SOFC profiles of solid temperature/oxidant

temperature gradients, Nernst potential, electrochemical losses, current density, composition gradient and heat generation are underway.

2.7 Acknowledgement

The authors would like to thanks all people involved in this collaboration work between NETL and McMaster University, Paolo Pezzini and Nana Zhou from NETL for their contribution in the execution of the experimentation and also greatly acknowledge Universiti Teknologi Malaysia and Ministry of Higher Education Malaysia for the financial support. This work was funded by the U.S. Department of Energy (DOE) Crosscutting Research program, administered through the National Energy Technology Laboratory (NETL).

2.8 References

[1] Serra, L. M., Lozano, M.-A., Ramos, J., Ensinas, A. V., and Nebra, S. A., 2009, "Polygeneration and Efficient Use of Natural Resources," Energy, 34(5), pp. 575–586.

[2] Li, S., Gao, L., Zhang, X., Lin, H., and Jin, H., 2012, "Evaluation of Cost Reduction Potential for a Coal Based Polygeneration System With CO_2 Capture," Energy, 45(1), pp. 101–106.

[3] Becker, W. L., Braun, R. J., Penev, M., and Melaina, M., 2012, "Design and Technoeconomic Performance Analysis of a 1 MW Solid Oxide Fuel Cell Polygeneration System for Combined Production of Heat, Hydrogen, and Power," J. Power Sources, 200, pp. 34–44.

[4] Qian, Y., Liu, J., Huang, Z., Kraslawski, A., Cui, J., and Huang, Y., 2009, "Conceptual Design and System Analysis of a Poly-Generation System for Power and Olefin Production from Natural Gas," Appl. Energy, 86(10), pp. 2088–2095.

[5] Chen, Y.-H., Chen, C.-Y., and Lee, S.-C., 2011, "Technology Forecasting and Patent Strategy of Hydrogen Energy and Fuel Cell Technologies," Int. J. Hydrogen Energy, 36(12), pp. 6957–6969.

[6] McLarty, D., Brouwer, J., and Samuelsen, S., 2013, "Hybrid Fuel Cell Gas Turbine System Design and Optimization," ASME J. Fuel Cell Sci. Technol., 10(4), pp. 041005-041005-11.

[7] Traverso, A., Magistri, L., and Massardo, A. F., 2010, "Turbomachinery for the Air Management and Energy Recovery in Fuel Cell Gas Turbine Hybrid Systems," Energy, 35(2), pp. 764–777.

[8] Haynes, C., and Wepfer, W. J., 2000, "Design for Power of a Commercial Grade Tubular Solid Oxide Fuel Cell," Energy Convers. Manage., 41(11), pp. 1123–1139.

[9] Adams, T. A. II, Nease, J., Tucker, D., and Barton, P. I., 2012, "Energy Conversion with Solid Oxide Fuel Cell Systems: A Review of Concepts and Outlooks for the Short- and Long-Term," Ind. Eng. Chem. Res., 52(9), pp. 3089–3111.

[10] Tucker, D., Lawson, L., and Gemmen, R., 2005, "Characterization of Air Flow Management and Control in a Fuel Cell Turbine Hybrid Power System using Hardware Simulation," ASME Paper No. PWR2005-50127.

[11] Tucker, D., Lawson, L., Gemmen, R., and Dennis, R., 2005, "Evaluation of Hybrid Fuel Cell Turbine System Startup with Compressor Bleed," ASME Paper No. GT2005-68784.
[12] Tucker, D., Liese, E., and Gemmen, R., 2009, "Determination of the Operating Envelope for a Direct Fired Fuel Cell Turbine Hybrid using Hardware Based Simulation," Proceedings of the International Colloquium on Environmentally Preferred Advanced Power Generation (ICEPAG 2009), Newport Beach, CA, Feb. 10–12, Paper No. ICEPAG2009-1021.
[13] Hughes, D., Wepfer, W. J., Davies, K., Ford, J. C., Haynes, C., and Tucker, D., 2011, "A Real-Time Spatial SOFC Model for Hardware-based Simulation of Hybrid Systems," ASME Paper No. FUELCELL2011-54591.
[14] Eguchi, K., Kojo, H., Takeguchi, T., Kikuchi, R., and Sasaki, K., 2002, "Fuel Flexibility in Power Generation by Solid Oxide Fuel Cells," J. Solid State Ionics, 152–153, pp. 411–416.
[15] Yi, Y., Rao, A. D., Brouwer, J., and Samuelsen, G. S., 2005, "Fuel Flexibility Study of an Integrated 25kW SOFC Reformer System," J. Power Sources, 144(1), pp. 67–76.
[16] Tucker, D., Smith, T. P., and Haynes, C., 2006, "Evaluation of Cathodic Air Flow Transients in a Hybrid System Using Hardware Simulation," ASME Paper No. FUELCELL2006-97107.
[17] Pezzini, P., Tucker, D., and Traverso, A., 2013, "Avoiding Compressor Surge during Emergency Shut-Down Hybrid Turbine Systems," ASME J. Gas Turbines Power, 135(10), pp. 102602-102602-10.
[18] Saravanamuttoo, H., Rogers, G., Cohen, H., and Straznicky, P., 2009, Gas Turbine Theory, Pearson Education Ltd., Upper Saddle River, NJ, pp. 47–69.

3 OPEN LOOP AND CLOSED LOOP PERFORMANCE OF SOLID OXIDE FUEL CELL TURBINE HYBRID SYSTEMS DURING FUEL COMPOSITION CHANGES

3.1 Publication Highlights

This chapter presents the impacts of fuel composition changes on the dynamic performance of solid oxide fuel cell gas turbine hybrid systems in open loop and closed loop operations. The work herein focuses on the difference in transient response obtained from open loop and closed loop cases that is mainly driven by turbine speed control modes. In open loop case, the system is uncontrolled while in the closed loop case, turbine speed is maintained constant throughout the test. The impacts on the key process variables, such as fuel cell thermal effluent, turbine temperatures, and cathode inlet conditions are discussed.

Similarly, the tests in this section were conducted using hardware-based simulation facility by me, with helps from authorized personnel at the U.S. Department of Energy, National Energy Technology Laboratory (NETL) - Dr. David Tucker, Dr. Paolo Pezzini, Dr. Nana Zhou (University of Chongqing), and Valentina Zaccaria (University of Genoa). Dr. David Tucker and Dr. Adams also helped me in analyzing data, planning and revising the manuscript.

Open Loop and Closed Loop Performance of Solid Oxide Fuel Cell Turbine Hybrid Systems during Fuel Composition Changes

Authors: Nor Farida Harun[a], David Tucker[b], and Thomas A. Adams II[a]
[a]Department of Chemical Engineering, McMaster University, 1280 Main Street West, Hamilton, Ontario L8S 4L7, Canada
[b]U.S. Department of Energy, National Energy Technology Laboratory, 3610 Collins Ferry Road, Morgantown, West Virginia 26507-0880, United States

3.2 Abstract

The dynamic behaviour of a solid oxide fuel cell gas turbine hybrid system (SOFC/GT) from both open and closed loop transients in response to sudden changes in fuel composition was experimentally investigated. A pilot-scale (200 kW – 700 kW) hybrid facility available at the U.S. Department of Energy, National Energy Technology Laboratory was used to perform the experiments using a combination of numerical models and actual equipment.

In the open loop configuration, the turbine speed was driven by the thermal effluent fed into the gas turbine system, where the thermal effluent was determined by the feedforward fuel cell control system. However, in the closed loop configuration, a load-based speed control system was used to maintain the turbine speed constant at 40,500 rpm by adjusting the load on the turbine, in addition to the implementation of the fuel cell system control.

The open loop transient response showed that the impacts of fuel composition changes on key process variables, such as fuel cell thermal effluent, turbine speed and cathode feed stream conditions in the SOFC/GT systems were propagated over the course of the test, except for the cathode inlet temperature. The trajectories of the aforementioned variables are discussed in this paper to better understand the resulting mitigation/propagation behaviours. This will help lead to the development of novel control strategies to mitigate the negative impacts experienced during fuel composition transients of SOFC/GT systems.

3.3 Introduction

As shown in Figure 3.1, a public research test facility, called HyPer (Hybrid Performance project) at the National Energy Technology Laboratory (NETL) has been used for many years to explore operability and controllability of recuperated solid oxide fuel cell gas turbine (SOFC/GT) hybrid systems.

A combination of actual equipment and numerical models of fuel cell systems was used in fully coupled hardware-based simulations. The setup has been used for a variety of research purposes, such as the exploration of the system transients during startup and shutdown [2, 3], operating envelopes of cathode air flow [4], compressor stall and surge studies, emergency shutdown strategies [2], and the most recent studies on the accelerated fuel cell degradation [5].

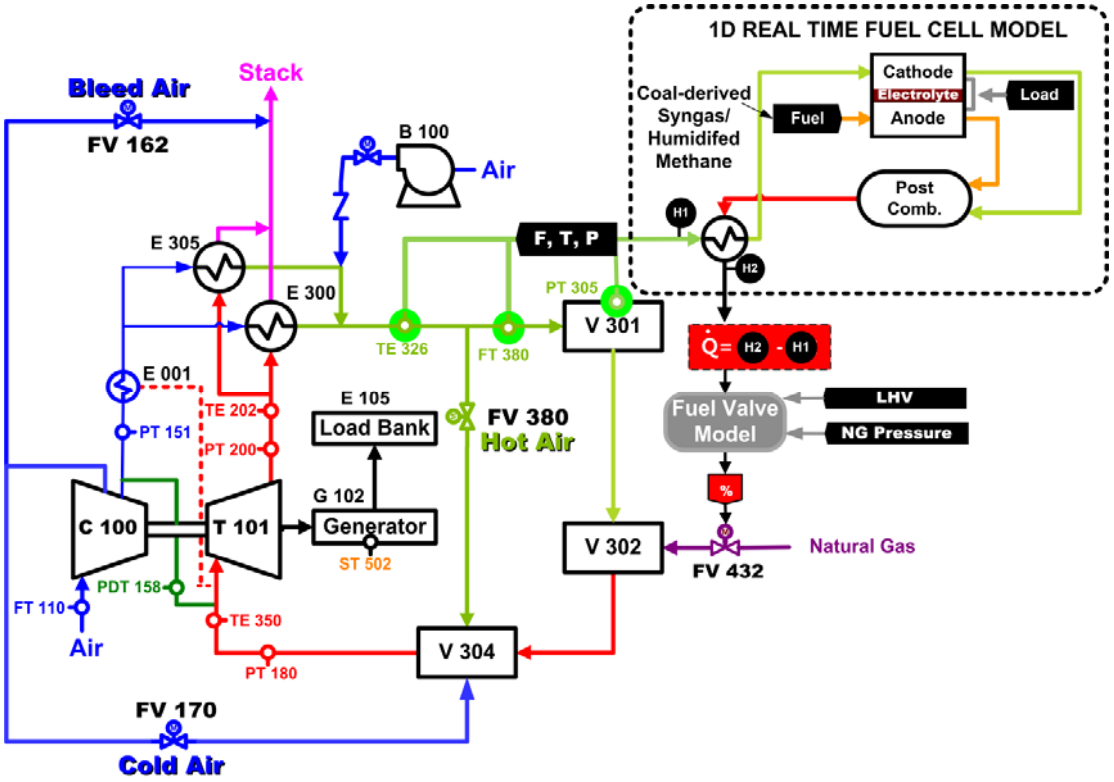

Figure 3.1: The recuperated SOFC/GT hybrid test facility at NETL [1]

One of the advantages that make the SOFC/GT hybrid particularly attractive is the potential to generate power in fuel flexible environments, such that one fuel type/quality can be switched to another fuel type/quality during operations [6-8]. For steady state operations with one type of fuel, this feature helps deal with variability in the fuel quality. It is expected that some systems are likely to experience non-trivial fuel composition variations in real time, particularly in syngas applications [9]. A small compositional change could occur during transient events. A large compositional change is less likely for traditional single-fuel power plants, but possible.

However, in some systems, large changes in fuel composition can be expected by design. For example, in flexible polygeneration systems such as in the co-generation of electric power, liquid fuels and methanol, profitability can be significantly increased if the relative amounts of each product can be adjusted in response to changing market demand and prices [10]. For example, during the night, syngas is diverted to different process trains such that less electricity is produced and more chemicals are produced, and vice versa during the day. Because the process trains are integrated such that off-gases and purge-gases are mixed and used for power generation, the flow rates and composition of that mixed gas fuel can change significantly with each portfolio change throughout the day.

Although SOFC/GT systems are an attractive power generation strategy for flexible polygeneration applications, previous research has shown that SOFC/GT systems possess

undesirable characteristics when experiencing fuel composition transients which adversely affect the entire hybrid system performance. Among the most concerning problems is thermal shock to the SOFCs when the direct electrochemical conversion of a different fuel takes place in the SOFCs. The need for thermal management in the hybrid SOFC/GT system with regard to fuel composition changes was demonstrated experimentally in a preliminary study [1].

The goal of this paper is to better understand transient effects during fuel composition changes, and determine the open loop and closed loop SOFC/GT hybrid characteristics. These are necessary requirements for the development of an appropriate control strategy for SOFC/GT systems which experience fuel composition transitions.

3.4 SOFC/GT Hybrid Test Facility

A pilot-scale (200 kW – 700 kW) HyPer project available at a laboratory in the NETL was used to perform the tests discussed herein. This facility was built by NETL to examine fundamental issues associated with dynamic operability of recuperated SOFC/GT hybrid systems. The HyPer project research objectives were described in detail in previous publications [11].

The HyPer setup is designed to simulate a real hybrid system. A 120 kW Garret Series 85 auxiliary power unit (APU) with a single shaft gas turbine (T-101) and a two-stage compressor (C-100) in the HyPer project were modified such that the original combustion chamber was removed and a different combustion chamber with a larger volume is placed between C-100 and T-101. As shown in Figure 3.1, some additional equipment placed between C-100 ad T-101, such as heat exchangers, air plenum vessels, and piping, contribute additional volume to the system and thus increase the residence time of gases between C-100 and T-101, which affects the system dynamics. The total volume is increased by about two orders of magnitude compared to the original combustion chamber, which likely increases the risk of compressor stall and surge during transient events. The turbine/compressor is also attached to a 400 Hz gear-driven generator (G-102). An adjustable resistive load can be loaded on the turbine shaft by a 120kW resistor load bank (E-105).

The recuperated energy from the SOFC system is used to compress the system inlet air flow as well as to preheat the cathode inlet air flow. Two primary surface heat exchangers, E-300 and E-305, with a nominal effectiveness of 89% are installed to preheat the compressor discharge streams by using the high temperature exhaust gas (around 900 K) from the turbine. The hot sides of the heat exchangers are directed to the inlet of the SOFC cathode. The third heat exchanger, E-001, is used to preheat the compressor discharge before the heat exchanger manifolds. It consists of a one-pass arrangement of combustor (cold side) and turbine discharge in the turbine shell.

In this system, two air plenums, with a capacity of 200 L (V-301) and 600 L (V-304) are used to replicate the missing fuel cell volume and the post combustor volume respectively. The air flow fed to the fuel cell cathode, V-301, can be modulated via bypass air valves. There are 3 bypass valves in place; bleed air valve (FV-162), cold air valve (FV-170) and hot air valve (FV-380). All bypass valves are positioned at the operational minimal requirements to avoid compressor stall and surge during startup.

In addition, each valve has a particular function. The bleed air valve (FV-162) is often used to add some load on the turbine shaft to control the turbine speed. On the other hand, the cold air bypass valve, FV-170, provides some aid for turbine thermal management. Bleeding flow through the cold air bypass valve can decrease the turbine inlet temperature and therefore the cathode inlet temperature. It bypasses the heat exchangers and the fuel cell simulator (V-302) while maintaining constant turbine inlet flow. The hot air valve, FV-380, is used for steady flow adjustments to the fuel cell cathode inlet. Without fuel cell simulations, the hot air bypass flow has little to zero impact on the turbine thermal input. For the fully coupled fuel cell and turbine system, however, significant impacts on the fuel cell performance and turbine speed were identified. It was shown previously that this actuator could be potentially employed for fuel cell thermal management [12].

During fuel cell simulations, the hybrid system is affected by the results of the fuel cell model. This means that the opening of a physical fuel valve in the plant, FV-432, is determined by the fuel cell thermal effluent value (Q) calculated by the numerical model in real time. Empirical correlations based on the physical fuel conditions (temperature, pressure and fuel heating value) are used to determine the fuel valve opening as a function of Q.

The combustion of air flowing from the air plenum, V-301, and natural gas occurs in the fuel cell hardware simulator, V-302, in order to simulate the thermal characteristic of the fuel cell thermal output, Q. The combustion continues in a larger post combustor volume, V-304.

3.5 Hardware-based Simulation of SOFC/GT Hybrid

The overall method of hardware-based simulations used in this study is summarized in Figure 3.2. The most prominent benefit of hardware-based simulations is that it can avoid the destruction of expensive fuel cell equipment while maintaining the fluid dynamics of the hybrid system by physically simulating the balance-of-plant hardware. With the flexibility provided by the dynamic fuel cell model, a relatively extensive study of SOFC system performances during transient operations can be conducted. However, the hardware-based simulations are limited by the fidelity associated with the hybrid hardware.

As indicated in Figure 3.1, to guarantee a fully coupled interaction between the real-time fuel cell model and the balance of plant hardware, parts of the model inputs such as cathode feed conditions (i.e. air mass flow rate, temperature and pressure) were provided by the real-time data measured by FT-380, TE-326 and PT-305 sensors. In contrast, fuel stream conditions as well as the other operating fuel cell parameters and fuel cell geometry were all user defined inputs. The detailed fuel cell configuration specified for this study is presented in Table 3.1. Prior to the experiment execution, the fuel cell system model was set to the initial conditions described in Table 3.1. A lower operating fuel utilization (67%) was chosen since the fuel utilization does not affect the hybrid system efficiency significantly unlike standalone fuel cell systems, such that the lifetime of fuel cells can be extended [5, 13].

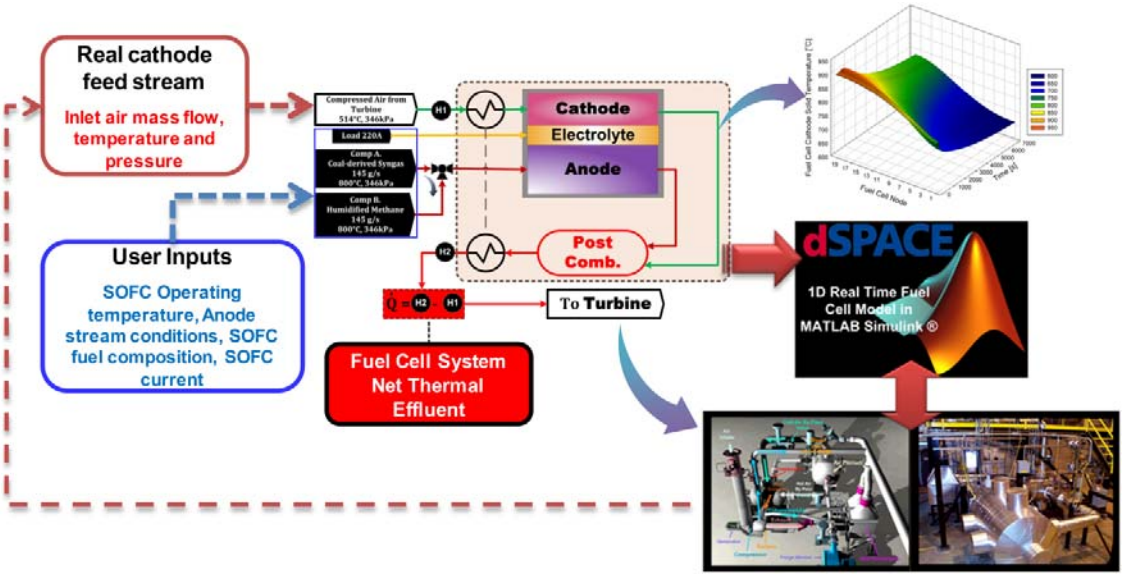

Figure 3.2: Hardware-based simulations of SOFC/GT hybrid system

Table 3.1: SOFC parameters and initial operating conditions

System parameter	
Fuel cell load	220 A
Anode recycle	0%
Initial fuel cell temperature	800 °C
Total cell area	200 mm x 200 mm
Anode thickness	0.5 mm
Electrolyte thickness	0.008 mm
Cathode thickness	0.05 mm
Oxidant/fuel channel size	2 mm x 2 mm
Stack size	2500 cells
Total stack mass	3500 kg
Total stack heat capacity	2625 kJ/K
Fuel cell cathode inlet condition	
Air mass flow rate	1.03 kg/s
Air temperature	705 °C
Air pressure	347 kPa
Air composition	21% O_2, 79% N_2
Fuel cell anode inlet condition	
Fuel mass flow rate	145 g/s
Fuel temperature	800 °C
Fuel pressure	347 kPa

Fuel cell initial condition	
Cell voltage	0.83 V
Fuel utilization	67%

The model simulates the preheating of cathode inlet stream and the dynamics of the fuel cell. As a result of the simulation, the model returns a value of the fuel cell thermal effluent, Q, to the actual fuel valve FV-432 every 80 ms. This ultimately supplies the thermal input to the turbine shaft to power the compressor and to preheat the real cathode feed stream via recuperator configuration (Figure 3.1), which in turn, affects the response of Q. With that interaction loop, the hardware-based simulation is completed.

3.6 Test Procedure

Regardless of any diffusion of hydrogen during transport lag to extend the concentration gradients in the fuel, the worst case of composition variations would be a step change from one fuel composition to another. Upon the initiation of fuel composition changes in the case study presented herein, a step change from coal-derived syngas to methane-rich gas composition was applied.

Such a drastic transition in the fuel feed was important to provide insights of the transient characteristics of the hybrid system at the maximum operational limits. This information ultimately will be used the development of control architectures that can help deal with the potential issues regarding fuel composition changes.

To begin the hardware-based simulation, the system was first brought to a nominal turbine speed at 40,500 rpm without the real-time fuel cell model in the loop. The system was heated up for about 2 hours after the ignition state until the entire hardware system achieved a steady state.

This steady state has a fairly constant skin temperature of the post combustor, V-304, which poses the largest thermal mass in the system. Based on prior experience, the fluctuation of this temperature must not exceed 0.1K for 30s before the initiation of dynamic tests. At this stage, the system was in fuel valve speed control, where the turbine speed was maintained constant at its set point by adjusting the fuel flow through FV-432 (i.e. fuel valve opening). Practically, to accelerate the heating up process to the steady state, a 40 kW electrical load on turbine was employed, such that the fuel flow and therefore the thermal input to turbine system increased.

The online simulation of the fuel cell system was started once the system conditions were stable in fuel valve speed control mode. The coal-derived syngas composition as described in Table 3.2 was used as the initial fuel feed to the model [14]. The composition is consistent with other studies used for the evaluation of degradation and cycle analysis [5].

As soon as smooth interaction between the model and the hardware was achieved at the equivalent heat rate (meaning both the fuel cell model and the hardware were at steady state), the fuel valve speed controller was disengaged and the fuel cell model output, Q, was used as the feedforward control input to the fuel valve, FV-432. This fully integrated the fuel cell model into the hardware system.

Table 3.2: Coal-derived syngas and humidified methane compositions

Composition	Syngas (mole %)	Methane (mole %)
X_{CH4}	0.000	0.136
X_{CO2}	0.120	0.000
X_{CO}	0.286	0.000
X_{H2}	0.291	0.000
X_{H2O}	0.271	0.864
X_{N2}	0.032	0.000
X_{O2}	0.000	0.000

The turbine speed control was either kept in open-loop mode or closed-loop mode depending on the test. In the open loop test, the turbine speed changed freely, depending on the variability of turbine thermal input associated with fuel cell dynamics. In this case, no feedback was sent to system to control the turbine speed. In contrast, a load based speed control, as shown in Figure 3.3, was employed in the closed loop test to maintain a constant turbine speed at 40,500 rpm. The turbine speed data used by the controller was the average real-time measurement from three rotational speed sensors (ST-502) mounted in the hardware turbomachinery system.

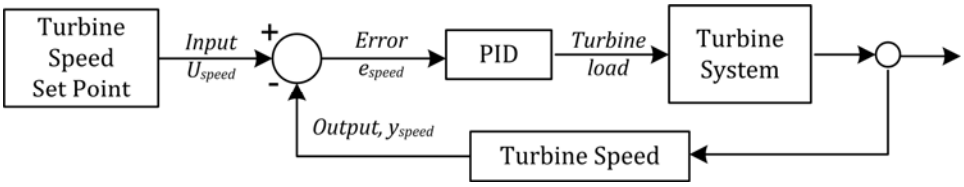

Figure 3.3: Load based speed control scheme [1]

After the fully integrated system had reached steady state, a step change in composition to a humidified methane fuel with a lower heating value (shown in Table 3.2) was enacted, and denoted as time zero in this paper. The operational boundaries related to the change of input heating value were quantified previously in order to comply with the transient limitations of the turbine cycle [1]. A switch to the humidified methane with a lower heating value was favourable since a change in the fuel feed at the same heating value caused a dangerous transient increase of 60% in Q. However, the tolerable heat change in the turbomachinery was only 20% [1].

The fuel mass flow rate and SOFC current were held constant throughout the experiment. These conditions were selected in order to eliminate the interactive impacts of fuel utilization and fuel cell load from the fuel composition transients on the hybrid performance. In this study, the mass flow rate of the humidified methane was considered on a wet basis. Data were recorded for about 2 hours during each experimentation run, including the 5 minutes prior to each step change.

3.7 Result and Analysis

In this study, the performance of the recuperated SOFC/GT hybrid system in response to open loop transients during fuel composition changes was compared against the performance in closed loop operation. The impacts of the control methods on turbine speed and the corresponding turbine load during open and closed loop configurations are presented for each case in Figure 3.4.

Without any turbine speed controller, the initiation of fuel composition change at time 0s caused a significant inverse response in turbine speed. As seen in Figure 3.4, a sudden increase in turbine speed to a maximum of 4% (42,200 rpm) was observed. But shortly after the maximum speed, turbine speed slowly decreased by 4,000 rpm (6% from the initial speed before the step time) to the slowest speed (38,200 rpm). The resulting turbine load feedback profile during open loop test was intuitive since it was proportionally correlated to the response of turbine speed.

To compensate for the same change in the thermal input to the shaft as exhibited in the open loop experiment, turbine load was modulated by the load-based speed control in the closed loop approach following a similar trend, from 15 kW to 45 kW, to maintain the nominal speed (Figure 3.4).

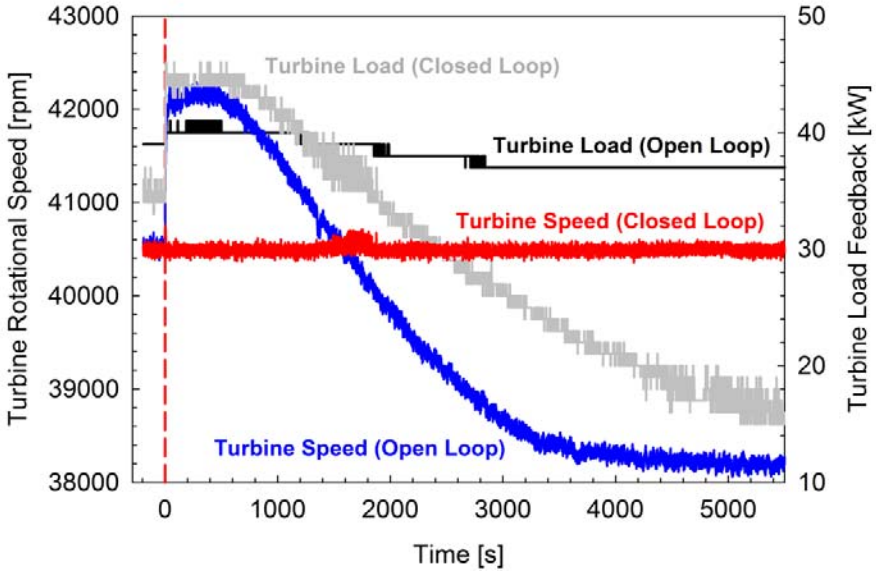

Figure 3.4: Turbine speed and turbine load responses for open and closed loop configurations

3.7.1 Fuel Cell Thermal Effluent, Q, and Turbine Temperatures

The dynamic transients of the fuel cell thermal effluent, Q, were identified to be the key process perturbations during the fuel composition transition. Q primarily caused the subsequent open and closed loop responses in the SOFC/GT hybrid system. Thus, the

resulting Q, as demonstrated in Figure 3.5, was first analyzed. The initial fuel cell thermal effluent in the open loop and closed configurations were respectively at 760 kW and 755 kW.

Over the course of 5,500 s test duration, a dramatic change in the open loop was evident by comparing the slopes of Q profiles, as presented in Figure 3.5. The magnitude of the rate change in Q from the open loop response was relatively higher than in the closed loop especially in the period between 600 s and 3,000 s after the fuel transition. In comparison to the closed loop results, it was shown that there were propagation impacts in the open loop transients.

In response to the fuel composition change, the system exhibited a combination of changes in competing factors which affect Q, which can explain both the initial transient increase and the following transient reduction. The change in Q is the result of complex interactions of fuel cell heat flux, fuel cell thermal energy storage and compositional gradients within the cell. These interactions were studied and quantified, but the details are beyond of the scope of this paper and will be presented in a future work.

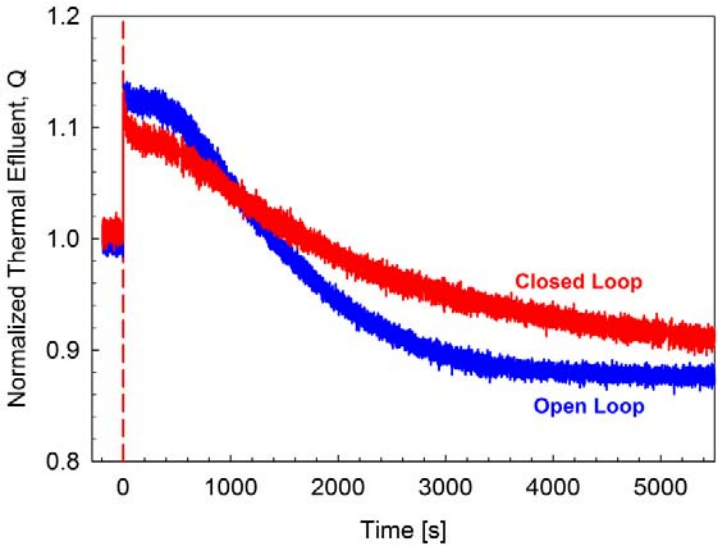

Figure 3.5: A comparison profiles of fuel cell thermal effluent for open loop and closed loop tests

The detailed analysis showed that the sharp increase in Q after the step change was strongly influenced by the fuel conversion of humidified methane. Given a constant fuel mass flow rate at a constant SOFC current, changing the SOFC fuel to humidified methane caused a significant increase in the heating value of the unutilized fuel from the anode side. Due to this fact, the thermal effluent from the post combustor increased. The consequent decrease in Q was more affected by cathode inlet conditions. The variation in cathode feed conditions was in turn a result of turbine speed variability and the changes in turbine inlet temperature.

The sudden increase in the open loop test was approximately 1% higher than in the closed loop test. Q increased by 14%, from around 760 kW to a maximum value of 872 kW

in the open loop configuration. Meanwhile, Q increased rapidly by 13%, from a similar initial point to about 845 kW in the closed loop test. This was followed by a reduction in Q by 13% and 10% below the initial value at the final state, in the open loop and the closed loop, respectively.

The impacts of the fluctuation in Q were further indicated by the relevant profiles of turbine inlet and exhaust temperatures given in Figure 3.6(a) and 3.6(b). As clearly shown in Figure 3.6 (b), magnitude of change in turbine temperatures during the closed loop operation was greater and more significant than in the open loop operation. As expected, during the closed-loop mode, the turbine exhaust temperature (TET) closely followed the response of turbine inlet temperature (TIT).

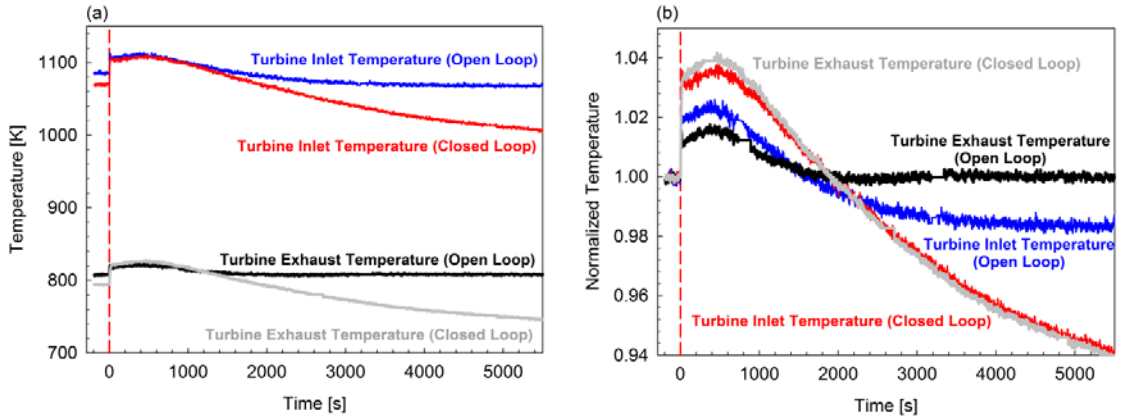

Figure 3.6: A comparison of turbine inlet and exhaust temperatures for open loop configuration versus closed loop configuration, (a) the real profiles, and (b) the normalized profiles

In the closed-loop case, both TIT and TET increased by 4% to the maximum temperature, and reduced by 6% to the lowest temperature at 5,500 s, relatively from the initial temperature. Theoretically, the decrease in TIT caused a drop in gas turbine expansion capability, which resulted in decreased gas turbine performance.

For the open loop configuration, the TIT profile in Figure 3.6(b) explained well the variation in the turbine speed (Figure 3.4) since both of the variables were strongly related. The maximum increase of TIT (about 2.5%) resulted from the immediate increase in Q caused 4% increase in the turbine speed. As the Q decreased, the TIT also decreased gradually by 1.6% below the initial temperature to the final value, but this caused 6% reduction in the turbine speed.

Interestingly, as demonstrated in Figure 3.6(b), there was a significant difference between the resulting open loop profiles of TIT and TET, from 1,600 s to the end of the test. During this period, TET did not follow the reduction in TIT. The data showed that the subsequent decrease in TET was offset by reduction in system air flow due to turbine speed decrease, so that, TET appeared to be approximately at the same initial temperature. Based on this result, it was expected that turbine efficiency changed significantly.

3.7.2 Cathode Inlet Mass Flow

The associated result of cathode feed mass flow is provided in Figure 3.7, which shows that significant propagating effects were discovered in the cathode air mass flow transients, as a consequence of the fuel composition dynamics in the open loop experiment. Figure 3.7 shows the normalized values of the indicated process variables for ease of comparison.

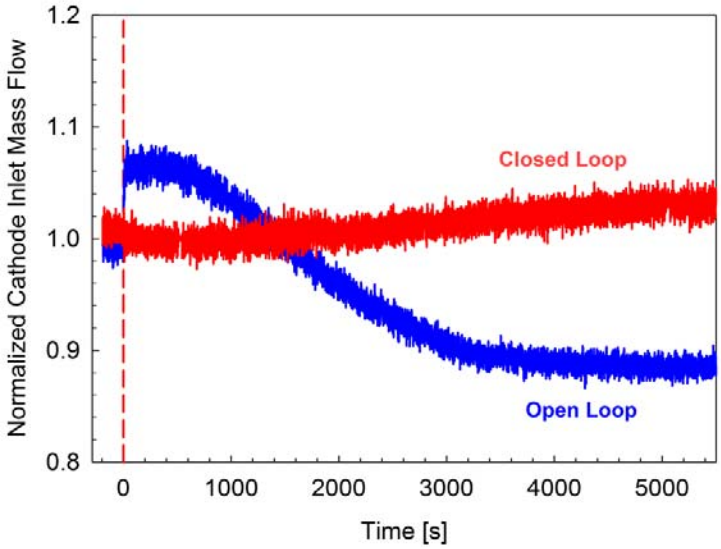

Figure 3.7: A comparison of cathode inlet mass flow for open loop configuration versus closed loop configuration

Over the first 500 s, the cathode inlet mass flow increased by almost 8%, from 1.04 kg/s at the initial point to 1.11 kg/s. But, this was followed by a remarkable reduction of 20% to the final steady mass flow, at about 0.92 kg/s.

In contrast, owing to a constant turbine speed in the closed loop test, the cathode inlet mass flow was fairly constant at 1.03 kg/s over the entire test period. Only a very mild decrease was appeared at the initial transient region, and also with a little increase over the last 1,000 s.

The open loop response in Figure 3.8(a) clearly contrasts the closed loop response in Figure 3.8(b) for the air mass flow with the corresponding compressor discharge pressure in response to turbine speed changes. As shown in Figure 3.8(a), the system air mass flow; compressor inlet mass flow, cathode inlet mass flow, and compressor discharge pressure changed at a very similar rate, closely following the trend in the turbine speed fluctuations.

Turbine speed was not shown in Figure 3.8(b) since it did not change during the test. As expected, due to the steady turbine speed at 40,500 rpm, the system air mass flow and compressor discharge pressure were also maintained approximately at the initial value.

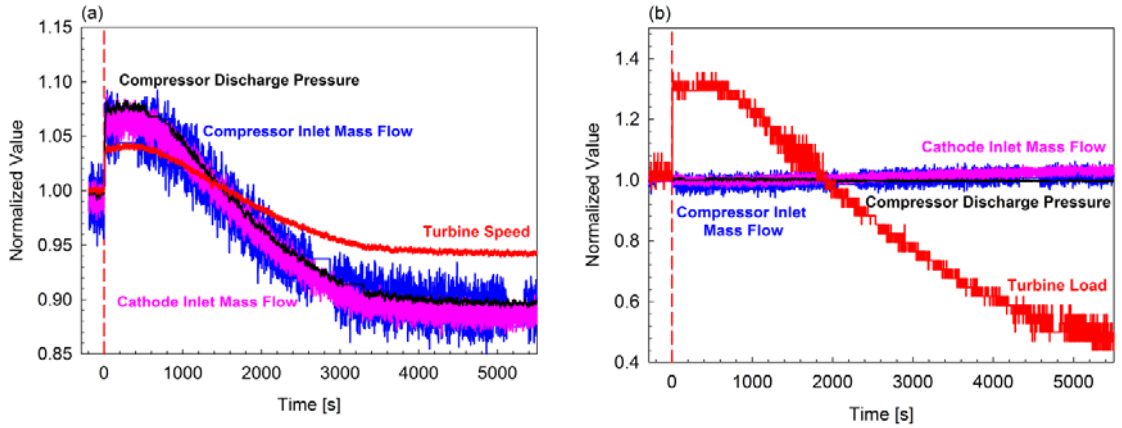

Figure 3.8: Normalized profiles of, (a) system mass flow, compressor discharge pressure and turbine speed for open loop configuration, and (b) system mass flow, compressor discharge pressure and turbine load for closed loop configuration

3.7.3 Cathode Inlet Pressure

The resulting impacts on cathode inlet pressure are plotted in Figure 3.9. For the open loop configuration, the cathode inlet pressure varied from 246 kPag at the initial condition, to the lowest pressure of 210 kPag at the final state, 10% below the initial pressure. Its highest transient increase of 8% was achieved at 275 kPag, as soon as the initiation of the step changes from coal-derived syngas composition to methane-rich composition. As described in Figure 3.10(a), this sharp increase was the result of the 4% initial increase in turbine speed.

Figure 3.9 also shows that the cathode inlet pressure was constant in the closed loop configuration, similar to the transient response of cathode inlet mass flow in Figure 3.7. This was the effect of a constant turbine speed by manipulating turbine load. In this case, as indicated in Figure 3.10(b), turbine load increased by 35% during the overshoot region, and reduced by 58% (from the initial point) to the final condition.

3.7.4 Cathode Inlet Temperature

The analysis of the cathode inlet temperature is presented in Figure 3.11, featuring self-mitigating thermal effects in the open loop operation, and the control effects in the closed loop test.

It was observed that there was an initial increase to a local maximum point in the cathode inlet temperature, in both open and closed loop operations, from 973 K to 986 K, and 975 K to 1,004 K, respectively, before gradually decreasing to their final temperatures. As demonstrated in Figure 3.11, the relevant magnitude of change in cathode inlet temperature during the initial transient increase for the closed loop (3%) is three times higher than the response in the open loop (1%).

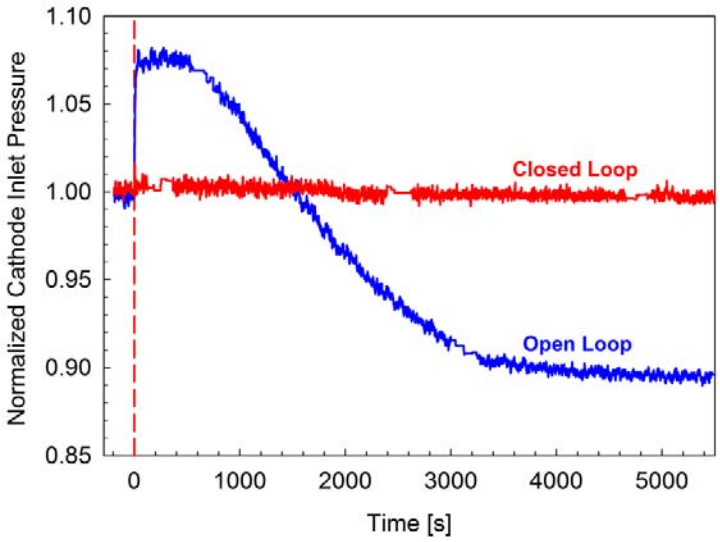

Figure 3.9: A comparison of cathode inlet pressure for open loop configuration versus closed loop configuration

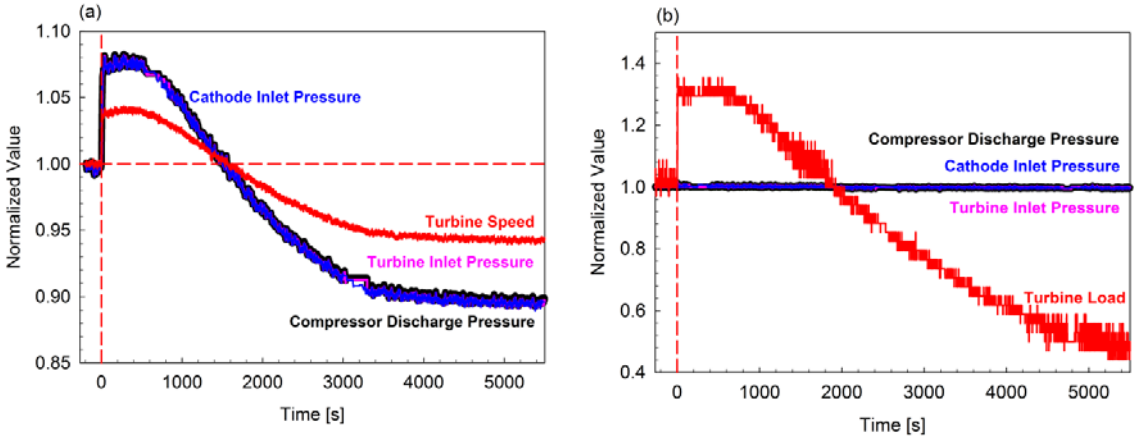

Figure 3.10: Normalized profiles of, (a) system pressures and turbine speed for open loop configuration, and (b) system pressures and turbine load for closed loop configuration

An approximately 18K difference was the result of the variation in system thermal input and thus, the turbine speed, which eventually affected the air supply to support the SOFC operation. Increasing turbine speed in the open loop configuration increased the air supply. This helped the system to moderate the temperature elevation by providing some cooling impacts on the SOFC cathode inlet temperature. In the recuperated SOFC/GT hybrid system, the cathode inlet temperature and turbine inlet temperature were coupled via recuperator units (E-300 and E-305).

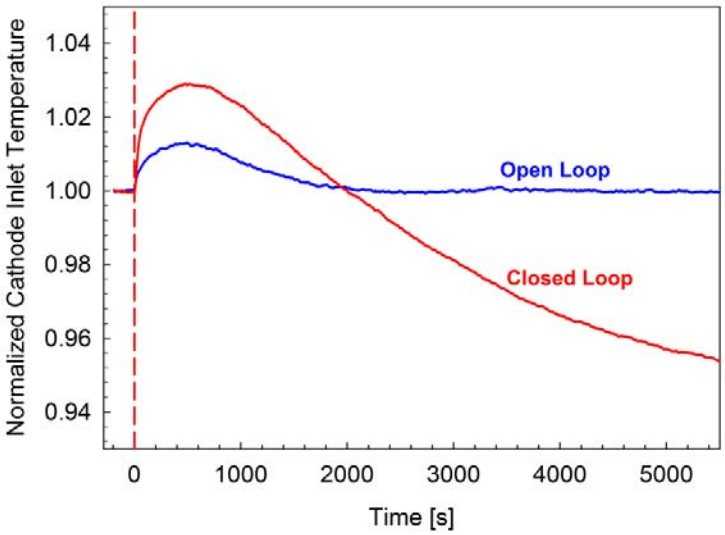

Figure 3.11: A comparison of cathode inlet temperature for open loop configuration versus closed loop configuration

The following response after the initial increase was indicated by a gradual reduction in the cathode inlet temperature. Self mitigating effect was observed in the open loop test when the temperature reduction stopped at 2,000 s after the fuel composition change. The system settled approximately at the same initial temperature, 973 K, until the end of the test period, as shown in Figure 3.11. This mitigating impact was highly promoted by the combined dynamics of fuel cell waste heat, turbine speed and air mass flow.

In contrast, for the closed-loop system, the subsequent decrease in cathode inlet temperature reached the lowest temperature (around 930 K and still dropping) at the end of the test. Since the turbine speed was maintained constant over the course of the experiment, the change in cathode inlet temperature was dominated by the fuel cell thermal effluent, which has great impact in determining the turbine inlet and exhaust temperatures.

3.7.5 Analysis of Mitigating versus Propagating Effects

3.7.5.1 Open Loop Transients

The open loop transients started when an immediate increase in Q occurred upon the initiation of fuel composition switch to humidified methane, as the conversion of chemical energy took place in the fuel cells (Figure 3.5). Thus, fuel flow through FV-432 increased correspondingly to the Q value.

This event ultimately increased the thermal input to the gas turbine system, and thereby increased turbine inlet temperature (Figure 3.6), and turbine speed (Figure 3.4). For this reason, the turbine shaft had additional energy to power the compressor, which then caused an increase of compressor inlet mass flow, and thus, increased cathode inlet mass flow (Figure 3.7).

Due to the coupled effects between turbine inlet temperature and cathode inlet temperature in the recuperated SOFC/GT hybrid system, an initial increase in cathode inlet temperature was also observed (Figure 3.11). However, this increase was temporary since the cooling impacts exhibited by the increased cathode inlet mass flow were more significant in the long run, causing the subsequent reduction in Q. The reduction in Q was also affected by the changes in fuel cell thermal energy storage, heat flux and the heating value of unutilized fuel from the anode side.

The decreasing Q caused the reversed dynamics in the hybrid system, which then restricted the system air mass flow due to turbine speed reduction. The decrease in cathode inlet mass flow increased the stack temperature. From a more detailed analyses, not included herein, it was determined that the reduction in Q due to fuel cell temperature increase was dominated by the reduction in fuel cell heat flux to the cathode airflow.

The mitigating thermal impact obtained in the open loop configuration was the result of interaction between decreasing turbine inlet temperature and decreasing cathode inlet mass flow. This transient cycle continued until a balanced state between the temperature effects from the recuperator and air mass flow was finally achieved.

3.7.5.2 Closed Loop Transients

Similarly, the sudden increase in Q resulted in increasing thermal input to turbine shaft. However, owing to the turbine speed controller actions, compressor mass flow and cathode inlet mass flow were maintained constant, which consequently amplified the sudden rise in cathode inlet temperature, in comparison to the open loop response (Figure 3.11).

After the initial transient in Q, it is most likely that the cathode inlet mass flow was not enough to increase the heat flux to deliver the thermal effluent and to compete with the elevation of the fuel cell thermal energy storage. Therefore, Q reduced. Decreasing Q reduced turbine inlet temperature, and thus, cathode inlet temperature. This event was carried on until a condition with an excessive air flow was achieved, resulting in cooling impacts that led to a continuous reduction in Q. There was no significance change in all cathode feed conditions with a constant turbine speed except the cathode inlet temperature.

3.8 Conclusions and Future Work

An extended characterization of open loop transients in an SOFC/GT hybrid system during fuel composition changes was compared against the closed loop transients. A summary of the transient results for each case studied in this paper is presented in Table 3.3. The percentage described in Table 3.3 represents the change (Δ) of all process variables from their initial values.

Without a turbine speed controller, the fuel cell thermal effluent, Q, cathode inlet mass flow, and pressure exhibited significant propagation effects. The magnitude of change in cathode inlet mass flow and pressure were about double than the transient response in turbine speed.

Table 3.3: Summary of open loop and closed loop transient response

Variables	Open loop		Closed loop	
	Initial response	Final response	Initial response	Final response
ΔQ	14%	-13%	13%	-10%
ΔTurbine speed	4%	-6%	-	-
ΔTurbine load	-	-	35%	58%
ΔCathode inlet mass flow	8%	-12%	-	-
ΔCathode inlet pressure	8%	-10%	-	-
ΔCathode inlet temperature	1%	-	3%	-5%

It is important to note that cathode inlet flow has a strong influence on the Q transients, which can lead to unfavourable effects on fuel cell temperature response if the turbine speed is not controlled. The propagation effects observed in cathode inlet pressure are expected to cause potential fuel cell failures associated with the pressure difference between the anode and cathode sides. This problem would result in potentially destructive events in fuel cells such as cracking and cell delamination.

For the closed loop configuration, the propagation impacts were demonstrated in the resulting Q and cathode inlet temperature profiles. This behaviour was influenced by the response of cathode air mass flow. Cathode inlet mass flow and pressure were kept constant as the result of turbine speed controller. The constant cathode inlet mass flow moderated the rate of change in Q with no potential failure associated with the cathode-anode pressure difference.

From the analysis, it was shown that the requirement for control is extremely important to mitigate the resulting negative impacts caused by the fuel cell thermal effluent and the corresponding hybrid system response. Cathode inlet air flow management can potentially be used in new mitigation strategies.

Future work will consider transfer function development to investigate the particular dynamic correlation between the fuel composition changes and the process system output response. The developed transfer functions will be mapped to the actuator actions in controlling cathode inlet mass flow fed to the SOFC system. Thus, operability and performance of the SOFC/GT hybrid systems can be improved to realize fuel flexibility.

3.9 Acknowledgement

The authors would like to thank Nana Zhou, Paolo Pezzini, Valentina Zaccaria and Dave Ruehl from NETL for their contribution in the execution of the experimentation, and also greatly acknowledge the Universiti Teknologi Malaysia and Ministry of Higher Education Malaysia for financial support. This work was funded by the U.S. Department of Energy Crosscutting Research program, implemented through the Strategic Center for Coal in The Office of Fossil Energy.

3.10 References

[1] Harun, N. F., Tucker, D., and Adams, T. A. II, 2014, "Fuel Composition Transients in Fuel Cell Turbine Hybrid for Polygeneration Applications," ASME J. Fuel Cell Sci. Technol., 11(6), pp. 061001-061001-8.

[2] Pezzini, P., Tucker, D., and Traverso, A., 2013, "Avoiding Compressor Surge during Emergency Shut-Down Hybrid Turbine Systems," ASME J. Gas Turbines Power, 135(10), pp. 102602-102602-10.

[3] Tucker, D., Tsai, A., Jablonski, P., Hughes, D. O., Haynes, C. L., and Sellers, J., 2010, "Initial Transient Response during Fuel Cell Turbine Hybrid System Startup," Proceedings of the International Colloquium on Environmentally Preferred Advanced Power Generation (ICEPAG 2010), Costa Mesa, CA, Feb. 9-11, Paper No. ICEPAG2010-3414.

[4] Tucker, D., Liese, E., and Gemmen, R., 2009, "Determination of the Operating Envelope for a Direct Fired Fuel Cell Turbine Hybrid using Hardware Based Simulation," Proceedings of the International Colloquium on Environmentally Preferred Advanced Power Generation (ICEPAG 2009), Newport Beach, CA, Feb. 10–12, Paper No. ICEPAG2009-1021.

[5] Tucker, D., Abreu-Sepulveda, M., and Harun, N. F., 2014, "SOFC Lifetime Assessment in Gas Turbine Hybrid Power Systems," ASME J. Fuel Cell Sci. Technol., 11(5), pp. 051008-051008-7.

[6] Eguchi, K., Kojo, H., Takeguchi, T., Kikuchi, R., and Sasaki, K., 2002, "Fuel Flexibility in Power Generation by Solid Oxide Fuel Cells," J. Solid State Ionics, 152–153, pp. 411–416.

[7] Yi, Y., Rao, A. D., Brouwer, J., and Samuelsen, G. S., 2005, "Fuel Flexibility Study of an Integrated 25 kw SOFC Reformer System," J. Power Sources, 144(1), pp. 67–76.

[8] Adams, T. A. II, and Barton, P. I., 2011, "Combining Coal Gasification, Natural Gas Reforming, and Solid Oxide Fuel Cells for Efficient Polygeneration With CO_2 Capture and Sequestration," Fuel Process. Technol., 92(10), pp. 2105-2115.

[9] Chen, Y., Adams, T. A. II, and Barton, P. I., 2010, "Optimal Design and Operation of Static Energy Polygeneration Systems," Ind. Eng. Chem. Res., 50(9), pp. 5099-5113.

[10] Chen, Y., Adams, T. A. II, and Barton, P. I., 2011, "Optimal Design and Operation of Flexible Energy Polygeneration Systems," Ind. Eng. Chem. Res., 50(8), pp. 4553-4566.

[11] Winkler, W., Nehter, P., Williams, M. C., Tucker, D., and Gemmen, R., 2006, "General Fuel Cell Hybrid Synergies and Hybrid System Testing Status," J. Power Sources, 159(1), pp. 656-666.

[12] Zhou, N., Yang, C., and Tucker, D., "Evaluation of Cathode Air Flow Transients in a SOFC/GT Hybrid System using Hardware in the Loop Simulation," ASME Paper No. FUELCELL2014-6563.

[13] Haynes, C., and Wepfer, W. J., 2000, "Design for Power of a Commercial Grade Tubular Solid Oxide Fuel Cell," Energy Convers. Manage., 41(11), pp. 1123-1139.

[14] Trembly, J. P., Gemmen, R. S., and Bayless, D. J., 2007, "The Effect of Coal Syngas Containing AsH_3 on the Performance of SOFCs: Investigations into the Effect of Operational Temperature, Current Density, and AsH_3 Concentration," J. Power Sources, 171(2), pp. 818-825.

4 IMPACT OF FUEL COMPOSITION TRANSIENTS ON SOFC PERFORMANCE IN GAS TURBINE HYBRID SYSTEMS

"Reproduced from "Harun, N.F., Tucker, D., and Adams, T. A. II, 2015, "Impact of Fuel Composition Transients on SOFC Performance in Gas Turbine Hybrid Systems," *Submitted to Applied Energy*. In review.

4.1 Publication Highlights

As an extension from the investigation presented in Chapter 2, this section primarily focuses on dynamic characterization of fuel cell parameters. The fuel cell parameters discussed in this chapter are related to dynamic thermal performance including solid and gas temperature on the cathode side, axial heat generation within the cell, partial pressures of major components in the anode side, Nernst potential, polarization losses, and local current density. The detailed dynamic trajectories of each key fuel cell variables are evaluated thoroughly to quantify their contributions to operability and controllability of the hybrid system. The analyses are based on distributed profiles across the fuel cell length resulted from the closed loop operation.

The results presented in this chapter were obtained from the same experiment conducted in Chapter 2. Basically, all tests were conducted by me with some helps from a few colleagues from the U.S. Department of Energy, National Energy Technology Laboratory (NETL) - Dr. David Tucker, Dr. Paolo Pezzini, Dr. Nana Zhou, and Valentina Zaccaria. Again, Dr. David Tucker assisted with data analysis and interpretation, as well as editing and preparation/submission of the manuscript. Meanwhile, Dr. Thomas A. Adams II provided helps in the preparation/revision process to strengthen the content of the manuscript.

Impact of Fuel Composition Transients on SOFC Performance in Gas Turbine Hybrid Systems

Authors: Nor Farida Harun[a], David Tucker[b], and Thomas A. Adams II[a]
[a]Department of Chemical Engineering, McMaster University, 1280 Main Street West, Hamilton, Ontario L8S 4L7, Canada
[b]U.S. Department of Energy, National Energy Technology Laboratory, 3610 Collins Ferry Road, Morgantown, West Virginia 26507-0880, United States

4.2 Abstract

This paper presents a dynamic study of fuel cell gas turbine (SOFC/GT) hybrid systems, focusing on the response to a drastic transient in anode fuel composition for constant turbine speed operations. This work is motivated by the potential of fuel cells for fuel flexibility, which could extend the opportunities for sustainability and profitability in energy conversion systems. A combination of hardware and numerical models in a hybrid simulator is used to investigate the transient trajectories of fuel cell process variables as well as the consequent impacts of fuel cell thermal effluent on the integrated gas turbine engine. The conversion of thermal energy stored in the fuel cell stack to chemical energy during the reforming at the beginning of the cell resulted in a 17% increase in thermal effluent from the fuel cell to the turbine in the first few seconds of the transient. Fuel cell solid temperature gradients increased by 39% at 250 s from the initiation of the transient. The distributed dynamic performance of the fuel cell in terms of the fuel composition gradient, thermal and electrochemical performance across the fuel cell length was carefully characterized, considering their interactions and their impacts on the total system performance.

Keywords: Fuel cell gas turbine hybrid; fuel composition transients; fuel flexibility; hardware-based simulations

4.3 Introduction

Hybridization of high temperature fuel cells, such as solid oxide fuel cells (SOFCs), with gas turbines has been widely recognized as a compelling advanced power system for high efficiency energy production with low emissions. [1-4]. In particular, the SOFC gas turbine hybrid system offers an improvement of system efficiency by recovering high temperature waste heat from the fuel cell for additional power production from the gas turbine. Research and development efforts initiated by the U.S Department of Energy using a pilot-scale system revealed that the operating envelope of fuel cell gas turbine (SOFC/GT) hybrid systems has an opportunity to achieve 85% turndown [5].

The ability of high temperature fuel cells to directly use various types of fuels also greatly extends the interest in applications of fuel cell gas turbine (SOFC/GT) hybrid systems. Theoretically, it is feasible to run the SOFC/GT system using non-hydrogen fuels such as methane or biogas and even liquid fuels at selected operating conditions [6-9].

Furthermore, there are several potential applications where it might be very beneficial to have a power system that can handle drastic changes in the type of fuel used. First, if the market prices of fuels experiences sudden shifts, or, perhaps new regulations place environmental restrictions on the fuel type, it may be beneficial to switch the fuel used to take advantage of the new economic situation. For example, suppose a power plant uses primarily gasified coal, but the price of natural gas suddenly drops, or, a new carbon tax takes effect; it could be more profitable to switch the main fuel from coal to natural gas.

Second, recent studies have shown that flexible polygeneration systems which co-produce electricity with fuels or chemicals can take advantage of monthly or even daily shifts in energy prices (such as electricity) by changing the mixture of products that it produces in response to these changing market conditions. [1, 10, 11].For example, one may want to produce more electricity and less fuels during the day when power prices are high, and then switch to producing more fuels and less electricity at night when power prices are low. To maximize efficiency, flexible polygeneration are designed to tightly integrate the chemicals/fuel production and electricity production sections such that when these transitions occur, the feed rates, heating value, and composition to the power generation system changes significantly [11, 12].

In either case, SOFC/GT systems are potentially a very suitable technology to use as the power generation mechanism since they are highly efficient and fuel-flexible. Although SOFC/GT hybrids can be used in both the power plant and polygeneration plant contexts, this study focuses on the former kind of transition (coal to natural gas) because it is the more extreme of the two.

However, SOFC/GT hybrid systems are not yet commercially ready due to practical problems associated with dynamic operations [3, 6, 13, 14]. The highly interactive effects between fuel cell systems and turbine cycles during transient events always lead to complicated process dynamics that require problematic control development [15, 16]. For instance, although methane fueled systems can provide means to cool the fuel cell stack due to the endothermic reforming reaction [7, 8], a dramatic temperature gradient across the fuel cell must be avoided to limit the thermal stress in the material [17]. Also, any variations in the fuel cell thermal effluent (which is the thermal energy of the SOFC exhaust streams) caused by transients in fuel composition can upset the stability of the turbine cycle, which in turn affects the fuel cell stacks [18, 19]. Fuel starvation could be another potential failure in the system arising from the effects of transient behaviour [14, 20]. The result is that transient effects can cause complicated impacts to the fuel cell system and materials.

Despite many promising simulation studies that explore the operability of SOFCs using different type of fuels, there has been no prior published experimental data or detailed analyses of SOFC/GT system performance during fuel composition transients. To the best of our knowledge, almost all existing studies focus on steady state operation [6-8, 21-23]. However, if effective controls are to be developed to take advantage of the extensive operating envelope offered by SOFC/GT hybrids [5, 24], a dynamic characterization of fuel cell parameters is essential. Our understanding of the risks and challenges of fuel flexible SOFC/GT hybrid systems must be expanded.

Therefore, in this work, the dynamics of fuel composition changes in the recuperated direct-fired SOFC/GT hybrid system were experimentally investigated using a hybrid test facility with real recuperated turbomachinery equipment. While our prior work outlined the coupling effects on turbine portion of the system [25], this work characterizes the

detailed fuel cell dynamic trajectories in response to fuel transitions (specifically from coal-derived syngas to humidified methane). Distributed profiles of key fuel cell variables were evaluated thoroughly to quantify their contributions to operability and controllability of the hybrid system.

4.4 Methodology

4.4.1 Hardware System

A public testing facility of SOFC/GT at the U.S Department of Energy, National Energy Technology Laboratory (NETL), Morgantown, West Virginia, was used to carry out the test on fuel composition changes. As shown in a simplified flow diagram in Figure 4.1, this system combines a real-time fuel cell dynamic model (shown in the dashed-line box) and the balance of the plant for a potential recuperated SOFC/GT hybrid system [26, 27]. The balance of the hybrid system is designed using real equipment and piping systems. With such configuration, this facility serves as a valuable research tool in steady state or dynamic studies to explore the key operational challenges and opportunities of the SOFC/GT hybrid system in terms of dynamic control development for future system commercialization [3, 24, 28-32].

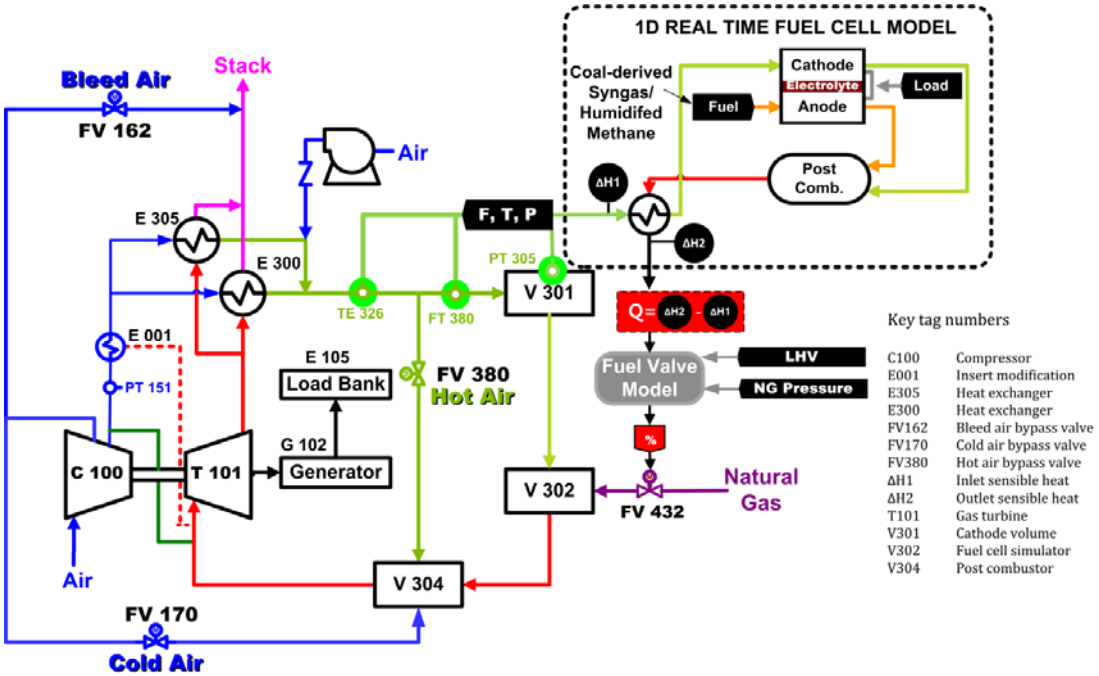

Figure 4.1: The physical system of SOFC/GT hybrid test facility at NETL [25].

A 120 kW auxiliary power unit (APU) consisting of a single shaft turbine (T-101) attached to a two-stage compressor (C-100), a 400 Hz gear-driven generator (G-102), and two primary surface heat exchangers (E-300 and E-305) are among the major parts of the hardware system. Air plenums are also used to emulate cathode volume (V-301) and post combustor volume (V-304) for a real direct-fired SOFC/GT system. In a constant turbine-speed operation, an adjustable 120 kW load bank system (E-105) is also connected to the system as an independent system variable to maintain the turbine speed.

In this work, the effect of the fuel cell waste heat is embedded in a fuel cell model output variable, which is the fuel cell model net thermal effluent, Q. The definition of Q can be simplified by the following equation, Eq. 1 [25]:

$$Q = \dot{m}_2 \Delta H_2 - \dot{m}_1 \Delta H_1 \qquad (1)$$

Where ΔH_1 and ΔH_2 are the sensible heats of the cathode feed stream before preheating and the postcombustion exhaust after cooling with a reference to standard conditions, as shown in Figure 4.1. Meanwhile, $\dot{m}_1$and $\dot{m}_2$ are the mass flow rate of the respective streams.

During a fully coupled SOFC/GT test, a complete interaction cycle between the fuel cell model and the hardware system is achieved in real-time (as fast as 80 ms) by feeding the sensor measurement of a real cathode feed stream in the hardware system to the software part as model inputs. To close the system loop, a model output (the fuel cell net thermal effluent) relevant to the study is fed to the hardware system in feedforward fashion. The Q value is used to manipulate the natural gas flow through a real fuel valve (% FV432) simulating the energy input for turbomachinery. In summary, the fuel cell thermal effluent (i.e. Q value) calculated by the fuel cell model is the control input of the fuel valve, which represents the equivalent amount of heat available going into turbine in the hybrid system.

4.4.2 Model Description

To achieve the objective of the case study presented herein, a previously developed one-dimensional (1D) real-time distributed fuel cell model has been modified to enable fuel composition changes in the simulated SOFC fuel feed [26]. The implementation of fuel composition transitions in the emulator of solid oxide hybrid systems is graphically shown in Figure 4.2. The fuel cell model is based on an anode-supported fuel cell system with the standard material and co-flow configuration [26].

Given the initial operating condition as described in Table 4.1, at a desired set of fuel cell configuration parameters (Table 4.2) [25], the model simulates the distributed fuel cell profiles as function of time and local position for 20 nodes along the length of the cell in real-time based on the sensor measurements of recuperated compressed air being delivered to the cathode inlet (mass flow rate-FT380, temperature-TE326, and pressure-PT305). Sensitivity studies have shown that using 20 nodes provides the optimum balance in measurement speed and accuracy in capturing the fuel cell dynamics, particularly for millisecond time scales [33, 34]. It was shown that increasing the number of nodes above 20 does not improve the solution accuracy but increases the the computational time exponentially [34].

The model evaluates most of the key fuel cell process variables, in terms of thermal performance including solid and gas temperature on the cathode side, axial heat generation within the cell, partial pressures of major components in the anode side, Nernst potential, polarization losses, and local current density [26, 33]. The detailed fuel cell parameters and initial operating conditions used in this study are shown in Table 4.1.

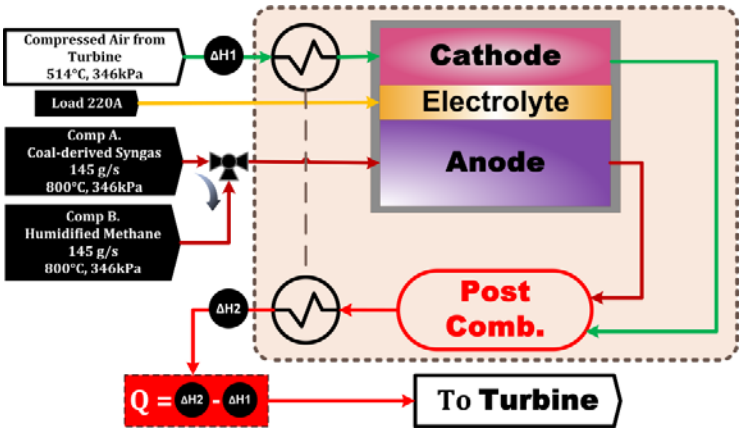

Figure 4.2: 1D-Real time fuel cell dynamic model.

Table 4.1: Inlet conditions for fuel cell cathode and anode streams. Based on Harun et.al [25]

Measured cathode inlet condition at initial steady state	
Air mass flow rate	1.04 kg/s
Air temperature	705 °C
Air pressure	346 kPa
Simulated anode inlet condition	
Fuel mass flow rate	145 g/s
Fuel temperature	800 °C
Fuel pressure	346 kPa

Table 4.2: Specification of SOFC system parameters. Based on Harun et.al [25].

Fuel cell load	220 A
Anode recycle	0%
Initial fuel cell temperature	800 °C
Total cell area	200 mm x 200 mm
Anode thickness	0.5 mm
Electrolyte thickness	0.008 mm
Cathode thickness	0.05 mm
Oxidant/fuel channel size	2 mm x 2 mm
Stack size	2500 cells

Total stack mass	3500 kg
Total stack heat capacity	2625 kJ/K

4.4.3 Hardware-based Simulation of SOFC Fuel Composition Transient

The recuperated turbine cycle was first brought up to a nominal turbine speed at 40,500 rpm without the fuel cell model in the loop. Before integrating the fuel cell model into the test facility, the startup step was continued by heating the hardware system for about two hours to a thermally steady state condition, approaching 0.1 K/min in the skin temperature gradient post combustor (V-304). During this period, a 40 kW turbine load and different bleed air bypass valve openings were used to accelerate the heating up process.

For this initial system steady state, the model input parameters for the fuel feed to the SOFC were specified to be CH_4 0%, CO_2 12%, CO 28.6%, H_2 29.1%, H_2O 27.1%, N_2 3.2% (mole fraction). This coal-derived syngas was selected based on previous studies and because the SOFC/GT hybrid system properties are well known under these conditions [35, 36]. It was assumed that air composition in the cathode stream was O_2 21% and N_2 79%. Since it has been shown that the overall SOFC/GT system efficiency of direct fired configurations was insensitive to fuel utilization in the fuel cell [37], a lower value of overall fuel utilization (67%) was chosen. However, the overall fuel utilization was not kept constant. Instead, the test was run at a constant fuel mass flow rate (145 g/s) and a constant fuel cell load (220 A). Thus, the impacts of fuel composition variations could be decoupled from the interaction of the changes in the mass flow and fuel cell load.

The integration of the real-time fuel cell model into the hybrid test facility was initiated once steady state conditions in both the recuperated hardware and the virtual SOFC system were achieved. The fuel feed was then switched from the initial steady state with the syngas composition to a methane rich fuel composition (CH_4 14% and H_2O 86%) at the same fuel mass flow rate (145 g/s). This step change represented a 17% reduction in the overall heat input (i.e. lower heating value of fuel) of the SOFC system (Figure 4.2). No change was made in any other operating parameters during the fuel composition transition. This means that the operation using humidified methane was continued with the resulting steady state condition for syngas.

In a prior work, this composition was determined as a tolerable transition to ensure safe heat change in turbomachinery system in the hybrid configuration, and with this humidified methane mixture, no chance for the occurrence of carbon deposition [25]. Fuel diffusion effects were not taken into account. The step change from coal-derived syngas to this methane-rich fuel represents the “worst case possible” because in a previous study, it was found that switching from coal-syngas to humidified methane with more than 14% methane could not be tolerated due to the transient limitations in the turbine cycle [25]. For transitions to fuels with larger than 14% methane, the fuel cell dynamics caused a rapid and extreme transient increase in the turbine speed which could destroy the turbine.

In this paper, the step time was indicated as time zero in the result plots. The transient profiles were observed for approximately 7,000 s after the step time. Based on operator experience, no significant transient response beyond 7,000 s of the experimental test was expected.

4.5 Results and Discussions

4.5.1 Distributed Analysis for the Initial Steady State with Coal-Derived Syngas Feed

Due to the absence of methane (CH_4) content in the coal-derived syngas used in this study, as shown in Figure 4.3a, the composition gradient of each gas component was primarily driven by the water-gas shift (WGS) kinetics (Eq. 2) and the electrochemical hydrogen (H_2) oxidation (Eq. 3). The direct electrochemical oxidation of CO and CH_4 was assumed to be negligible, since (1) there is excess water in the system; (2) the kinetics of CO and CH_4 oxidation are significantly slower than H_2 oxidation; (3) less surface area is available for electrochemical oxidation at the three-phase-boundary as compared to the area available for catalytic reforming and WGS along the anode channel; and (4) CO and CH_4 has slower mass transfer to the triple-phase boundary [38].

As clearly illustrated in Figure 4.3b, the most rapid reduction in CO appeared to be at the first two nodes or 10% of the cell length, diminishing by 20%. The sharp initial decline in CO partial pressure was due primarily to the shifting of CO to obtain the equilibrium condition. This was followed by the slow almost linear decline in CO towards the exit of the fuel cell as hydrogen was consumed, driving the shift reaction to consume the CO to the final mole fraction of 0.09.

Water-gas shifting:

$$CO + H_2O \rightleftharpoons H_2 + CO_2 \quad (\Delta H^\circ = -41\ kJ/mol) \tag{2}$$

Hydrogen oxidation:

$$H_2 + \frac{1}{2}O_2 \rightarrow H_2O \ \ (\Delta H^\circ = -286\ kJ/mol) \tag{3}$$

Figure 4.3 also shows the resulting changes in carbon dioxide (CO_2), increasing from 0.120 at node 1 to approximately 0.310 at node 20. Intuitively, the mole fraction gradient of CO_2 was completely controlled by the CO mole fraction as well as the WGS kinetics. Thus, it reflected closely the CO conversion along the fuel channel.

As the results of both WGS and H_2 oxidation in the fuel cell, higher H_2 mole fraction at the entrance of the cell and lower H_2 mole fraction at the end of the cell were observed. As shown in Figure 4.3b, an initial increase in H_2 mole fraction was evident between the first two nodes, from 0.291 to 0.334, before decreasing through the remaining cell length. This suggested that there were strong impacts of WGS kinetics at the beginning of the cell, whereas the electrochemical activities had greater influence on the downstream path.

The change in H_2 mole fraction was reflected by the change in water (H_2O) mole fraction. As opposed to the maximum level of H_2, the minimum H_2O mole fraction (0.228) was observed at the same location shortly after the cell entrance (Figure 4.3a). This was due to H_2O consumption in WGS to yield H_2 in the system, which also stimulated the remarkable decrease in CO. Starting from node 2, H_2O mole fraction steadily increased to the highest level of 0.461 at the cell outlet as the hydrogen oxidation outweighed the effects of other reactions.

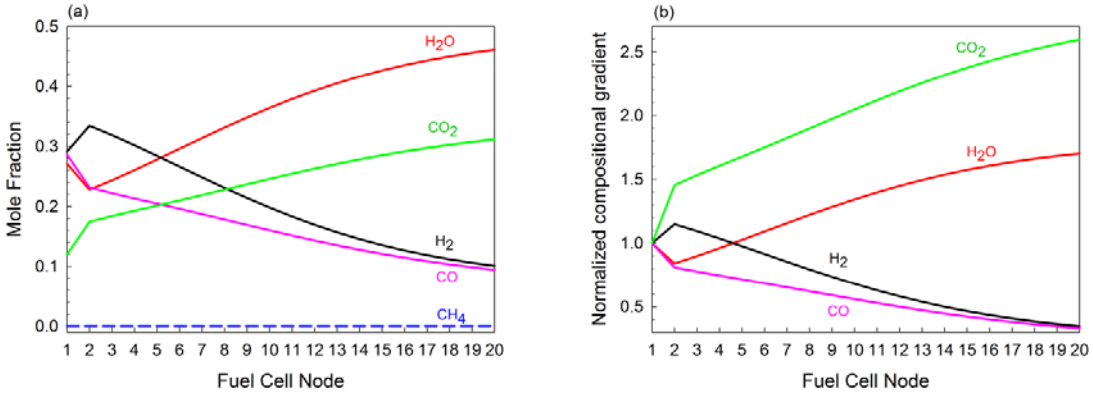

Figure 4.3: Distributed profiles of composition gradient in the anode at the initial steady state using syngas feed, (a) real values on mole-basis, and (b) normalized values

The Nernst potential was quantified using an expression shown in Eq. 4. This function reveals that the Nernst potential is correlated to fuel cell temperature, as well as the partial pressure of H_2 and H_2O in the anode and O_2 in the cathode. There is no significant change in O_2 mole fraction in since the air mass flow rate in the cathode coming from the recuperated hybrid system is very high, so the effect of O_2 on the Nernst potential transient is negligible. The O_2 utilization was maintained very low, approximately at 19%, with the maximum variation less than 3% over the entire course of experiment. In Eq. 4, the net value of the first term, which consists of the Gibbs free energy of water at the standard condition, is a positive value. Meanwhile, as the consequence of operating in excess water condition, the net value of the second term, as a function of temperature and component partial pressure is a negative value. In this case, there is a reversed effect of fuel cell temperature on the Nernst potential.

Nernst potential:

$$V_{Nernst} = -\frac{\Delta G^{\circ}_{H_2O}}{2F} + \frac{R_u T}{2F} ln\left[\frac{p_{H_2} . p_{O_2}^{0.5}}{p_{H_2O}}\right] \qquad (4)$$

The corresponding effects on Nernst potential, current density, and polarization losses for a steady state with syngas feed are presented in Figure 4.4. The normalized profiles are plotted in Figure 4.4b to show the magnitude of change in each variable. Regardless of increased polarization losses at the entrance of the fuel cell, a 1% increase in Nernst potential from the initial condition was identified in the H_2 concentrated region (Figure 4.4b), as expected. Likewise, as shown in Figure 4.4a, current density also increased significantly within the first two nodes. However, the highest current density (0.720) was found at around node 6.

The significant reduction in H_2 partial pressure in the downstream region decreased Nernst potential by 13% to its lowest value at the cell outlet (Figure 4.4b). This response was also influenced by the increasing fuel cell temperature. On the other hand, the electrochemical losses reduced substantially with the increasing temperature. The greater discrepancy in the transients between the Nernst potential and the electrochemical losses

(increased voltage) eventually caused the significant decrease in current density (60% from the inlet) at the cell outlet.

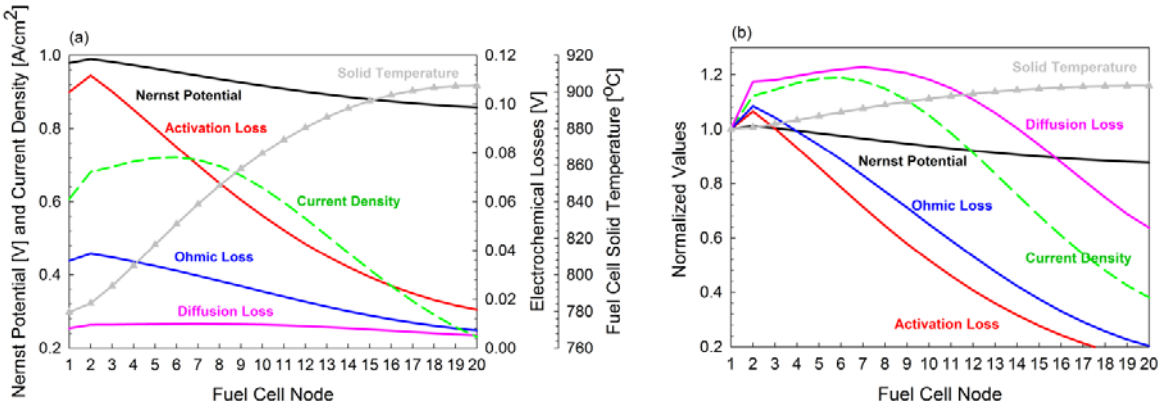

Figure 4.4: Nernst potential, current density, and electrochemical losses at the initial steady state using syngas feed, (a) real values, and (b) normalized values

4.5.2 Transient Analysis of Fuel Composition Change Impacts

4.5.2.1 Compositional Gradient and Localized Fuel Utilization

CH_4 Mole fraction

The transient CH_4 mole fraction profile after the step change in fuel composition is presented in Figure 4.5. Figure 4.5 shows that rapid conversion of CH_4 occurred in the first six nodes. With respect to the selected initial conditions and the fuel cell configuration, the residence time of the fuel cell subsystem was on the order of hundreds of milliseconds, which is slower than the resolution of 80 ms captured by the dynamic model used in this study. Zero to very low CH_4 mole fraction was observed at approximately halfway down the fuel cell length immediately after the transient, approaching a complete CH_4 conversion.

The analysis suggests that the behaviours in the fuel cell upstream would be strongly affected by the steam methane reforming (SMR) kinetics (Eq. 5) due to the observed significant variations. This reaction was initially stimulated by the elevated fuel cell thermal condition. Owing to the aggressive CH_4 conversion in this region, the fuel cell solid temperature was expected to decrease in the long run, which would cause undesirable changes in the spatial temperature gradient and deceleration of the SMR kinetics.

The effects of reduced fuel cell solid temperature were clearly demonstrated by slower CH_4 consumption at the end of the test. At the final state (at time 7,000 s), as presented in Figure 4.5b, the system exhibited a fairly distributed CH_4 profile along the cell. CH_4 was skewed from the highest level (0.140) at node 1 towards the lowest level (0.050) at the outlet. The CH_4 conversion was still incomplete until the fuel cell outlet.

Overall, the result suggests that future control strategies of SOFC/GT hybrid system will need to include thermal management of fuel cell temperature. The regulation of turbine

speed to modulate cathode air flow may be an important tool for controlling fuel cell temperature.

Steam methane reforming:

$$CH_4 + H_2O \rightleftharpoons 3H_2 + CO \quad (\Delta H^\circ = 206\ kJ/mol) \qquad (5)$$

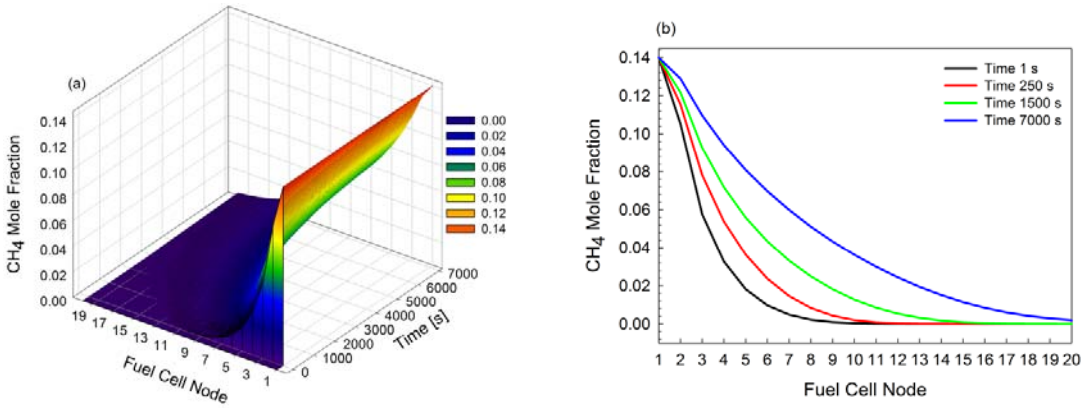

Figure 4.5: Variations in methane partial pressure, (a) a 3D mesh plot, as function of local position along the cell node and time, and (b) distributed profiles at time 1 s, 250 s, 1,500 s, and 7,000 s after the step change

CO Mole fraction

The profile of the CO composition gradient is shown in Figure 4.6, indicating a region of high CO concentration around the centre of the cell in the initial transient period. As shown in Figure 4.6, CO steeply increased to the highest point at node 7, approximately at 0.040, at 80 ms after the fuel step change, and reduced at the end of the cell.

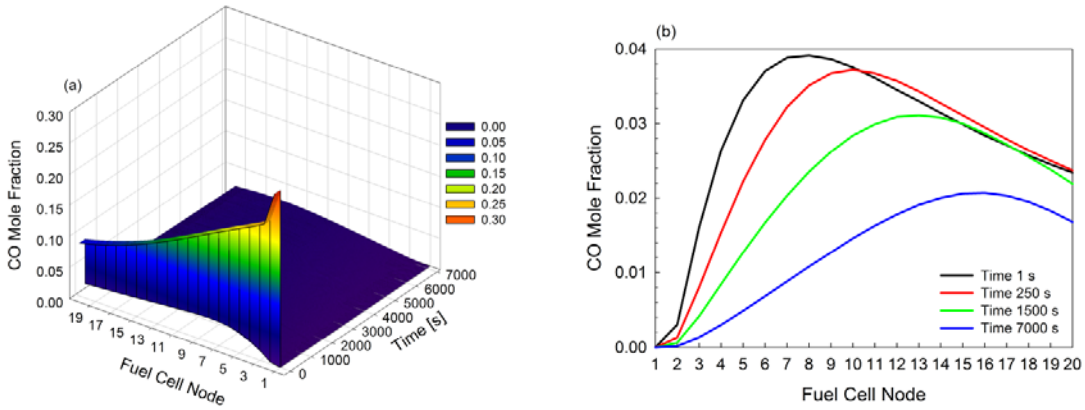

Figure 4.6: Transient response of carbon monoxide composition, (a) a 3D mesh plot, as function of local position along the cell node and time, and (b) Distributed profiles at time 1 s, 250 s, 1,500 s, and 7,000 s after the step change

Changes in CO mole fraction gradient along the fuel cell length were highly reflected by the presence of CH_4 in the system, as expressed in Eq. 5. The dramatic accumulation of CO in the fuel cell upstream (Figure 4.6b) was correspondingly promoted by the rapid consumption of CH_4 (Figure 4.5b). The highest CO mole fraction was achieved when almost all CH_4 was converted to SMR products. The complete CH_4 consumption subsequently initiated the depletion in CO in the downstream region, which was due to WGS reactions (Eq. 2).

However, the maximum CO reduced by about half and shifted to node 16 within 7,000 s. As shown in Figure 4.6b, there was appreciable reduction in CO level between node 8 to the exit after 1,500 s. The shift of the maximum CO from node 7, 35% from the inlet, downstream to node 16 at 7,000 s was strongly motivated by the reduction of cell temperature. As the test progressed, decreasing fuel cell solid temperature decreased SMR kinetics. This ultimately reduced the formation of CO, and thus, moved the region of high CO concentration to the end of the fuel cell.

CO_2 Mole fraction

The relevant profile of CO_2 composition is provided in Figure 4.7. Figure 4.7 shows that CO_2 increased from zero at the inlet to about 0.090 at the outlet over the entire test period, without significant fluctuation in the last six nodes. This dramatic increase in CO_2 at the beginning of the cell was following by a gradual increase to the fuel cell exit.

Although the trend of CO_2 profile after the fuel transition was similar to that observed at the initial steady state (Figure 4.7a), the percentage of CO_2 mole fraction accumulation in methane-rich operation was far less. This difference was due to the initial CO content in the fuel cell.

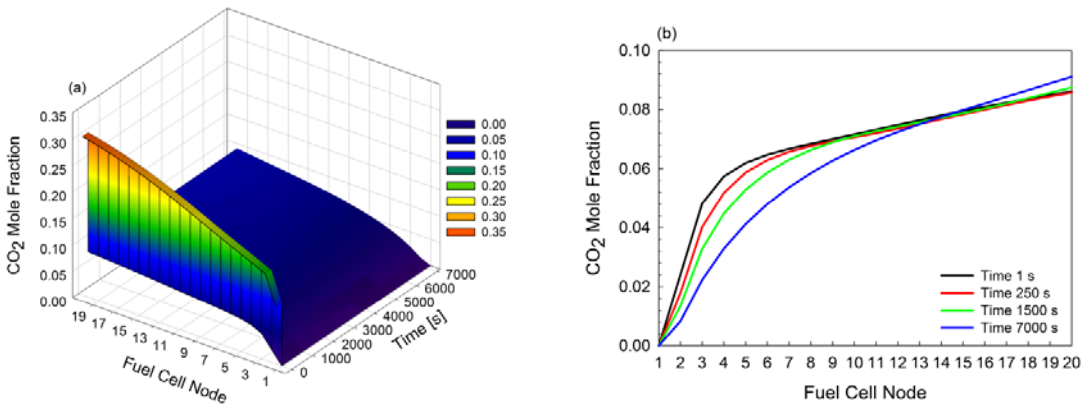

Figure 4.7: Transient response of carbon dioxide composition, (a) a 3D mesh plot, as function of local position along the cell node and time, and (b) distributed profiles at time 1 s, 250 s, 1,500 s, and 7,000 s after the step change

Theoretically, the formation of CO_2 was accelerated by the WGS kinetics (Eq. 2). Nevertheless, in this case, this reaction was also indirectly dependent on the formation of CO from SMR reactions. As observed in the fuel cell downstream, SMR kinetics decelerated. The

absence or very low CH_4 in this region caused the decrease in CO and the following decrease in the rate of CO_2 production. At the final steady state, a more distributed profile of CO_2 mole fraction was achieved (Figure 4.7b), reflecting to the profiles of CH_4 and CO, as shown respectively in Figures 4.5 and 4.6.

H_2 Mole fraction

The change in the H_2 content over the entire course of the experiment is shown in Figure 4.8. Figure 4.8 illustrates that H_2 increased drastically from its lowest point at the cell entrance to the maximum mole fraction of 0.310 at node 6 after the transient. Then, H_2 started to decline to about half (0.146) at the cell outlet, relatively from the highest peak.

The coupled effects from WGS, H_2 oxidation as well SMR, as shown in Eq. 2, Eq. 3, and Eq. 5, have determining influence on the H_2 mole fraction profile. The initial transient increased in H_2 mole fraction in the first half of the cell length followed closely the dramatic reformation of methane. As the result of the high production of H_2 as well as the decreasing SMR kinetics and WGS reaction, the impact of H_2 oxidation became more noticeable in the second half region. Within this region, H_2 was consumed faster than its formation. As such, significant reduction in H_2 mole fraction level was observed. Theoretically, increasing H_2 consumption should have shifted the equilibrium of WGS process further to product side, and so moderating the H_2 reduction. However, this effect was insignificant due to diminishing CH_4 content that restricted CO generation from methane reforming.

Due to the corresponding effects of SMR on the fuel cell solid temperature over 7,000 s time studied, the local maximum of H_2 mole fraction gradually shifted to the end of the cell to a lower level (0.220), featuring a more even distribution curve. It is also interesting to note that the H_2 concentration at the exit was effectively the same during the entire transition, despite the shifting internal profiles. This illustrates the usefulness of a model which can predict shifting internal profiles that could not otherwise be detected by experiment since spatial measurements are very difficult to obtain inside the SOFC.

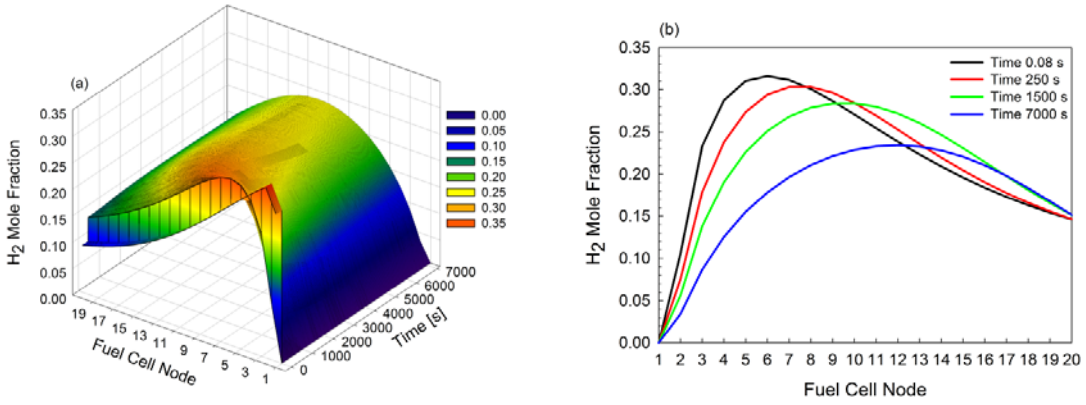

Figure 4.8: Hydrogen mole fraction gradient, (a) a 3D mesh plot, as function of local position along the cell node and time, and (b) distributed profiles at time 1 s, 250 s, 1,500 s, and 7,000 s after the step change

H_2O Mole fraction

The corresponding change in H_2O mole fraction is illustrated in Figure 4.9. With higher H_2O at both ends of the cell, the lowest H_2O composition was observed within node 6 to node 12 over 7,000 s (Fig 9b). The smallest H_2O mole fraction gradually increased and shifted downstream over the long test run. As shown in Figure 4.9, the resulting variations in H_2O mole fraction were inversely correlated to H_2 dynamic response (Figure 4.8).

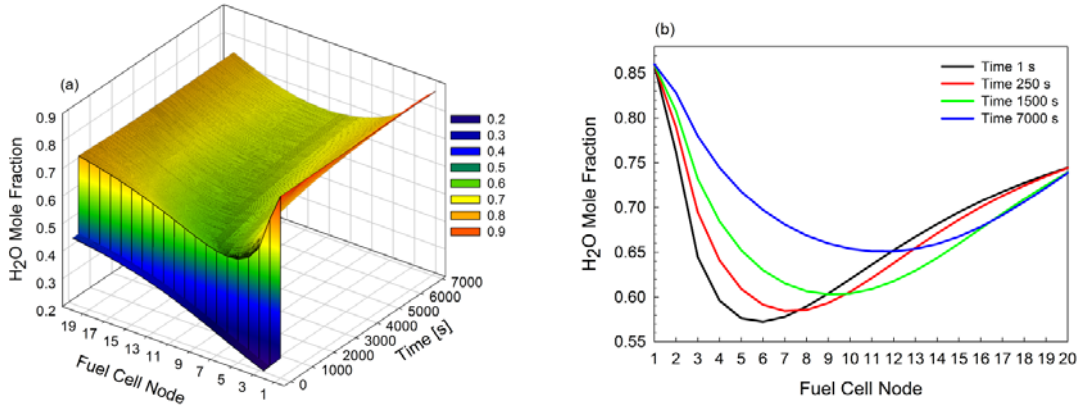

Figure 4.9: Water mole fraction gradient, (a) a 3D mesh plot, as function of local position along the cell node and time, and (b) distributed profiles at time 1 s, 250 s, 1,500 s, and 7,000 s after the step change

As presented in Figure 4.9b, substantial reduction in H_2O partial pressure was more apparent at the beginning of the cell, between node1 to node 6, following the rapid methane reformation and WGS reactions. Similarly, the shifting in the local minimum points of H_2O was attributed to the effect of slower methane conversion indicated in Figure 4.5. Significant formation of H_2O due to electrochemical reactions was identified at node 6 onwards when H_2O mole fraction started to increase up to its final level at the fuel cell outlet. Over 7,000 s, the final H_2O mole fraction at the fuel cell exit was about 0.740, slightly lower than the inlet mole fraction (0.860).

Fuel Utilization

The changes in fuel utilization in response to fuel composition transition are shown in Figure 4.10. As can be seen in Figure 4.10a, fuel utilization at the initial steady state was almost uniformly distributed across the cell but with a lower level at both cell inlet and outlet. After switching the anode feed to humidified methane, fuel utilization was distributed in a non-linear fashion. The highest peaks were found at node 2 at 80 ms, and at node 19 after 7,000 s (Figure 4.10b). The highest fuel utilization at the beginning of the cell at the initial transition phase was likely due to rapid SMR reaction that led to significant variations in localized H_2 availability. Intuitively, this was promoted by the elevated initial fuel cell solid temperature.

At the beginning of the cell, fuel utilization reduced gradually over the course of the experiments, but these dynamics were reversed at the end of the cell. The analysis indicates that the variations at the beginning of the cell were significantly driven by the reduction of fuel cell temperature, which was also reflected by the reduction in CH_4 consumption over time studied. Meanwhile, as methane was almost completely consumed at the downstream region, the trends of fuel utilization were strongly related to the activities of electrochemical reactions.

At the end of the cell, fuel utilization increased over time with increasing current density and less available fuel. This is clearly illustrated because the hydrogen concentration in the last half of the cell was not significantly changing, as seen in Figure 4.8, while current density was increasing at the end of the cell, as will be shown in Figure 4.11.

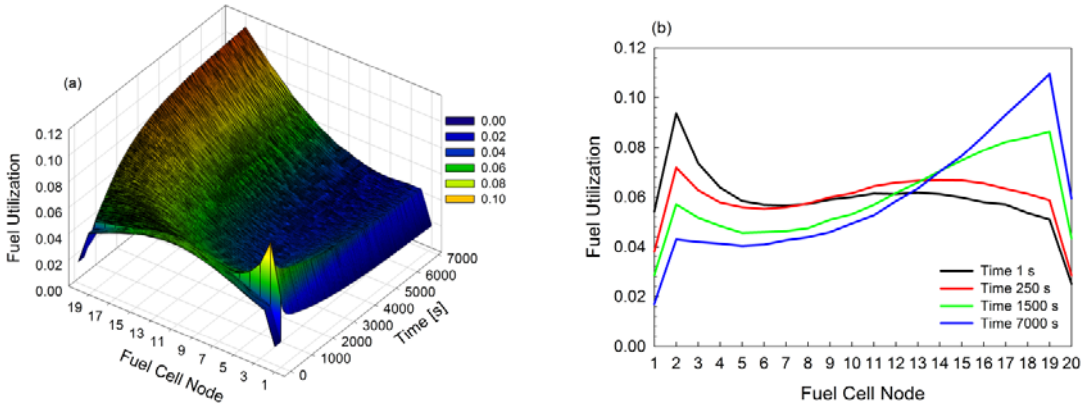

Figure 4.10: Localized fuel utilization, (a) a 3D mesh plot, as function of local position along the cell node and time, and (b) distributed profiles at time 1 s, 250 s, 1,500 s, and 7,000 s after the step change

4.5.2.2 Current Density, Nernst Potential, and Electrochemical Losses

Current Density

The local current density profiles are illustrated in Figure 4.11. As the result of switching the fuel to humidified methane at a constant fuel cell load, higher current density was observed at the end of the cell, as opposed to the profile at the initial steady state of syngas operation (Figure 4.11a).

As shown in Figure 4.11b, at 80 ms after the transient, current density increased to the highest value (0.73) at around node 8, 40% of the cell length, before slowly decreasing through the remaining fuel cell length. However, decreasing solid temperature over 7,000 s test subsequently shifted the maximum current density towards the end of the cell, resulting in the highest peak (0.83) at node 18. The distributed profile at the end of the test was mirrored the performance at the initial steady state.

The dynamics of current density were greatly coupled with the effects of H_2 partial pressure and Nernst potential. As expected, higher current density region was achieved in

the elevated solid temperature segments (Figure 4.16) at a relatively higher partial pressure of H_2 (Figure 4.5), as well as higher Nernst potential (Figure 4.12). Increasing current density at the end of the cell also promoted the fuel cell heat generation, as indicated in Figure 4.21.

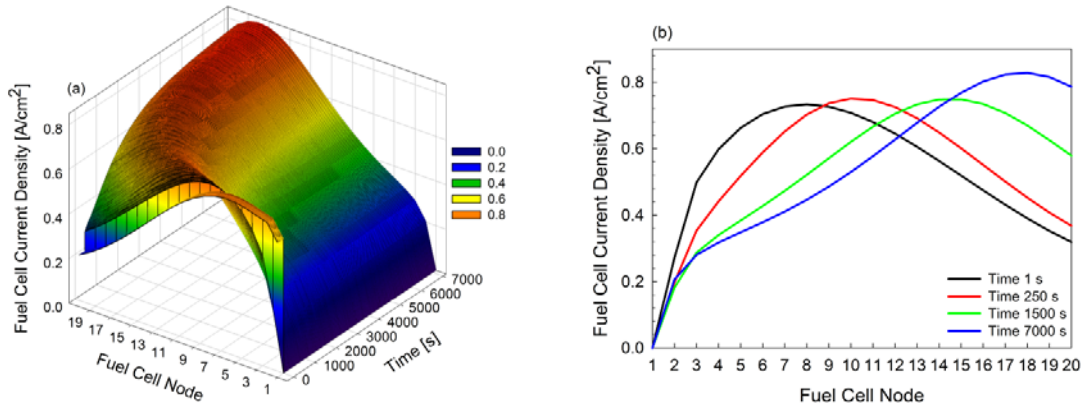

Figure 4.11: Local current density, (a) a 3D mesh plot, as function of local position along the cell node and time, and (b) distributed profiles at time 1 s, 250 s, 1,500 s, and 7,000 s after the step change

Nernst Potential

The resulting variation in Nernst potential is plotted in Figure 4.12. Over 7,000 s, a rapid increase in Nernst potential with insignificant variations with time was observed at the beginning of the cell, as illustrated in Figure 4.12b. This was due to dramatic increase in the H_2 mole fraction to 31% (Figure 4.8), which was also correlated to evenly distributed profiles in the local solid temperature gradient over time (Figure 4.16), and a 30% reduction in H_2O (Figure 4.9).

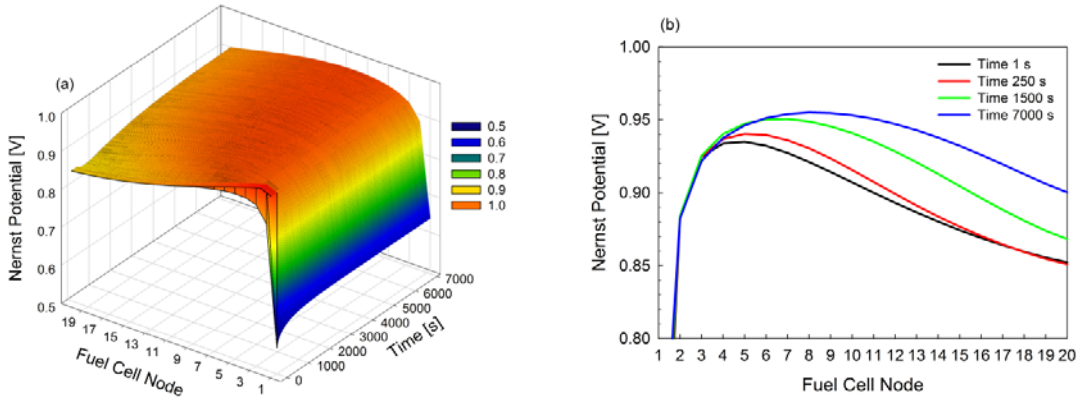

Figure 4.12: Nernst potential distribution, (a) a 3D mesh plot, as function of local position along the cell node and time, and (b) distributed profiles at time 1 s, 250 s, 1,500 s, and 7,000 s after the step change

Meanwhile, the Nernst potential dynamics in the second half of the cell was most likely influenced by the fuel cell temperature changes rather than the partial pressures of H_2 and H_2O. As presented in Figures 4.8 and 4.9, the H_2 and H_2O contents did not change significantly. Although the H_2 mole fraction reduced over the time studied, the Nernst potential of the cell increased with decreasing fuel cell temperature. Over 7,000 s, the peaks of the Nernst potential were scattered between node 5 and node 8 (20% to 40% of the cell length) from approximately 0.93 V to 0.96 V.

Electrochemical Losses

The variations in activation loss in response to the fuel composition change are shown in Figure 4.13. The activation loss represents the polarization resistance due to the required activation energy to initiate electrochemical reactions [21]. In this test, as presented in Figure 4.13b, the cell initially exhibited a very low activation resistance at node 1 in the absence of H_2 molecules. But, it steeply increased with time to a higher resistance at around node 4 to node 8 (20% to 40% from the fuel cell inlet), followed by a steady decrease to the outlet shortly after the maximum point.

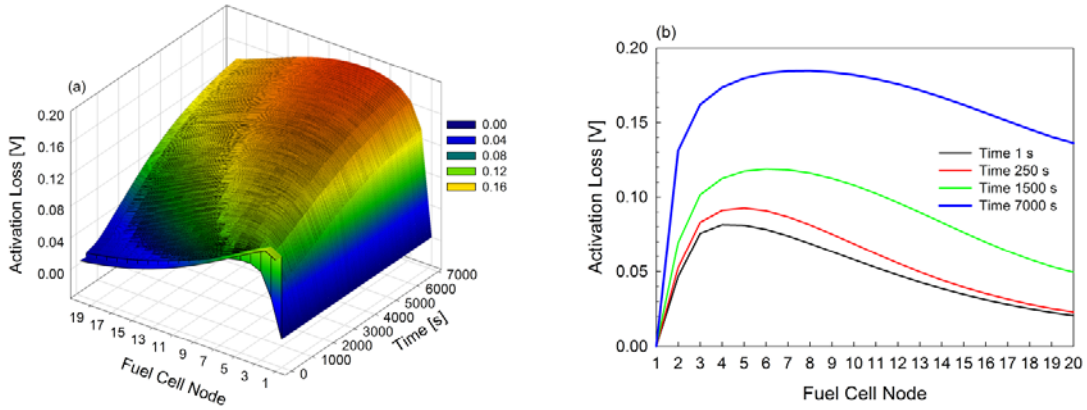

Figure 4.13: Activation loss distribution, (a) a 3D mesh plot, as function of local position along the cell node and time, and (b) distributed profiles at time 1 s, 250 s, 1,500 s, and 7,000 s after the step change

The analysis indicates that higher activation loss was obtained at higher H_2 partial pressure (Figure 4.8), current density (Figure 4.11), and Nernst potential (Figure 4.12). As expected, the significant reduction in fuel cell temperature over 7,000 s test substantially increased activation loss. However, it was expected that the influence of partial pressure changes was greater than the impacts of temperature in determining the activation loss at the beginning of the cell.

As shown in Figure 4.14 due to similar correlation to fuel cell temperature, changes in ohmic loss closely followed the trend observed in activation loss distribution. Figure 4.14b shows that over the entire course of the transient, ohmic loss increased with the decreasing fuel temperature. Overall, the distributed ohmic resistance varied between 0.01

V to 0.057 V with respect to the variations in the fuel cell temperature, approximately between 660 °C to 900 °C.

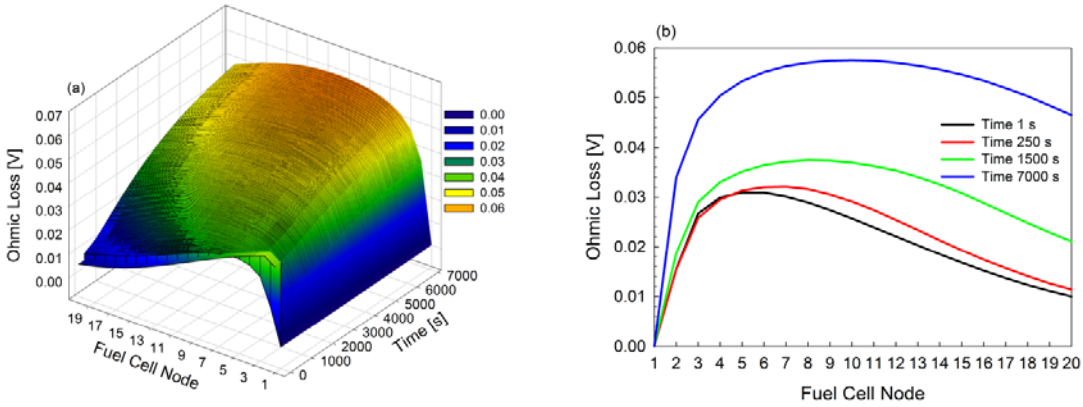

Figure 4.14: Ohmic loss profile, (a) a 3D mesh plot, as function of local position along the cell node and time, and (b) distributed profiles at time 1 s, 250 s, 1,500 s, and 7,000 s after the step change

The transient response of diffusion loss is shown in Figure 4.15. Theoretically, this loss results from the resistance associated with the transportation of chemical compounds to the reaction sites [21]. Intuitively, diffusion loss is strongly correlated to the mole fraction gradients across the cell. However, variations in the local current density and the fuel cell temperature also contribute some impacts on the changes in this polarization resistance.

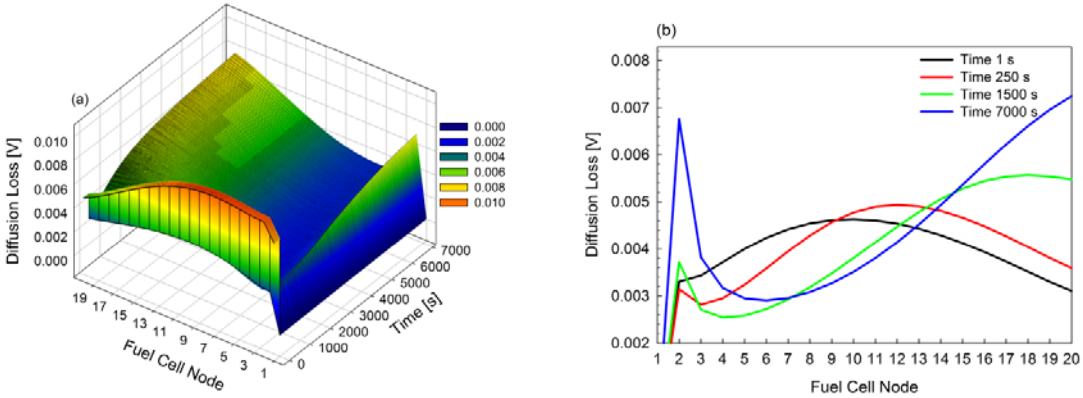

Figure 4.15: Transient profile of diffusion loss, (a) a 3D mesh plot, as function of local position along the cell node and time, and (b) distributed profiles at time 1 s, 250 s, 1,500 s, and 7,000 s after the step change

In comparison to other polarization resistance, the diffusion loss had the least impact on the fuel cell, since a thin electrode was used. Overall, over 7,000 s of test, the system started at very low diffusion resistance at the cell inlet, and sharply increased at node 2, as shown in Figure 4.15b. The diffusion loss at node 2 increased with time, reflecting the increase in localized H_2O mole fraction or the reduction in H_2O consumption (Figure 4.9)

when the fuel cell solid temperature dropped. Toward the end of the test, the increase at node 2 was more significant, with a substantial decrease immediately after node 2.

In the first 250 s of the transient, the maximum diffusion resistance was demonstrated at node 10, and gradually shifted to the cell exit to higher values over 7,000 s. Without significant variation in H_2O mole fraction, the diffusion loss at the end of the cell increased with decreasing fuel cell temperature, and increasing current density (Figure 4.11).

4.5.2.3 Fuel Cell Thermal Performance

Cathode Solid Temperature

The result of solid temperature distribution is presented in Figure 4.16. During the initial steady state, as shown before time 0 s in Figure 4.16a, the solid temperature inclined from node 1 to node 20, in a range of 780 °C at the inlet, to 903 °C at the outlet, with an average temperature of 857 °C. This resulted from an initial operating temperature of 800 °C using coal-derived syngas feed. In response to the fuel composition switch, the local solid temperature decreased significantly afterwards, except just a slight increase at the cell outlet during the first few minutes after the transient.

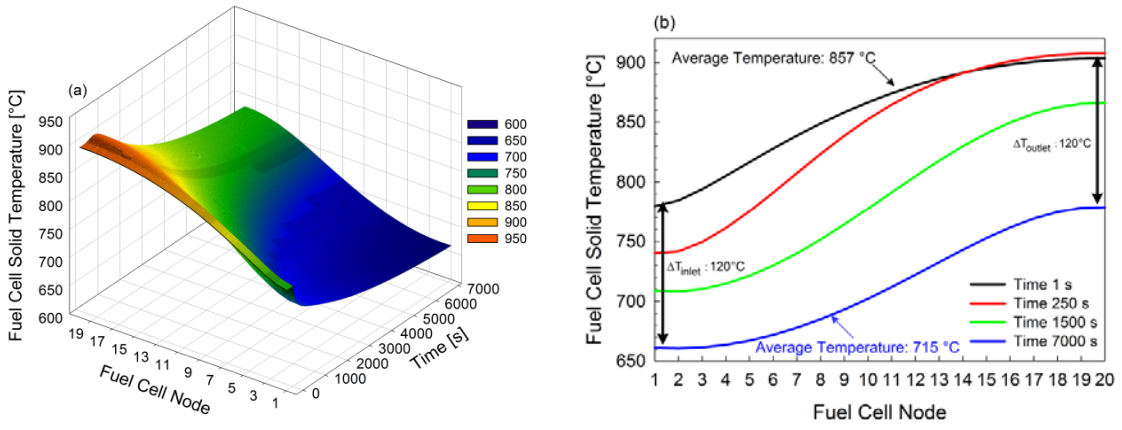

Figure 4.16: The dynamic profiles of fuel cell temperature, (a) a 3D mesh plot, as function of local position along the cell node and time, and (b) distributed profiles at time 1 s, 250 s, 1,500 s, and 7,000 s after the step change

The slight increase in the solid temperature at the end of the cell occurred at the first 250 s is clearly illustrated in Figure 4.16b. This dynamic was driven by the increase in fuel utilization (Figure 4.10), current density (Figure 4.11), and heat generation (Figure 4.20). In a short-term period, due to the large heat capacity of the fuel cells, the increase in fuel cell temperature was not offset by the temperature reduction promoted by the steam methane reforming reactions.

Unlike the end of the cell, the substantial reduction in solid temperature at the beginning of the cell was highly correlated to the drastic localized methane reforming as indicated in Figure 4.5, and heat flux, as reflected by the solid-gas temperature difference in Figure 4.21. As the consequence, 33% of the total temperature change at the cell entrance region took place in 250 s after the transient, and about 60% temperature drop occurred within the first 1,500 s (Figure 4.16b).

This cooling impact was remarkable even though there was a 2% decrease in cathode air mass flow during the first 1,500 s of test (Figure 4.17), which should have mitigated the impact on the solid temperature. Due to the control action taken by the system to maintain constant turbine speed at 40, 500 rpm, a 40% increase in turbine load caused a 1% increase in compressor discharge pressure. This resulted in a 4% reduction of compressor inlet flow which eventually reduced the cathode air flow by 2% [25].

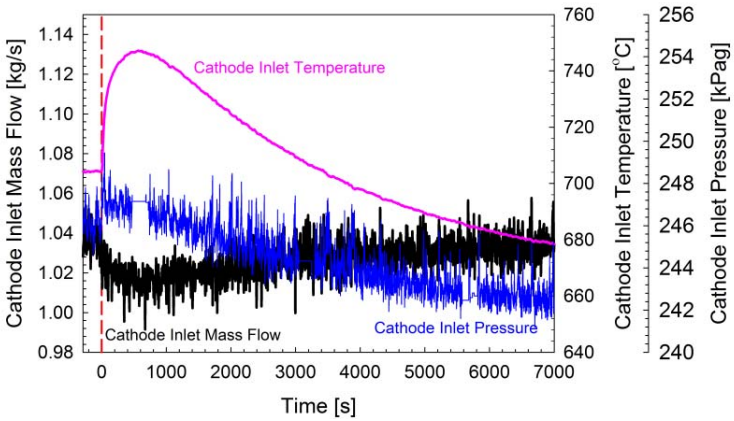

Figure 4.17: Fuel cell cathode inlet conditions

As presented in Figure 4.16b, despite the small temperature changes observed around the first and the last few nodes, the solid temperature across the cell increased to the maximum temperature region near the outlet. The increase in solid temperature occurred in the downstream region where CH_4 mole fraction was almost complete, while significant H_2 oxidation was observed. Hence, it resulted in less heat consumption in the reforming reaction. In addition, higher current density was also localized at the downstream region.

As the test progressed, the cell exit eventually cooled off to the point where the new steady state temperature profile was identical to the initial steady state profile (i.e. before fuel composition switch), but at a lower average temperature (715 °C). Decreasing the solid temperature decelerated the SMR kinetics that ultimately led to a more gradual CH_4 conversion. At the end of the test, the fuel cell temperature was distributed more evenly between 661 °C at node 1, and 778 °C at node 20. Due to shifted localized SMR towards the end of the cell, greater temperature reduction occurred at the cell outlet between time 1,500 s and 7,000 s. However, after 7,000 s, the fuel cell temperature difference between the initial and the final steady state at the cell inlet was about 120 degrees, similar to that observed at the cell exit.

Figure 4.18 presents the relevant solid temperature gradient between fuel cell nodes, dT/dx, for selected critical nodes. For control system development, fuel cell temperature gradient is a critical control variable because uneven temperature changes across the fuel cell length during transient processes can lead to dramatic localized thermal stress on the material, which contributes to fuel cell material destruction. As the result of the initial average temperature of 857 °C with a 113 °C temperature difference across the cell before the fuel composition change, the maximum dT/dx of 11.5 K/cm occurred at node 5, 25% down the cell inlet.

The maximum temperature gradient remained at the same location over 100 s after the step change, featuring an increasing value up to 15.8 K/cm. Unfortunately, over the 7,000 s test period, the greatest change in the localized fuel cell temperature of 16 K/cm was indicated at node 7, 250 s after the fuel transition. The highest peak of dT/dx was then shifted node by node towards the cell outlet as the test continued. However, beyond 3,100 s, the maximum dT/dx remained at node 13, with a lower final value (10 K/cm) at the end of the test.

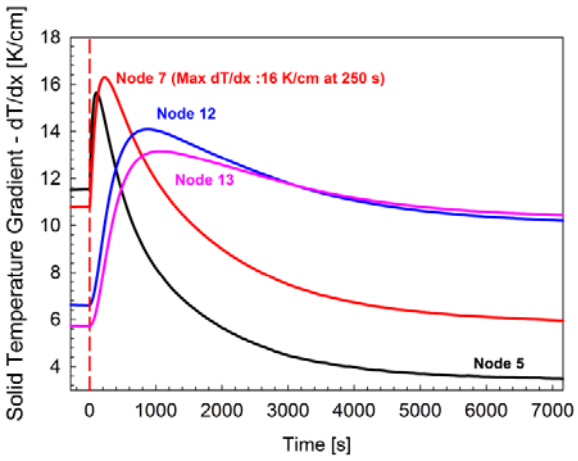

Figure 4.18: Spatio-fuel cell temperature gradient, $\boldsymbol{dT/dx}$

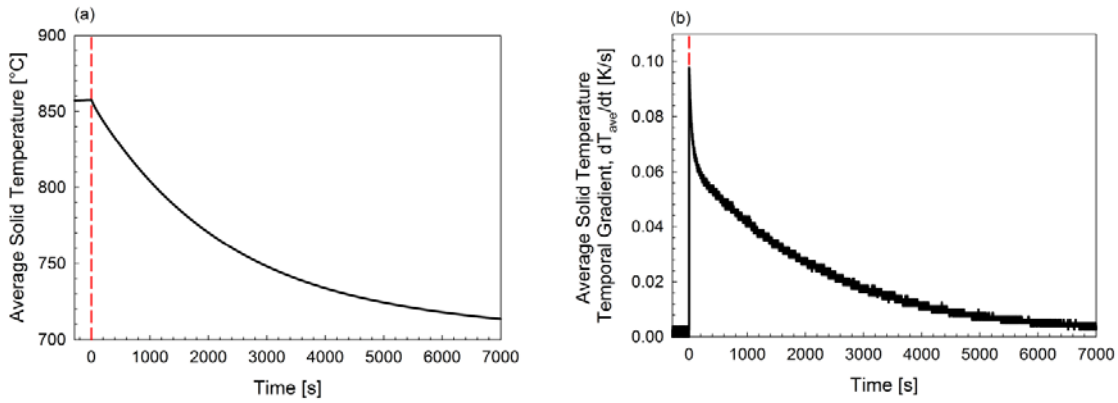

Figure 4.19: Average solid temperature profile, (a) average solid temperature profile as a function of time, and (b) temporal changes of average solid temperature, $\boldsymbol{dT_{ave}/dt}$

The profile of average solid temperature in Figure 4.19a shows that there was a gradual change over the 7,000 s test period. Meanwhile, Figure 4.19b illustrates that the most extreme transient in average solid temperature gradient as a function of time, dT_{ave}/dt, was not more than 0.10 K/s.

Cathode Gas Temperature

The associated dynamic response in the gas temperature is highlighted in Figure 4.20. Overall, the profile of cathode gas temperature features gradual decay characteristics toward its final value, with a slight increase at the cell outlet within the first few minutes, similar to the fuel cell solid temperature trends. However, as shown in Figure 4.20a, the cathode gas temperature at the fuel cell inlet did not follow the drastic decrease observed in the solid temperature (Figure 4.16a). In contrast, the profile of cathode gas temperature at the cell entrance was dominated by the 40 °C increase in cathode inlet air temperature (Figure 4.18) over the first 600 s after the initiation of the fuel composition change, due to the integrated system effects on the gas turbine system.

As depicted in Figure 4.20b, the cathode gas temperature at the initial steady state monotonically increased from 704 °C at node 1 to 902 °C at the last node, approaching a 200°C difference across the cell. After the fuel transition, an increasing gas temperature towards the end of the cell was locally distributed in S-shaped curves with the lowest temperature observed at around nodes 4 and 5. Correspondingly, over 7,000 s, the changes in gas temperature closely followed the distribution of fuel cell solid temperature. The detailed analysis suggests that the dynamic response at the beginning of the fuel cell was driven by the heat flux, unlike the changes occurred at the exit of the cell. At the final state, gas temperature difference across the cell length reduced by about 50% with the decreasing local gas temperature, in comparison to the initial steady state.

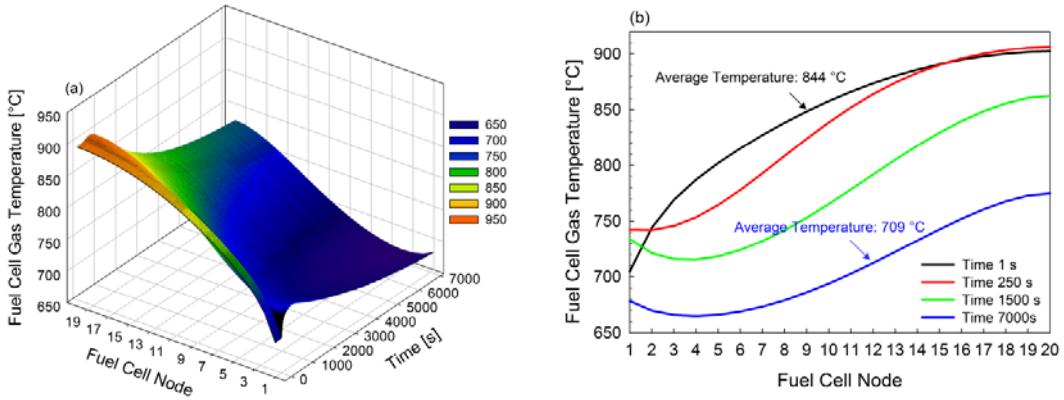

Figure 4.20: Cathode gas temperature profiles, (a) a 3D mesh plot, as function of local position along the cell node and time, and (b) distributed profiles at time 1 s, 250 s, 1,500 s, and 7,000 s after the step change

Heat Generation

The dynamic trajectory of heat generation in the fuel cell unit per given length of each node is shown in Figure 4.21. As the consequence of operating the fuel cell at 220 A total current with 67% fuel utilization using syngas, a maximum of 17 W/cm of heat was generated at the inlet, decreasing to a minimum of 3 W/cm at the outlet (Figure 4.21a). More heat was accumulated in the region in which contained higher current density (Figure 4.4), as expected.

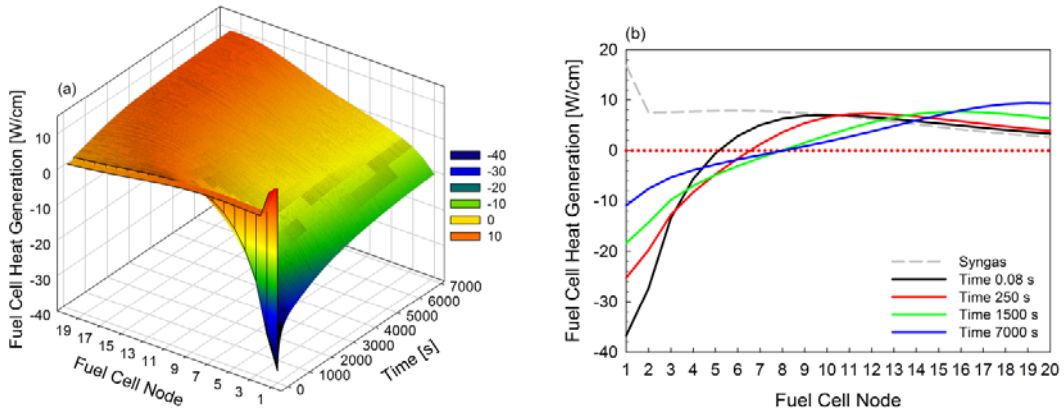

Figure 4.21: Fuel cell heat generation, (a) a 3D mesh plot, as function of local position along the cell node and time, and (b) distributed profiles at time 1s, 250 s, 1,500 s, and 7,000 s after the step change

After shifting the syngas feed to methane-rich gas, a detrimental reduction in heat generation was evident at the beginning of the cell, resulting in an immediate drop of 53 W/cm at the first node from 17 W/cm at the initial state to a -36 W/cm at 80 ms after the step change. But, heat generation increased gradually towards the maximum region at the fuel cell downstream.

The coupled effects of the sudden decrease in the fuel cell heat generation at the cell inlet (Figure 4.21) were reflected by the remarkable reduction in solid temperature (Figure 4.16). This change was due to higher heat consumption in the highly endothermic methane reformation at the cell upstream when the system was fed by 14% methane. Meanwhile, as the highly exothermic H_2 oxidation significantly took place in the second half of the cell length, the solid temperature started to increase, as shown in Figure 4.16.

In a longer experimental run, the contribution of deceleration in steam methane reforming was demonstrated clearly at the cell entrance, in which heat generation at the first node increased gradually with decreasing rate in methane conversion. Beyond more than 7,000 s after the step change, the heat generation across the cell moderately fluctuated, but its highest peak shifted from the centre to the end of the cell.

Solid-Gas Temperature Difference

The fuel cell thermal performance was further analyzed by quantifying the local temperature difference between solid and cathode gas temperatures ($T_{solid} - T_{gas}$), as provided in Figure 4.22. The local and the overall temperature difference are shown in Figures 4.22a and 4.22b respectively. As shown in Figure 4.22a, the profile of temperature difference in the first half of the cell length was quite distinct from the dynamic response in the second half of the cell, indicating appreciable changes in the beginning of the cell, and insignificant transient response at the end of the cell. Variations of temperature difference at the cell exit were between 1°C to 10 °C over 7,000 s.

At the initial transient period that is denoted as time 0.08 s in Figure 4.21a, the temperature difference reduced dramatically by about 80%, from 75 °C to 14.5°C, within the first 5 nodes (25% of the cell length), following by a slow decrease to 1 °C gap at the cell exit. Such a transient implies that the cathode airflow was initially cooling the fuel cell, mostly at the first 25% of the cell length. Decreasing the temperature gap across the fuel cell length reduced the heat exchange from the solid to the air flow. Therefore, the cooling process progressed slowly as the air delivered through the end of the cell. Likewise, reducing the temperature difference at 100 s after the fuel transition also lowered the cooling impact of air flow at the inlet region.

The results in Figure 4.22a also show that as soon as 250 s after the transient, the cathode inlet airflow was being used to heat the beginning of the cell. This occurred once the solid temperature dropped below the gas temperature due to the rapid heat consumption in SMR, reducing the temperature difference to negative values. The thermal effects of cathode airflow was far more complicated in the period between 1,500 s after the transient to the final state, in which the heating and the cooling effects of cathode airflow alternated as moving from the inlet down through the cell outlet. But in this period, the airflow cooled the downstream region more than in the initial steady state.

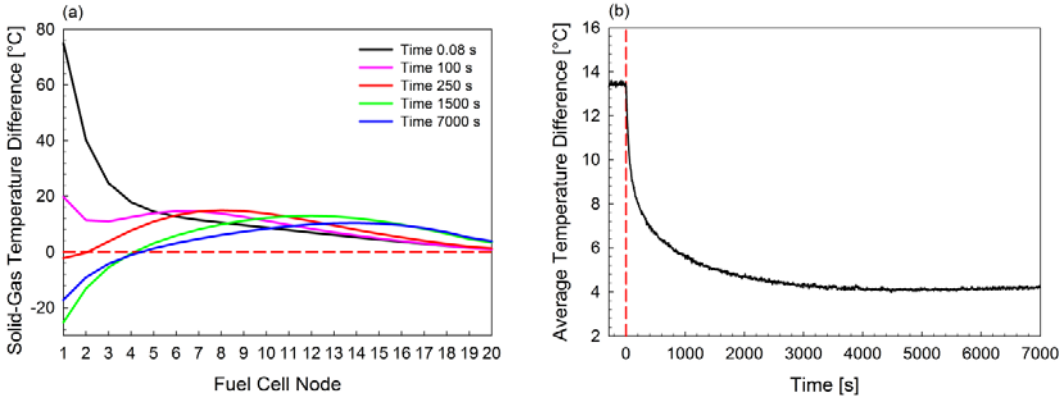

Figure 4.22: The profile of solid-gas temperature difference ($\boldsymbol{T_{solid} - T_{gas}}$), (a) distributed temperature profile across the cell at different time, and (b) average temperature difference as function of time

As such, this work reveals the real challenges in modulation of airflow for thermal management of SOFC/GT hybrid system for fuel composition changes. Alternative strategies might need to be considered to compensate for the variations in solid temperature due to methane reforming and the impact of cathode airflow.

4.5.2.4 Dynamic Response of Fuel Cell Thermal Effluent

Previous studies of the SOFC/GT hybrid system show that the fuel cell waste heat in the direct fired SOFC/GT hybrid configuration is a very important process variable for system performance controls and safety [34].

When the humidified methane was fed into the anode, methane reformation occurred immediately, as observed in Fig 5. This reaction was initially driven by the elevated fuel cell thermal energy provided in the cathode stream as well as the available chemical energy level contained in the fuel mixture. However, the available energy state was insufficient to facilitate the reactions while maintaining the fuel cell temperature. As such, the fuel cell thermal energy storage was extracted, resulting in a sudden initial increase in fuel cell thermal effluent in a short term period, as highlighted in Figure 4.23.

As shown in Figure 4.23b, the dissipation rate of thermal energy stored in the fuel cell was 260 kW immediately after the fuel transition. This thermal energy was transformed to chemical energy via the reforming reaction which increased the low heating value (LHV) of the anode effluent. This subsequently increased the fuel cell thermal effluent, which then increased the thermal energy entering the turbine by 120 kW, or about 17%. This in turn caused an increase in turbine exhaust temperature, which caused a higher heating duty in E300 and E305, which finally caused the rise in cathode inlet temperature discussed previously (Figures 4.17 and 4.20).

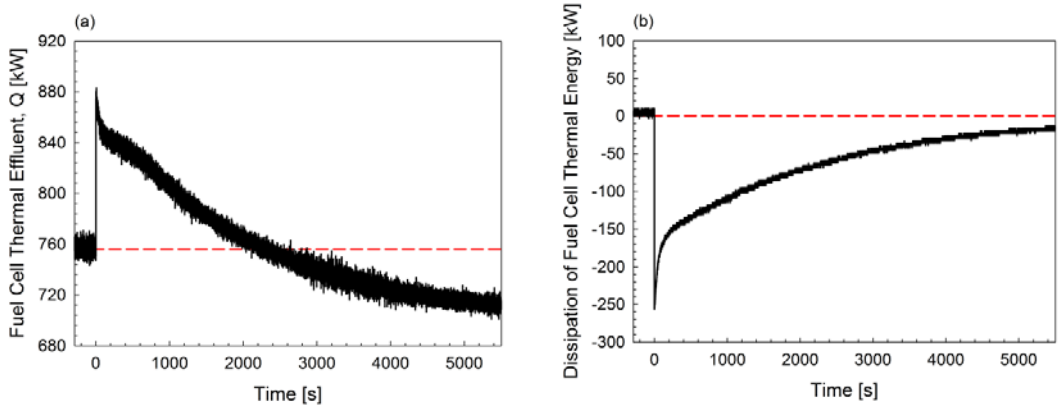

Figure 4.23: (a) Fuel cell model thermal effluent transient, (b) Dissipation of fuel cell thermal energy storage

The total mass-heat capacity contained in the simulated 2500 cell-stack with a total mass of 3500 kg was approximately 2625 kJ/K. Under the nominal operating condition, the fuel cell itself stored approximately 2.1 GJ of thermal energy. Theoretically, reducing the temperature of the fuel cell average temperature by 142 °C over the 7,000 s test (Figure

4.19) would significantly decrease the total thermal energy storage in the fuel cell by about 18%. Approaching the new steady state, Q decreased gradually, following the reduction in LHV of the fuel feed. As the result of highly coupled interactions in SOFC/GT hybrid system, this dynamic transient subsequently reduced the thermal effluent that ultimately decreased the cathode inlet temperature.

4.6 Conclusions

This work has presented the detailed analysis of fuel cell dynamic performance in SOFC/GT hybrid system during a transition from syngas-fueled to methane-fueled operation, including the interactive effects among the key operating variables.

It was found that it was feasible to suddenly switch from a coal-derived syngas to a humidified methane fuel (with 14% methane content) and transition to a new steady state within two hours without causing compressor stall or surge, violating SOFC safe operating constraints, or otherwise adversely affecting the hardware or functionality of the SOFC/GT system. It may also be possible to transition from coal-syngas to humidified methane fuels with an even higher energy content if the transition was gradual instead of a step change, although this is a subject for future research.

It was found that the fuel transition exhibited a rapid transient increase of fuel cell thermal effluent by 17% in the time scale of milliseconds. The primary driver for the dramatic change in thermal effluent was the conversion of thermal energy stored in the fuel cell stack to chemical energy. Over the course of the 7,000 s period studied, 18% of the total thermal energy stored in the fuel cell stack itself was extracted.

In the initial period after the transient, methane was all used up by node 8 (40%), but node 20 by 7,000 s. As a consequence of the cooling effects of methane reformation, the maximum spatial temperature gradient, dT/dx, increased from 11 K/cm to 16 K/cm at around 35% from the cell inlet 250s after initiation of the transient. Maximum current density also increased by 15%, indicating a shift from node 5 (25%) to node 18 (90%).

Thermal management using modulation of cathode air flow could be a potential strategy to mitigate this unfavourable transient impact. However, due to alternating cooling and heating transient effects of cathode air flow observed across the cell, advanced control strategies may be required to mitigate the unfavourable transient impact as well as to increase the flexibility of SOFC/GT hybrid system.

4.7 Acknowledgements

This work was funded by the U.S Department of Energy Crosscutting Research program, implemented through the Strategic Center for Coal in The Office of Fossil Energy. The authors would like to thank Nana Zhou, Paolo Pezzini, Valentina Zaccaria and Dave Ruehl from NETL for their contribution in the execution of the experimentation, and also greatly acknowledge the Universiti Teknologi Malaysia and Ministry of Higher Education Malaysia for financial support.

4.8 References

[1] Adams, T. A. II, 2014, "Future Opportunities and Challenges in The Design of New Energy Conversion Systems," Comput. Chem. Eng., 34, pp. 5-14.

[2] Zhang, X., Chan, S. H., Li, G., Ho, H. K., Li, J., and Feng, Z., 2010, "A Review of Integration Strategies for Solid Oxide Fuel Cells," J. Power Sources, 195(3), pp. 685-702.

[3] Winkler, W., Nehter, P., Williams, M. C., Tucker, D., and Gemmen, R., 2006, "General Fuel Cell Hybrid Synergies and Hybrid System Testing Status," J. Power Sources, 159(1), pp. 656-666.

[4] McLarty, D., Brouwer, J., and Samuelsen, S., 2014, "Fuel Cell–gas Turbine Hybrid System Design Part I: Steady State Performance," J. Power Sources, 257(2014), pp. 412-420.

[5] Restrepo, B., Banta, L. E., and Tucker, D., 2011, "Characterization of a Solid Oxide Fuel Cell Gas Turbine Hybrid System Based on a Factorial Design of Experiments using Hardware Simulation," ASME Paper No. FuelCell2011-54146.

[6] Yi, Y., Rao, A. D., Brouwer, J., and Samuelsen, G. S., 2005, "Fuel Flexibility Study of an Integrated 25 kW SOFC Reformer System," J. Power Sources, 144(1), pp. 67-76.

[7] Santin, M., Traverso, A., and Magistri, L., 2009, "Liquid Fuel Utilization in SOFC Hybrid Systems," Appl. Energy, 86(10), pp. 2204-2212.

[8] Leone, P., Lanzini, A., Ortigoza-Villalba, G. A., and Borchiellini, R., 2012, "Operation of a Solid Oxide Fuel Cell Under Direct Internal Reforming of Liquid Fuels," Chem. Eng. J., 191(2012), pp. 349-355.

[9] Cimenti, M., and Hill, J. M., 2009, "Direct Utilization of Liquid Fuels in SOFC for Portable Applications: Challenges for the Selection of Alternative Anodes," Energies, 2(2009), pp. 377 - 410.

[10] Chen, Y., Adams, T. A. II, and Barton, P. I., 2011, "Optimal Design and Operation of Flexible Energy Polygeneration Systems," Ind. Eng. Chem. Res., 50(8), pp. 4553-4566.

[11] Adams, T. A. II, Nease, J., Tucker, D., and Barton, P. I., 2013, "Energy Conversion with Solid Oxide Fuel Cell Systems: A Review of Concepts and Outlooks for the Short- and Long-Term," Ind. Eng. Chem. Res., 52(9), pp. 3089-3111.

[12] Adams, T. A. II, and Barton, P. I., 2009, "A Dynamic Two-dimensional Heterogeneous Model for Water Gas Shift Reactors," Int. J. Hydrogen Energy, 34(21), pp. 8877-8891.

[13] Song, T. W., Sohn, J. L., Kim, T. S., and Ro, S. T., 2006, "Performance Characteristics of a MW-class SOFC/GT Hybrid System Based on a Commercially Available Gas Turbine," J. Power Sources, 158(2006), pp. 361-367.

[14] Mueller, F., Jabbari, F., and Brouwer, J., 2009, "On the Intrinsic Transient Capability and Limitations of Solid Oxide Fuel Cell Systems," J. Power Sources, 187(2), pp. 452-460.

[15] Mueller, F., Gaynor, R., Auld, A. E., Brouwer, J., Jabbari, F., and Samuelsen, G. S., 2008, "Synergistic Integration of a Gas Turbine and Solid Oxide Fuel Cell for Improved Transient Capability," J. Power Sources, 176(1), pp. 229-239.

[16] McLarty, D., Brouwer, J., and Samuelsen, S., 2014, "Fuel Cell–gas Turbine Hybrid System Design Part II: Dynamics and Control," J. Power Sources, 254(2014), pp. 126-136.

[17] Nakajo, A., Wuillemin, Z., herle, J. V., and Favrat, D., 2009, "Simulation of Thermal Stress in Anode-Supported Solid Oxide Fuel Cell Stacks Part I: Probability of Failure of the Cells.," J. Power Sources, 193(2009), pp. 201-215.
[18] Mueller, F., Tarroja, B., Maclay, J., Jabbari, F., Brouwer, J., and Samuelsen, S., 2010, "Design, Simulation and Control of a 100 MW-class Solid Oxide Fuel Cell Gas Turbine Hybrid System," ASME. J. Fuel Cell Sci. Technol., 7(3), pp. 031007-031007-11
[19] Traverso, A., Magistri, L., and Massardo, A. F., 2010, "Turbomachinery for the Air Management and Energy Recovery in Fuel Cell Gas Turbine Hybrid Systems," Energy, 35(2), pp. 764-777.
[20] Gaynor, R., Mueller, F., Jabbari, F., and Brouwer, J., 2008, "On Control Concepts to Prevent Fuel Starvation in Solid Oxide Fuel Cells," J. Power Sources, 180(1), pp. 330-342.
[21] Hernandez-Pacheco, E., Mann, M. D., Hutton, P. N., Singh, D., and Martin, K. E., 2005, "A Cell-level Model for A Solid Oxide Fuel Cell Operated with Syngas from a Gasification Process," Int. J. Hydrogen Energy, 30(2005), pp. 1221 - 1233.
[22] Ishak, F., Dincer, I., and Zamfirescu, C., 2012, "Energy and Exergy Analyses of Direct Ammonia Solid Oxide Fuel Cell Integrated with Gas Turbine Power Cycle," J. Power Sources, 212(2012), pp. 73-85.
[23] Li, Y., and Weng, Y., 2011, "Performance Study of a Solid Oxide Fuel Cell and Gas Turbine Hybrid System Designed for Methane Operating with Non-designed Fuels," J. Power Sources, 196(2011), pp. 3824 - 3835.
[24] Tucker, D., Liese, E., and Gemmen, R., 2009, "Determination of the Operating Envelope for a Direct Fired Fuel Cell Turbine Hybrid using Hardware Based Simulation," Proceedings of the International Colloquium on Environmentally Preferred Advanced Power Generation (ICEPAG 2009), Newport Beach, CA, Feb. 10-12, ICEPAG Paper No. ICEPAG2009-1021.
[25] Harun, N. F., Tucker, D., and Adams, T. A. II, 2014, "Fuel Composition Transients in Fuel Cell Turbine Hybrid for Polygeneration Applications," ASME J. Fuel Cell Sci. Technol., 11(6), pp. 061001-061001-8.
[26] Hughes, D., Wepfer, W. J., Davies, K., Ford, J. C., Haynes, C., and Tucker, D., 2011, "A Real-time Spatial SOFC Model for Hardware-based Simulation of Hybrid Systems," ASME Paper No. FuelCell2011-54591.
[27] Tucker, D., Liese, E., VanOsdol, J. G., Lawson, L. O., and Gemmen, R. S., 2002, "Fuel Cell Gas Turbine Hybrid Simulation Facility Design," ASME Paper No. IMECE2002-33207.
[28] Tucker, D., Lawson, L., and Gemmen, R., 2005, "Characterization of Air Flow Management and Control in a Fuel Cell Turbine Hybrid Power System using Hardware Simulation," ASME Paper No. PWR2005-50127.
[29] Tucker, D., Lawson, L., Gemmen, R., and Dennis, R., 2005, "Evaluation of Hybrid Fuel Cell Turbine System Startup with Compressor Bleed," ASME Paper No. GT2005-68784.
[30] Tucker, D., Pezzini, P., and Banta, L., 2013, "Equivalence Ratio Startup Control of a Fuel Cell Turbine Hybrid System," ASME Paper No. GT2013-94809.
[31] Pezzini, P., Tucker, D., and Traverso, A., 2013, "Avoiding Compressor Surge during Emergency Shut-down Hybrid Turbine Systems," ASME J. Gas Turbines Power, 135(10), pp. 102602-102602-10.
[32] Pezzini, P., Traverso, A., Banta, L., and Tucker, D., 2014, "Decentralized Control Strategy for Fuel Cell Turbine Hybrid Systems," Proceedings of the 57th Annual ISA

Power Industry Division Symposium, Scottsdale, Arizona, June 1-6, Paper No. ISA-PWID2014-52.

[33] Hughes, D. O., 2011, "A Hardware-based Transient Characterization of Electrochemical Start-Up in an SOFC/Gas Turbine Hybrid Environment using a 1-D Real Time SOFC Model," Doctor of Philosophy, Georgia Institute of Technology, Atlanta, Georgia.

[34] Cheddie, D. F., and Munroe, N. D. H., 2007, "A Dynamic 1D Model of a Solid Oxide Fuel Cell for Real Time Simulation," J. Power Sources, 171(2), pp. 634-643.

[35] Trembly, J. P., Gemmen, R. S., and Bayless, D. J., 2007, "The Effect of Coal Syngas Containing AsH_3 on the Performance Of SOFCs: Investigations into the Effect of Operational Temperature, Current Density and AsH_3 Concentration," J. Power Sources, 171(2), pp. 818-825.

[36] Tucker, D., Abreu-Sepulveda, M., and Harun, N. F., 2014, "SOFC Lifetime Assessment in Gas Turbine Hybrid Power Systems," ASME J. Fuel Cell Sci. Technol., 11(5), pp. 051008-051008-7.

[37] Haynes, C., and Wepfer, W. J., 2000, "'Design for Power of a Commercial Grade Tubular Solid Oxide Fuel Cell," Energy Convers. Manage., 41(11), pp. 1123-1139.

[38] EG&G Technical Services, Inc., 2004, Fuel Cell Handbook, U.S. Department of Energy, Office of Fossil Energy, National Energy Technology Laboratory, Morgantown, West Virginia.

5 COUPLING EFFECTS OF FUEL COMPOSITION TRANSITION AND CATHODE AIR MASS FLOW ON DYNAMIC PERFORMANCE OF SOFC/GT HYBRID SYSTEMS

To be submitted to *Applied Energy*

5.1 Publication Highlights

This part is dedicated for a more serious discussion on the dynamic performance of SOFC/GT hybrid systems, leading to future system identification of this technology during fuel composition transients. Similarly, the finding obtained in Chapter 3 is expanded and presented herein. This chapter particularly emphasizes on the characterization of linking dynamic events associated with fuel composition changes (i.e. cathode air mass flow variations). Comparison of the open loop dynamic performance and closed loop performance for the important fuel cell parameters is carried out to determine the integration issues that could affect the dynamic performance of SOFC/GT hybrid system as well as to identify potential opportunities for dynamic controls of SOFC/GT hybrid systems during fuel composition changes.

The results in this section were obtained from the same experiments conducted in Chapter 3. The majority of this work was performed me, but I got assistance from Dr. David Tucker, Dr. Paolo Pezzini, Valentina Zaccaria, and Nana Zhou to execute the tests. In addition, Dr. Thomas A. Adams II and Dr. David Tucker helped me in data analysis and preparation of this manuscript.

Coupling Effects of Fuel Composition Transition and Cathode Air Mass Flow on Dynamic Performance of SOFC/GT Hybrid Systems

Authors: Nor Farida Harun[a], David Tucker[b], and Thomas A. Adams II[a]
[a]Department of Chemical Engineering, McMaster University, 1280 Main Street West, Hamilton, Ontario L8S 4L7, Canada
[b]U.S. Department of Energy, National Energy Technology Laboratory, 3610 Collins Ferry Road, Morgantown, West Virginia 26507-0880, United States

5.2 Abstract

Considering the limited turndown potential of gasification technologies, supplementing a fuel cell turbine hybrid power system with natural gas provides flexibility that could improve economic viability. The dynamic characterization of fuel composition transients is an essential first step in completing the system identification required for controls development. In this work, the open loop transient response of the fuel cell in a solid oxide fuel cell (SOFC) gas turbine (GT) hybrid system to fuel composition changes were experimentally investigated using hardware-based simulations. A transition from coal-derived syngas to methane rich gases with no turbine speed control was studied. The distributed performance of fuel cell was analyzed in detail with temporal and spatial resolution across the cell.

Dramatic changes in fuel cell system thermal effluent resulting from anode composition changes drove turbine transients that caused significant cathode airflow fluctuations, by as much as 8% in less than a minute. In comparing the open loop responses to identical tests conducted under closed loop conditions without significant airflow changes, it was discovered that the cathode airflow change was a major linking event in short-term system transient response. The results suggested that modulating cathode air flow in response to fuel composition changes offers promise for the dynamic control of SOFC/GT hybrid systems with fuel flexibility.

Keywords: Open loop characterization, solid oxide fuel cell, distributed analysis, fuel cell gas turbine hybrid, fuel flexibility, hardware-based simulations

5.3 Introduction

In order to accelerate the commercialization of solid oxide fuel cell gas turbine (SOFC/GT) hybrid systems, the dynamics of the system must be better understood in order to create control systems which allow for its safe operation [1-3]. Although SOFC/GT hybrid systems are very promising due to their improved system performance and reduced costs compared to stand-alone solid oxide fuel cell systems, there are many challenges associated with the integration of SOFCs with existing turbomachine technologies [4-6]. For example, SOFC/GT hybrid systems have been previously shown to exhibit problematic nonlinearities in certain dynamic behaviours as well as exhibit debilitating issues associated with the coupling of some of the subcomponents in the hybrid system [7]. This is primarily due to the

large mass-heat capacity of fuel cell stacks and the fast dynamic response of turbomachinery, which together may cause large transient changes in response to even small disturbances as well as delays in system response [8, 9].

Some other common operational challenges associated with SOFC/GT hybrid systems include fuel cell thermal management and fuel cell degradation that can significantly affect the fuel cell stack performance and its useful lifetime. In addition, transient variations in load and fuel composition, associated with rapid cycling changes, setpoint changes, or disturbances can strongly impact system pressure, gas flow rates, and other properties [10]. Undoubtedly, these or other unexpected fluctuations can significantly impact the performance and reliability of the hybrid system. Severe fuel cell damage, shaft overspeed, and/or compressor stall and surge may occur if proper safety measures and controls are not available [6, 7, 10].

In order to prevent faults, damage, and operational failures during both steady-state and transient SOFC/GT hybrid system operations, sufficient control architectures need to be implemented. However, in order to construct a suitable control system, we need a better understanding of the dynamic coupling interactions between the different system components, such as the fuel cell, gas turbine, compressor and heat exchangers, as shown in Figure 5.1. Since fuel cell dynamics in SOFC/GT hybrid systems are strongly linked to the balance of the plant (which is subject to operational constraints), the characterization of the coupling between the different components of the systems during any transient change imposed on the system is essential. As such, restrictions on the transient capabilities and potential control strategies can be identified. Nevertheless, the exploration of this coupling is not trivial, because most of the time, the interactions cannot be captured by simulations only. Therefore, hardware-based simulations are the most effective approach to study coupling properties during transients. At the U.S department of Energy, National Energy Technology Laboratory (NETL), a hardware-based simulation test facility for SOFC/GT hybrid was developed. This hybrid test facility incorporates actual equipment of direct-fired recuperated gas turbine and a cyber-physical fuel cell subsystem, which ensures that the key coupling effects between components of the systems can be studied experimentally.

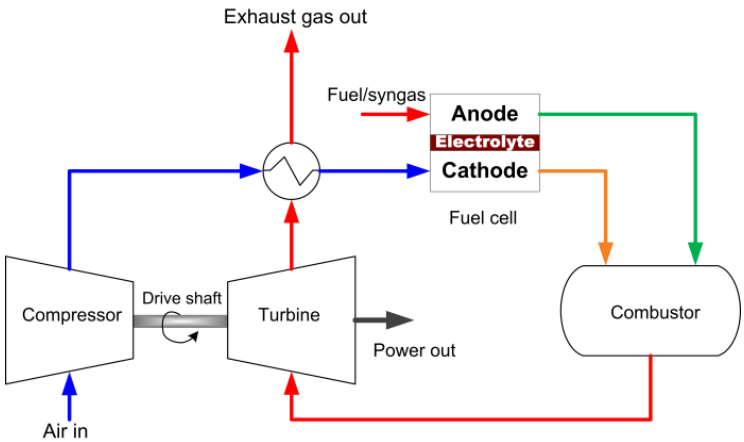

Figure 5.1: Basic flow diagram of a SOFC/GT hybrid system

In this work, the characterization of the dynamic response of SOFC/GT hybrid systems with regard to the impacts of fuel composition changes was discussed. This was to address the issues relevant to fuel flexibilities in SOFC hybrid systems. Open loop performance of the hybrid system was investigated under a perturbation using a step change in fuel composition. Comparison of the open loop dynamic performance and closed loop performance was carried out to determine the integration issues that could affect the dynamic performance of SOFC/GT hybrid systems and to identify potential opportunities for dynamic controls of SOFC/GT hybrid systems during fuel composition changes.

5.4 Background

In favour of simplicity in exploring the unknown dynamic behaviours in a highly integrated system of SOFC/GT, characterization of this hybrid system in closed loop operation was first performed [11]. The impacts of a step change from coal-derived syngas to humidified methane containing 14% CH_4 and 86% steam was investigated in the previous work. The closed loop tests provided valuable insights of relationships among the key process variables in a base case condition of fuel composition changes with very minimal disturbances and risks of system failure. Particularly, the closed loop test was conducted in constant turbine speed and constant cathode air mass flow environment due to turbine speed control actions [11, 12].

On the other hand, open loop identification of SOFC/GT hybrid systems is important for empirical control model development. This paper focuses on the first approach taken prior to detailed system identification, in which open loop transient response is characterized and compared to closed loop performance. Early scoping studies and analysis of fuel valve transient response based on the test facility suggested that transitioning to methane-rich gas with 13.6% CH_4 and 86.4% steam in open loop case was favourable because a change to 14% CH_4 and 86% steam was dangerous and restricted by the turbine speed safety limit. Thus, the open loop results presented herein were from fuel composition changes to humidified methane containing 13.6% CH_4 and 86.4% steam.

Nevertheless, the results obtained in the open loop test using 13.6% CH_4 and 86.4% steam was not comparable to the results of closed loop test using 14% CH_4 and 86% steam discussed in a prior work [11]. A 3% difference in methane content (13.6% CH_4 versus 14% CH_4) resulted in substantial difference in the dynamic performance of SOFC/GT hybrid systems. An example of the difference in the comparison of fuel cell solid temperature between the open loop case using 13.6% CH_4 and closed loop case using 14% CH_4 as well as 13.6% CH_4 is presented in Figure 5.2. As shown in Figure 5.22, the difference in methane content resulted in a 62% difference in the crossover time associated with fuel cell solid temperature at the beginning of the cells. Therefore, it was essential to repeat all the closed loop tests at 13.6% CH_4 and 86.4% steam for the comparison highlighted herein.

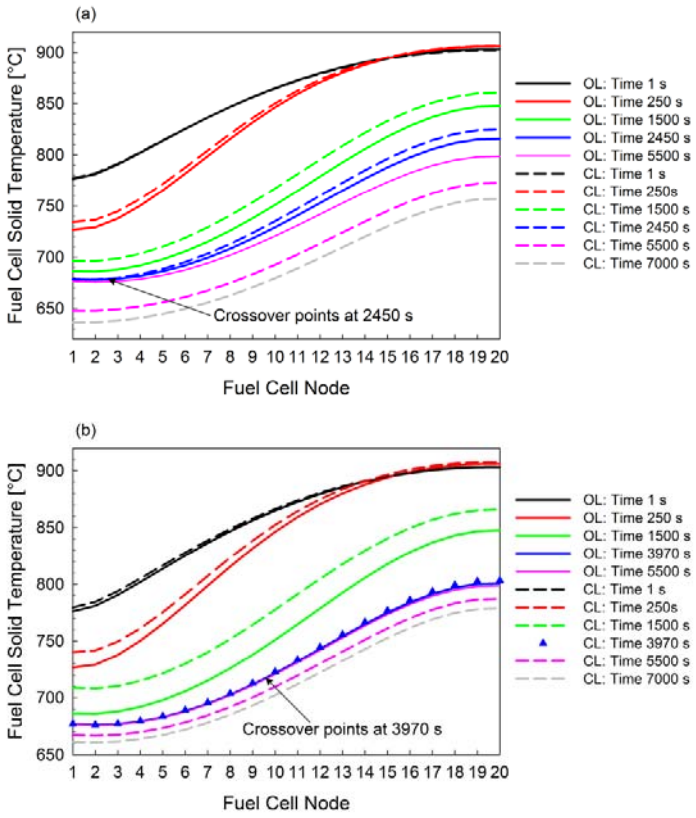

Figure 5.2: Comparison of fuel cell solid temperature performance, (a) between the open loop and closed loop with 13.6% CH_4 content, and (b) between the open loop (13.6% CH_4) and the closed loop (14% CH_4)

5.5 Methodology

5.5.1 Description of Hardware-based Simulation System

The U.S Department of Energy, National Energy Technology Laboratory (NETL) in Morgantown, West Virginia has developed a dynamic fuel cell model for applying hardware-based simulations in real time to emulate SOFC/GT dynamic performance using both real and simulated components [13, 14]. This facility helps to perform tests for transient response characterization of SOFC/GT systems, addressing system identification and transient capabilities of the system that associated with operating envelope, coupling effects between fuel cell subsystem and gas turbine cycle, and highly complex dynamic control strategies [7, 15-18]. The layout of this system is shown in Figure 5.3. The real cathode stream is emulated in the hardware system, while, the anode fuel stream is simulated in a real-time one-dimensional (1D) temporal and spatial SOFC dynamic model that runs every 80 ms [14]. Both hardware and software are well integrated in real time applications,

allowing for the hardware-based simulation to closely represent real SOFC/GT hybrid dynamic behaviours.

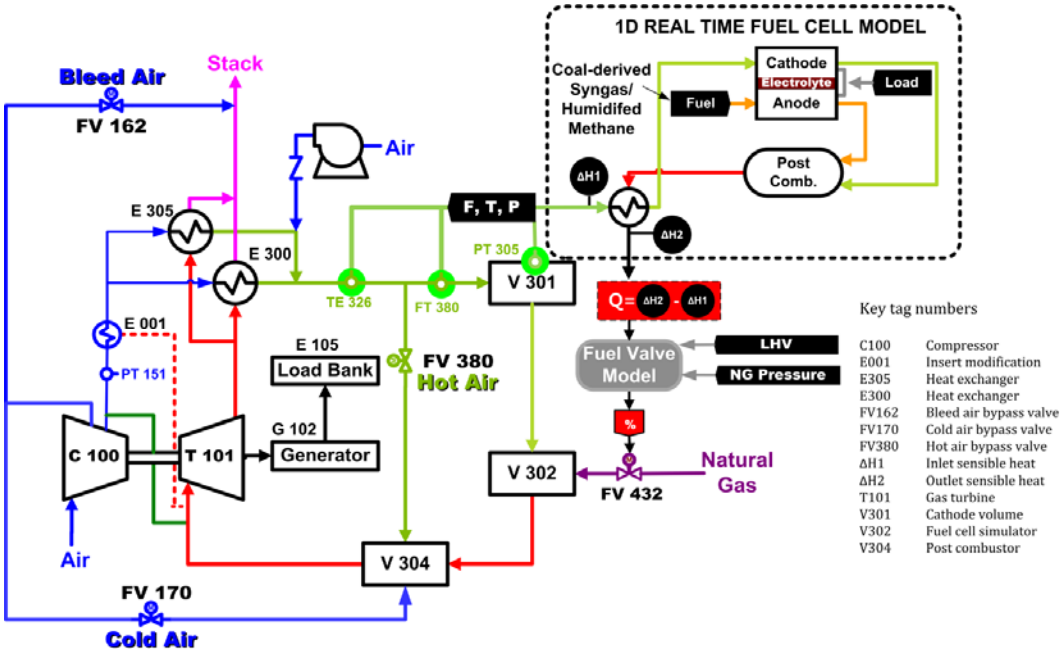

Figure 5.3: The layout of SOFC/GT testing facility at NETL

The real-time SOFC model used in this study was previously developed based on a planar design and co-flow fuel cell configuration, characterizing the fuel performance on a distributed basis with respect to space in the direction of fuel and oxidant flow [14]. Fuel constituents fed into the system model could be a combination of CH_4, CO, CO_2, H_2, H_2O, and N_2, assuming hydrogen is the only electrochemically active component for hydrogen oxidation, as expressed in Eq. 1 [19]. The direct internal reforming reaction of methane and water-gas shift reaction for carbon monoxide were considered in the model, according to Equations 2 and 3. Assuming that shifting reaction was faster than methane reforming kinetics at the temperature range used in this study, the shifting reaction was assumed to occur at equilibrium [19].

Hydrogen electrochemical oxidation:

$$H_2 + O^{=} \rightarrow H_2O + e^{=} \quad (\Delta H^{\circ} = -286\ kJ/mol) \tag{1}$$

Water-gas shifting:

$$CO + H_2O \rightleftharpoons H_2 + CO_2 \quad (\Delta H^{\circ} = -41\ kJ/mol) \tag{2}$$

Steam methane reforming:

$$CH_4 + H_2O \rightleftharpoons 3H_2 + CO \quad (\Delta H^{\circ} = 206\ kJ/mol) \tag{3}$$

In general, the model incorporated dynamic calculation for thermal performance (heat generation, solid and gas temperature profiles), electrochemical characterization (Nernst potential, polarization losses, current density and voltage), anode composition gradient, and associated fuel cell variables (power, fuel cell thermal effluent, etc.). Finite difference and finite volume were respectively used for the resolution of thermal profiles, and electrochemical performance. A more detailed description of the model development was published elsewhere [14].

5.5.2 Open Loop and Closed Loop Test Procedures

The standard startup procedures established by NETL researchers were performed in hardware-based simulations using a coal-derived syngas feed as the fuel until a steady state was reached [20]. Once steady state was achieved, a step transition in SOFC fuel composition from coal-derived syngas to methane-rich gases was simulated, with methane-rich fuel containing 13.6% CH_4 and 86.4% steam at constant fuel flow (145 g/s). The SOFC load (220 A) was held constant. The fuel composition transient was implemented by instantaneously changing the input parameters to the SOFC model without taking into account the lag in the fuel manifold process [12]. This fuel composition change resulted in a 20% decrease in lower heating value (LHV) of the anode feed [12, 21] and the corresponding initial fuel utilization was approximately 67% [12]. Prior scoping studies had indicated that since for the open loop test there are no controllers, the new fuel composition had to have a lower heating value than the base case (i.e. humidifed methane with 14% CH_4) in order to avoid any adverse impacts on the functionality of SOFC/GT hardware facility [21]. Meanwhile, the settings for the fuel flow rate and the SOFC load in the test were selected such that the impacts of fuel composition on the SOFC/GT hybrid system could be uniquely investigated, without confounding the data with the dynamic impacts of fuel flow and SOFC load.

This study used a switch from coal-derived syngas to natural gas as the transition of interest because it is one of the more drastic types of fuel composition transients that could reasonably be expected from among the various expected uses of SOFC/GT systems. For example, such a fuel transition may be potentially useful when SOFC/GT systems are integrated with chemical production trains in a polygeneration plant where purge gases of various compositions are used as the fuel for the SOFC. Such polygeneration plants can be designed to change the types or amounts of chemicals produced depending on the market price, thus resulting in changes to the purge gases and thus changes to the SOFC [22]. Or, when SOFC/GT systems are used for strictly power generation, shifts in market conditions such as changes in natural gas price, carbon taxes, or carbon restrictions, may motivate a drastic shift from coal-derived syngas to natural gas (or vice versa) to maximize the plant profit.

Previous studies have shown that hardware-based simulations were effective tools in the development of transfer functions using a first order plus delay time or second order plus delay time approach in the development of control systems when considering other types of transient behaviour [18]. Therefore, in this study, the same approach is used to develop a better understanding of system transients for the future development of control systems which consider fuel composition transients.

Table 5.1: SOFC parameters and initial operating conditions [12]

System parameter	
Fuel cell load	220 A
Anode recycle	0%
Initial fuel cell temperature	800°C
Total cell area	200mm x 200mm
Anode thickness	0.5mm
Electrolyte thickness	0.008mm
Cathode thickness	0.05mm
Oxidant/fuel channel size	2mm x 2mm
Stack size	2500 cells
Total stack mass	3500kg
Total stack heat capacity	2625 kJ/K
Fuel cell cathode inlet condition	
Air mass flow rate	1.03 kg/s
Air temperature	705°C
Air pressure	347 kPa
Air composition	21% O_2, 79% N_2
Fuel cell anode inlet condition	
Fuel mass flow rate	145 g/s
Fuel temperature	800°C
Fuel pressure	347 kPa
Initial composition	CH_4 0%, CO_2 12.0%, CO 28.6%, H_2 29.1%, H_2O 27.1%, N_2 3.2%
Final composition	CH_4 13.6%/H_2O 86.4%
Fuel cell initial condition	
Cell voltage	0.83V
Fuel utilization	67%

For the purposes of comparison, the test procedures and conditions used for the open-loop tests and the closed loop tests in this work were identical, including the fuel compositions, initial conditions of SOFC/GT hybrid test facility, the cell geometry, and hardware operation techniques. However, unlike the closed-loop studies where a control system placed a modulated electrical load (or resistive turbine load) on the turbine shaft to maintain constant turbine speed at 40,500 rpm, no turbine speed control scheme was used in the open loop tests. As such, the turbine responds directly in real-time to the total amount of SOFC thermal energy in the SOFC exhaust stream (i.e. fuel cell thermal effluent), which is delivered to the turbine inlet as shown in Figure 5.1. In this work, the calculation of the SOFC waste heat was performed by the 1D real-time SOFC model using real-time inputs of the cathode stream in addition to user-defined inputs and fuel cell geometry described in Table 5.1 [14, 23]. For hardware-based simulations, the SOFC waste heat computed by the

model was converted to an equivalent fuel valve position of FV432 in Figure 5.3, at every 80 ms simulation time step. The fuel valve position maps to an equivalent mass flow rate of fuel with the same thermal energy as computed by the model.

5.6 Results and Discussion

5.6.1 Turbine Speed and Cathode Air Mass Flow Transient Responses

The trajectories of turbine speed and cathode inlet mass flow for the open loop and the closed loop tests in response to fuel composition changes are shown in Figure 5.4 (the time at which the step change in fuel composition occurred is indicated as time t=0). For the open loop case, the turbine speed varied depending on the changes in fuel cell thermal effluent. The turbine speed was highly coupled to the fuel cell cathode inlet air mass flow (with R^2=0.993) because the compressor (C100, see Figure 5.3) was driven by the rotating shaft of the gas turbine (T101). As such, variations in turbine speed directly affected the fuel cell cathode air mass flow rate.

As shown in Figure 5.4b, an 8% initial transient increase in cathode air mass flow was observed as a consequence of increasing turbine speed by 4% immediately after the step change in fuel composition, presented in Figure 5.4a. This was followed by a steady decrease of both loops to a new steady state with the turbine speed 6% lower and the cathode air flow rate 12% lower than it was at the initial condition. For comparison, the results of the same transition but for a closed loop system in which the turbine speed was controlled at a constant 40,500 rpm is also shown in Figure 5.4. The so-called "crossover point" (the point at which the open loop and the closed loop values were the same) is at around 1,600 s after the step change for both properties.

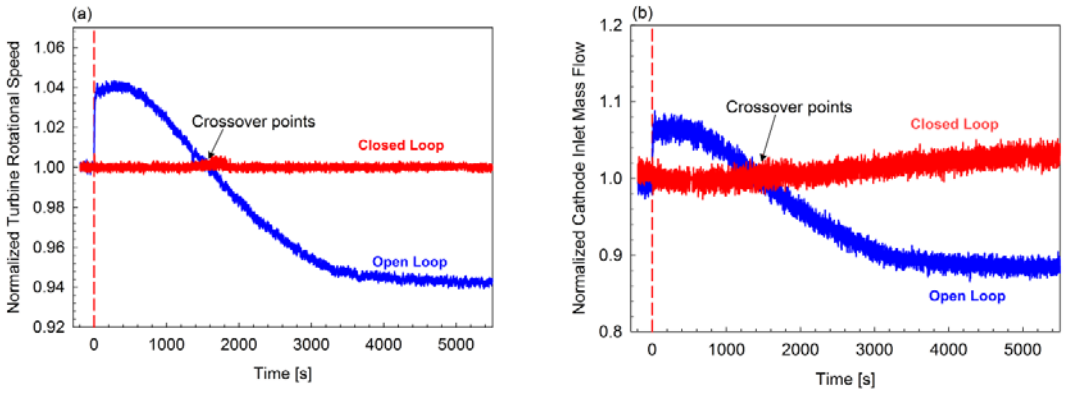

Figure 5.4: Comparison of variations in turbine speed and cathode air mass flow for open loop and closed loop

In general, crossover points were used to provide some ideas on the difference of open loop case as compared to base case study (closed loop operation). Thus, this point was further used to evaluate the interactive impacts on other process variables including the response delay.

5.6.2 Transient Characterization of Fuel Cell Thermal Performance

Fuel Cell Cathode Solid Temperature

The trajectories of fuel cell solid temperature are shown in Figure 5.5, indicating the open loop trends in Figure 5.5a and the closed loop dynamic transients in Figure 5.5b. As shown in Figure 5.5, the fuel cell solid temperatures for both the open loop and close loop increased across the fuel cell length, but reduced with time to a lower final average temperature as the test continued over the course of 5,500 s. In the open loop test, fuel cell solid temperature was distributed along the cell length at 125 °C temperature difference between the cell inlet and the cell exit at both the initial steady state, before the fuel composition change, and at the final steady state after the fuel composition change. The same inlet to outlet temperature difference across the cell was observed for the closed loop case, but a lower average temperature was achieved at the final steady state as compared to the open loop case since airflow was maintained at a higher level in the closed loop case to the final steady state.

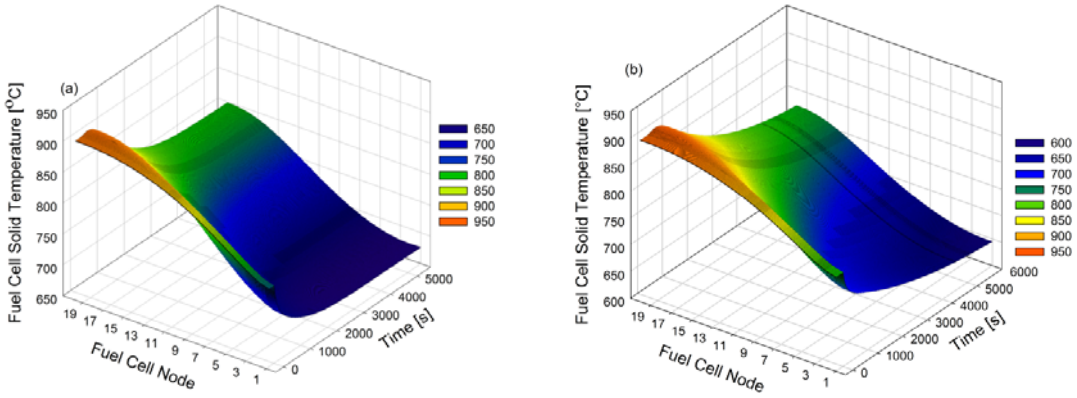

Figure 5.5: Fuel cell solid temperature as a function of time, (a) open loop (b) closed loop

To better visualize the difference between the open loop and closed loop trends, a selection of the data are plotted in Figure 5.6. Figure 5.6a shows the distributed profiles of solid temperature at certain times, resulting from the open loop and closed loop tests. Figure 5.6b highlights the magnitude of difference between the open loop and closed loop solid temperature profiles over 5,500 s, ($T_{solid_{CL}} - T_{solid_{OL}}$), for selected nodes.

Although both the open loop and closed loop tests started at the same initial states, indicated by the overlapping profile at 1 s in Figure 5.6a, the solid temperature in the closed loop test was generally higher than in the open loop over the first 2,450 s. As shown in Figure 5.6b, the greatest temperature difference within the first 650 s was found at node 2, due to substantial reduction in solid temperature from the open loop test. This transient was highly correlated to the resulting rapid increase in turbine speed in the open loop case that increased the amount of cathode air mass flow to the maximum value, on the order of few seconds after the fuel composition changes. With that variation, the fuel cell solid was further cooled by the increased cathode air mass flow, in addition to direct influence of steam methane reforming. Thus, the fuel cell solid temperature decreased faster than in the

closed loop case. This impact was initially more evident at the beginning of the cell as shown by the increasing the temperature gaps between the open loop and closed loop cases.

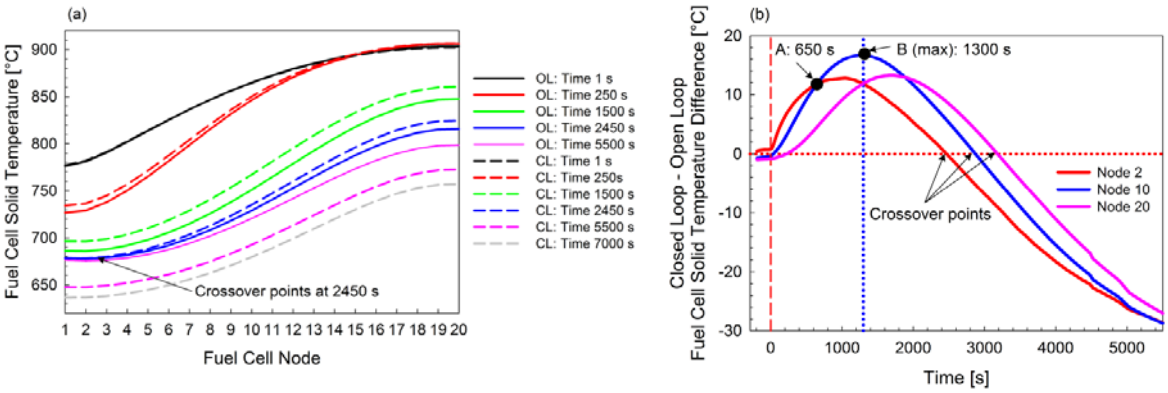

Figure 5.6: Comparison of fuel cell solid temperature performance, between the open loop and the closed loop tests (a) distributed data as a function of time, and (b) the response of solid temperature difference at selected fuel cell nodes

As indicated in Figure 5.6b, the location of the greatest temperature difference shifted further from node 2 to node 10, at point A. Although at the same time turbine speed and cathode air mass flow shown in Figure 5.4 started to reduce from the maximum values, the decrease in the open loop solid temperature was more significant half way down the fuel cell length. Decreasing cathode air mass flow should have mitigated fuel cell solid temperature reduction but the cooling effects were still significant because the total cathode air mass flow in the open loop system was still higher than in the closed loop, and the dynamic response of temperature was slow. Thus, at 1,300 s after the fuel composition change, the maximum temperature difference of 17 °C between both cases (point B) was observed at node 10, as a result of the most detrimental decrease in solid temperature experienced by the open loop system. Following the subsequent decrease in cathode air mass flow after the crossover in turbine speed at 1,600 s, the reduction in fuel cell solid temperature continued slowly until the temperature crossover point was reached.

It is shown in Figures 5.6a and 5.6b that crossover points of solid temperature at the beginning of the cell were achieved at 2,450 s after the step change, whereas the crossover points for the end of the cell were delayed 12 minutes later than the cell entrance. Such a significant difference in crossover points between the cell entrance and the cell exit was dominated by the resulting temperature profiles from the open loop and closed loop tests, indicating coupling between the temperature reduction due to convective heat transfer and methane reforming kinetics. In general, the increased cathode air mass flow before the crossover point of turbine speed caused the decreased in solid temperature, which finally decelerated the reforming reaction. As a result, this modified the distribution of methane in the fuel cell, which in turn, affected the solid temperature.

The comparison shown in Figure 5.6 demonstrated a greater drop in the closed loop solid temperature after the crossover points. The solid temperature in the closed loop test kept decreasing until 7,000 s after the fuel composition switch, at which time the test was terminated. Unlike the open loop process, the constant cathode air mass flow provided by

the constant turbine speed operation in closed loop continued to propagate the reduction in fuel cell solid temperature throughout the test. This was clearly reflected by cathode inlet temperature profiles shown in Figure 5.7.

In contrast, as a result of continuous decrease in cathode air mass flow in the open loop case after the crossover point, no substantial change was observed approximately after 3,000 s from the start of the test. The operation with variable turbine speed consequently brought the system close to a thermal equilibrium state faster than the closed loop system. Because of the variations in cathode air mass flow, the system exhibited two distinct and opposite coupling trends in the short-term period and the long-term period. This implied that multiple strategies of thermal management might be required to avoid severe cooling or heating in the fuel cell stack because both conditions could affect degradation mechanisms.

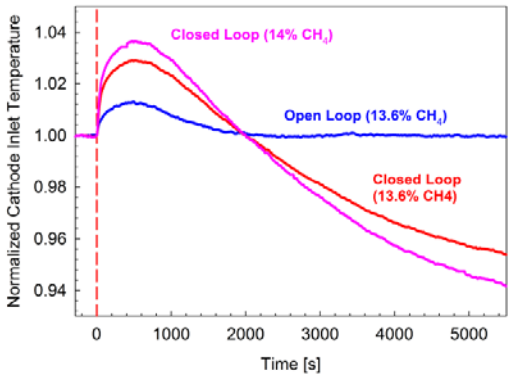

Figure 5.7: Cathode inlet temperature profiles for the open loop and closed loop systems using 13.6% CH_4 content and for the closed loop operation using 14% CH_4 content

Spatial Gradient of Fuel Cell Solid Temperature

The impact of fuel composition changes on fuel cell solid temperature was further characterized by quantifying the spatial temperature gradient (dT/dx) along the cell, as indicated in Figure 5.8. Note that the spatial temperature gradient is an important characteristic that must be limited to 12 K/cm to prevent fuel cell failure. The distribution of the temperature gradient for 20 nodes resulting from the open loop test is shown in Figure 5.8a, while the maximum spatial temperature gradients at critical nodes for open loop and closed loop tests are presented in Figure 5.8b.

Qualitatively, both tests demonstrated the same variations and locations of the maximum dT/dx, as simplified in Figure 5.8b. However, the values of maximum dT/dx resulting from the open loop test were slightly higher than in the closed loop. Before fuel composition was switched in the open loop operation, the highest temperature gradient of 11.7 K/cm occurred at node 5, 25% of the total fuel cell length, and gradually shifted to the next node towards the cell exit after initiation of the transient. After 5,500 s using humidified methane feed, the greatest dT/dx of 17 K/cm appeared at node 7, 35% of the way down from the inlet. This value exceeded the limit of dT/dx. Thus, adequate thermal management was required since there was high risk of thermal stress due to the excessive

dT/dx, which could also lead to high degradation rate impact. The maximum dT/dx was settled at node 13, 65% of the way down the length from the cell entrance, at approximately 1950 s after the transient where cathode air mass flow was 4% below its initial value (Figure 5.4b).

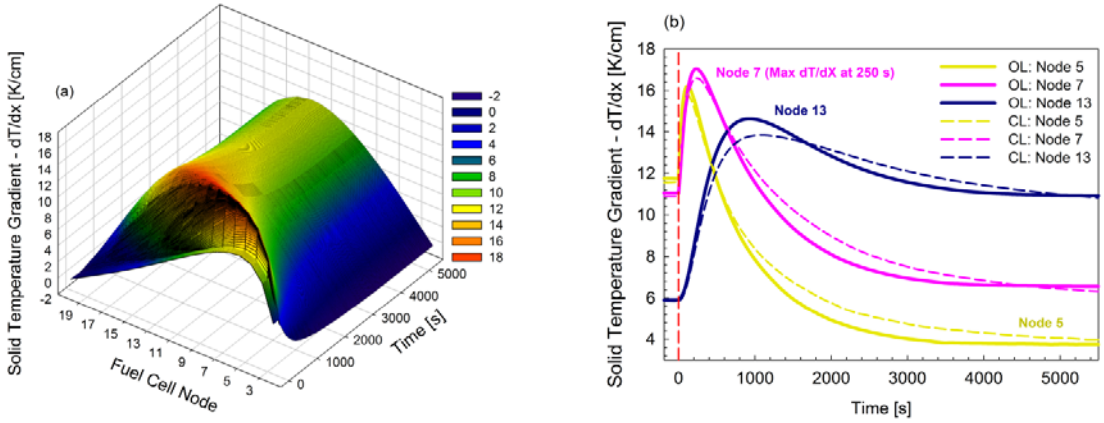

Figure 5.8: Spatial temperature gradient as a function of time, (a) open loop transient response (b) comparison of open loop and closed loop solid temperature gradients at critical nodes

As shown in Figure 5.9, the maximum discrepancy in the dT/dx between the open loop and closed loop at node 5 and node 7, were about 0.45 K/cm at 250 s, and 1 K/cm difference at node 13, at 650 s after the transient. As presented in Figure 5.9, the increasing difference in dT/dx, $(dT/dx_{OL} - dT/dx_{CL})$ was evident within the first 650 s (region I) and after 1,600 s (region III), which respectively collocated with increasing cathode air flow, before the crossover point, and decreasing cathode air mass flow after the crossover point.

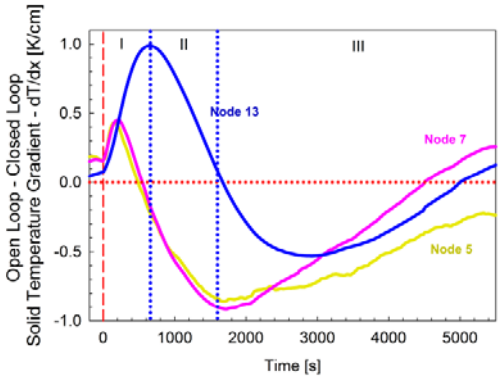

Figure 5.9: The difference in solid temperature gradient at critical nodes

Fuel Cell Cathode Gas Temperature

The dynamic transients of the fuel cell gas temperature are illustrated in Figure 5.10. To determine the significance of the open loop and closed loop dynamic response, profiles of

fuel cell gas temperature obtained from the open loop were also compared to those obtained from the closed loop, as presented in Figure 5.10b.

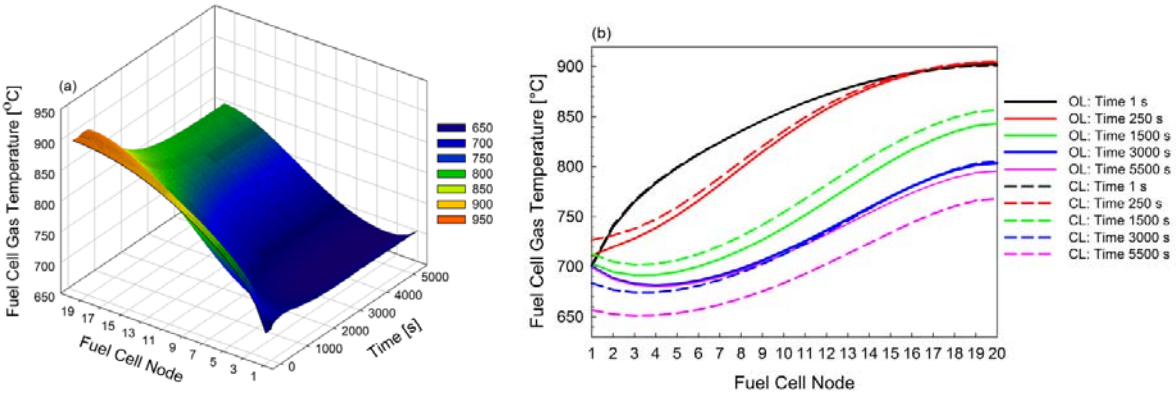

Figure 5.10: Fuel cell gas temperature as a function of time, (a) open loop transient response content (b) comparison of open loop and closed loop transients

As clearly shown in Figure 5.10b, there was significant variation in fuel cell gas temperature at the beginning of the cell between the open loop and closed loop profiles at 250 s. This transient was correlated to the combined effects of cathode air mass flow and cathode inlet air temperature. Although both tests demonstrated the initial transient rise in cathode inlet air temperature in response to fuel composition changes (Figure 5.7), the open loop case experienced 1% increase, while the closed loop case experienced 3% increase [12]. This discrepancy in temperature increase existed in spite of the higher turbine inlet temperature of the open loop operation because of the turbine efficiency improvement at the higher speeds exhibited in the open loop case [12, 24]. As a consequence of the impacts of lower cathode air mass flow with higher cathode inlet air temperature, gas temperature of the closed loop test at the cell entrance was higher than the open loop system at 250 s.

It was observed that at higher turbine speed (in open loop case), the increase in turbine exhaust temperature was not as significant as the increase in turbine inlet temperature, which resulted in lower turbine exhaust temperature, in comparison to the closed loop case. However, the investigation of the cause of this behaviour is subject of the future work that requires detailed characterization of turbomachinery dynamics.

The detailed fuel cell gas temperature difference at the selected nodes is illustrated in Figure 5.11, representing the cell entrance, centre, and cell exit. Over 5,500 s of test, the system exhibited significant variation in the magnitude of gas temperature difference across the fuel cell length, as a result of increasing cathode air mass flow at the beginning of the test, and decreasing cathode air mass flow toward the end of the test in the open loop case.

Similar to the dynamic performance of fuel cell solid temperature shown in Figure 5.6a, the long term trends of gas temperature started to twist after the crossover points. Due to the impacts of constant cathode air mass flow and decreased fuel cell solid temperature in a longer experimental run, gas temperature in the closed loop system reduced faster than in the open loop case. In contrast, as shown in Figure 5.10b, fuel cell gas temperature in the open loop test changed slowly as cathode air mass flow decreased, leading to insignificant temperature drop between 3,000 s and 5,500 s.

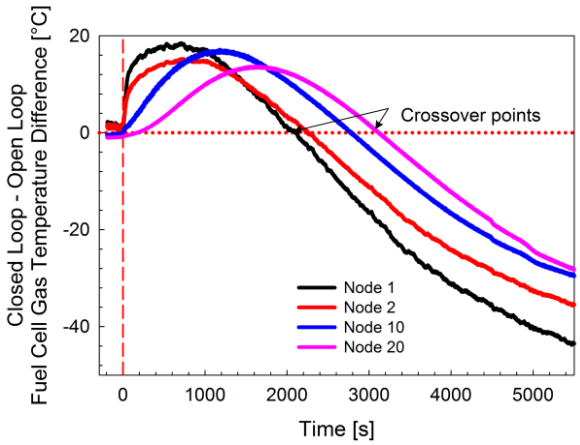

Figure 5.11: Crossover points in fuel cell gas temperature difference between the open loop and the closed loop for selected local fuel cell positions

Cathode Solid and Gas Temperature Difference and Heat Flux

Figure 5.12 shows the resulting temperature difference between fuel cell solid and gas temperature ($T_{solid} - T_{gas}$). The distributed profile of the temperature difference for the open loop test is presented in Figure 5.12a, and the comparison between the open loop and closed loop performance is presented in Figure 5.12b. As shown in Figures 5.12a and 5.12b, the temperature difference at most of the beginning nodes reduced drastically in the initial state of transients, and the fluctuations in temperature difference at the first 5 nodes were more significant as compared to the remaining fuel cell length. Figure 5.12b shows that the temperature difference at the cell inlet dramatically reduced from 76 °C to slightly lower than -20 °C over the course of experiment, whereas the temperature difference at the end of the cell was maintained fairly constant.

As can be seen in Figure 5.12b, within 250 s after the initiation of the fuel composition changes, the temperature difference in the open loop test was higher than in the closed loop. This difference was strongly driven by the influence of increased cathode air mass flow (Figure 5.4b) and lower cathode inlet air temperature (Figure 5.7) before the crossover points. Intuitively, the impacts of such transients on the gas temperature drop were more remarkable and direct than on the solid temperature drop, particularly at the beginning of the cell. As such, the gas temperature in the open loop reduced faster than the solid temperature, resulting in higher temperature difference. This consequently promoted higher heat flux from the solid to the gas that ultimately propagated the reduction in open-loop solid temperature. The profiles of heat flux in the fuel cell subsystem are presented in Figure 5.13, indicating a strong qualitative reflection of the fuel cell solid-gas temperature difference, following the correlation expressed in Eq. 4.

Fuel cell heat flux:

$$\dot{q} = \frac{k_g Nu}{D}\left(T_{solid} - T_{gas}\right) \qquad (4)$$

where $k_g$is the thermal conductivity of gas, Nu is the Nusselt number, D is the hydraulic diameter of the gas channel, T_{solid} is the solid temperature, and T_{gas} is the gas temperature.

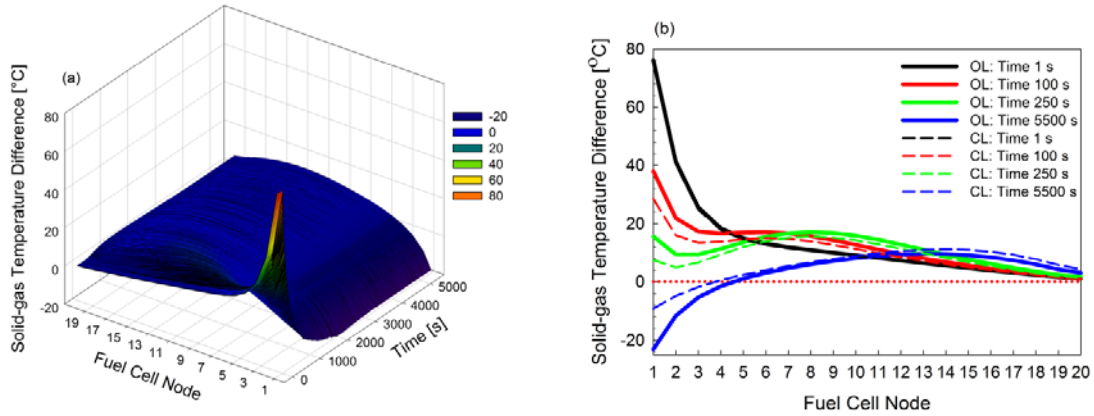

Figure 5.12: Fuel cell solid-gas temperature difference as a function of time, (a) open loop transient response, (b) comparison of open loop and closed loop transients

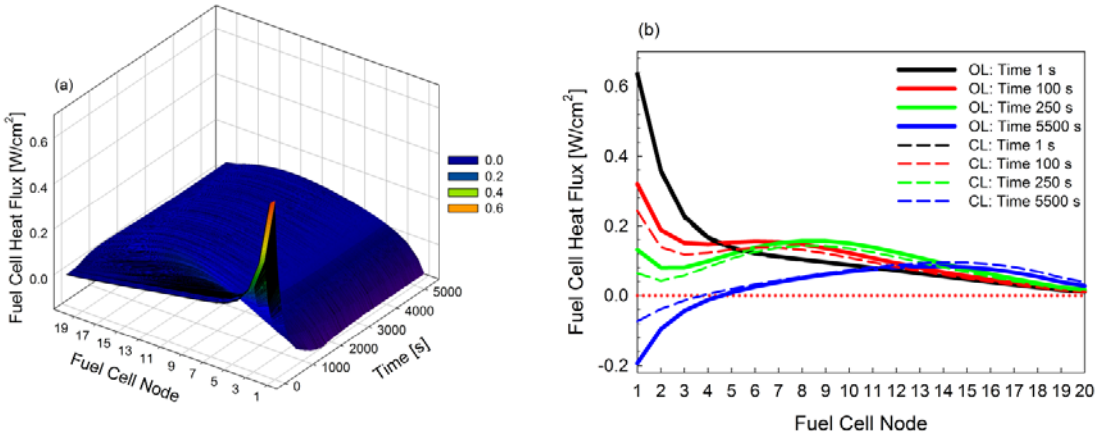

Figure 5.13: Heat flux of a fuel cell stack as a function of time, (a) open loop transient response, (b) comparison of open loop and closed loop transients

Similarly, due to the reversed trends of cathode air mass flow and cathode inlet air temperature after the crossover points, the dynamic transients of heat flux at 5,500 s contrasted the initial transient trends, featuring a more negative heat flux in the open loop test than in the closed loop test. As a result of decreasing cathode air mass flow and higher cathode inlet air temperature, the increase in the gas temperature resulting from the open loop test was faster than in the solid temperature, which subsequently reduced the solid-gas temperature difference. Based on the temperature difference profile at 5,500 s in Figure

5.12b, the gas temperature was higher than the solid temperature, such that the direction of heat flux in the long-term operation changed from the solid-to-air flow to air flow-to-solid. In short, the fuel cell began to be heated by the air flow in the system after 470 s. Despite the same initial performance at 1 s and the similar heating impacts at the beginning of the cell at 5,500 s, the heat flux of the closed loop case was much lower in magnitude than the open loop profiles throughout the test.

At 5,500 s, the beginning of the cell was heated by the airflow, while the remainder of the fuel cell was cooled by the airflow. This was a consequence of decreasing fuel cell solid temperature toward the end of the test and the methane reformation region shifting further down the fuel cell length.

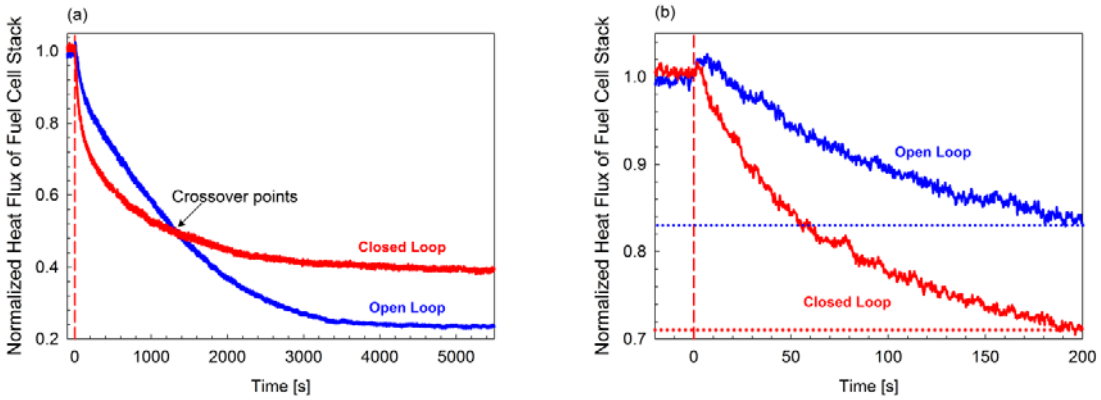

Figure 5.14: Normalized profiles of total heat flux in a fuel cell stack for open loop and closed loop, (a) over 5,500 s of test period, (b) over the first 200 s after fuel composition transition

The normalized profiles of the total heat flux in the fuel stack for both operation modes are shown in Figure 5.14, with the initial values of 62 kW and 61 kW respectively for the open loop and closed loop tests. As shown in Figure 5.14a, the crossover point in the heat flux was achieved approximately at 1,300 s after the step change, as the heat flux dropped to about 50% from their initial values. The crossover time for heat flux was the same as the time where the maximum difference in fuel cell solid temperature was observed, point B shown in Figure 5.6b. Owing to the consequent impacts of lower cathode inlet air temperature within the first 1,300 s, the total heat flux in the open loop case was higher than in the closed loop. These trends are clearly represented by the dynamic response over the first 200 s as shown in Figure 5.14b, indicating a 17% reduction in the open loop system and near to 30% reduction in the closed loop system. However, a 12% reduction in cathode air mass flow over 5,500 s of the open loop test ultimately resulted in an 80% decrease in the total heat flux. In contrast, with constant cathode air flow, the total heat flux for the closed loop only reduced by about 60% from the initial values.

Fuel Cell Heat Generation

The detailed response in heat generation (HG) on an area specific basis is shown in Figure 5.15. In this work, heat generation for an operating fuel cell was calculated using Eq. 5.

Fuel cell heat generation:

$$HG = HG_{cell} + HG_{SMR} + HG_{WGS} \quad (5)$$

The terms of HG_{cell}, HG_{SMR}, and HG_{WGS} respectively represent the by-product heat generation from the electrochemical oxidation polarizations, heat generation from steam methane reforming, and water-gas shift reactions.

As illustrated in Figure 5.15a, heat generation at the beginning of the cell reduced dramatically immediately after the step change in fuel composition, following by a slow increase toward the new steady state at 5,500 s. The heat generation profile obtained from the open loop was similar to the closed loop profiles, as shown in Figure 5.15b.

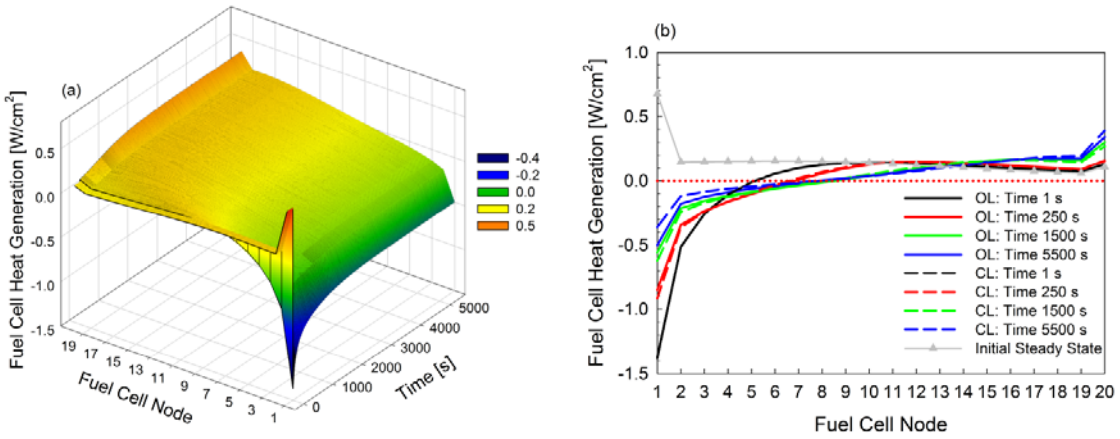

Figure 5.15: Fuel cell heat generation as a function of time, (a) open loop transient response (b) comparison of open loop and closed loop transients

From detailed analysis, it was shown that at the initial steady state, the magnitude of heat generation in Figure 5.15b matched the magnitude of heat flux shown in Figure 5.13b, resulting in fairly constant solid and gas temperature performance, respectively presented in Figures 5.6 and 5.9. However, as the fuel was switched to humidified methane, the most detrimental reduction in heat generation was indicated at the cell entrance, reducing from 0.7 W/cm^2 to about -1.4 W/cm^2. This demonstrates that the heat at the cell entrance was absorbed by the steam methane reforming reaction. As compared to the steady state profile of heat flux in Figure 5.13b, no significant fluctuation in heat flux was observed at 1 s after the step change due to delay in dynamic response of fuel cell temperatures.

As shown in Figure 5.15b, the heat generation at the cell entrance increased gradually as the test progressed. To be specific, the magnitude of heat generation at the beginning of the cell decreased with decreasing methane conversion as the fuel cell solid temperature decreased. Because of the insignificant difference in CH_4 mole fraction at 1 s

between the open loop and closed loop tests (Figure 5.16), the same profiles of heat generation density were obtained. However, the performance of heat generation at the beginning of the cell from both operations started to deviate slowly throughout the test, which reflected to the trends in CH_4 mole fraction and the corresponding fuel cell solid temperature.

At the centre of the cell length, heat generation decreased over time as more CH_4 mole fraction, as shown in Figure 5.16, shifted toward the elevated temperature region at the second half of the fuel cell length. In contrast, heat generation at the back of the cell gradually increased over the time studied, which was due more to electrochemical reactions. This behaviour was found to be consistent with the trends in current density.

Since the inlet temperature at the end of the test was higher in the open loop than in the closed loop, more methane reforming was facilitated, and thereby the heat generation in the open loop case was more strongly negative, as depicted by the profile at 5,500 s in Figure 5.15b. At 5,500 s the total average heat generation of the stack was 14.5 kW, which is comparable to the 14.7 kW of heat flux shown in Figure 5.14, indicating that a new steady state has been achieved.

5.6.3 Transient Analysis of Fuel Compositions

Methane, CH_4

The variations in methane mole fraction in 20 nodes resulting from the open loop operation are presented in Figure 5.16a. Methane was consumed in the system over the entire course of the experiment, reducing from the inlet composition at node 1 to near zero mole fractions at the cell outlet. These results are also compared to the closed loop as presented in Figure 5.16b.

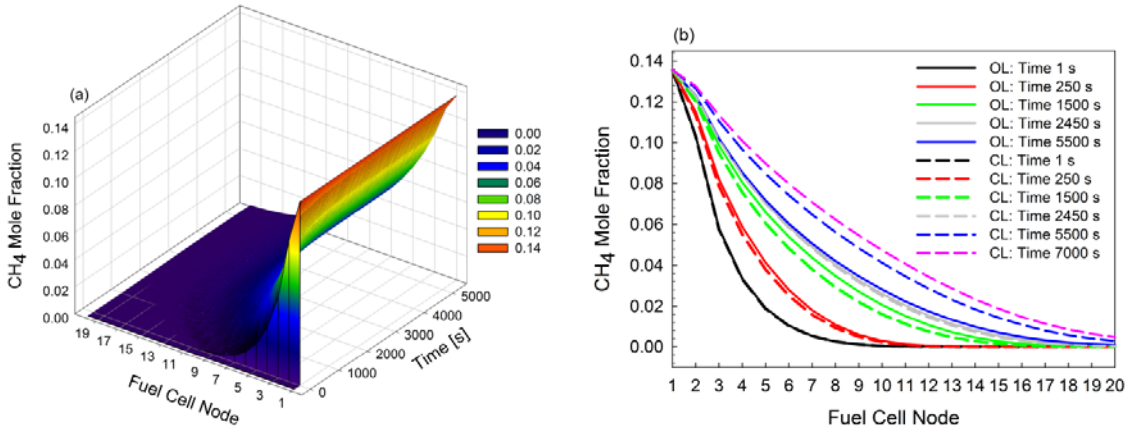

Figure 5.16: Methane mole fraction as a function of time, (a) open loop transient response (b) comparison of open loop and closed loop transients

Figure 5.16b describes the comparison of changes in CH_4 mole fraction associated with the corresponding fuel cell solid temperature fluctuations in both open loop and closed

loop operations. As shown in Figure 5.16b, within the first 2,450 s after the step change in fuel composition, CH_4 reduced more slowly in the operation with variable turbine speed, as compared to the operation with constant turbine speed. In the open loop case, lower CH_4 consumption was primarily driven by lower fuel cell solid temperature. Greater reduction in the open loop solid temperature resulted in the first transient period due to the effects of increased cathode air mass flow significantly decelerating the methane reforming, and thereby reducing the CH_4 consumption. In contrast, faster conversion of methane in the closed loop test was promoted by its higher operating temperature, as shown in Figure 5.6.

However, the opposite trends resulted in the following period, after 2,450 s toward the end of the test, in which a more rapid CH_4 conversion was demonstrated in the open loop case, since the open loop solid temperature was much higher than the closed loop solid temperature. For a long-term period of test, the reduction in cathode air mass flow in the open loop system subsequently induced the more rapid depletion of CH_4 in the fuel cell subsystem. It was found that the crossover points for CH_4 mole fraction were very close to those obtained for fuel cell solid temperature. However, unlike temperature, only insignificant changes in the methane mole fraction profile were observed after the crossover point. As shown in Figure 5.16b, the open loop dynamics obtained at 2,450 s followed the closed loop dynamics very closely, with a very small variation at the end, due to delay in the solid temperature crossover in the second half of the cell length presented in Figure 5.6b.

Both operations demonstrated reduction in methane consumption over time studied, featuring a more distributed profile of CH_4 mole fraction toward the end of the test. This closely followed the decrease in solid temperature, implying the temperature influence on the endothermic steam methane reforming kinetics. This consequently shifted methane toward the cell exit, which in turn caused significant solid temperature decrease in the second half of the fuel cell length, as shown in Figure 5.6a, which highlighted the highly coupled nature of the dynamic.

Other Fuel Composition Gradients and Fuel Utilization

The corresponding effects on other fuel constituents, such as CO, CO_2, H_2, and H_2O are respectively presented in Figure 5.17 through Figure 5.20. Accordingly, the changes observed in CO, CO_2, H_2, and H_2O mole fractions were primarily driven by the dynamic responses of fuel cell solid temperature and the presence of CH_4 in the fuel cell subsystem. The slower and consequently rate limiting CH_4 reforming reaction primarily influenced the formation and consumption of the other fuel components participating in water-gas shift and electrochemical oxidation.

Since the fuel fed to system was switched to humidified methane, the increase in CO mole fraction at the first half of the cell length shown in Figure 5.17 was strongly reflected by the decrease in CH_4 mole fraction (Figure 5.16). In contrast, the decrease in CO at the downstream region was greatly promoted by a complete conversion of CH_4 as well as a transition in the water-gas shift reaction toward the product side. However, higher formation of H_2O was still observed at the end of the cell due to significant electrochemical reaction that was reflected by consumption of H_2. The relative differences in the open loop tests as compared to the closed loop tests were seen to be more significant for CO than CH_4 in Figure 5.17. At 5,500 s, the maximum CO mole fraction in the open loop test was 0.022 at

node 15. Whereas for the closed loop case, the maximum value in CO mole fraction was 0.018 at node 16, a 22% relative difference in the value. This was attributed to the higher temperature at the end of the cell in the open loop case which would favour reforming and inhibit water gas shift as written in Eq. 2, both of which result in higher CO partial pressures.

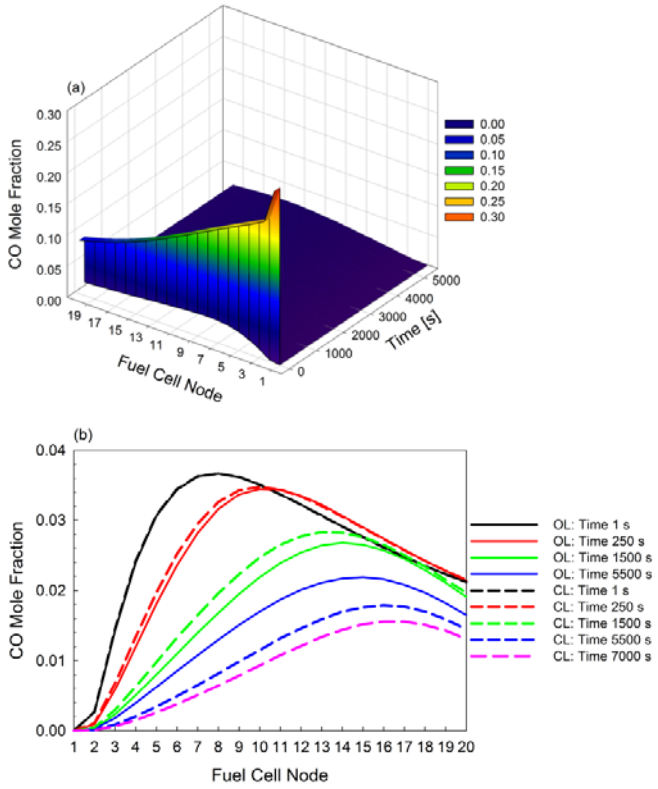

Figure 5.17: Carbon monoxide mole fraction as a function of time, (a) open loop transient response (b) comparison of open loop and closed loop transients

As shown in Figure 5.18, a significant increase in CO_2 was also observed in the beginning of the cell, resulting from the acceleration of steam methane reforming kinetics and water-gas shift equilibrium. The trends in the open loop and closed loop performance were qualitatively similar until the crossover point in temperature. As methane was completely consumed at the end of the cell, the CO_2 mole fraction kept increasing but gradually since the rate of CO_2 formation reduced with the depletion in CO. As with the methane mole fraction, the CO_2 mole fraction approached a linear distribution toward the end of the cell as a new steady state was achieved in the closed loop and remained closer to the initial (1 s) non-linear profile in the open loop.

The changes in localized H_2 mole fraction during the test are shown in Figure 5.19, featuring increasing H_2 mole fraction at the first half of the fuel cell length before a gradual reduction in the remaining fuel cell length. Similarly, the increase in H_2 was also highly correlated to the presence of CH_4 and the kinetics of steam methane reforming. Because of higher temperature at the initial steady state shown in Figure 5.6, the system was more

dominated by endothermic methane reforming rather than water-gas shifting. Therefore, the H_2 mole fraction increased with decreasing methane content at the beginning of the cell but reduced afterwards as it was electrochemically oxidized toward the end of the cell.

Although at 1 s, the current density (shown in Figure 5.22) was increasing to a maximum around node 6, the H_2 mole fraction was also at the maximum (Figure 5.19), indicating that the formation of H_2 from steam methane reforming was significantly higher than its consumption in the electrochemical oxidation. The high CO content was due to a combination of CO produced by the steam methane reforming reaction and the CO produced by the water gas shift reaction in reverse (Eq. 2). The reverse water gas reaction took place due to the large amount of hydrogen produced by the reforming reaction. Even though the current density was also at its highest point near node 6, the fuel utilization was at a local minimum near node 6, as shown in Figure 5.21 for the 1 s curve. This clearly illustrated that large amounts of thermal energy in the fuel cell was being converted to chemical energy in this region. Hence, this caused more reduction in solid temperature at the beginning of the cell. As there was less energy in the cell, represented by lower temperature and thereby lower sensible heat, methane became more distributed and the H_2 partial pressure reduced.

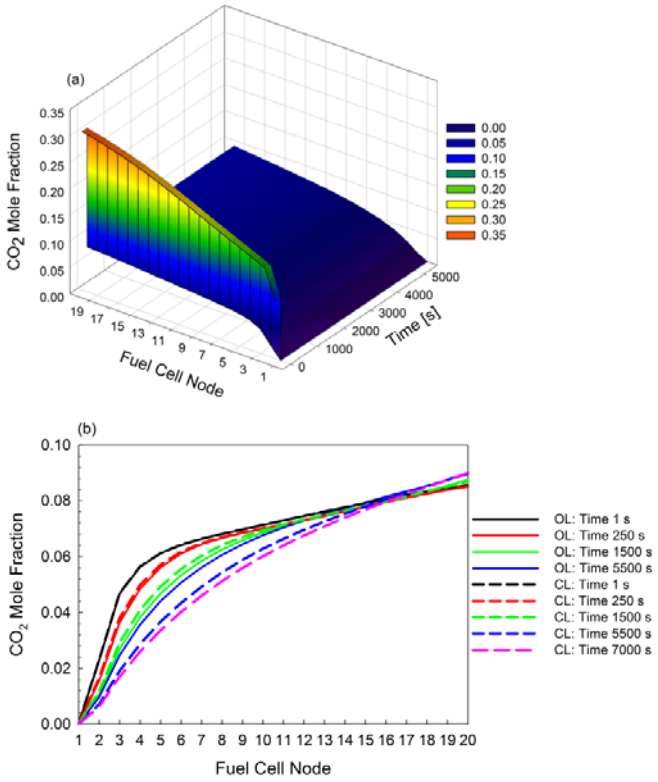

Figure 5.18: Carbon dioxide mole fraction as a function of time, (a) open loop transient response (b) comparison of open loop and closed loop transients

As the test progressed, the decrease in H_2 in the open loop case was more apparent than in the closed loop, following the faster solid temperature reduction and decreasing rate of methane consumption before the crossover point. As expected, the transients of CO mole

fraction closely followed the reduction in H_2 content. Due to the higher solid temperature in the open loop system at 5500 s, H_2 mole fraction did not reduce as much as in the closed loop. Following the increase in current density (Figure 5.22) and the decrease in H_2 content toward the end of the cell at 5500 s, the system accordingly exhibited higher fuel utilization at the end of the cell (Figure 5.21).

As a result of consuming H_2O in both methane reforming and water gas shift and producing H_2O in electrochemical oxidation of H_2, the resulting dynamic transient of H_2O shown in Figure 5.20 was a mirror image of H_2 content. Initially, H_2O significantly reduced in the upstream region of the fuel cell length as methane reforming was facilitated at higher temperature. However, the rate of H_2O depletion decreased with decreasing methane content over the course of the experiment. With higher temperature in the open loop at 5500 s, the reduction of H_2O was faster than in the closed loop.

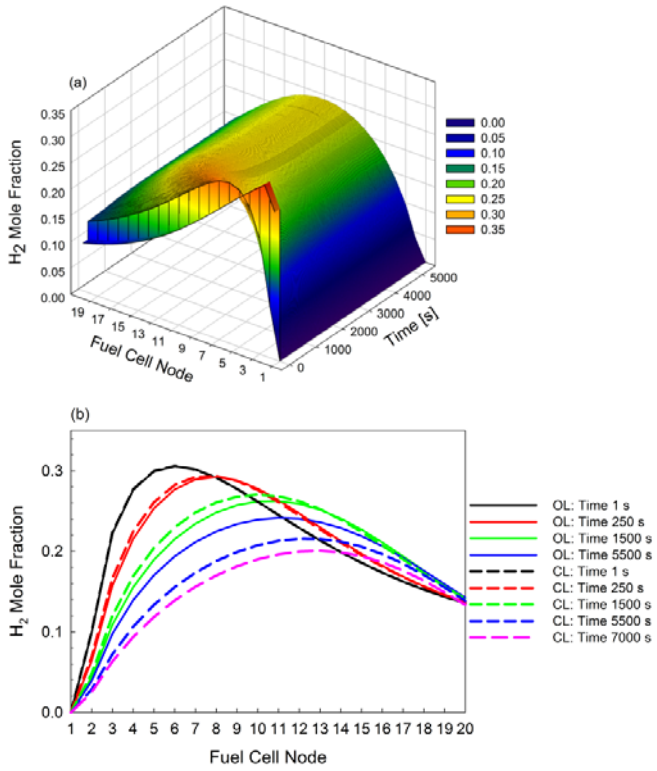

Figure 5.19: Hydrogen mole fraction as a function of time, (a) open loop transient response (b) comparison of open loop and closed loop transients

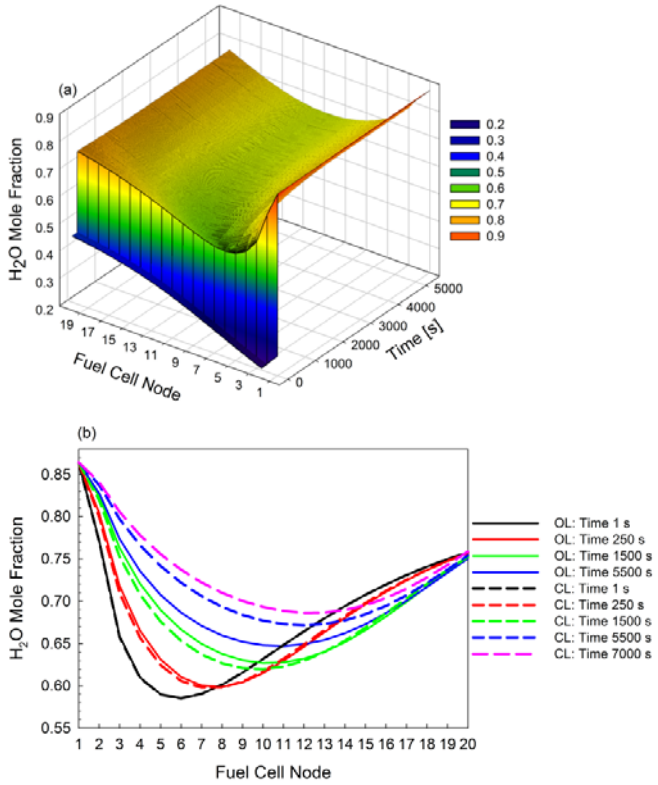

Figure 5.20: Water mole fraction as a function of time, (a) open loop transient response (b) comparison of open loop and closed loop transients

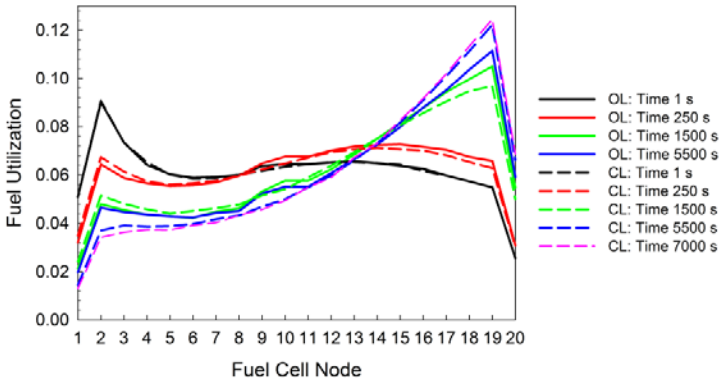

Figure 5.21: Fuel utilization in open loop and closed loop cases

5.6.4 Current density

The corresponding changes in current density profiles are presented in Figure 5.22. As clearly shown in Figure 5.22a, as the fuel composition was switched, the concentrated current density region significantly shifted from the beginning of the cell to the end of the cell. The longer the test, the closer the maximum current density moved to the cell outlet. For the open loop operation, the local maximum level of current density slowly increased from 0.74 to 0.8 over 5,500 s, distributing from node 8 to node 17. It was observed that the maximum current density at 1500 s and 5500 s were identical, and the curves were close together, having come to equilibrium much faster than in the closed loop case. While, for the closed loop case, the trends were similar to the open loop case except for the trend at 5500 s which showed an 8% higher current density.

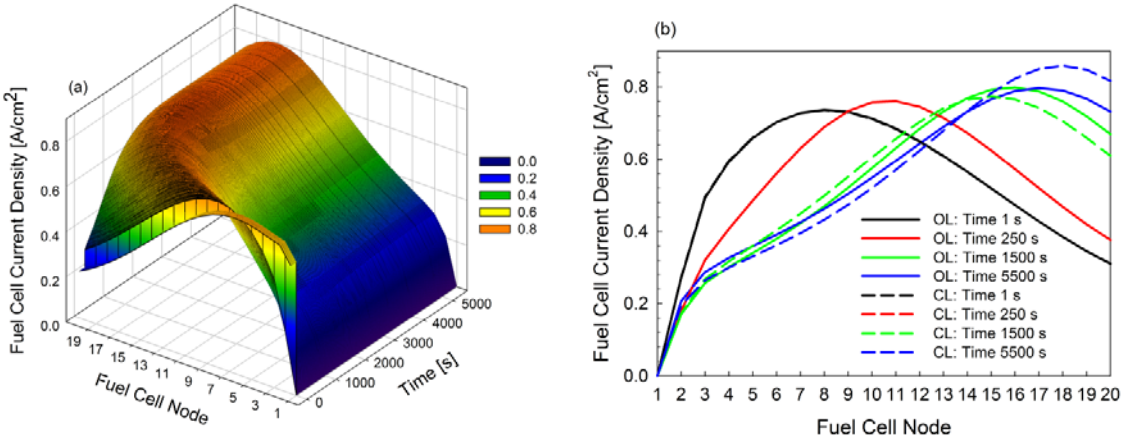

Figure 5.22: Fuel cell current density as a function of time (a) open loop transient response (b) comparison of open loop and closed loop transients

Immediately after the fuel composition change, the current density was highest in node 8 with high H_2 partial pressure, low H_2O partial pressure, and higher solid temperature, all of which promoted the electrochemical oxidation of hydrogen and contributed to higher localized current density. However, in the open loop case, the solid temperature at the inlet dropped by 52 K in just 250 s. The corresponding conductivity likewise reduced, reforming slowed, the hydrogen mole fraction local maximum shifted further down the cell, as did the water local minimum, and the maximum current density shifted from node 8 to node 11. Since there was only slight differences in the dynamic transients of fuel cell solid temperature and fuel constituents within the first 250 s after the fuel composition change, the profiles of current density for the open loop test was the same as observed in the closed loop.

In the open loop case, temperature changes after the crossover point were not as significant as in the closed loop case. Therefore, not much change in local current density profiles was seen between 1500 s and 5500 s. In the closed loop, the solid temperature continued to drop until the end of the test, and more substantial changes in current density profiles were observed.

5.6.5 Transient Analysis of Fuel Cell Thermal Energy Storage and Fuel Cell Thermal Effluent

The profiles of the dissipation of fuel cell stored thermal energy and the corresponding fuel cell thermal effluent in response to the transition in fuel composition changes are presented in Figure 5.23. The initial transient decrease in the fuel cell stored thermal energy shown in Figure 5.23a was attributed to the acceleration of steam methane reforming. The associated dynamics of thermal energy conversion to chemical energy were clearly illustrated in the increasing H_2 generation at 1 s (Figure 5.19), resulting in lower fuel utilization (Figure 21) within increased current density region (Figure 5.22). Such transients finally caused a dramatic increase in fuel cell thermal effluent exiting the system, as indicated in Figure 5.23b. The rapid reduction in stored thermal energy subsequently caused dramatic reduction in solid temperature.

As indicated in Figure 5.23a, the recovery in the dissipation of stored thermal energy for the open loop case, before the crossover point at around 1300 s was slower than in the closed loop, indicating higher magnitude. But, as opposed to this profile, the magnitude of the dissipation term remained lower after crossover. It is clearly shown in Figure 5.23 that the new steady state achieved in the open loop far quicker than in the closed loop. The results suggested that the difference in the fuel cell thermal effluent shown in Figure 5.23b was attributed primarily to the difference in dissipation of stored thermal energy. The dynamic fuel cell thermal effluent remained higher than the initial value for about 1600 s before decreasing to the new steady state, following non-minimum phase behaviour (inverse transient response) as opposed to its steady state response [21]. This ultimately affected the response of turbine speed and cathode air mass flow, as presented in Figure 5.4. For future dynamic control development, it was expected that a simpler control model such as first-order-plus-dead-time (FOPDT) model or second-order-plus-dead-time (SOPDT) model would not be sufficient to describe the entire trajectories of fuel cell thermal effluent.

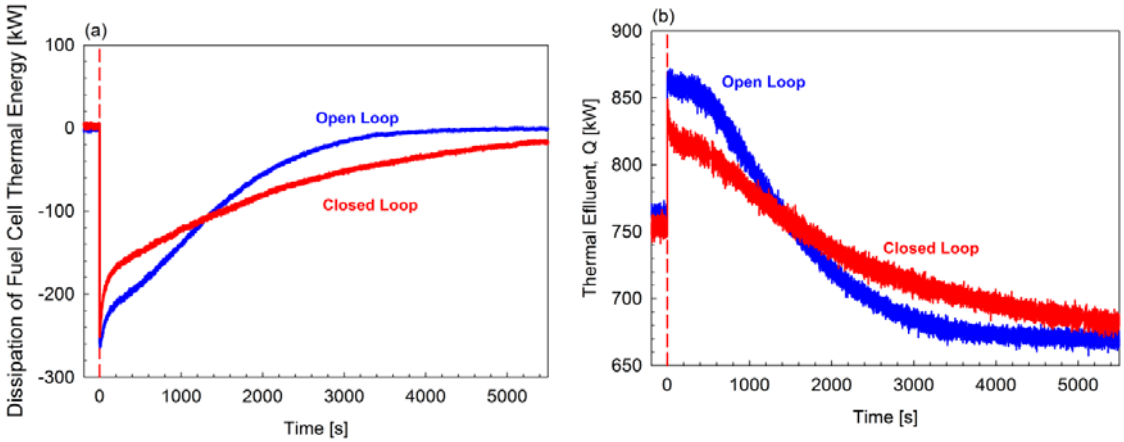

Figure 5.23: Dissipation of fuel cell thermal energy storage and fuel cell thermal effluent and for the open loop and the closed loop tests

5.7 Conclusions

The detailed characterization of the impacts on the SOFC/GT dynamic performance revealed that a transition from syngas composition to humidified methane composition caused:

a. enhanced conversion of fuel cell stored thermal energy into chemical energy immediately after the step change that ultimately caused a sudden transient inverse response in fuel cell thermal effluent
b. substantial reduction in fuel cell solid temperature 250 s after the step change due to propagation impacts of increased cathode air mass flow
c. detrimental spatial temperature gradient of 17 K/cm 250 s after the transient
d. significant variations in the dynamic transients of the cell inlet and the cell outlet
e. different impacts on cathode air mass flow during the short-term operation immediately after the fuel composition changes and during the long-term period, 1600 s after the step change.

Without turbine speed control, the open loop operation demonstrated significant variations in turbine speed and cathode mass flow in turbine speed. As much as 6% turbine speed variation from nominal condition was observed, resulting in a 12% variation in cathode mass flow, which ultimately helped the system to achieve a new steady state faster than the closed loop system. Changes in cathode air mass flow and/or turbine speed affected solid and gas temperature, which highly influenced temperature gradient across the fuel cell length, and the corresponding heat flux. Significant delay between solid temperature and the response of turbine response/cathode air mass flow was observed, indicated by 14 minute difference in the crossover time.

It was not intuitively obvious that small changes in turbine efficiency in the open loop over the closed loop tests affected fuel cell parameters such as heat flux through variations in cathode air inlet temperature. Detailed analyses on fuel composition gradients, fuel utilization, and current density revealed that the open loop system resulted in less detrimental impact after the crossover points, with higher temperature, lower current density, and lower fuel utilization than in the closed loop. Overall, it was analyzed that all key fuel cell parameters were highly coupled and solid temperature appeared to be the primary linking event of many mechanisms.

From the control perspective, controlling fuel cell solid temperature is critical; otherwise excessive temperature gradients could occur at any point along the fuel cell length. Depending on the initial composition of methane used, severe cooling effects might be localized at the beginning of the cell, which could not be tolerated by the fuel cell material. Even if no catastrophic cell failure occurred, intuitively, shorter cell lifetime would be expected due to increasing degradation risk since the system was operated at a lower temperature. Therefore, future dynamic control of SOFC/GT hybrid system must include effective thermal management, most likely implementing through cathode air flow management. Future work will make use of the result presented herein, emphasizing on the quantitative assessment of the dynamic impacts via development of transfer functions for dynamic control. However, the results show that the transfer functions are too complex to adequately explain with a first-order-plus-dead-time model, since some parameters

exhibited non-minimum phase behaviour (inverse transient response) , which is the subject of future work.

5.8 References

[1] Yi, Y., Rao, A. D., Brouwer, J., and Samuelsen, G. S., 2005, “Fuel Flexibility Study of an Integrated 25kW SOFC Reformer System,” J. Power Sources, 144(1), pp. 67–76.

[2] Mueller, F., Gaynor, R., Auld, A. E., Brouwer, J., Jabbari, F., and Samuelsen, G. S., 2008, "Synergistic Integration of a Gas Turbine and Solid Oxide Fuel Cell for Improved Transient Capability," J. Power Sources, 176(1), pp. 229-239.

[3] Yang, J. S., Sohn, J. L., and Ro, S. T., 2007, “Performance Characteristics of a Solid Oxide Fuel Cell/Gas Turbine Hybrid System with Various Part-Load Control Modes,” J. Power Sources, 166(1), pp. 155-164.

[4] Winkler, W., Nehter, P., Williams, M. C., Tucker, D., and Gemmen, R., 2006, "General Fuel Cell Hybrid Synergies and Hybrid System Testing Status," J. Power Sources, 159(1), pp. 656-666.

[5] Lim, T. H., Song, R. H., Shin, D. R., Yang, J. I., Jung, H., Vinke, I. C., and Yang, S. S., 2008, “Operating Characteristics of a 5kW Class Anode-Supported Planar SOFC Stack for a Fuel Cell/Gas Turbine Hybrid System,” Int. J. Hydrogen Energy, 33(3), pp. 1076-1083.

[6] Traverso, A., Magistri, L., and Massardo, A. F., 2010, "Turbomachinery for the Air Management and Energy Recovery in Fuel Cell Gas Turbine Hybrid Systems," Energy, 35(2), pp. 764-777.

[7] Pezzini, P., Tucker, D., and Traverso, A., 2013, "Avoiding Compressor Surge during Emergency Shut-down Hybrid Turbine Systems," ASME J. Gas Turbines Power, 135(10), pp. 102602-102602-10.

[8] Mueller, F., Jabbari, F., and Brouwer, J., 2009, "On the Intrinsic Transient Capability and Limitations of Solid Oxide Fuel Cell Systems," J. Power Sources, 187(2), pp. 452-460.

[9] Zhou N, Yang C, Tucker D, Pezzini P, Traverso A., 2015, “Transfer Function Development for Control of Cathode Airflow Transients in Fuel Cell Gas Turbine Hybrid Systems,” Int. J. Hydrogen Energy, 40(4), pp. 1967-1679.

[10] Wächter, C., and Joos, F., 2009, “Steady State Off-Design and Transient Behaviour of a Solid Oxide Fuel Cell/Gas Turbine Hybrid Power Plant with Additional Firing of the Gas Turbine Combustor,” ASME J. Eng Gas Turbines Power, 131(3), pp. 031701-031701-9.

[11] Harun N.F., Tucker, D., Adams, T.A. II, 2015, “Impact of Fuel Composition Transients on SOFC Performance in Gas Turbine Hybrid Systems,” Submitted to Applied Energy. In Review.

[12] Harun N.F., Tucker D., Adams, T.A. II, 2015, “Open Loop and Closed Loop Performance of Solid Oxide Fuel Cell Gas Turbine Hybrid Systems during Fuel Composition Changes,” ASME Paper No. GT2015-43609.

[13] Tucker, D., Liese, E., VanOsdol, J. G., Lawson, L. O., and Gemmen, R. S., 2002, "Fuel Cell Gas Turbine Hybrid Simulation Facility Design,” ASME Paper No. IMECE2002-33207.

[14] Hughes, D., Wepfer, W. J., Davies, K., Ford, J. C., Haynes, C., and Tucker, D., 2011, "A Real-time Spatial SOFC Model for Hardware-based Simulation of Hybrid Systems," ASME Paper No. FuelCell2011-54591.
[15] Tucker, D., Lawson, L., Gemmen, R., and Dennis, R., 2005, "Evaluation of Hybrid Fuel Cell Turbine System Startup with Compressor Bleed," ASME Paper No. GT2005-68784.
[16] Tucker, D., Liese, E., and Gemmen, R., 2009, "Determination of the Operating Envelope for a Direct Fired Fuel Cell Turbine Hybrid using Hardware Based Simulation," Proceedings of the International Colloquium on Environmentally Preferred Advanced Power Generation (ICEPAG 2009), Newport Beach, CA, Feb. 10-12, ICEPAG Paper No. ICEPAG2009-1021.
[17] Tucker, D., Pezzini, P., and Banta, L., 2013, "Equivalence Ratio Startup Control of a Fuel Cell Turbine Hybrid System," ASME Paper No. GT2013-94809.
[18] Pezzini, P., Traverso, A., Banta, L., and Tucker, D., 2014, "Decentralized Control Strategy for Fuel Cell Turbine Hybrid Systems," Proceedings of the 57th Annual ISA Power Industry Division Symposium, Scottsdale, Arizona, June 1-6, Paper No. ISA-PWID2014-52.
[19] EG&G Technical Services, Inc., 2004, *Fuel Cell Handbook*, U.S. Department of Energy, Office of Fossil Energy, National Energy Technology Laboratory, Morgantown, West Virginia.
[20] Tucker, D., Hughes, D., and Haynes, C., 2011, "IGFC Response to Initial Fuel Cell Load for Various Syngas Compositions," ASME Paper No. ESFuelCell2011-54450.
[21] Harun, N.F., Tucker, D., and Adams, T.A. II, 2014, "Fuel Composition Transients in Fuel Cell Turbine Hybrid for Polygeneration Applications," ASME J. Fuel Cell Sci. Technol., 11(6), pp. 061001-061001-8.
[22] Adams, T. A. II, Nease, J., Tucker, D., and Barton, P. I., 2013, "Energy Conversion with Solid Oxide Fuel Cell Systems: A Review of Concepts and Outlooks for the Short- and Long-Term," Ind. Eng. Chem. Res., 52(9), pp. 3089–3111.
[23] Hughes, D.O., 2011, "A Hardware-based Transient Characterization of Electrochemical Start-Up in an SOFC/Gas Turbine Hybrid Environment using a 1-D Real Time SOFC Model," Atlanta, Georgia: Georgia Institute of Technology.
[24] Pezzini P., Celestin S., and Tucker D., 2015, "Control Impacts of Cold-air Bypass on Pressurized Fuel Cell Turbine Hybrids," ASME J. Fuel Cell Sci. Technol., 12(1), pp. 011006-011006-8.

6 DEGRADATION ANALYSIS OF SOFC FOR VARIOUS SYNGAS COMPOSITIONS IN IGFC SYSTEMS

"Reproduced from "Harun, N.F., Zaccaria, V., Tucker, D., Traverso, A., and Adams, T. A. II, 2015, "Degradation Analysis of SOFC for Various Syngas Compositions in IGFC Systems," *Submitted to International Gas Turbine Congress 2015, Tokyo, Japan*. In review.

6.1 Publication Highlights

This section presents the impacts of fuel composition on fuel cell degradation rate, which is based on various coal-derived syngas resulting from different gasifier technologies. All of the syngas compositions used in this study contains different level of methane content. The degradation rate is evaluated using an empirical expression, indicating a correlation to three key fuel cell operating parameters; current density, fuel utilization, and cell temperature. The performance of fuel cell for each fuel composition is explained and compared to the case of humidified hydrogen to determine their influence on the degradation rate.

Dr. David Tucker helped with identifying the experimental design, and the editing of manuscript. Valentina Zaccaria assisted with data analysis and interpretation, as well as the preparation of the manuscript. The empirical expression of fuel cell degradation rate presented in this section was previously developed at NETL. Both Dr. Thomas A. Adams II and Dr. Alberto Traverso contributed their constructive comments in the preparation of the manuscript.

Degradation Analysis of SOFC for Various Syngas Compositions in IGFC Systems

Authors: Nor Farida Harun[a], Valentina Zaccaria[b], David Tucker[b], Alberto Traverso[c], and Thomas A. Adams II[a]

[a]Department of Chemical Engineering, McMaster University, 1280 Main Street West, Hamilton, Ontario L8S 4L7, Canada

[b]U.S. Department of Energy, National Energy Technology Laboratory, 3610 Collins Ferry Road, Morgantown, West Virginia 26507-0880, United States

[c]DIME (TPG), University of Genoa, Via Montallegro 1, 16145 Genoa, Italy

6.2 Abstract

One of the issues of the greatest concern in integrated gasification (IGFC) systems is the high risk of composition changes in coal-derived syngas, which is strongly influenced by coal qualities and/or gasifier technologies.

The main goal of this work was to assess the impacts of syngas compositions resulting from different gasifier technologies on the fuel cell degradation rate. The solid oxide fuel cell (SOFC) response to various syngas compositions was investigated using a one-dimensional (1D) distributed fuel cell model that incorporates an empirical expression of localized SOFC degradation as a function of fuel cell solid temperature, current density, and fuel utilization. The process performance using four different syngas compositions was also compared to a humidified hydrogen operation as a baseline.

The results showed a correlation of degradation most significantly with the methane content of the fuels selected. At constant stack power production and constant global fuel utilization, the results demonstrated that increasing the methane content in coal-derived syngas shifted the peak of degradation rate from the inlet toward the center of the cell. Overall, the highest localized degradation rate with respect to voltage in all five cases was observed at 3.65%/1000 hr. The lowest overall rate of 1.89%/1000 hr was indicated in the case for humidified hydrogen. Increasing methane content to 17% in syngas increased the overall degradation rate to 3.05%/1000 hr.

6.3 Introduction

Due to high potential for efficient coal utilization and power production at minimized environmental impacts, integrated gasification fuel cell (IGFC) systems combining coal-gasification process and solid oxide fuel cells (SOFCs) hold great promise to be used as the coal-based power plant of choice in the near future. The techno-economic performance of IGFC has been widely investigated, addressing the technical challenges as well as the feasibility of different system configurations, with or without carbon capture [1-6]. The high flexibility of solid oxide fuel cells to operate with different fuel compositions, together with their increased efficiency and reduced emissions, provide some advantages for system flexibility, such that the energy resources and the products can be varied in order to maximize the plant profit [7].

Most IGFC studies were conducted based on commercially available gasifiers, such as GE Energy gasifiers (formerly known as Chevron-Texaco), Lurgi, Prenflo, ChonocoPhillips E-gas, and Shell Coal Gasification Process gasifiers [4, 7, 8]. Different combinations of coal type and gasifier technology can result in different syngas compositions. In general, coal-derived syngas consists of 30% to 60% carbon monoxide (CO), 25% to 30% hydrogen (H_2), 0% to 5% methane (CH_4), 5% to 15% carbon dioxide (CO_2), with variable water vapor, sulphur constituents and contaminants [9].

The variability in sulphur and other contaminants which can occur during normal operations primarily drives the need for gas clean-up in IGFC plants for the removal of poisonous gases and impurities, and the need for the fabrication of fuel cells suited for fuel flexible environment [4]. It has been shown that degradation in fuel cells can be accelerated by the presence of impurities and carbon deposition [10, 11, 12]. In addition, fuel composition affects cell degradation in different ways. As such, different degradation mechanisms were proved to depend strongly on operating conditions, such as distributions of temperature gradients, current density, as well as fuel utilization [13-15]. It has been investigated that even without contaminants, the performance of those fuel cell parameters significantly changes with the amount of methane and hydrogen in syngas [16-21].

In order to take advantage of the improved environ-mental and economic benefits of IGFC technologies, the degradation impacts of fuel cell systems due to changes in fuel compositions must be quantified. Such information is important to further determine the direction of system design requirements for IGFC that could accommodate the potential operational constraints and extend the fuel cell life time.

Therefore, in this work, the risk of degradation in fuel cell systems dealing with different syngas compositions relevant to established gasifier technologies was evaluated. In addition to the assessment of overall degradation rate, the distributed performance of fuel cells simulated by a one dimensional (1D) model of a co-flow, anode-supported SOFC were also characterized in detail to quantify the potential localized degradation. This model was previously developed at the U.S. Department of Energy, National Energy Technology Laboratory (NETL) for cyber-physical simulations [22].

For comparison purposes, the same power output and global fuel utilization were maintained for all cases studied, and a system operated with humidified hydrogen was used as a base problem. The degradation rate was considered depending on three key fuel cell parameters: temperature, current density, and fuel utilization. It was assumed that different degradation mechanisms are all aggravated by high current density and fuel utilization and low operating temperature [13-15].

6.4 SOFC Model

A 1D real time dynamic fuel cell model was used to simulate the performance of a planar solid oxide fuel cell on a distributed basis in the direction of fuel and air flows [19]. Each cell was discretized in twenty volumes (or nodes) with a length of 1 cm each. A combination of finite difference and finite volume discretization techniques were used to quantitatively evaluate fuel cell thermal and electrochemical performance in terms of solid and gas temperature profiles on the cathode side, axial heat generation within the cell,

current density, Nernst potential, electrochemical losses, and fuel composition gradients [22].

In this study, the model was used for steady state simulation, in which steady state input for cathode and anode feed stream (air/fuel mass flow, temperature, and pressure) were specified by the user. On the other hand, real-time dynamic input could be supplied to the model for dynamic studies. Previous studies have shown that this model was capable to capture the fuel cell performance during electrochemical light off [19, 23], load transient [22], cathode air mass flow variations [24], and fuel composition changes [25].

In this model, SOFC geometries and operating conditions such as total number of fuel cells in a stack and fuel cell load were also user-specified parameters. For this work, the fuel cell stack was comprised of 2,500 cells.

Cell operating voltage was calculated according to Nernst potential, as explained by Eq. 1, from which polarization losses were subtracted shown in Eq. 2. The polarization losses for diffusion, activation and ohmic losses were respectively described through Equations 3 to 5.

$$V_{NERNST} = -\frac{\Delta G^0_{H_2O}}{nF} + \frac{R_u T}{nF} \ln\left(\frac{p_{H_2}\sqrt{p_{O_2}}}{p_{H_2O}}\right) \quad (1)$$

$$V_{cell} = V_{NERNST} - \eta_{dif} - \eta_{act} - \eta_{ohm} \quad (2)$$

$$\eta_{dif} = \frac{R_u T}{2F}\left(\ln\left(\frac{x_{H_2,bulk} \cdot x_{H_2O,TBP}}{x_{H_2O,bulk} \cdot x_{H_2,TBP}}\right) + \frac{1}{2}\ln\left(\frac{x_{O_2,bulk}}{x_{O_2,TBP}}\right)\right) \quad (3)$$

$$\eta_{act} = \frac{R_u T}{\alpha nF} \sinh^{-1}\left(\frac{i}{2i_0}\right) \quad (4)$$

$$\eta_{ohm} = R \cdot i \quad (5)$$

The model accounts for both water-gas shift and direct internal reformation reactions. Water-gas shift reactions are considered to occur at the equilibrium at the selected range of operating temperature and the equilibrium constant is calculated with the empirical expression presented in Eq. 6.

$$K_{p,shift} = \frac{p_{H_2} p_{CO_2}}{p_{H_2O} p_{CO}} \quad (6)$$

First order reaction kinetics with respect to partial pressure of methane was assumed for the internal reforming. The expression for the rate of consumed methane is presented in Eq. 7.

$$r_{sr} = 4328.61 \cdot p_{CH_4} \exp\left(-\frac{82000}{R_u T}\right) \cdot A_{react} \quad (7)$$

Localized fuel utilization was calculated from H_2, CO and CH_4 consumptions in each node, according to Eq. 8, , where *j* represents the current node, while *j+1* represents exit of the current node (i.e. the next node).

$$U_F(j) = \frac{x_{H_2}(j+1)+x_{CO}(j+1)+4x_{CH_4}(j+1)}{x_{H_2}(j)+x_{CO}(j)+4x_{CH_4}(j)} \quad (8)$$

Cell degradation was quantified with a degradation rate, which represented the percentage of voltage drop per 1000 hours of operation. The degradation rate was calculated using the empirical expression presented in Eq. 9, which related the degradation rate to three key operating parameters: current density, fuel utilization and cell temperature. This correlation was developed through curve fitting, which was based on data taken from experiments on two different physical SOFC test units, one located at the National Energy Technology Laboratory, and one at the Denmark Technical University [26]. The experiments measured voltage versus time for different current density and fuel utilizations at various operating temperatures and syngas compositions, and the detailed methodology was described in other works [26, 27]. Intuitively, fuel cell degradation could be accelerated by high current density, high fuel utilization, and low temperature operations.

$$r_d = \frac{0.59FU+0.74}{1+\exp\left(\frac{T-1087}{22.92}\right)}\left(e^{2.64i}-1\right) \quad (9)$$

6.5 Test Procedure

The purpose of this work was to simulate a pressurized IGFC plant taking into account variability of syngas compositions, corresponding to different gasifier technologies and coal types. Based on a previous study, four different syngas compositions were chosen: (i) a fuel composition with low methane content produced by Texaco entrained flow gasifier [28], (ii) a moderate methane content fuel from the British Gas Lurgi (BGL) pressurized moving bed gasifier [28], (iii) a modified fuel composition from the BGL gasifier with double methane content [16], and (iv) a benchmarking high methane syngas composition (17%) used by the International Energy Agency (IEA) [29].

In addition, humidified hydrogen with 10% steam was also used in this study as a baseline case, although the empirical data used for developing the degradation rates as a function of temperature, current density and fuel utilization were based on a syngas fuel [26]. A summary of the gas compositions is shown in Table 6.1.

The fuel cell subsystem was simulated using 1-dimensional (1D) real-time fuel cell dynamic model where the following constraints were applied to the system:

a. The power output was kept constant in all five cases in order to compare the system performance with the same power demand of 450 kW
b. Fuel utilization was kept constant at 80%

c. Average cell temperature was maintained as close as possible to 800°C, since this is the optimum compromise to have high efficiency, low degradation and safe condition for the ceramic electrolyte [19, 20].
d. The estimation accuracy of the cell degradation rate on different fuel compositions, particularly for humidified hydrogen is not validated, since no experimental data are available. However, it is expected that the cell degradation rate for the systems operated with humidified hydrogen is also a function of current density and fuel utilization. Even so, qualitative distributions of degradation rate along the cell would be fairly relevant.

Table 6.1: Fuel compositions studied for SOFC systems (mole %).

Fuel	**CH_4**	**CO**	**CO_2**	**H_2**	**H_2O**
Humid Hydrogen, **HH**	0.0	0.0	0.0	90.0	10.0
Texaco syngas, **M0**	0.08	19.1	6.91	14.3	58.6
BGL syngas, **M3.5**	3.56	27.2	1.87	14.5	53.0
BGL+ syngas, **M7.0**	7.12	27.0	1.83	14.6	47.5
IEA syngas, **M17**	17.10	2.94	4.36	26.3	49.3

To reduce potential inaccuracies in simulating the cell degradation rate for different fuel compositions, the solid temperature difference between the cell entrance and the cell exit, which strongly affects the distributed performance of current density and electrochemical activities in the cell, was maintained approximately at 120 °C across the fuel cell length.

In order to satisfy the aforementioned constraints, current load, fuel flow, air flow, and inlet temperature of cathode air were varied in the five tests, with the final values shown in Table 6.2. The system fed with humidified hydrogen required the lowest fuel cell current load, fuel flow demand, cathode air flow and inlet temperature to produce 450 kW at the specified fuel utilization and average operating temperature. In contrast, the system fueled with Texaco type-syngas M0 had to be operated at the highest current load, fuel supply, and cathode air flow, which was due to its lowest methane and hydrogen contents.

To mitigate the cooling impacts on the system operated with high methane IEA syngas M17, lower air flow was required to maintain the system at the desired temperature, in comparison to other syngas operations. The results of steady state performance of fuel cell subsystem using all five different fuel compositions were recorded and presented herein.

Table 6.2: Fuel cell stack inputs for different fuel compositions

Fuel	**Current density (A/cm^2)**	**Fuel flow (g/s)**	**Cathode air flow (kg/s)**	**Cathode air inlet temperature (°C)**
HH	0.527	13.7	0.84	665
M0	0.583	215.0	1.40	675
M3.5	0.563	129.0	1.28	690
M7.0	0.553	97.0	1.19	705
M17	0.545	59.0	1.17	730

6.6 Results and Discussion

6.6.1 Composition Gradients

The distributed profiles of methane (CH_4) composition gradients along the fuel cell length are illustrated in Figure 6.1. For the three syngas cases with significant CH_4 content (i.e. syngas M3.5, M7.0, and M17), complete consumption of CH_4 was observed approximately half way down the fuel cell length. These dynamics were the results of operating the fuel subsystem at a similar fuel cell current load, in a range of 0.545 A/cm^2 to 0.563 A/cm^2 (Table 6.2).

The significant CH_4 conversion at the beginning of the cell would be reflected in the reduction of fuel cell solid temperature. Since it was assumed that the steam-methane reforming follows the first order kinetics corresponding to CH_4 partial pressure, the operation of the highest methane IEA syngas case demonstrated a more rapid CH_4 conversion, followed by syngas M7.0 and M3.5.

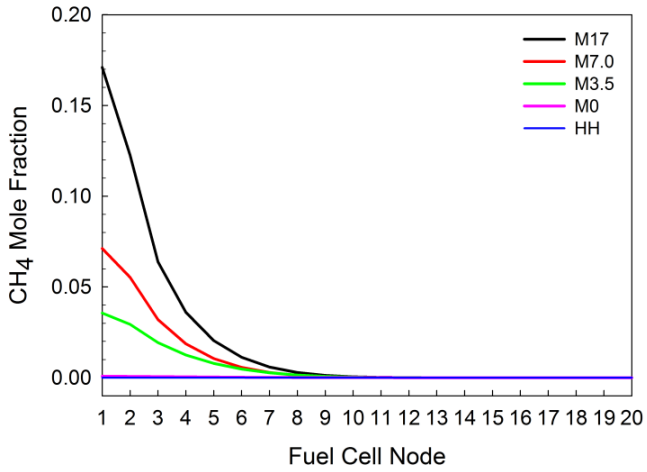

Figure 6.1: Distributed profiles of CH_4 mole fraction for the five fuel compositions studied

The corresponding dynamics of carbon monoxide (CO) mole fraction are presented in Figure 6.2. The changes in CO mole fraction in syngas were primarily driven by water-gas shift reactions. For syngas compositions with high CO contents (i.e. syngas M0, M3.5, and M7.0), CO reduced drastically at the first two nodes by slightly more than half from its initial composition. This was because of the shift in equilibrium condition in water-gas shift reaction toward the product side.

In contrast, in the case of high methane IEA syngas, the water-gas shift reaction equilibrium was shifted toward the reactants, since the fuel used contained very low CO and relatively higher H_2 and CO_2. The formation of CO was also induced by the steam-methane reformation. As such, no reduction was found at the cell entrance in the case of high methane IEA syngas. Carbon monoxide in IEA syngas M17 moderately increased to the highest mole fraction of 10% at node 9, 45% of the length of the channel, followed by reduction in CO toward the end of the cell as H_2 was consumed.

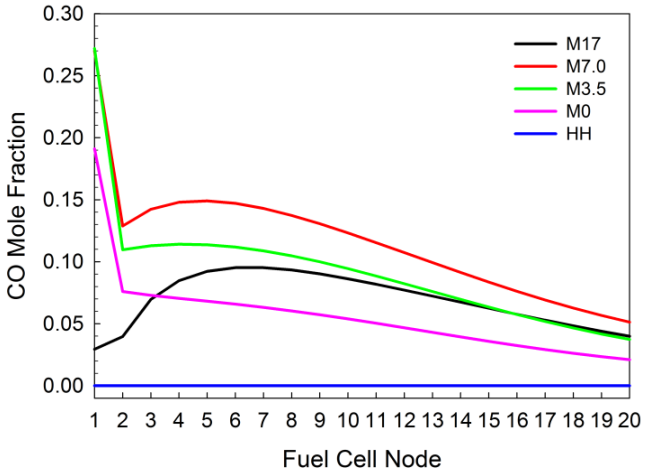

Figure 6.2: Distributed profiles of CO mole fraction for the five fuel compositions studied

Without methane content in syngas M0, CO started to decrease gradually after node 2 to the lowest value at the end of the cell. But, owing to the generation of CO and H_2 from methane reformation in syngas M3.5 and M7.0, slight increases in CO were demonstrated after node 2 to around 30% of the fuel cell length, before dropping afterwards. Theoretically, the depletion in CO mole fraction in the second half of the fuel cell length was associated with hydrogen consumption, which promoted the equilibrium of water-gas shift more toward product side. This ultimately contributed to the CO consumption.

The associated response of H_2 composition gradient across the fuel cell subsystem for all five different compositions is illustrated in Figure 6.3. For the case of humidified hydrogen as shown in Figure 6.3, the highest H_2 mole fraction was localized at the cell inlet, featuring a gradual reduction along the length of the cell as a result of H_2 oxidation. A total reduction of 80% in H_2 mole fraction for the humidified hydrogen operation was observed at the cell exit. Meanwhile, the trends in H_2 mole fraction for all syngas systems were almost identical, where the highest values were found at around 10% to 30% of the fuel cell length.

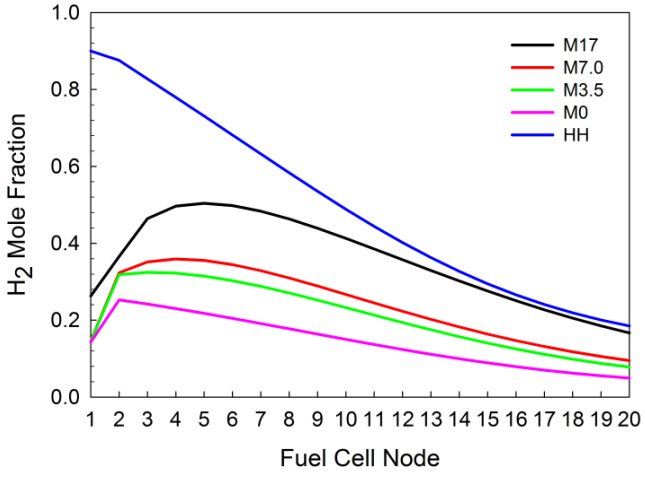

Figure 6.3: Distributed profiles of H_2 mole fraction for the five fuel compositions studied

For Texaco syngas M0 that does not have significant methane and lower amounts of CO, the H_2 mole fraction increase was only driven by the water-gas shift kinetics. Thus, in comparison to the other syngas compositions, it is clearly illustrated in Figure 6.3 that H_2 was distributed at a lower average mole fraction as compared to the other syngas compositions.

In contrast, both steam-methane reforming and water-gas shift kinetics greatly promoted the presence of H_2 in the operations using syngas M3.5, M7.0 and M17. The resulting H_2 mole fraction profiles from the syngas M3.5 and syngas M7.0 fueled systems were very close, as shown in Figure 6.3. The slight difference was due primarily to the difference in initial methane content (Table 6.1), since both systems were operated at very similar current load (Table 6.2).

Changes in CO mole fraction were reflected in the profiles of CO_2 mole fraction, as shown in Figure 6.4. Additionally, the distribution of CO_2 along the fuel cell length was also correlated to water-gas shift kinetics. But, indirect coupling effects from generation of CO via steam-methane reforming, particularly for syngas with significant methane content, contributed to the changes in CO_2 composition gradient. As shown in Figure 6.4, the dramatic increase in CO_2 at the first two nodes observed in the syngas cases with lower to moderate amount of methane (M0, M3.5, and M7.0) was primarily caused by the rapid reduction in CO due to the water-gas shift reactions.

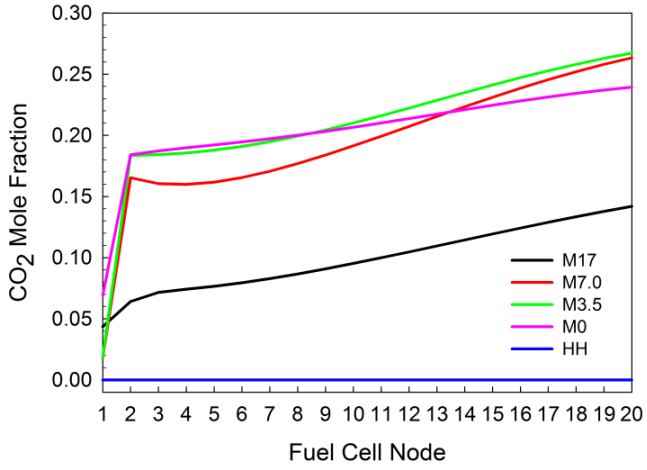

Figure 6.4: Distributed profiles of CO_2 mole fraction for the five fuel compositions studied

But after node 2, CO_2 in most syngas systems increased slowly with decreasing CO concentration because of changing in water-gas shift equilibrium to the product side. This resulted in the highest CO_2 mole fraction values at the end of the cell. Due to the interacting effects between methane reformation and water-gas shift equilibrium, CO_2 increased more moderately in the case of high methane IEA syngas M17 (Figure 6.4).

As presented in Figure 6.5, the trends of H_2O mole fraction for the three syngas cases without significant methane and moderate methane content were similar, indicating slight differences which were expected because of the initial H_2O mole fraction (Table 6.1). Overall, the changes in H_2O mole fraction were driven by steam-methane reforming and

water-gas shift kinetics in the first half of the cell and electrochemical oxidation in the second half of the cell, similar to the H_2 mole fractions shown in Figure 6.3 and resulting in a qualitative reflection of the those trends.

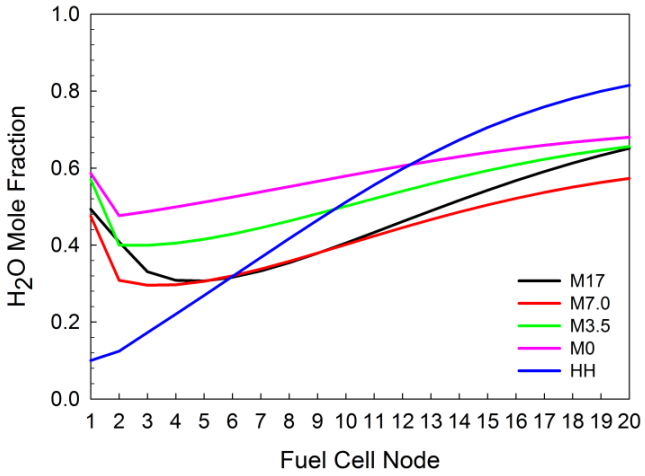

Figure 6.5: Distributed profiles of H_2O mole fraction for the five fuel compositions studied

6.6.2 Fuel Utilization

Distributed data for fuel utilization in response to all five compositions studied is shown in Figure 6.6. As a consequence of operating the fuel cell subsystem at 80% fuel utilization for 450 kW power production, the localized fuel utilizations were varied significantly, depending on the consumption of hydrogen presented in Figure 6.3 as well as the availability of CH_4 and CO shown in Figures 6.1 and 6.2.

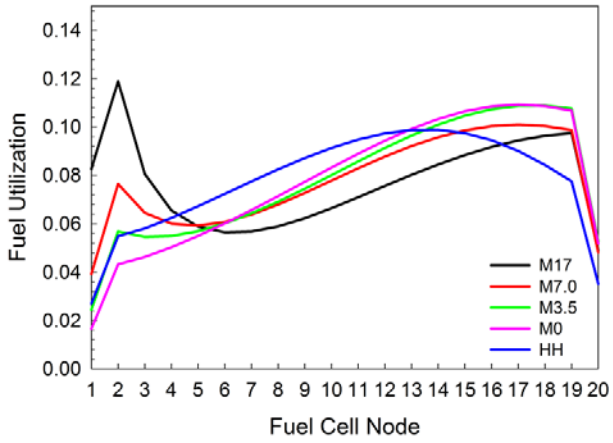

Figure 6.6: Distributed data of fuel utilization for the five fuel compositions studied

For all case studies, it was observed that there was a rapid increase in fuel utilization from the cell inlet to node 2. Increasing methane content in syngas fuel compositions increased the peak of fuel utilization at this particular position, resulting from rapid conversion of CH_4 at the cell entrance.

As depicted in Figure 6.6, the distributed fuel utilization of humidified hydrogen clearly contrasted the syngas profiles. The fuel utilization for syngas without significant amount of methane, M0, as shown in Figure 6.6, was quite close to the trend of humidified hydrogen operation.

But, the case of humidified hydrogen demonstrated higher fuel utilization at the beginning of the cell, and lower fuel utilization at the end of the cell than the observed profile in syngas M0. Meanwhile, for the remaining cases, the systems resulted in two clear peaks in fuel utilization at the beginning as well as at the end of the cell, before dropping in the last 10% of the fuel cell length.

6.6.3 Fuel Cell Solid Temperature

The responses of fuel cell solid temperature are shown in Figure 6.7, whereas the associated profiles of temperature gradient, dT/dx, along the fuel cell length are presented in Figure 6.8. The temperature gradient was calculated based on the temperature change occurred between the respective nodes.

As shown in Figure 6.7, all cases demonstrated non-linear increase in temperature along the cell from inlet to outlet with a constant solid temperature difference between the fuel cell inlet and the outlet. Variations in the average fuel cell temperature for each case are summarized in Table 6.3.

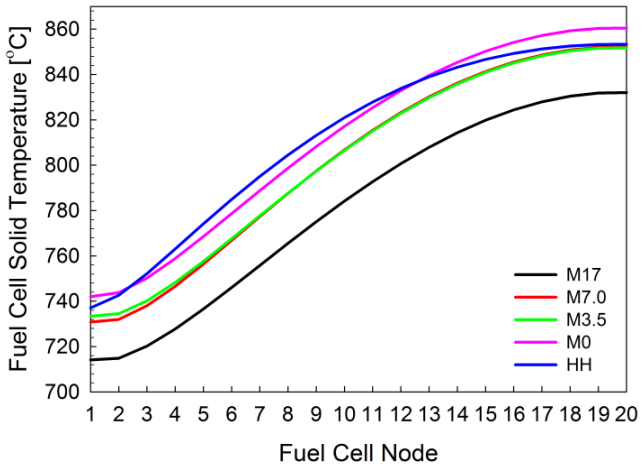

Figure 6.7: Distributed data of fuel cell solid temperature for the five fuel compositions studied

The fuel cell solid temperature for high methane IEA syngas was distributed at the lowest average temperature among the cases tested, as shown in Figure 6.7. However, in

comparison to the other syngas operations as summarized in Table 6.2, less cathode air mass flow was required for this system, such that the average operating temperature could be maintained at around 800 °C since the cooling impact of steam-methane reformation was stronger. In addition, this system was only operated at a lower current density, which was expected to result in a lower heat generation in the fuel cell. Lowering methane content in syngas increased the average fuel cell temperature, and thereby, more cathode air flow was required to cool down the system.

Table 6.3: Average fuel cell solid temperature

Case Study	HH	M0	M3.5	M7.0	M17
Average Temperature, (°C)	811	811	802	802	782

Unlike syngas cases, the resulting average solid temperature for humidified hydrogen was the highest, closely following the trend in syngas M0 operation. But, the humidified hydrogen system was operated at far less current load, fuel flow, cathode air flow, as well as cathode air inlet temperature in order to produce approximately the same power, 450 kW, at 80% fuel utilization. This was driven primarily by a greater partial pressure of H_2 in the system for electrochemical oxidation along the cell.

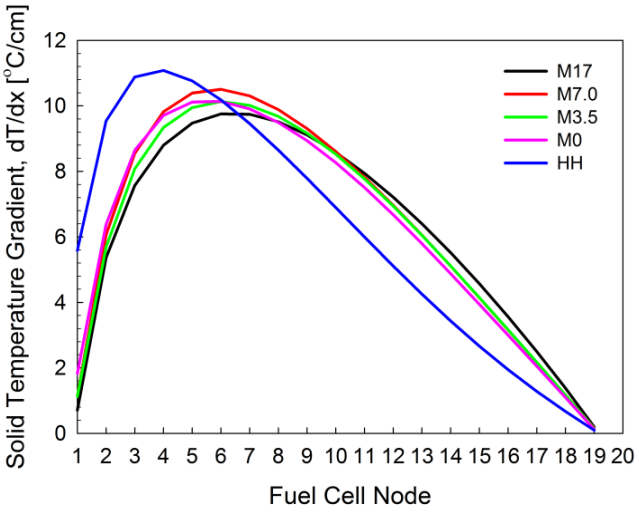

Figure 6.8: Distributed data of fuel cell solid temperature gradient, dT/dx for the five fuel compositions studied

Although the average fuel cell solid temperature for humidified hydrogen and BGL syngas M0 were the same, there was significant difference in the distribution of temperature gradient across the channel. As a result of operating the hydrogen fueled system at average temperature of 811 °C with approximately 120 °C temperature difference, the maximum temperature gradient, 11.5 °C/cm, was indicated between node 4 and node 5. This value was the greatest temperature gradient among all five case studies. In comparison to the syngas compositions, the humidified hydrogen operation resulted in higher temperature

gradient in the first 30% of the fuel cell length, following by a lower temperature gradient in the remaining sections.

As can be seen in Figure 6.8, the temperature gradient across the cell was fairly constant for all syngas cases, indicating the highest dT/dx between node 6 and node 7, approximately at 9.5 °C/cm to 10.5 °C/cm.

6.6.4 Nernst

The corresponding effects on Nernst potential for each case study are presented in Figure 6.9, showing higher Nernst potential at the upstream region of the cell for all compositions studied. Nernst potential increased with increasing H_2 mole fraction shown in Figure 6.3, and decreasing fuel cell solid temperature shown in Figure 6.7.

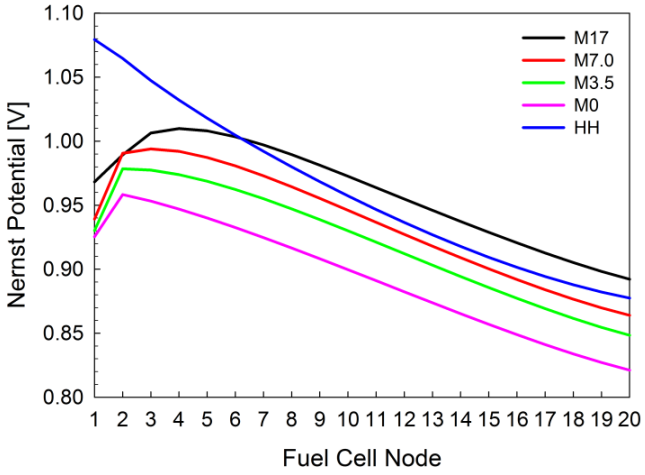

Figure 6.9: Distributed data of Nernst potential for the five fuel compositions studied

6.6.5 Current Density

The profiles of localized current density for all five cases studied at the nominal conditions are shown in Figure 6.10, indicating the maximum level at the cell entrance for humidified hydrogen and at around 50% of the fuel cell length for syngas compositions.

Although the system fueled with humidified hydrogen was operated at the lowest average current load, 0.527 A/cm² (Table 6.2), this case resulted in the highest localized current density at the beginning of the cell, 0.68 A/cm². It is apparent that the highest current density of the humidified hydrogen fueled system was achieved at the highest H_2 mole fraction, decreasing gradually to the lowest current density at the cell exit as H_2 decreased.

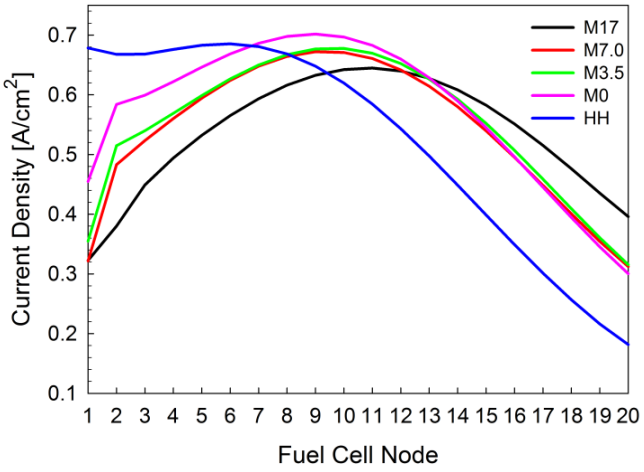

Figure 6.10: Distributed data of current density for the five fuel compositions studied

The case of syngas M0 demonstrated the highest localized current density of 0.70 A/cm^2 at node 9. For syngas operations, it was demonstrated that the maximum current density reduced with increasing methane content, and shifted toward the end of the cell. The same maximum current density, 0.67 A/cm^2, was obtained for the case of Texaco syngas M3.5 and M7.0, operating at 0.563 A/cm^2 and 0.553 A/cm^2 respectively. From the detailed analysis, a higher current density for syngas cases was found at relatively higher H_2 mole fraction, Nernst potential, and fuel cell solid temperature.

6.6.6 Degradation Rate

The impacts of fuel cell degradation in response to different fuel compositions fed into the system are illustrated in Figure 6.11. The distribution of localized degradation rate impacts in all cases studied was strongly coupled to the current density, fuel utilization, and fuel cell solid temperature, as described in previous studies [26, 27, 30]. Since the average temperature was maintained close to 800 °C in all the cases, degradation rate profiles are dominated by local current density.

For the humidified hydrogen case, the peak in local current density was shown at the cell inlet, and then current density gradually decreased toward the end of the cell. In addition, the lowest solid temperature was located in the beginning of the cell as well, contributing to increment degradation rate. For these reasons, for hydrogen higher degradation rate (3.65%/1000 hr) was observed at the beginning of the cell, as indicated in Figure 6.11. As current density uniformly decreased and solid temperature increased along the cell, the degradation rate showed a slow decrement within the first 30% of the fuel cell length, followed by a substantial reduction from the 3%/1000 hr in node 6 to 0.5%/1000 hr in node 13. In the last part of the cell, where current density was low and solid temperature reached 840 °C, local degradation rate was found to be less than 0.2%/1000 hr. The increase in fuel utilization at the cell downstream that should have aggravated the degradation

impacts was offset by greater influence of reduced current density and increased solid temperature.

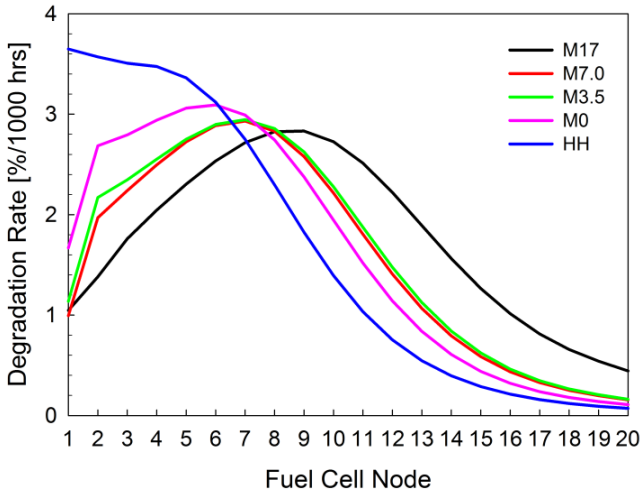

Figure 6.11: Distributed data of degradation rate impacts for the five fuel compositions studied

For the syngas cases, variations in localized degradation showed a strong dependence on the methane content in the fuel. Accordingly, the fuel cell degraded faster at the higher current density region which was within the first half of the cell, before decelerating gradually to the exit with increasing fuel cell solid temperature. The maximum degradation rate decreased and shifted toward the cell exit with increasing methane content. But, for methane-fueled operations the minimum solid temperature and the maximum current density were not located in the same node. The upstream region of the fuel cell was primarily used for steam-methane reforming and water-gas shift, which contributed to decrease the solid temperature and increase fuel utilization, and hence induce higher degradation rate even if the generated current in this first part of the cell was significantly lower than in the hydrogen case. In Figure 6.10 it is possible to see that for syngas M17, current density in the first node presented the same value as for hydrogen at node 16 (0.32 A/cm^2), but the two associated degradation rates were substantially different: 1%/1000 hr for syngas M17 at node 1 and 0.2%/1000 hr for humidified hydrogen at node 16. This significant difference was mainly caused by the different temperatures. At the cell outlet, the degradation rate was higher with increasing content of methane in the fuel, due to higher current density and fuel utilization.

Increasing the amount of methane in the syngas, a lower average current density was required in order to maintain the same power output, and it contributed to obtain a minor peak in local current density and consequently in degradation rate. But, the distributions of current density and temperature along the cell resulted in higher degradation rate at the cell outlet when the methane content was higher, and in a more evenly distributed degradation rate profile. In contrast, in hydrogen-fueled operation, degradation rate was concentrated in the very first part of the fuel cell, where the negative impacts of current density and temperature on degradation were summed to each other.

When the fuel cell is fed with hydrogen, this degradation rate distribution could be critical, because if the degradation rate is high enough it could result in a quick failure of the beginning of the cell. On the other hand, humidified hydrogen presented the lowest overall degradation rate, as Table 6.4 shows, thanks to a lower required average current density. In order to understand the impact of fuel composition on the fuel cell life time assessment, a more complex analysis would be recommended.

The maximum localized and average degradation rate impacts for all five cases are presented in Table 6.4. Overall degradation was calculated with average current density, average temperature and global fuel utilization. The maximum localized degradation rate for the cases varied in a range between 2.83%/1000 hr to 3.65%/1000 hr, in the order of M17<M7.0<M3.5<M0<HH. The reverse was observed for the overall degradation in each case. It implies that with a higher amount of methane in the fuel, the cell would degrade more uniformly but significantly faster. With syngas M17 the overall degradation was 60% higher than with humidified hydrogen, while the maximum localized degradation rate was only 30% lower compared with the hydrogen-fueled system.

Although the fuel cell behaviour in the long term can be inferred from these results, a more complete work will be necessary to evaluate the cell lifetime. As part of the cell degrades, it would result in an increase of the impedance, which would change the current density distribution as well as all the other parameters. Hence, the degradation distribution along the cell would vary during time. In addition, in order to maintain constant power as the voltage degrades, the average current density needs to be increased, and this would significantly affect the degradation rate. A time-dependent analysis of fuel cell degradation has been done previously for a single syngas composition [27]. However, a vast space is open for future investigations.

Table 6.4: Maximum degradation rates

Case Study	**HH**	**M0**	**M3.5**	**M7.0**	**M17**
Localized degradation rate (%/1000 hr)	3.65	3.09	2.94	2.93	2.83
Overall degradation rate (%/1000 hr)	1.89	2.24	2.50	2.41	3.05

6.7 Conclusions

The impacts of fuel compositions on degradation rate for fuel cell subsystems in IGFC were evaluated at a steady state condition for a fixed power production. Four different syngas compositions with variety of methane and carbon contents, as well as humidified hydrogen fuel with 10% steam were tested.

A comparison of the fuel cell distributed performance revealed that the highest degradation rate was localized at the beginning of the cell for the humidified hydrogen case, and at 30% to 45% of the fuel cell length for the syngas compositions. However, syngas operations resulted in more distributed localized degradation rate across the fuel cell length at a lower risk.

For the analysis of localized degradation rate, the highest value of 3.65%/1000 hr was observed in the humidified hydrogen operation, whereas the lowest rate of

2.83%/1000 hr was recorded in the IEA syngas case. Meanwhile, the overall degradation rate for the humidified hydrogen case was the lowest at 1.89%/1000 hr, and the IEA syngas resulted in the highest overall rate of 3.05%/1000 hr.

Although the beginning of the cell was exposed to higher localized degradation for humidified hydrogen, power generation could be maintained as the current density shifted toward the cell exit, implying that a greater lifetime would be realized from the lower overall degradation. This would assume no catastrophic cell failure due to high localized degradation. The converse was observed for the methane rich IEA syngas case, where the overall degradation rate was highest and localized degradation was indicated in the middle of the cell. The other syngas cases fell between the HH and M17 cases, indicating a high correlation between degradation and methane content.

6.8 References

[1] Verma, A., Rao, A. D, and Samuelsen, G. S., 2006, "Sensitivity Analysis of a Vision 21 Coal Based Zero Emission Power Plant", J. Power Sources, 158(1), pp. 417-427.

[2] Colpan, C. O., Yoo, Y., Dencer, I., and Hamdullahpur, F, 2009, "Thermal Modeling and Simulation of An Integrated Solid Oxide Fuel Cell and Charcoal Gasification System," AICHE J. Environ. Prog. Sustain. Energy, 28(3), pp. 380-385.

[3] Perdikaris, N., Panopoulos, K. D., Fryda, L., and Kakaras, E., 2009, "Design and Optimization of Carbon-free Power Generation Based on Coal Hydrogasification Integrated with SOFC," Fuel, 88(8), pp. 1365-1375.

[4] Spallina, V., Romano, M. C., Campanari, S., and Lozza, G., 2011, "A SOFC-Based Integrated Gasification Fuel Cell Cycle With CO_2 Capture," ASME J. Gas Turbines Power, 133, pp. 071706-071706-10.

[5] Li, M., Rao, A. D., Brouwer, J., and Samuelsen, G. S., 2011, "Effects of carbon capture on the performance of an advanced coal-based integrated gasification fuel cell system," *Proceedings of the Institution of Mechanical Engineers Part A: Journal of Power and Energy*, Vol. 225.

[6] Li, M., Powers, J. D., and Brouwer, J., 2010, "A Finite Volume SOFC Model for Coal-based Integrated Gasification Fuel Cell Systems Analysis," ASME J. Fuel Cell Sci Technol., 7(4), 041017-041017-12.

[7] Adams, T. A. II, and Barton, P. I., 2011, "Combining Coal Gasification, Natural Gas Reforming, and Solid Oxide Fuel Cells for Efficient Polygeneration with CO_2 Capture and Sequestration," Fuel Process. Technol., 92(10), pp. 2105-2115.

[8] Ghosh, S., and De, S., 2003, "Thermodynamic Performance Study of an Integrated Gasification Fuel Cell Combined Cycle—an Energy Analysis," Proc. Inst. Mech. Eng., Part A, Vol. 217, pp. 137–147.

[9] U.S. Department of Energy, National Energy Technology Laboratory, "*Industrial Size Gasification for Syngas, Substitute Natural Gas and Power Production*," Final report, 2007, DOE/NETL-401 / 040607.

[10] Bao, J., Krishnan, G. N., Jayaweera, P., Perez-Mariano, J., and Sanjurjo, A., 2009, "Effect of Various Coal Contaminants on the Performance of Solid Oxide Fuel Cells: Part I. Accelerated Testing," J. Power Sources, 193(2), pp. 607-613.

[11] Trembly, J. P., Marquez, A. I., Ohrnl, T. R., and Bayless, D. J., 2006, "Effects of Coal Syngas and H_2S on the Performance of Solid Oxide Fuel Cells: Single-cell tests," J. Power Sources, 158(1), pp. 263-273.
[12] Hackett, G., 2009, "Interaction of Nickel-based SOFC Anodes with Trace Contaminants from Coal-derived Synthesis Gas," *PhD Thesis*, College of Engineering and Mineral Resources at West Virginia University, Morgantown, WV.
[13] Liu, R. R., Kim, S. H., Taniguchi, S., Oshima, T., Shiratori Y., Ito, K., and Sasaki K., 2011, "Influence of Water Vapor on Long-Term Performance and Accelerated Degradation of Solid Oxide Fuel Cell Cathodes," J. Power Sources, 196(17), pp. 7090-7096.
[14] Hagen, A., Barfod, R., and Hendriksen, P. V., 2006, "Degradation of Anode Supported SOFCs as a Function of Temperature and Current Load," J. Electrochem. Soc., 153(6), pp. A1165-A1171.
[15] Hagen, A., Liu, Y. L., Barfod, R., and Hendriksen P. V., 2008, "Assessment of the Cathode Contribution to the Degradation of Anode-Supported Solid Oxide Fuel Cells," J. Electrochem. Soc., 155(10), pp. B1047-B1052.
[16] Dey, T., Singdeoa, D., Pophaleb, A., Bosea, M., and Ghosha, P. C., 2013, "SOFC Power Generation Systems by Bio-gasification," *4th International Conference on Advances in Energy Research (ICAER 2013)*, Bombay, India, Vol. 54, pp. 748-755.
[17] Suwanwarangkul, R., Croiset E., Entchev, E., Charojrochkul, S., Pitzker, M.D., Fowler, M.W., Douglas, P.L., Chewathanakup, S., and Mahaudom, H., 2006, "Experimental and Modeling Study of Solid Oxide Fuel Cell Operating with Syngas Fuel," J. Power Sources, 161(1), pp. 308-322.
[18] Jiang, Y., and Virkar, A. V., 2003, "Fuel composition and Diluent Effect on Gas Transport and Performance of Anode-supported SOFCs," J. Electrochem. Soc., 150(7), pp. A942-A951.
[19] Tucker, D., Hughes, D. O., and Haynes C. L., 2011, "IGFC response to initial fuel cell load for various syngas compositions," ASME Paper No. FuelCell2011-54450.
[20] Selimovic, A., Kemm, M., Torisson, T., and Assadi, M., 2005, "Steady State and Transient Thermal Stress Analysis in Planar Solid Oxide Fuel Cells," J. Power Sources, 145(2), pp. 463-469.
[21] Janardhanan, V. M., Heuveline, V., and Deutschmann, O., 2007, "Performance Analysis of a SOFC under Direct Internal Reforming Conditions," J. Power Sources, 172(1), pp. 269-307.
[22] Hughes, D., Wepfer, W. J., Davies, K., Haynes, C., and Tucker, D., 2011, "A Real-time Spatial SOFC Model for Hardware–Based Simulation of Hybrid Systems," ASME Paper No. FuelCell2011-54591.
[23] Tucker, D., Pezzini, P., and Banta, L., 2013, "Equivalence Ratio Startup Control of a Fuel Cell Turbine Hybrid System," ASME Paper No. GT2013-94809
[24] Zhou, N., Yang, C., Tucker, D., Pezzini, P., and Traverso, A., 2015, "Transfer Function Development for Control of Cathode Airflow Transients in Fuel Cell Gas Turbine Hybrid Systems," Int. J. Hydrogen Energy, 40(4), pp. 1967-1679.
[25] Harun, N.F., Tucker, D., Adams, T.A. II, 2015, "Impact of Fuel Composition Transients on SOFC Performance in Gas Turbine Hybrids," Submitted to Applied Energy. In review.

[26] Abreu-Sepulveda, M., Harun, N. F., Hackett, G., Hagen, A., and Tucker, D., 2015, "Accelerated Degradation for Hardware in the Loop Simulation of Fuel Cell Gas Turbine Hybrids," ASME J. Fuel Cell Sci Technol., 12(2), pp. 021001-021001-7.

[27] Zaccaria, V., Tucker, D., and Traverso, A., 2015, "A Real-time Degradation Model for Hardware in the Loop Simulation of Fuel Cell Gas Turbine Hybrid Systems," ASME Paper No. GT2015-43604.

[28] Zheng, L., and Furinsky, E., 2005, "Comparison of Shell, Texaco, BGL and KRW Gasifiers as Part of IGCC Plant Computer Simulations," Energy Convers. Manage., 46(11-12), pp. 1767–1779.

[29] Achenbach, E., 1996, "*SOFC Stack Modeling, Final Report of Activity A2, Annex II: Modeling and Evaluation of Advanced Solid Oxide Fuel Cells, International Energy Agency Programme on R, D&D on Advanced Fuel Cells*", International Energy Agency, Juelich, Germany.

[30] Tucker, D., Abreu-Sepulveda, M., and Harun, N. F., 2014, "SOFC Lifetime Assessment in Gas Turbine Hybrid Power Systems," ASME J. Fuel Cell Sci Technol., 11(5), pp. 051008-051008-7.

7 CONCLUSIONS

7.1 Summary

One of the key strengths of solid oxide fuel cell gas turbine (SOFC/GT) hybrid systems is the potential of producing electricity in fuel flexible environments. It helps deals with variability in fuel composition or transition between different kinds/qualities of fuels during operations. Such transient capability is beneficial for meeting time-varying environmental regulations, flexible polygeneration (electricity and chemicals or fuels) operations, and improving profitability. However, there are several technical challenges during transient events associated with fuel cell thermal management, compressor stall and surge, and fuel cell degradation that need to be overcome before commercialization. Future dynamic controls of SOFC/GT hybrid systems must include effective control strategies to avoid operational failure and equipment damage.

Therefore, in this study, detailed characterization of SOFC/GT dynamic performance in response to fuel composition changes was performed to evaluate and identify:

1. impacts on key fuel cell parameters and their interactions,
2. impacts on the balance of the plant,
3. coupling issues between fuel cell and gas turbine subsystems,
4. operational challenges including impacts on fuel cell degradation rate, and
5. opportunities for dynamic controls of SOFC/GT hybrid systems

The dynamic behaviour of SOFC/GT hybrid systems during fuel composition changes was studied using a practical approach via hardware-based simulations. Combination of a real equipment of direct-recuperated gas turbine system (including gas turbine, compressor, heat exchangers, etc.) and a cyber-physical fuel cell subsystem (1D real-time fuel cell dynamic model, fuel cell simulator, post combustor, and air volumes) was used to take advantage of the flexibility and fidelity offered by software and hardware

respectively. Hence, the coupling exhibited by SOFC/GT hybrid systems during transient operations could be adequately captured, without high risk of destroying the most expensive equipment (i.e. fuel cell stacks). To the best of our knowledge, most existing studies of fuel composition variations focused on steady state performance, and none of them has been studied and tested with hardware simulations.

Closed loop tests using turbine speed control, with regard to a switch from coal-derived syngas to humidified methane at 14% methane (CH_4) and 86% steam were initially carried out to provide critical insights of transient response of SOFC/GT hybrid systems and system operability in a safe-operating condition. Hence, system disturbances and risk of test failure could be reduced. The results from this test were then used to determine next experimental designs.

The examination of SOFC/GT dynamic performance was continued with the analysis of open loop performance to investigate the system transient capabilities and the real coupling issues. Since a transition to 14% CH_4 content could not be performed in open loop tests due to the safety restrictions of fuel valve and turbine speed, a switch from the same syngas composition to humidified methane at 13.6% methane content was selected for open loop case. However, the results of the open loop test were not comparable to the results obtained in the closed loop test at 14% methane. Thus, it was essential to completely redo all the closed loop tests for a transition to 13.6% methane and 86.4% steam for the purpose of a fair comparison between open loop and closed loop performance.

In terms of the investigation of fuel cell degradation, a separate study was specifically conducted to quantify the effects of different syngas compositions associated with different gasifier technologies. Previously developed empirical expressions that correlated degradation rate to current density, temperature, and fuel utilization were used. It was assumed that all degradation mechanisms were aggravated by the high current density, high fuel utilization, and low fuel cell temperature.

7.2 Concluding Remarks and Contribution

The specific key findings of this study were summarized in the following list:

Exploration study of fuel composition changes from coal-derived syngas to humidified methane via closed loop tests:

1. Fuel composition changes in SOFC/GT hybrid systems were basically restricted by carbon deposition in fuel cells and excessive heat change in gas turbine input. Based on the known effects of C-H-O composition on carbon deposition, the maximum limit of carbon deposition avoidance for humidified methane would be around 43% methane (CH_4) content. As opposed to only a 20% allowable change in gas turbine thermal input (fuel cell thermal effluent), this transient resulted in a 500% increase.

2. Switching the fuel cell anode feed from the coal-derived syngas (CH_4 0%, CO_2 12.0%, CO 28.6%, H_2 29.1%, H_2O 27.1%, N_2 3.2%) to humidified methane (CH_4 17.0%, H_2O 83.0%) represented a transition to an equivalent lower heating value (LHV) fuel. However, scoping studies showed that this transient would cause destruction of

turbomachinery in the HyPer facility due to rapid transient increase (60%) in fuel cell thermal effluent.

3. Further study showed that changing the fuel to humidified methane containing 14% CH_4 content was found to be viable for closed loop operation using turbine speed control.

4. For closed loop tests using 14% CH_4 content, the system demonstrated a 17% transient increase in fuel cell thermal effluent immediately after the step change in spite of a 17.4% reduction in LHV from the syngas. The fuel cell thermal effluent remained higher than the initial state for about 40 minutes before decreasing toward the final steady state.

5. The results obtained in real-time simulations (remark #4) contrasted the steady state analysis. It was expected that the system would experience an 8% reduction in fuel cell thermal effluent following the step change. And in fact, in real-time simulations, this was observed after approximately two hours from the composition change.

Comparison of open loop and closed loop performance based on a transition from coal-derived syngas to humidified methane (13.6% CH_4 content):

1. Fuel cell solid temperature was determined as the primary linking event during fuel composition changes that drove many mechanisms in the fuel cell subsystem. Therefore, the difference in solid temperature between open loop case and closed loop case caused the difference in the transient response of many other fuel cell parameters.

2. The cell inlet was most likely to have high risk for detrimental temperature gradients in response to fuel composition changes from coal-derived syngas to humidified methane. This was primarily driven by domination of steam methane reforming over other processes. Beginning with a maximum temperature gradient of 11 K/cm at node 5 during the initial steady state, a maximum of 17 K/cm temperature gradient was found at node 7 250 s after the fuel composition transition.

3. For open loop case, a total 100 K reduction in solid temperature at the cell inlet was observed over 5500 s test. However, the cell inlet experienced 50% of the total reduction in solid temperature in just 250 s after the step change.

4. Both operations using coal-derived syngas and humidified methane resulted in lower solid/gas temperature at the beginning of the cell and higher solid/gas temperature at the end of the cell. For humidified methane operations, the average fuel cell solid temperature at the final steady state in open loop case was 5.6% higher (i.e. 41 K relative difference) than in closed loop case.

5. Over the course of experiment, the local maximum point of current density shifted from the cell inlet to the cell outlet after switching the fuel from syngas to humidified methane. The maximum values of both open loop and closed loop tests were in the same range between 0.74 to 0.80 A/cm^2. Despite this, the results of closed loop case at 5500 s showed 8% higher than the results of open loop case.

6. A huge amount of fuel cell stored thermal energy was converted to chemical energy, which was evident at the initial phase of fuel composition transition. This was explained by steam methane reforming and equilibrium water-gas shift reactions through extremely high formation of H_2 and CO collocated with maximum current density on a localized basis, but extremely low fuel utilization. Ultimately, this caused the initial transient increase in fuel cell thermal effluent, which then increased thermal energy entering turbomachinery and the consequent increase in turbine inlet temperature. In general, changes in the fuel cell thermal effluent were attributed to the changes in fuel cell thermal energy stored.

7. For the operations using 13.6% CH_4 content (i.e. 20% LHV relative difference to the syngas), a 14% transient initial increase in fuel cell thermal effluent was observed in open loop test. Meanwhile, a 13% transient increase was obtained in closed loop case. The difference in fuel cell thermal effluent between both modes of tests was driven by the difference in dissipation of stored thermal energy.

8. As much as 6% turbine speed variation and 12% cathode air mass flow (from initial values) were observed in open loop, as a consequence of a 14% fuel cell thermal effluent increase. Crossover points in turbine speed and cathode air mass flow were achieved at 1600 s, 14 minutes before the crossover points in fuel cell solid temperature. A crossover point referred to a point where the value of fuel cell parameter obtained from open loop and closed loop were exactly the same.

9. A 3% difference in CH_4 content (14% CH_4 versus 13.6% CH_4) resulted in a 62% delay in crossover points associated with fuel cell solid temperature (2450 s versus 3970 s). This was due to the difference in fuel cell thermal effluent response in closed loop tests (17% increase vs 13% increase). This showed that there was a significant sensitivity to methane content. It also showed the limiting range of the applicability of the results to different compositions where methane content varied to any appreciable extent.

10. With increased cathode air mass flow and improved turbine efficiency in open loop case, the initial increase in cathode inlet air temperature was three times lower than in closed loop case in spite of higher turbine inlet temperature in the open loop case. In addition, the decreased cathode air flow in a longer open loop test helped the system to maintain constant cathode inlet air temperature at the same value as its initial condition (973 K). On the other hand, as a result of turbine speed control in closed loop case, constant cathode air flow propagated decrease in cathode inlet air temperature to about 930 K.

11. Small changes in turbine efficiency were discovered to indirectly affect heat flux of the fuel cell subsystem through variations in cathode inlet air temperature.

12. The open loop operation revealed that compressor inlet flow, compressor discharge pressure, turbine inlet pressure, cathode inlet air mass flow and pressure were strongly coupled. All of the aforementioned variables varied in the same transient trends. As much as an 8% increase before their crossover points and 10% to 12% reduction from nominal condition after their crossover points were observed. Such transients were the results of a 4% increase in turbine speed.

13. The resulting variations in cathode inlet pressure could potentially cause fuel cell destruction. Thus, this required sufficient attention in dynamic control development.

14. Without turbine speed control, the long–term performance of open loop system (i.e. after crossover points in cathode air mass flow) was better than its short-term performance. The short-term operation was limited to substantial decrease in fuel cell solid temperature, which was attributed to the initial increase in cathode air mass flow. However, further reduction in solid temperature was mitigated by the reduced cathode air mass flow in the long-term operation. This consequently helped the system to operate in less taxing conditions and achieve a faster final steady state, as compared to closed loop case.

Degradation rate analysis for various coal-derived syngas compositions:

1. The highest degradation rate for syngas compositions was localized at 30% to 40% of the fuel cell length, and at the beginning of the cell for humidified hydrogen case.

2. For the analysis of localized degradation rate, the highest value of 3.65%/1000 hr was observed in the humidified hydrogen operation, whereas the lowest rate of 2.83%/1000 hr was recorded in the IEA syngas case. Meanwhile, the overall degradation rate for the humidified hydrogen case was the lowest at 1.89%/1000 hr, and the IEA syngas resulted in the highest overall rate of 3.05%/1000 hr.

3. Although the beginning of the cell was exposed to higher localized degradation for humidified hydrogen, power generation could be maintained as the current density shifted toward the cell exit, implying that a greater lifetime would be realized from the lower overall degradation. This would assume no catastrophic cell failure due to high localized degradation. The converse was observed for the methane rich IEA syngas case, where the overall degradation rate was highest and localized degradation was indicated in the middle of the cell. It was indicated that there was a high correlation between degradation and methane content.

In summary, the fuel feed in the SOFC/GT hybrid systems could be potentially changed between different fuel types or compositions for flexible polygeneration application and/or for meeting time-varying environmental regulations, etc. In this study, it was shown that it was feasible for this hybrid system to deal with a sudden change from

coal-derived syngas to humidified methane (14% CH_4 content or less) and transition to a new steady state within two hours without adversely affected the functionality of SOFC/GT hardware. However, there were some restrictions that required careful management and sufficient dynamic controls to extend the flexibility of the system, in terms of:

a. changes in methane content between fuel compositions because of its influence on carbon deposition, steam methane reforming, and fuel cell degradation rate impacts,
b. the fuel cell thermal performance: solid temperature reduction and temperature gradient across the cell length, particularly in the first 250 s after the fuel composition changes,
c. the inverse transient response of fuel cell thermal effluent, which might cause intolerable dramatic changes in turbine speed and turbomachinery dynamics,
d. the interactive effects of variations in cathode air mass flow that strongly influenced the temperature of fuel cell subsystem.

7.3 Recommendation for Future Work

Based on the findings from this study, there appears to be interesting topics that could be undertaken to further investigate and expand the study of fuel flexibilities in SOFC/GT hybrid systems. Some of potential directions for future research are outlined as the following:

- ***Impacts of various fuel composition transitions on SOFC/GT dynamic performance***

Since this study covered the characterization of a switch from coal-derived syngas to humidified methane, the next study would be the reversed fuel composition transition, from humidified methane to coal-derived syngas using the same sets of composition. This particular direction would provide critical insights about the effects of a complete cycle of fuel composition transitions, switching to syngas and humidified methane back and forth.

In addition, different syngas composition can be used to represent different gasifier technologies or pre-reforming process. For more practical approaches, delays in fuel manifold in SOFC/GT hybrid systems might be included, which could be implemented through ramp changes in fuel composition.

- ***Coupling effects of fuel composition changes and cathode air mass flow on the dynamic performance of SOFC/GT hybrid systems***

To expand the transient capabilities of SOFC/GT hybrid systems in dealing with fuel composition transitions, the potential system variable that could be manipulated for thermal management need to be determined. This study provided some definitive evidence that cathode air flow was the key to controlling the fuel cell thermal performance but the role of cathode air mass flow was not thoroughly explored in a quantitative manner.

It was expected that reducing cathode air mass flow could help the system to avoid substantial reduction in solid temperature and/or maintaining higher fuel cell operating temperature. As such, it was possible to mitigate the dissipation of thermal energy storage into chemical energy during the process, resulting in moderate and gradual impacts on the

balance of the plant. However, methane conversion could be accelerated at high operating temperature, which then led to significant decrease in fuel cell solid temperature.

Such coupling impacts need to be considered in the development of control strategies to meet the temperature gradient constraint in the fuel cell subsystem. It is therefore necessary to study the effects of decreasing and increasing cathode air mass flow simultaneously with fuel composition changes. Different perturbations in cathode air mass flow could be investigated to provide important information of operability of SOFC/GT hybrid systems.

- ***Development of dynamic controls for SOFC/GT hybrid systems with fuel flexibilities***

If cathode air mass flow was considered for dynamic controls of SOFC/GT hybrid systems for fuel flexible applications, detailed transfer functions might be required to sufficiently explain transient trajectories of key SOFC/GT parameters. Future control strategies must consider the significant initial transient response, response delay, coupling between fuel cell and gas turbine nonlinearities, as well as the different short-term and long-term transients. Such complexity must involve more than First-Order-Plus-Dead-Time (FOPDT), since some parameters exhibited non-minimum phase behaviour.

A basic study of transfer function development was initiated, but it only emphasized the initial phase transient response [1]. Padé approximation was used to estimate the Laplace domain of the First-Order-Plus-Dead-Time (FOPDT) transfer functions. Although the developed FOPDT transfer functions were comparable to the actuator actions of cathode air mass flow investigated in previous studies, the controls have not yet been tested on the hardware [2, 3].

In the existing test facility (HyPer), management of cathode air mass flow could be realized by modulating air flow around hot air bypass valve before the cathode inlet and/or bypassing air flow around compressor discharge to the post combustor via cold air bypass. However, these final control elements also introduce additional challenges as each strategy can cause different impacts on system efficiency and gas turbine dynamics.

- ***Detailed Characterization of compressor/gas turbine dynamics***

A complete detailed analysis of system (compressor, turbine, heat exchanger, and combustor in the balance of the plant) could be another potential research direction. For example, if hot air was used to bypass flow around the fuel cell during a syngas to methane transition for thermal management, air flow to the fuel cell would change, which consequently changed air flow going through all other bypass valves (bleed air and cold air), the combustor, and every other components in the SOFC/GT hybrid system.

Ultimately this would modify component pressure losses and compressor surge margin, which were strongly coupled to the entire system reliability. Therefore, in order to have effective management of SOFC/GT transient operations, future control strategies might take into consideration the dynamics of turbomachinery simultaneously with fuel cell fuel compositions in a multi-input multi-output (MIMO) application. Although most important variables of compressor/gas turbine including the component pressure losses (PDTs) were measured in this study, detailed characterization of the turbomachinery was not performed.

- ***Impacts of fuel composition changes on SOFC/GT lifetime***

For fuel cell degradation studies, there is quite a number of directions that could be further investigated. First, the impacts of switching between syngas and humidified methane or between other sets of compositions on fuel cell degradation rate could be evaluated using hardware-based simulations. The analysis might include detailed economic assessment involving system efficiency and fuel cell lifetime. Development of real-time fuel cell models with degradation rate expressions and incorporation of such dynamic models into the hardware-based simulation are needed to accomplish this goal. Second, degradation studies could also be oriented toward management of fuel cell degradation, which might involve quantification of potential control strategies. Different control configurations could be developed and tested to verify the effectiveness and robustness for fuel cell degradation controls.

7.4 References

[1] Harun, N. F., Tucker, D., and Adams, T. A. II, 2015, "Dynamic Response of Fuel Cell Gas Turbine Hybrid to Fuel Composition Changes using Hardware-based Simulations," Computer Aided Chemical Engineering, 37, pp. 2423-2428.

[2] Zhou, N., Yang, C., and Tucker, D., 2015, "Evaluation of Cathode Air Flow Transients in a SOFC/GT Hybrid System using Hardware in the Loop Simulation," ASME J. Fuel Cell Sci. Technol., 12(1), pp. 011003-011003-7.

[3] Zhou, N., Yang, C., Tucker, D., Pezzini, P., and Traverso, A., 2015, "Transfer Function Development for Control of Cathode Airflow Transients in Fuel Cell Gas Turbine Hybrid Systems," Int. J. Hydrogen Energy, 40(4), pp. 1967-1679.